

**Towards a First Precision Measurement
of the Mass of the W-Boson
with the ATLAS Detector
at $\sqrt{s} = 7 \text{ TeV}$**

**Dissertation
zur Erlangung des Grades
"Doktor
der Naturwissenschaften"
am Fachbereich Physik, Mathematik und Informatik
der Johannes Gutenberg-Universität
in Mainz**

Christoph Zimmermann

geb. in Essen
Mainz, den 10. Juli 2016

Ich versichere, dass ich diese Arbeit selbstständig verfasst und keine anderen als die angegebenen Quellen und Hilfsmittel benutzt, sowie Zitate kenntlich gemacht habe.

I hereby affirm that this thesis has been written by me and that it is the record of work carried out by me. All passages quoted from publications or paraphrased from these sources are indicated as such. No sources and aids aside from those indicated were used.

Mainz, den 10. Juli 2016

A. Zimmermann

Advisors:

████████████████████
████████████████

Date of Defense / Tag der Verteidigung: 5. Juli 2016

Thesis committee:

1st Referee: ████████████████████████████████
2nd Referee: ████████████████████████████████

For [REDACTED]

Zusammenfassung

Als Austauschteilchen der schwachen Wechselwirkung ist das W -Boson ein zentraler Bestandteil des Standardmodells der Teilchenphysik. Seine Masse ist im Rahmen des Standardmodells ein fundamentaler Parameter, der sich nicht vollständig aus der Theorie ergibt. Nur mithilfe experimenteller Messungen solcher Größen lassen sich aus dem Standardmodell Vorhersagen über tatsächlich beobachtete Prozesse ableiten. Darüber hinaus erlaubt eine genaue Kenntnis der Masse des W -Bosons auch einen Test der inneren Konsistenz des Standardmodells. Dies ist von besonderem Interesse, da im Allgemeinen angenommen wird, dass es sich bei dem Standardmodell nur um eine effektive Theorie handelt, von der erwartet wird, dass sie eine Vereinfachung einer tieferen, weitreichenderen Theorie darstellt.

Die Messung der Masse des W -Bosons stellt sehr hohe Ansprüche an das Verständnis der Prozesse, die zu seiner Produktion führen, wie auch des Detektors, der zum Nachweis seiner Zerfallsprodukte genutzt wird. Letzteres beinhaltet insbesondere die Wahrscheinlichkeit, dass diese Zerfallsprodukte aufgezeichnet und korrekt identifiziert werden.

Der ATLAS-Detektor, beheimatet am Europäischen Labor für Teilchenphysik (CERN) nahe Genf, ist einer der fortschrittlichsten Teilchendetektoren, die gegenwärtig in Betrieb sind. Durch die weltweit unerreicht hohe Energie und Intensität der Protonenstrahlen, die vom LHC bereit gestellt werden, und die in seinem Inneren zur Kollision gebracht werden, konnten im Jahr 2011 über zehn Millionen leptonische Zerfallsereignisse von W -Bosonen bei einer Schwerpunktsenergie von 7 TeV aufgezeichnet werden. Dies lässt eine hochpräzise Messung der W -Masse zu.

Basierend auf einer aussagekräftigen Teilmenge dieser Ereignisse, entsprechend einer integrierten Luminosität von 100 pb^{-1} , wird in dieser Dissertation eine erste Messung der W -Masse mit Daten des ATLAS-Detektors im myonischen Zerfallskanal des W -Bosons vorgestellt. Das Ergebnis dieser Messung ist $M_W = 80.380 \pm 0.045(\text{stat.}) \pm 0.021(\text{sys.}) \text{ GeV}$. Darüber hinaus werden neben der eigentlichen Messung Studien präsentiert, die zu dem dafür notwendigen Detektorverständnis beigetragen haben.

Abstract

The W boson, being one of the exchange bosons of the weak interaction, is one of the fundamental particles in the Standard Model of particle physics. The value of its mass cannot be derived within the framework of the Standard Model; on the contrary, it is one of the free parameters which have to be measured experimentally in order for the Standard Model to make predictions. Moreover, an experimental determination of the mass of the W boson allows for a test of the internal consistency of the Standard Model, which is of high importance, since the Standard Model is expected to be only an effective theory. This means, that beyond a certain threshold of precision, inconsistencies within the Standard Model are expected to appear, pointing at a new, underlying theory of broader scope and explanatory power.

A precision measurement of the mass of the W boson is challenging both in terms of modeling the processes leading to its production, as well as the understanding of the particle detector with which its decay products are measured.

The ATLAS detector used for this task is one of the most advanced particle detectors currently in use. It is located at the European Laboratory for Particle Physics (CERN) close to Geneva, Switzerland. Supplied by the Large Hadron Collider with proton beams of intensities and energies never reached before in a laboratory environment, ATLAS detected more than ten million events containing leptonic decays of W bosons at a center of mass energy of 7 TeV in the year 2011. This allows for a precise measurement of the mass of the W boson.

Based on a significant sub-set of these events, corresponding to an integrated luminosity of 100 pb^{-1} , a first measurement of M_W based on muonic W boson decays observed at ATLAS, is presented in this thesis. The resulting value is $M_W = 80.380 \pm 0.045(\text{stat.}) \pm 0.021(\text{sys.}) \text{ GeV}$. Apart from the measurement itself, studies necessary for an accurate modeling of the detector are presented.

Contents

I. Introduction	1
1. Motivation	3
2. Theoretical Foundations	7
2.1. Standard Model	7
2.2. Electroweak Interaction	10
2.3. Higgs Mechanism	12
2.4. Perturbation Theory	15
2.5. Renormalization	16
3. Production of Electroweak Gauge Bosons at the Large Hadron Collider	21
3.1. Kinematics of the W and Z Production	22
3.2. Parton Distribution Functions	25
3.3. Higher-order effects	28
3.4. Underlying Event	29
3.5. Pile-up	30
3.6. Background Processes	30
3.7. Overview of Previous Measurements	32
4. Experimental Setup	35
4.1. Large Hadron Collider	35
4.2. Overview of Detectors	37
4.3. ATLAS Detector	38
4.4. Data Acquisition and Triggering	48
4.5. Event Reconstruction	49
5. Monte Carlo Simulation	55
5.1. Event Generators	55
5.2. Detector Simulation	57
5.3. Overview of Monte Carlo Samples	58
5.4. Additional Corrections	59
II. Muon Performance	65
6. Overview of Muon Efficiency Corrections	67
6.1. Tag and Probe method	70
6.2. Event Selection and Background Subtraction	70
6.3. Treatment of Uncertainties	75

7. Muon Reconstruction Efficiency	77
7.1. Methodology, Event Selection and Corrections	77
7.2. Efficiency and Scale Factor Determination	82
7.3. Comparison with Previous Results	90
8. Muon Trigger Efficiency	91
8.1. Methodology, Event Selection and Corrections	91
8.2. Efficiency and Scale factor Determination	96
8.3. Comparison with Previous Results	110
9. Muon Isolation Efficiency	111
9.1. Methodology, Event Selection and Corrections	111
9.2. Efficiency and Scale Factor Determination	116
10. Closure Test of the Obtained Scale Factors	123
10.1. Closure Test for the Z Boson Selection	123
10.2. Closure Test for the W Boson Selection	130
III. Towards a First Measurement of the Mass of the W-Boson	135
11. Overview of the Measurement	137
11.1. Reweighting	138
11.2. Fitting Procedure	138
11.3. Estimation of Uncertainties	140
12. Validation with Z Bosons	147
12.1. Selection	147
12.2. Background Estimation	150
12.3. Control Plots	150
12.4. Monte Carlo-based Cross-Checks	152
12.5. Data-based Cross-Checks	154
12.6. Results	160
13. First Measurement of the Mass of the W Boson	163
13.1. Selection	163
13.2. Background Estimation	168
13.3. Control Plots	170
13.4. Monte Carlo-based Cross-Checks	172
13.5. Data-based Cross-Checks	174
13.6. Result	179
13.7. Summary and Outlook	184
IV. Conclusion	189
14. Conclusion	191

V. Appendix	193
A. Forward Electron Performance	195
A.1. Introduction	195
A.2. Methods	198
A.3. Results	209
A.4. Conclusion	218
B. Further Results on the Study of Muon Trigger Efficiencies	219
C. Muon ID Track Efficiency	233
C.1. Methodology, Event Selection and Corrections	233
C.2. Efficiency and Scale Factor Determination	236
D. Acknowledgments	241
Bibliography	243
List of Tables	257
List of Figures	259
E. Curriculum Vitae	265

Part I.

Introduction

1. Motivation

From the earliest times, man's dream has been to comprehend the complexity of nature in terms of as few unifying concepts as possible.

Abdus Salam [1]

One of the greatest goals of modern physics is the explanation of the cosmos with a set of simple rules and through a small set of entities. The feasibility of this undertaking seems to be supported by a view back into the history of the field. Since the time of the renaissance and its rebirth of the empirical study of nature, physicists were able to describe seemingly unconnected phenomena with unified theories of ever broader scope. Beginning with Newton's insight in the 17th century, that motions on earth and of celestial bodies follow the same pattern; Maxwell's unification of electrical and magnetic phenomena with his equations for the electromagnetic field; Einstein's theories of special and general relativity, unifying mechanics, electromagnetism and gravity; up to the Standard Model of particle physics¹ which now is the state of the art, this research program turned out to be very successful. As will be explained in detail later on, it now seems as if numerous phenomena in the cosmos, as well as the evolution and origin of cosmos itself, could be explained by a set of 17 particles, 12 antiparticles and their interactions.

However, it is clear that this cannot be the final word. On the contrary, the Standard Model leaves open questions. For example, up until now it seems that gravity cannot be included in the formalism of the Standard Model. Simple approaches lead to results which in themselves indicate fundamental problems. On the other hand, General Relativity, which describes gravity extremely well, suffers from its missing modeling of quantum effects, leading to similar problems. These are, for example, the singularities predicted in black holes, as well as the singularity at the seeming beginning of the universe, the Big Bang. These singularities are expected to vanish in a unified theory.

Apart from these formal points, measurements also indicate that a large fraction of the universe cannot be explained by the Standard Model in its present form. According to the Planck satellite probe (cf. ref. [2]), almost 96% of the matter-energy content of the universe seem to consist of an unknown energy called Dark Energy and unknown particles called Dark Matter. Together, both form the Dark Universe, for which the Standard Model seems to be unable to account.

The Standard Model needs experimental input. There exist 26 (cf. ref. [3]) free parameters² — also known as physical constants — which need to be measured for the Standard

¹As is common, this will be shortened to *Standard Model* or SM.

²Ref. [3] counts these free parameters as follows: The masses of the twelve fundamental fermions; the three coupling constants of the electromagnetic, weak and strong interaction; the two parameters describing the Higgs potential; the eight mixing angles of the Pontecorvo-Maki-Nakagawa-Sakata (PMNS) and Cabibbo-Kobayashi-Maskawa (CKM) mixing matrices; and the strong CP phase, which is measured to be close or identical to zero.

1. Motivation

Model to give predictions. From a philosophical point of view, this feature is unwanted in a theory: The principle of Occam's razor, commonly applied in the natural sciences, prefers the theory with the least number of free parameters (cf. ref. [4]). This is because a false theory can be 'protected' by a large number of free parameters, since these allow for the theory to be modified in such a way as to be consistent with all measured data.

For these reasons, there is a large number of theories aiming to replace and supersede the Standard Model: Two modern and far-reaching examples are string theory and loop quantum gravitation. However, there are no experimental data preferring one or the other over the current knowledge. Therefore, it seems natural that a stepping stone towards a new theory is defining a clearer picture of the inconsistencies and shortcomings which are expected to exist within the Standard Model.

Since the discovery of the Higgs boson at the ATLAS and CMS experiments (cf. ref. [5, 6]), the Standard Model is now complete. This means, that all particles predicted by the Standard Model have been discovered, and that the internal consistency of the Standard Model can be stringently tested through precise measurements of its free parameters. One example for such a consistency test is the measurement of the mass of the top quark M_t , the Higgs mass M_H and the mass of one of the exchange bosons of the weak interaction – the mass of the W boson, M_W . In the Standard Model, all these three values are connected via quantum effects. The current state of this test is illustrated in Figure 1.1. As can be seen, the direct measurements, represented by the green bands for M_t and M_W , and by the bold gray line for M_H , show an agreement at the 2σ level. As can also be seen, this test is limited by the current knowledge of M_W and very sensitive to its uncertainty.

This thesis presents work leading to an improvement of this consistency test — a precision measurement of M_W at the ATLAS experiment. For comparison, the current value of the world average is (80.385 ± 0.015) GeV (cf. ref. [8]). This corresponds to a relative uncertainty of 1.9×10^{-4} , indicating the high level of precision needed in all studies leading up to the final measurement.

It is structured as follows: Section 2 contains a detailed discussion of the Standard Model, followed by an introduction to the process of its production at the Large Hadron Collider in Section 3. In the latter, the kinematics and the connection between the observables accessible at ATLAS and the mass of the W boson will also be laid out. The experimental setup is described in Section 4, and the method to obtain precise theoretical predictions through simulations — a prerequisite to the measurement — is discussed in Section 5.

Part II deals with studies performed in order to improve the understanding of the detector, necessary for realistic simulations. These studies resulted in a set of correction factors for the simulations used, also known as scale factors. Chapter 6 gives an introduction to the method for obtaining the necessary event samples; to the estimation and correction of the background admixtures; and to the calculation of the scale factors and their uncertainties. In Chapter 7 the studies performed to obtain the scale factors for the muon reconstruction efficiency are presented. A similar discussion for the muon trigger and isolation efficiencies is found in Chapter 8 and Chapter 9, respectively. Part II of the thesis is concluded by a closure test of the obtained scale factors in Chapter 10.

In Part III all these discussions will be synthesized in order to perform a first measurement of the mass of the W boson with muons in the final state at ATLAS. It begins with an introduction to the fitting method, including the sources and propagation of uncertainty on the final result in Chapter 11. This is followed by a closure test of the analysis chain in Chapter 12, where Z events were selected and the mass of the Z boson, M_Z , was measured. Since the world

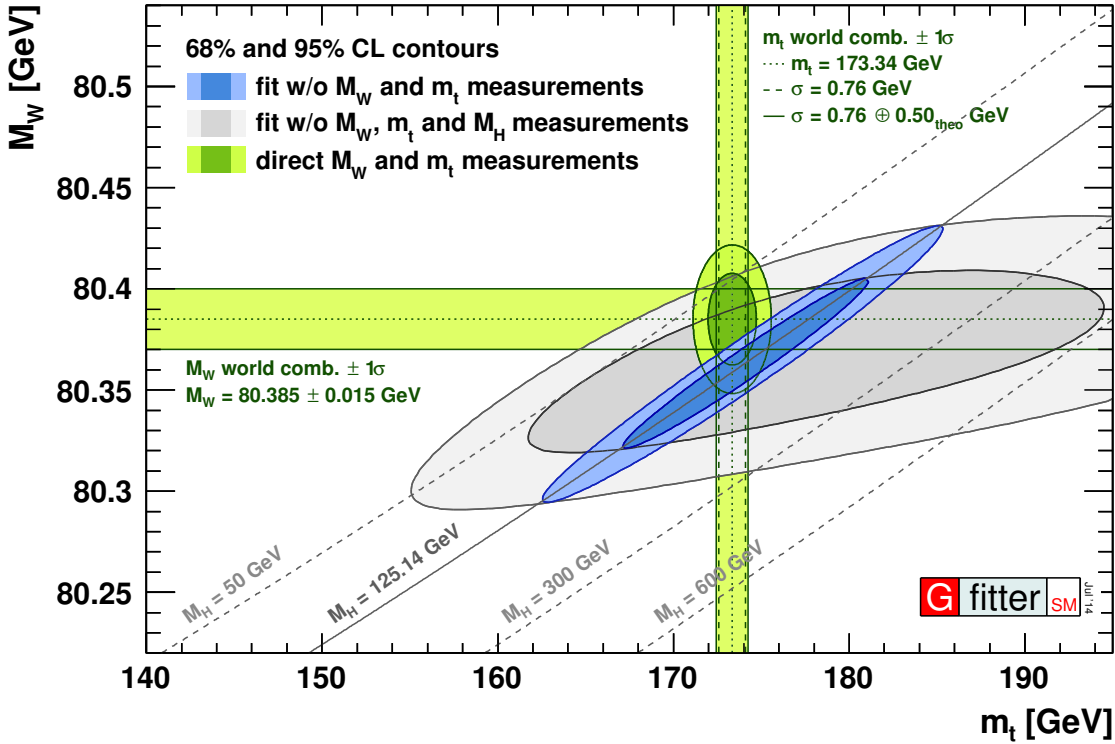


Figure 1.1.: Current state of the consistency test of the Standard Model via the mass of the W boson M_W , of the Higgs boson M_H and of the top quark M_t . The x axis shows the mass of the top quark, the y axis that of the W boson. The dashed gray diagonal lines represent hypothetical masses of the Higgs boson, while the bold line represents the mass obtained at ATLAS and CMS. The gray contours represent the 68% and 95% confidence intervals if M_W , M_H and M_t are excluded from the fit to the Standard Model, while the blue contour includes the direct measurement of M_H . Taken from ref. [7].

average of M_Z (cf. ref. [8]) was used in the calibration of the muon momentum scales, this measurement is expected to reproduce this value. Finally, in Chapter 13 the first measurement of the mass of the W boson with a sub-set of the data gathered in 2011 is discussed.

The appendix contains a study performed with electrons in the final state, using data gathered in 2012, in Appendix A. In this study, an identification algorithm for electrons close to the beam axis, so-called *forward electrons*, based on machine learning techniques was derived; and associated scale factors for the Monte Carlo simulation used were obtained. Using these electrons, studies of kinematic regions otherwise inaccessible to the ATLAS detector can be performed, including such which are expected to reduce the systematic uncertainty on M_W significantly. In addition, the appendix contains a discussion of the muon reconstruction efficiency in the inner detector in Appendix C, which acts as a prerequisite for the studies discussed in Part II.

As is common in high energy physics, natural units with $\hbar = c = 1$ are used throughout this thesis. Furthermore, anti-particles are denoted by the same name as the particles they correspond to. In particular, *electron* denotes both e^- and e^+ , and *muon* both μ^- and μ^+ .

2. Theoretical Foundations

The Standard Model explains and summarizes most of the results obtained so far in physics. It allows for very precise predictions, able to be tested experimentally with high accuracy, as highlighted by the results of global fits discussed above. The following discussion of the theoretical foundations for this thesis is built on ref. [8–10].

2.1. Standard Model

The Standard Model is defined by its particle content and the rules describing the interaction of these particles. Four forces — or interactions — are known in nature: Gravity, electromagnetic interaction, as well as the weak and strong interaction.

Gravity, while playing a large role on the scales of the visible universe, usually plays a negligible role in particle physics. For the results presented in this thesis, no discernible effect is expected. This can easily be seen by comparing the typical strength of the electric and gravitational attraction between the particles involved: For two protons, the electromagnetic force is 36 orders of magnitude larger. Interestingly, it is unclear whether gravity can be described in the framework of the Standard Model at all. It is expected that the interaction is mediated by so-called *gravitons*, particles with spin 2.

The *electromagnetic interaction* acts on particles with non-zero electric charge Q . It is mediated by photons. In the Standard Model, it is the only force which acts on long range due to the fact that photons are massless and do not carry an electric charge. The quantum field theory of electromagnetic interactions is called Quantum Electrodynamics (QED).

The *weak interaction* acts on particles with non-vanishing weak isospin T , a concept introduced in greater detail later on. It is mediated by the vector bosons W and Z . The W boson interacts only with left-handed fermions and right-handed antifermions. This is due to the $V - A$ nature of the weak interaction. Moreover, the W and Z bosons are massive and therefore only play a role at small distances. In the 1960s, Glashow, Weinberg and Salam were able to merge the theory of the electromagnetic interaction with that of the weak interaction (cf. ref. [11]). The resulting interaction is called the electroweak interaction. Since this interaction plays a central role in this thesis, it will be discussed in more detail in Section 2.2.

One of the properties of the weak interaction is the fact that the quark eigenstates, usually defined with respect to the strong interaction, are not the eigenstates of the weak interaction. This means, the quark eigenstates of the weak interaction — denoted as primed variables — and strong interaction can be connected with a unitary matrix according to:

$$\begin{pmatrix} d' \\ s' \\ b' \end{pmatrix} = \begin{pmatrix} U_{ud} & U_{us} & U_{ub} \\ U_{cd} & U_{cs} & U_{cb} \\ U_{td} & U_{ts} & U_{tb} \end{pmatrix} \begin{pmatrix} d \\ s \\ b \end{pmatrix} \quad (2.1)$$

This matrix is called the Cabibbo-Kobayashi-Maskawa (CKM) matrix. Due to this mixing, the weak interaction can produce transitions between the three different generations.

2. Theoretical Foundations

The *strong interaction* acts on particles with a color charge. The associated quantum field theory is called Quantum Chromodynamics (QCD). Unlike the electric charge, three different types of color charge exist, called *red*, *green* and *blue*. The naming of these charges is due to an analogy with additive color mixing: Objects neutral to the strong interaction are called *colorless*, a state which can be achieved by carrying an equal amount of red, green and blue color charge, or same amounts of color and anticolor. In the SM, the strong interaction is mediated by eight types of gluons, which have no mass, but carry different color charges and can thus self-interact. This behavior is fundamentally different from the electromagnetic interaction, where the photon is electrically neutral. Due to this feature of the strong interaction, the effective value of the strong coupling constant $\alpha_s(Q^2)$ shows a strong dependence on the squared momentum transfer Q^2 in the interaction. In hard scattering processes, where Q^2 is large — corresponding to probing small distances — the strong coupling constant α_s , and therefore the strength of the strong interaction almost vanishes. This is called the *asymptotic free* behavior of the strong interaction. On the other hand, at small values of Q^2 — corresponding to probing large distances — the strong interaction gains in strength, such that particles carrying a color charge cannot be observed isolated. This is called the *confinement* regime. It is believed that this is the reason for the range of the strong interaction being limited to sub-atomic distances¹.

As discussed above, the interactions are mediated by bosons — particles with integer spin S . Table 2.1 gives an overview of these bosons. Apart from the bosons carrying the fundamental interactions, the Standard Model also contains an additional boson, the so-called *Higgs boson*. This boson has a mass of (125.7 ± 0.4) GeV (cf. ref. [8]) and spin $S = 0$. It plays an important role in the so-called Higgs mechanism, which leads to the observed masses for the particles in the SM. The Higgs mechanism will be explained in Section 2.3.

Boson	Interaction	Mass M	Electric Charge Q	Spin S
Photon γ	Electromagnetic	0	0	1
W^\pm	Weak	(80.385 ± 0.015) GeV	± 1	1
Z^0	Weak	(91.1876 ± 0.0021) GeV	0	1
Gluon g	Strong	0	0	1
Graviton ² G	Gravity	0	0	2

Table 2.1.: Exchange bosons in the Standard Model. Note that eight types of gluons with different combinations of color can be exchanged. Masses taken from ref. [8].

Apart from the bosons discussed above, the Standard Model also contains fundamental fermions — particles carrying spin $S = 1/2$. These can be viewed as the building blocks of matter, and can be ordered in three families, or generations. This is similar to the periodic system of chemical elements, and in the same way hints at an underlying theory able to explain this structure. An overview is given in Table 2.2.

In addition to their spin, the particles are characterized by further so-called quantum numbers. These are the weak isospin T , and its third component T^3 , the hypercharge Y and the

¹It has to be noted that up until now, the existence of confinement within the theory of QCD has not been proven, and the quest for a deeper mathematical understanding of QCD is one of the Clay millenium problems (cf. ref. [12]).

²Gravitons have not yet been observed. On the contrary, the description of gravity within the frame of the Standard Model has to be viewed as hypothetical possibility at the time of writing.

color C . The values of these quantum numbers govern the interaction between the particles. Hypercharge and weak isospin will be discussed in greater detail in Section 2.2.

Generations			Quantum Numbers				
1	2	3	T	T^3	Y	Q	C
Leptons							
$\begin{pmatrix} \nu_e \\ e^- \end{pmatrix}_L$	$\begin{pmatrix} \nu_\mu \\ \mu^- \end{pmatrix}_L$	$\begin{pmatrix} \nu_\tau \\ \tau^- \end{pmatrix}_L$	$\begin{pmatrix} 1/2 \\ 1/2 \end{pmatrix}$	$\begin{pmatrix} 1/2 \\ -1/2 \end{pmatrix}$	$\begin{pmatrix} -1 \\ -1 \end{pmatrix}$	$\begin{pmatrix} 0 \\ -1 \end{pmatrix}$	$\begin{pmatrix} 0 \\ 0 \end{pmatrix}$
e_R^-	μ_R^-	τ_R^-	0	0	-2	-1	0
Quarks							
$\begin{pmatrix} u \\ d \end{pmatrix}_L$	$\begin{pmatrix} c \\ s \end{pmatrix}_L$	$\begin{pmatrix} t \\ b \end{pmatrix}_L$	$\begin{pmatrix} 1/2 \\ 1/2 \end{pmatrix}$	$\begin{pmatrix} 1/2 \\ -1/2 \end{pmatrix}$	$\begin{pmatrix} 1/3 \\ 1/3 \end{pmatrix}$	$\begin{pmatrix} 2/3 \\ -1/3 \end{pmatrix}$	$\begin{pmatrix} r, g, b \\ r, g, b \end{pmatrix}$
u_R	c_R	t_R	0	0	4/3	2/3	r, g, b
d_R	s_R	b_R	0	0	-2/3	-1/3	r, g, b

Table 2.2.: Particle content of the Standard Model, with additional quantum numbers. Note that here Q denotes the electric charge and should not be confused with the squared momentum transfer Q^2 . Taken from ref. [13]

Local Gauge Symmetry

One of the foundations of the Standard Model is the connection between global symmetries and conservation laws via Noether's theorem. This theorem states that for each continuous symmetry of a physical system a conservation law, and thus a conserved charge, exists (cf. ref. [9]).

It can be shown that the interactions described by the Standard Model can be introduced by forcing not only global, but local gauge symmetry. This concept can best be introduced for the case of the electromagnetic interaction, which is $U(1)$ symmetric. Starting from the Lagrangian describing the field of a single free fermion with mass m :

$$\mathcal{L}(x) = \bar{\psi}(x)(i\gamma^\mu\partial_\mu - m)\psi(x) \quad (2.2)$$

the Dirac equation can be obtained through the principle of least action:

$$(i\gamma^\mu\partial_\mu - m)\psi(x) = 0 \quad (2.3)$$

Here, $\psi(x)$ is the four-component spinor describing the fermion, and $\partial_\mu := \partial/\partial x^\mu$. The symbol γ^μ denotes the Dirac matrices, and, as is common in these calculations, Einstein's sum convention is used.

A global transformation of this system can be introduced by:

$$\psi(x) \rightarrow \psi'(x) = e^{-i\theta}\psi(x) = U_\theta\psi(x) \quad (2.4)$$

In this equation, θ is a constant, real number. It can be shown that this transformation is unitary and Abelian. It is commonly denoted as $U(1)$. According to Noether's theorem, it leaves the equations of motion invariant. This transformation can easily be made local by letting θ vary with x , i.e.

$$\psi(x) \rightarrow \psi'(x) = e^{-i\theta(x)}\psi(x) \quad (2.5)$$

2. Theoretical Foundations

With this transformation, the new Lagrangian reads:

$$\mathcal{L} \rightarrow \mathcal{L}' = \bar{\psi}'(x)(i\gamma^\mu\partial_\mu - m)\psi'(x) \quad (2.6)$$

$$= \bar{\psi}(x)(i\gamma^\mu\partial_\mu - m)\psi(x) + \bar{\psi}(x)\gamma^\mu\psi(x)\partial_\mu\theta(x) \quad (2.7)$$

$$= \mathcal{L} + j^\mu(x)\partial_\mu\theta(x) \quad (2.8)$$

Here, the vector current carried by the fermion, $j^\mu(x) = \bar{\psi}(x)\gamma^\mu\psi(x)$, is introduced. As can be seen, this local transformation leads to a modification of \mathcal{L} yielding modified equations of motion. This can be prevented by replacing the derivative in Equation 2.2 with the so-called covariant derivative:

$$\partial_\mu \rightarrow D_\mu = \partial_\mu - ieA_\mu(x) \quad (2.9)$$

This *minimal coupling* transforms Equation 2.2 to:

$$\mathcal{L} = \bar{\psi}(x)(i\gamma^\mu D_\mu - m)\psi(x) \quad (2.10)$$

$$= \bar{\psi}(x)(i\gamma^\mu\partial_\mu - m)\psi + ej^\mu A_\mu \quad (2.11)$$

The field $A_\mu(x)$ is required to transform as:

$$A_\mu \rightarrow A'_\mu = A_\mu - \frac{1}{e}\partial_\mu\alpha(x) \quad (2.12)$$

In this way, the resulting Lagrangian is invariant under local $U(1)$ transformations; however, at the same time, a further vector field A_μ had to be introduced. In the case of the electromagnetic interaction, this field describes the photon. To obtain the full Lagrangian, terms describing the kinetic energy and mass of this new particle have to be introduced. As can be shown, each form of mass term would violate local gauge invariance, leading to $m = 0$ for the photons as observed in nature. The kinetic energy is known from the theory of electromagnetism to be given by $-\frac{1}{4}F_{\mu\nu}F^{\mu\nu}$, with the field-strength tensor $F_{\mu\nu}$ given by:

$$F_{\mu\nu} = \partial_\mu A_\nu - \partial_\nu A_\mu \quad (2.13)$$

In summary, the full Lagrangian is now given by:

$$\mathcal{L} = \bar{\psi}(x)(i\gamma^\mu D_\mu - m)\psi(x) - \frac{1}{4}F_{\mu\nu}F^{\mu\nu} \quad (2.14)$$

The strong and weak interaction can also be introduced in a similar fashion via minimal coupling. The difference is to be found in the symmetry — while the electromagnetic interaction corresponds to an Abelian $U(1)$ symmetry, the strong interaction corresponds to a non-Abelian $SU(3)$ symmetry, and the weak interaction to a non-Abelian $SU(2) \times U(1)$ symmetry.

2.2. Electroweak Interaction

The theory of the electroweak interaction is one of the cornerstones of the Standard Model. It was first proposed in the late 1960s by Glashow, Weinberg and Salam (cf. ref. [11]) and is therefore also known as the *GWS model*. In this model, electromagnetic and weak interaction appear as two aspects of a unified electroweak interaction. The W and Z bosons predicted by this theory were first discovered by the UA1 and UA2 experiments at CERN in the early 1980s (cf. ref. [14–17]). Precision studies on the properties of the W and Z bosons were subsequently

performed by the experiments at LEP and Tevatron. A review of these measurements is given in ref. [8].

The GWS model can be developed from the observation that only left-handed leptons and right-handed anti-leptons take part in weak processes, such as the β decay. This approach follows ref. [9]. Assuming one generation of fermions — an electron e and a massless neutrino³ ν_e — it is possible to write the amplitudes associated with the β decay in terms of charged currents, defined as:

$$J_\mu(x) = J_\mu(x)^+ = \bar{\nu}_{eL}(x)\gamma_\mu e_L(x) = \frac{1}{2}\bar{\nu}_e(x)(\gamma_\mu - \gamma_\mu\gamma_5)e(x) \quad (2.15)$$

$$J_\mu(x)^\dagger = J_\mu(x)^- = \bar{e}_L(x)\gamma_\mu\nu_{eL}(x) = \frac{1}{2}\bar{e}(x)(\gamma_\mu - \gamma_\mu\gamma_5)\nu_e(x) \quad (2.16)$$

The terms γ_μ and $\gamma_\mu\gamma_5$ transform as vector and axial-vector under Lorentz transformations, respectively. This V-A structure is characteristic for the weak interaction. The previous equations can be rewritten as:

$$J_\mu^+ = \bar{L}\gamma_\mu\tau^+L \quad (2.17)$$

$$J_\mu^- = \bar{L}\gamma_\mu\tau^-L \quad (2.18)$$

with τ^i the Pauli matrices and L a doublet under $SU(2)$ obtained as:

$$L = \frac{1 - \gamma_5}{2} \begin{pmatrix} \nu_e \\ e^- \end{pmatrix} = \begin{pmatrix} \nu_e \\ e^- \end{pmatrix}_L \quad (2.19)$$

This suggests the introduction of a neutral current in order for the weak currents to fulfill a $SU(2)$ symmetry according to:

$$J_\mu^3(x) = \bar{L}\gamma_\mu\frac{\tau^3}{2}L = \frac{1}{2}\bar{\nu}_e\gamma_\mu\nu_e - \frac{1}{2}\bar{e}_L\gamma_\mu e_L \quad (2.20)$$

The resulting triplet under $SU(2)$ can be written as:

$$J_\mu^i(x) = \bar{L}\gamma_\mu T^i L = \bar{L}\gamma_\mu\frac{\tau^i}{2}L \quad (2.21)$$

The charges associated to these currents can be written as:

$$T^i = \int J_0^i(x)d^3x \quad (2.22)$$

These charges follow the $SU(2)$ algebra:

$$[T^i, T^j] = i\varepsilon^{ijk}T^k \quad (2.23)$$

Since only left-handed Weyl fermions take part in this interaction, the associated symmetry is commonly denoted as $SU(2)_L$. Especially the right-handed component of the electron is sterile under this interaction and thus forms a singlet under $SU(2)$:

$$R = \frac{1}{2}(1 + \gamma_5)e = e_R \quad (2.24)$$

³Experimental observations of neutrino oscillations, i.e. transitions between the three different generations, show that the eigenstates of the weak interaction are not the eigenstates of the Hamiltonian, which is responsible for the evolution of the state in time. From these observations, it can be assumed that at least two neutrino flavors are massive, in contradiction to this model.

2. Theoretical Foundations

It is now feasible to include the electromagnetic interaction in a consistent way by requiring an additional local $U(1)$ symmetry. The charge connected with this symmetry has to commute with the charges of the $SU(2)_L$ symmetry and can therefore not be the electric charge. Instead, the so-called weak hypercharge⁴ Y is introduced as:

$$Y = 2(Q - T^3) \quad (2.25)$$

with T^3 the charge which is connected with the neutral current. The four charges are associated with four gauge fields, denoted $A_\mu^{(i)}$ and B_μ . The full Lagrangian for fermions and gauge bosons in this $SU(2)_L \times U(1)_Y$ theory reads:

$$\mathcal{L}_F = \bar{L}i\gamma^\mu(\partial_\mu - ig\frac{\vec{\tau}}{2} \cdot \vec{A}_\mu + \frac{i}{2}g'B_\mu)L + \bar{R}i\gamma^\mu(\partial_\mu + ig'B_\mu)R \quad (2.26)$$

$$\mathcal{L}_G = -\frac{1}{4}F_{\mu\nu}^i F^{i\mu\nu} - \frac{1}{4}B_{\mu\nu}B^{\mu\nu} \quad (2.27)$$

with:

$$F_{\mu\nu}^i = \partial_\mu A_\nu^i - \partial_\nu A_\mu^i + g\varepsilon_{ijk}A_\mu^j A_\nu^k \quad (2.28)$$

$$B_{\mu\nu} = \partial_\mu B_\nu - \partial_\nu B_\mu \quad (2.29)$$

Here, A_μ^i and B_μ are the gauge boson fields associated with the local $SU(2)_L$ and $U(1)_Y$ symmetries, respectively. The couplings g and g' correspond to $SU(2)_L$ and $U(1)_Y$.

Since possible mass terms for the fermions or bosons would violate gauge invariance, it is not feasible to incorporate the observed masses of the bosons in this theory. The solution for this is a spontaneous breaking of gauge invariance, called the Higgs mechanism. This is discussed in the next section.

2.3. Higgs Mechanism

2.3.1. Prerequisites

As was discussed before, the GWS predicts four gauge bosons, three bosons A_μ^i associated with the $SU(2)_L$ symmetry, and one boson B_μ , associated with the $U(1)_Y$ symmetry. All fermions and bosons in the GWS model are massless. This, however, does not agree with observations: In nature, three massive gauge bosons W^+, W^- and Z^0 , connected to the weak interaction, are observed. Only the photon, connected to the electromagnetic interaction, is massless. Moreover, the fermions are also massive. As stated above, this breaks the $SU(2)_L \times U(1)_Y$ symmetry.

One way to reconcile the GWS model with the observations is the Higgs mechanism. In its simplest form, an additional $SU(2)$ doublet of two complex scalar fields with weak hypercharge $Y = 1$ is introduced as:

$$\phi = \begin{pmatrix} \varphi^+ \\ \varphi^0 \end{pmatrix} \quad (2.30)$$

The two scalar fields φ^+ and φ^0 are positively charged and neutral, respectively. The Lagrangian for these scalar fields can be written as:

$$\mathcal{L}_s = (D_\mu\phi)^\dagger(D^\mu\phi) - V(\phi^\dagger\phi) \quad (2.31)$$

⁴The name stems from the analogy with the hypercharge in the Nakano-Nishijima-Gell-Mann relation for hadron classification, cf. ref. [9].

The covariant derivative D_μ is:

$$D_\mu \phi = \left(\partial_\mu - ig \frac{\vec{\tau}}{2} \cdot \vec{A}_\mu - \frac{i}{2} g' B_\mu \right) \phi \quad (2.32)$$

The potential V is given by:

$$V(\phi^\dagger \phi) = -\mu^2 \phi^\dagger \phi + \lambda (\phi^\dagger \phi)^2 \quad (2.33)$$

In this equation, μ^2 and λ are real constant parameters. Higher terms are not allowed in order to ensure renormalizability. For $\mu^2 > 0$ and $\lambda > 0$, this potential has a shape illustrated in Figure 2.1. Due to its form, it is sometimes referred to as *mexican hat* potential.

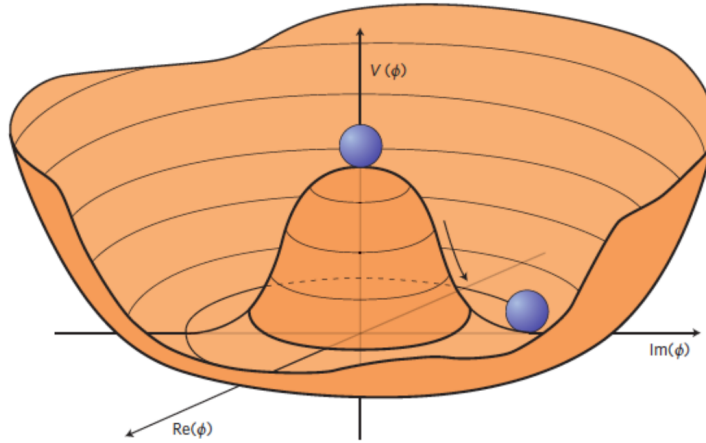


Figure 2.1.: Illustration of the potential $V = -\mu^2 \phi^\dagger \phi + \lambda (\phi^\dagger \phi)^2$ as a function of ϕ^+ and ϕ^0 . Before symmetry breaking, the vacuum is in the symmetric state in the center of the potential. After spontaneous symmetry breaking, its state corresponds to one of the points in the ring forming the minimum. Taken from ref. [18].

In addition, a Lagrangian representing the coupling between fermions — in the simple model discussed here, only electrons — and scalars can be introduced as:

$$\mathcal{L}_Y = -G_e (\bar{L} \phi R + \bar{R} \phi^\dagger L) + h.c. \quad (2.34)$$

In this equation, G_e acts as Yukawa coupling constant. This allows to write down the full Lagrangian of the GWS model, including the scalar field needed for the Higgs mechanism, as:

$$\mathcal{L} = \mathcal{L}_F + \mathcal{L}_G + \mathcal{L}_s + \mathcal{L}_Y \quad (2.35)$$

2.3.2. Spontaneous Symmetry Breaking

The potential $V(\phi^\dagger \phi)$ introduced above, with $\mu^2 > 0$ and $\lambda > 0$, has a minimum at:

$$\phi^\dagger \phi = \frac{v^2}{2}, \quad v = \sqrt{\frac{\mu^2}{\lambda}} \quad (2.36)$$

2. Theoretical Foundations

The values of φ^+ and φ^0 , for which the potential is minimized, are no longer unique. Moreover, for all of these points, the vacuum expectation value of ϕ is non-zero. Through spontaneous symmetry breaking, the vacuum assumes one of these possible values, such that:

$$\langle 0 | \phi | 0 \rangle = \begin{pmatrix} 0 \\ v/\sqrt{2} \end{pmatrix} \quad (2.37)$$

This new vacuum breaks the $SU(2)_L$ and $U(1)_Y$ symmetry, and a new symmetry, $U(1)_{em}$ arises with the electric charge Q as the associated conserved charge.

It is now feasible to perform a $SU(2)$ gauge transformation on the Lagrangian above. In this process, it is useful to rewrite ϕ as:

$$\phi = \begin{pmatrix} \varphi^+ \\ \varphi^0 \end{pmatrix} = e^{i\vec{\tau} \cdot \vec{\xi}/2v} \begin{pmatrix} 0 \\ (v + H)/\sqrt{2} \end{pmatrix} \quad (2.38)$$

Here, ξ^i are three real fields, absorbed into the W and Z bosons as discussed below, and H is a Higgs boson. Apart from this, the following substitutions can be used:

$$W_\mu^\pm = \frac{1}{\sqrt{2}} \left(W_\mu^{(1)} \mp iW_\mu^{(2)} \right) \quad (2.39)$$

$$W_\mu^{(3)} = \frac{gZ_\mu + g'A_\mu}{\sqrt{g^2 + g'^2}} \quad (2.40)$$

$$B_\mu = \frac{-g'Z_\mu + gA_\mu}{\sqrt{g^2 + g'^2}} \quad (2.41)$$

Now $\tan \theta_W = g'/g$ can be defined, where θ_W is the so-called weak mixing angle, also known as Weinberg angle. Using this relation, Equation (2.40) and (2.41) can be rewritten as:

$$W_\mu^{(3)} = \sin \theta_W Z_\mu + \cos \theta_W A_\mu \quad (2.42)$$

$$B_\mu = -\cos \theta_W Z_\mu + \sin \theta_W A_\mu \quad (2.43)$$

The Lagrangian can now be rewritten in such a way that mass-like terms for the H , W and Z bosons appear. To this end, the following relations are introduced:

$$M_W = \frac{1}{2}gv \quad (2.44)$$

$$M_Z = \frac{1}{2} \frac{v}{\cos \theta_W} \quad (2.45)$$

$$M_H = \sqrt{2}\mu^2 \quad (2.46)$$

The resulting Lagrangian now reads:

$$\begin{aligned} \mathcal{L}_s = & \frac{1}{2} \partial_\mu H \partial^\mu H - \frac{1}{2} M_H^2 H^2 - \lambda v H^3 - \frac{\lambda}{4} H^4 \\ & + \frac{g^2}{8} (H^2 + 2Hv) \left(\frac{1}{\cos^2 \theta_W} Z_\mu Z^\mu + 2W_\mu^+ W^{-\mu} \right) \\ & + M_W^2 W_\mu^+ W^{-\mu} + \frac{1}{2} M_Z^2 Z_\mu Z^\mu \end{aligned} \quad (2.47)$$

Similarly, the Lagrangian \mathcal{L}_Y can be rewritten such that a mass term for the electron appears, leading to a mass of:

$$m_e = \frac{G_e}{\sqrt{2}}v \quad (2.48)$$

From experiments, v can be measured to be 246 GeV. It is feasible to extend this simplified model to include all known fermions and to endow all of these particles with mass. Together with the $SU(3)_c$ of QCD, the full symmetry of the Standard Model is given by $SU(3)_c \times SU(2)_L \times U(1)_Y$.

It can be shown that the GWS model requires quarks with three color degrees of freedom in order for so-called anomaly cancellation to occur (cf. ref. [9]). This hints at a deeper connection between the strong and electroweak interaction, as well as an underlying symmetry different from the current Standard Model.

2.4. Perturbation Theory

In high energy physics, the predominant picture of the movement and interaction of particles was shaped by Richard Feynman (cf. ref. [19]). It is built on three postulates:

- The probability p for a particle to move from a space-point x^μ to a space-point y^μ is the absolute square of a complex number called the *probability amplitude* $\mathcal{A}_{xy} = \langle x|y \rangle$.
- The probability amplitude \mathcal{A}_{xy} is the sum of the complex amplitudes connected to each possible path from x^μ to y^μ .
- The amplitudes from each path have the same magnitude, but their phase φ is given by the action S calculated along the path, where $S = \int \mathcal{L}(\dot{x}(t), x(t))dt$.

Mathematically, these postulates can be summarized as:

$$p = |\langle x|y \rangle|^2 = |\mathcal{A}_{xy}|^2 \quad (2.49)$$

$$\mathcal{A}_{xy} = \int D[x] \exp(iS) \quad (2.50)$$

Here $\int D[x]$ denotes the integral over all possible paths. This gives a direct connection between the mathematical expression, which has to be evaluated, and a space-time interpretation, which can be expanded to include also interactions. If interactions are considered, the amplitude for the full process is the sum over the amplitudes for each possible processes leading from the initial state to the final state.

The expressions for the transition probabilities can be transformed into pictorial descriptions as suggested by Feynman in ref. [20]. These pictorial descriptions are called Feynman diagrams. As an example, one of the processes for the scattering of two electrons is shown in Figure 2.2. The rules for the transformation between Feynman diagrams and the connected amplitudes are the so-called Feynman rules. While these rules differ for each theory, the basic principles are:

- Each vertex y_i corresponds to a factor $\sqrt{\alpha} \int d^4y_i$, where α gives the coupling strength.
- Each line between two points y_i and y_j corresponds to the amplitude \mathcal{A}_{ij}

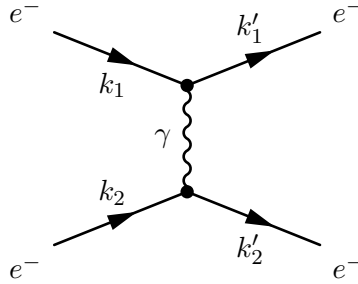


Figure 2.2.: Feynman diagram for one of the processes for electron scattering.

As can be seen, each vertex is associated with an additional factor $\sqrt{\alpha}$. If α is less than unity, amplitudes corresponding to diagrams with a higher number of vertices, are suppressed, giving a natural order for the evaluation of different diagrams. It has to be noted, that the power of α only acts as a rough estimate for the amplitude connected with each diagram. This is because each amplitude is a complex number with magnitude and phase, and because the magnitude of the amplitude can still be large for high powers of α if the remaining factors are large. Mathematically, the amplitude for the full process can be decomposed:

$$\mathcal{A} = \mathcal{A}(\alpha^1) + \mathcal{A}(\alpha^2) + \dots \quad (2.51)$$

In the example in quantum electrodynamics, α is on the order of $1/137$, meaning that diagrams with larger number of vertices are strongly suppressed. In this case, the calculation of the full amplitude can be performed by calculating the diagram with the lowest number of vertices first, called the leading order diagram. The following diagrams are called higher-order diagrams and are treated as *perturbations*, or corrections, to the original result. Such a perturbative ansatz is only feasible in the case of small couplings. As was discussed before, in quantum chromodynamics, the coupling strength can become very large if long distances are considered. This feature renders perturbative solutions impossible for such cases. Instead, non-perturbative techniques, such as lattice QCD (cf. ref. [21]), have to be used.

2.5. Renormalization

The Standard Model appears to be only an effective theory. This means, that similar to thermodynamics, which can be traced back to the behavior of single atoms and molecules, it is assumed that the Standard Model can be traced back to an underlying theory describing structures at much smaller scales than probed by current particle detectors. In this underlying theory, which is assumed to unify gravity, quantum effects and special relativity, it is expected that the gravitational constant G , the reduced Planck constant \hbar and the speed of light c appear. Combining these quantities⁵ in such a way that the result has the dimension of length leads to (cf. ref. [8]):

$$\ell_p = \sqrt{\frac{\hbar G}{c^3}} = 1.61 \times 10^{-35} \text{ m} \quad (2.52)$$

This quantity is known as the Planck length. Using this quantity as de Broglie wavelength, the associated Planck momentum of $p_p = h/\ell_p = 7.8 \times 10^{19} \text{ GeV}$ is far beyond the reach of any

⁵Note that in this equation, in contrast to the remaining discussion, international units are used.

particle detector. It may be assumed that both Planck lengths and momenta occur naturally in the underlying theory, hinting to the scale at which the Standard Model breaks down. This is called the Planck scale.

However, within the framework of the SM, it is common that integrals sum over all momenta, including those larger than p_p , if loops are involved in the processes under investigation. As can be expected, these integrals commonly lead to unphysical results. The divergences introduced by these integrals have to be removed by the so-called renormalization procedure, which introduces effective values for physical observables.

An example is the charge of the electron e , or equivalently the QED fine structure constant $\alpha_{0,QED} = e^2/4\pi$. Consider the case of electron-electron scattering. In leading order, this process can be described by the Feynman diagram shown in Figure 2.3.

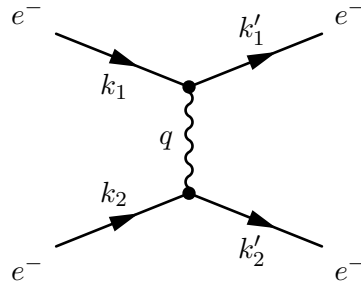


Figure 2.3.: Leading order diagram for the e^-e^- scattering process. Taken from ref. [9], modified.

The amplitude corresponding to this diagram is:

$$-iM = [ie\bar{u}(k'_1)\gamma^\mu u(k_1)] \frac{-ig_{\mu\nu}}{q^2} [ie\bar{u}(k'_2)\gamma^\nu u(k_2)] \quad (2.53)$$

In $\mathcal{O}(\alpha_{0,QED}^2)$, it can be shown that the so-called Ward-Takahashi identity leads to cancellation of all contributions with the exception of the diagram shown in Figure 2.4.

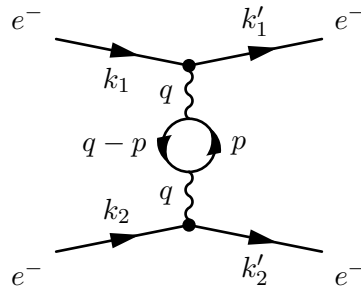


Figure 2.4.: Next-to-Leading order diagram for the e^-e^- scattering process. Taken from ref. [9], modified.

It can be shown that the effect of this diagram can be written as a modification of the photon propagator:

$$\frac{-ig_{\mu\nu}}{q^2} \rightarrow \frac{-ig_{\mu\nu}}{q^2}(1 - I(q^2)) \quad (2.54)$$

2. Theoretical Foundations

In this equation, the quantity $I(q^2)$ is given by:

$$I(q^2) = \frac{\alpha_{0,QED}}{3\pi} \int_{m^2}^{\infty} \frac{dp^2}{p^2} - \frac{2\alpha_{0,QED}}{\pi} \int_0^1 dx x(1-x) \log \left(1 - \frac{q^2(1-x)}{m^2} \right) \quad (2.55)$$

Here, the symbol m represents the mass of the particle in the loop. The first term in this equation is divergent, therefore the upper bound is replaced by a so-called cut-off parameter, or regulator, Λ . Note that in general the introduction of such a cut-off is not the only way by which such expressions could be regularized. For example, the dimensionality of the loop integral could be reduced from $d = 4$ to $d = 4 - \varepsilon$. This is called dimensional regularization.

For the case that $(-q^2) = Q^2 \gg m^2$, it can be shown that the result is equivalent to introducing an effective fine structure constant α_{QED} , which can be related to the so-called bare fine structure constant $\alpha_{0,QED}$ via:

$$\alpha_{QED}(Q^2) = \frac{\alpha_{0,QED}}{1 + \frac{\alpha_{0,QED}}{3\pi} \log \left(\frac{\Lambda^2}{Q^2} \right)} \quad (2.56)$$

While this equation cannot be used to calculate the effective fine structure constant from first principles, it allows to connect values of α_{QED} measured at different values of Q^2 . In this way, given a measured value at a defined scale $Q^2 = \mu^2$, it is feasible to calculate the values at all other scales Q^2 . Similarly, it can be shown that in the case $(-q^2) = Q^2 \ll m^2$, the divergence arising from the first integral in Equation (2.55) can be absorbed into an effective fine-structure constant.

In conclusion, the fine structure constant α_{QED} depends on the squared momentum transfer Q^2 of the photon with which the electron interacts. This is the so-called *running* of the coupling constant, which can also be interpreted as an effective charge which the electron is carrying. In a similar way, the masses and field strengths involved in the theory have to be modified. In this way, divergences are kept from appearing in physical results, such as cross sections. This procedure is called *renormalization*, and it can be shown to work for all results obtainable in electroweak theory (cf. ref. [22]).

2.5.1. Radiative Corrections to M_W

Before considering the effects of renormalization and effective observables, a step back to Section 2.3 is needed. In this section, an overview of the connection between g , g' , M_W , M_Z , $\sin \theta_W$ and v was given. It can be shown (cf. ref. [23]) that a set of three of these parameters is sufficient to calculate the remaining ones. These three parameters are the so-called free parameters of the electroweak sector of the Standard Model, and the choice of these parameters is to some extent arbitrary. Instead of considering M_W a free parameter, it is common to consider the Fermi constant G_F , α_{QED} and M_Z as free parameters, since these can be measured with high precision (cf. ref. [23]). The Fermi constant G_F can be introduced by considering the interaction of electrons and neutrinos at small momentum transfer. In this case, the W exchange can be approximated by a point-like interaction, and the propagator of the W boson becomes independent of the momentum transfer (cf. ref. [24]):

$$\mathcal{M}_{fi} \propto g \frac{1}{Q^2 + M_W^2} g \xrightarrow{Q^2 \rightarrow 0} \frac{g^2}{M_W^2} \quad (2.57)$$

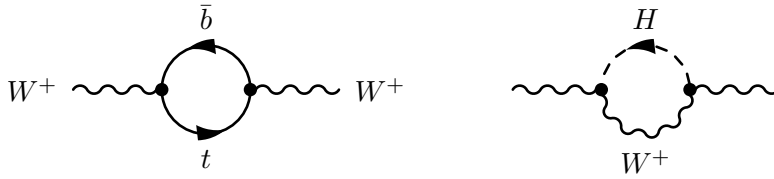


Figure 2.5.: Next-to-leading order corrections to the propagator of the W boson. The left example shows a loop with a t and \bar{b} quark, while the right example shows the interaction with a Higgs boson.

By including several constants for historic reasons, this expression can be rewritten as:

$$\frac{g^2}{M_W^2} = \frac{8}{\sqrt{2}} G_F \quad (2.58)$$

This means that G_F is directly connected to M_W . It can further be shown that $G_F = 1/(\sqrt{2}v^2)$. Using only M_Z , α_{QED} and G_F , M_W can be calculated through (cf. ref. [25]):

$$M_W^2 = M_Z^2 \left(\frac{1}{2} + \sqrt{\frac{1}{4} - \frac{\pi\alpha_{QED}}{\sqrt{2}G_F M_Z^2}} \right) \quad (2.59)$$

This relation, however, is only valid in leading order. In next-to-leading order, loop diagrams, very similar to those discussed in the last section, appear. Examples are shown in Figure 2.5. These higher order corrections lead to an effective value of M_W , which can be calculated by incorporating these corrections into a so-called form factor Δr . Equation 2.59 is then modified:

$$M_W^2 = M_Z^2 \left(\frac{1}{2} + \sqrt{\frac{1}{4} - \frac{\pi\alpha_{QED}}{\sqrt{2}G_F M_Z^2} [1 + \Delta r]} \right) \quad (2.60)$$

In reference [25], a parametrization of Δr in terms of M_t , M_Z , α_{QCD} , α_{QED} and M_H is given. It can be observed, that the largest impact is due to a quadratic dependence on M_t , with smaller contributions from M_Z , α_{QCD} and α_{QED} and basically only a logarithmic dependence on M_H . Using these corrections, a theoretical prediction of M_W of (80.358 ± 0.008) GeV is obtained (cf. ref. [7]), consistent with the value of the world average.

3. Production of Electroweak Gauge Bosons at the Large Hadron Collider

At the LHC, i.e. in proton-proton collisions, the predominant process for the production of the electroweak gauge bosons W and Z is the Drell-Yan process (cf. ref. [26,27]). In leading order, this process can be described by the Feynman diagrams shown in Figure 3.1. Since this thesis focuses on analyses with muons in the final state, only such diagrams are shown. However, for the study of electrons, as discussed in Appendix A, the muons and muon neutrinos in these diagrams have to be replaced with electrons and electron neutrinos.

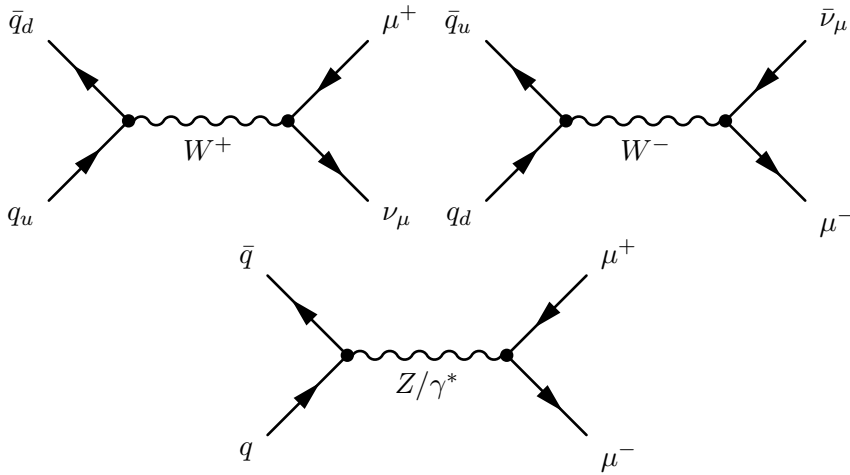


Figure 3.1.: Feynman diagram of the Drell-Yan process. The upper left diagram shows the production of W^+ bosons, the upper right diagram the production of W^- bosons. The lower diagram shows the diagram for the production of Z bosons. In all cases, only the decay into muons and the corresponding muon neutrino is shown.

In the lower diagram in Figure 3.1, a quark from one proton annihilates with an anti-quark from the colliding proton, producing a Z boson or photon. While the anti-quark has to be a sea quark, the quark can be either be a valence or a sea quark. The Z boson or photon then decays into a muon—anti-muon pair. Since both Z and γ exchange lead from the same initial state to the same final state, the amplitudes for both processes have to be added coherently. This leads to an interference term between both processes, which can in principle be used to measure the weak mixing angle $\sin \theta_W$. The magnitude of the amplitude for the Z exchange is much larger than for the photon exchange in the kinematic regime investigated in this thesis. Therefore, it is common to drop the photon exchange in the notation of this process.

The production and decay of the W boson, shown in the upper diagrams in Figure 3.1, is very similar to that of the Z boson. In this case, a quark from one proton interacts with the anti-quark from the same family, but different flavor¹. Depending on whether the quarks

¹It has to be noted that — as discussed in the last chapter — the quark eigenstates with respect to the electroweak interaction do not agree with the eigenstates with respect to the strong interaction.

involved are of up or down-type, a W^+ or W^- is produced and decays into a muon of the same charge, accompanied by a neutrino of opposite lepton number.

Although Z bosons always appear as internal lines in the Feynman diagrams above, it is common at ATLAS to define them as real instead of virtual if their mass lies between 66 GeV and 116 GeV.

3.1. Kinematics of the W and Z Production

The kinematics of the decay of a W or Z boson is governed by its mass. The decays are two-body decays, in which the exact values of E and \vec{p} of the decay leptons can be calculated through energy and momentum conservation. Following common nomenclature, the products of this decay are called *daughters*.

In the rest frame of the vector boson, the energy and momentum of the daughters can be calculated as:

$$E_1 = \frac{1}{2M}(M^2 + m_1^2 - m_2^2) \quad (3.1)$$

$$E_2 = \frac{1}{2M}(M^2 + m_2^2 - m_1^2) \quad (3.2)$$

$$\vec{p}_1^2 = \vec{p}_2^2 = \frac{1}{4M^2}(M^4 - 2M^2(m_1^2 + m_2^2) + (m_1^2 - m_2^2)^2) \quad (3.3)$$

$$\vec{p}_1 = -\vec{p}_2 \quad (3.4)$$

In this equation, M is the mass of the vector boson, 1 and 2 the indices of the daughters and m_1 and m_2 their masses. The momenta of both decay particles point into opposite directions, a configuration known as *back-to-back*. In the case of both the decay of W and Z bosons into muons and muon neutrinos, the mass of the leptons can be neglected, leading to:

$$E_1 = E_2 = \frac{M}{2}, \quad \vec{p}_1^2 = \vec{p}_2^2 = \frac{M^2}{4} \quad (3.5)$$

Both partons in the initial state of the Drell-Yan process carry only a fraction of the total proton momentum. In Section 3.2, it will be discussed that, in leading order, this quantity corresponds to the so-called Bjorken scale variable x_B . In the decay of W and Z bosons, x_B cannot be measured and the boost along the beam axis is of unknown size. For this reason, it is useful to limit the discussion to the plane transversal to the beam. At ATLAS, a coordinate system with the z axis parallel to the beam axis and an angle θ with respect to the beam axis is used (cf. Section 4.3). The component of the momentum in the transversal plane can be calculated as:

$$p_T = |\vec{p}| \sin \theta \quad (3.6)$$

As can be seen, it is essential to know the angle θ in order to calculate p_T . To this end, the angular distribution of the decay leptons has to be known. This distribution is governed by the $V - A$ nature of the weak interaction. For the decay² of $W \rightarrow \mu\nu_\mu$, it is given by (cf. ref. [28]):

$$\frac{d^2\sigma}{d\cos\theta d\varphi} \sim (1 + \cos^2\theta) \quad (3.7)$$

²Here, and in the following, the symbols denoting particles and anti-particles will not be shown. For example, by the notation $W \rightarrow \mu\nu$, the processes $W^+ \rightarrow \mu^+\nu_\mu$ and $W^- \rightarrow \mu^-\bar{\nu}_\mu$ are denoted.

Higher-order effects as discussed in Section 3.3 lead to additional terms, and the resulting distribution can be expanded as:

$$\begin{aligned} \frac{d^2\sigma}{d\cos\theta d\varphi} &\sim (1 + \cos^2\theta) + \frac{1}{2}A_0(1 - 3\cos^2\theta) + A_4\cos\theta \\ &+ A_1\sin(2\theta) + \frac{1}{2}A_2\sin^2\theta\cos(2\varphi) + A_3\sin\theta\cos\varphi \\ &+ A_5\sin\theta\sin(2\varphi) + A_6\sin(2\theta)\sin\varphi + A_7\sin\theta\sin\varphi \end{aligned} \quad (3.8)$$

In this expansion, the coefficients A_i are called the *angular coefficients*. Theoretically, it is very challenging to calculate these coefficients. As could be shown in ref. [13], different Monte Carlo generators (cf. Section 5) produce different predictions for A_i , which in part differ significantly from the observed distributions. The coefficients A_5 , A_6 and A_7 appear at second order in the QCD coupling constant α_S and can be neglected. If the dependence on φ is now removed through integration, the following distribution is obtained:

$$\frac{d\sigma}{d\cos\theta} = \cos^2\theta \left(1 - \frac{3}{2}A_0\right) + \cos\theta A_4 + \left(1 + \frac{1}{2}A_0\right) \quad (3.9)$$

This equation describes a parabola in $\cos\theta$. Now the differential cross section with respect to the transverse momentum can be calculated using the variable transformation:

$$\frac{d\sigma}{dp_T} = \frac{d\sigma}{d\cos\theta} \frac{d\cos\theta}{dp_T} \sim \frac{d\sigma}{d\cos\theta} \frac{2}{M} \frac{1}{\sqrt{M^2/4 - p_T^2}} \quad (3.10)$$

The shape of this spectrum is known as a *Jacobian* due to the common derivation using a transformation. As can be seen, the modeling of p_T is much more challenging than that of $|\vec{p}|$, because the shape of p_T also depends to a large extent on a correct modeling of the angular coefficients. The Jacobian is characterized by an edge at approximately $M/2$. This is illustrated through an MC simulation of 10 M events without detector effects, performed with PYTHIA8 (cf. ref. [29,30]) in Figure 3.2(a).

The mass of the vector boson can therefore be estimated from the shape of the transverse momentum spectrum of the decay lepton. As will be discussed in Section 4.5.5, the kinematics of a final-state neutrino in the transverse plane can be indirectly measured with the so-called Missing Transverse Energy E_T^{miss} , i.e. by assuming $p_T^\nu \sim E_T^{\text{miss}}$. From this, the transversal mass can be calculated as:

$$m_T = \sqrt{2p_T^\ell p_T^\nu (1 - \cos(\varphi^\ell - \varphi^\nu))} \quad (3.11)$$

The distribution of this variable is illustrated using events from the aforementioned simulation in Figure 3.2(b). As can be seen, the distribution of m_T shows a pronounced edge at $\sim M_W$, a value which is only reached if both decay leptons are emitted with $\theta = \pi/2$, i.e. perpendicular to the beam axis. Events in which the decay leptons are emitted with $\theta \neq \pi/2$, the value of m_T is smaller than M_W , and subsequently a long tail towards lower values can be observed. Note that the observed distributions differ significantly from these simulated distributions, since p_T^ν can only be estimated with a large uncertainty. This leads to a smearing in the observed distributions.

In the considerations above, the mass of the intermediary vector boson was assumed to be fixed. In reality, the bosons can be produced off-shell since they always appear as internal lines in

3. Production of Electroweak Gauge Bosons at the Large Hadron Collider

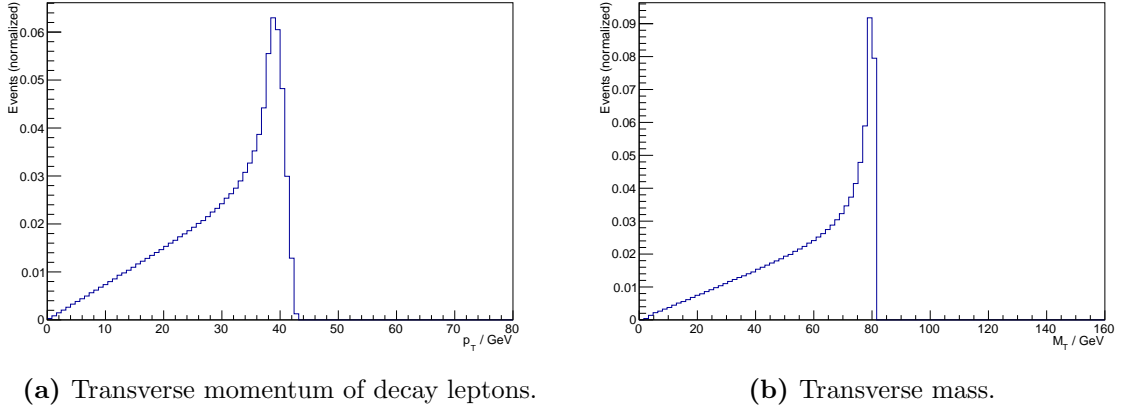


Figure 3.2.: Typical spectra of lepton p_T (left) and transverse mass m_T (right). As can be seen, lepton p_T has an edge at approximately $M_W / 2$. The distribution of m_T follows a similar shape, with an edge at approximately M_W .

the corresponding Feynman diagrams, or in other words, both W and Z bosons are unstable. This means, that in general $M^2 \neq p^2 = m^2$. In the case of W and Z bosons, the widths are small compared to their mass: for the W boson $\Gamma/M \sim 2.085 \text{ GeV}/80.385 \text{ GeV} = 2.6\%$ and for the Z boson $\Gamma/M \sim 2.4952 \text{ GeV}/91.1876 \text{ GeV} = 2.7\%$ are the current best estimates (cf. ref. [8]). This means that often a so-called narrow width approximation can be used, i.e., that the production of off-shell W and Z bosons usually plays a negligible role.

A significant impact on the distribution of the decay lepton p_T is due to the non-zero transverse momentum of the intermediary vector boson. Higher-order effects, as discussed in Section 3.3, lead to the production of particles such as gluons, quarks or photons, against which the vector boson recoils. This means, that the momentum of the decay lepton will be modified. Depending on the angle between the decay lepton and the vector boson, the transverse momentum of the decay lepton will either be higher or lower. This is reflected in a smearing of the Jacobian as illustrated in Figure 3.3.

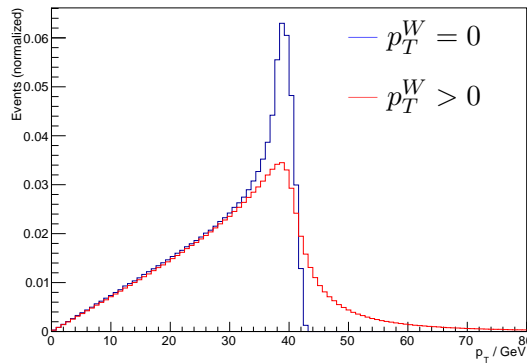


Figure 3.3.: Broadening of the distribution of lepton p_T due to non-zero transverse momentum of the intermediary vector boson. As can be seen, a significant smearing of the decay lepton p_T is introduced.

3.2. Parton Distribution Functions

Up until now, the exact origin of the partons which produce the W and Z bosons was not discussed. Therefore, a closer look at the proton is needed.

The proton can be regarded as consisting of three valence quarks uud and a large number of quark-antiquark pairs and gluons, forming the so-called sea. Due to the asymptotic freedom of the partons, each interaction with the proton can be treated as interaction with one of its partons independently of the remaining partons.

In the following, the interaction of a photon with the proton will be considered: If the interaction of the photon with the proton is viewed in a Breit system, a frame of reference in which the proton carries a high velocity and the energy transfer by the photon vanishes, the so-called Bjorken scale variable x_B can be introduced as (cf. ref. [24]):

$$x_B = \frac{Q^2}{2Pq} \quad (3.12)$$

Here, P denotes the four-momentum of the proton, and q the four momentum of the photon. The symbol Q^2 is introduced as $Q^2 = -q^2$. The variable x_B is called the Bjorken scale variable. In the frame of reference discussed above, x_B is equal to the fraction of the momentum P carried by the parton. Moreover, it can be shown that Q^2 is related to the spatial resolution λ of the probing photon via³:

$$\lambda = \frac{h}{\sqrt{Q^2}} \quad (3.13)$$

The process $pp \rightarrow Z + X \rightarrow \mu^+ \mu^- + X$ can now be divided into two parts. In the first part, the proton structure and the kinematics of the different partons is modeled. In the second part, the parton-parton interaction takes place as discussed in the previous section. The ability to perform this separation is ensured by a factorization theorem (cf. ref. [31]). Historically, the Drell-Yan process is the paradigm process for this approach (cf. ref. [32]). In this approach, the cross-section for the production of massive lepton-antilepton pairs can be written as:

$$\sigma_{pp \rightarrow Z/\gamma^* + X \rightarrow \ell^+ \ell^- + X} = \sum_q \int dx_a dx_b f_{a/A}(x_a, \mu_F^2) f_{b/B}(x_b, \mu_F^2) \times [\hat{\sigma}_0 + \alpha_{QCD}(\mu_R^2) \hat{\sigma}_1 + \dots]_{q\bar{q} \rightarrow Z/\gamma^* \rightarrow \ell^+ \ell^-} \quad (3.14)$$

In this equation, A and B are the indices of both protons taking part in the interaction, while a and b stand for the partons from proton A and B . The functions $f_{a/A}(x_a, \mu_F^2)$ and $f_{b/B}(x_b, \mu_F^2)$ are parton distribution functions (PDFs), which encode the probability of finding a parton at a given value of Bjorken x . It has to be noted, that apart from Bjorken x , these functions also depend on the so-called factorization scale μ_F . The latter can be thought of as the scale separating the long-distance physics encoded in the PDFs and the short-distance processes of the parton-parton interaction. The dependence on μ_F arises because the PDFs contain real and virtual gluon emissions (cf. ref. [32]). The so-called hard interaction of the partons is shown in square brackets. It consists of the leading order cross-section $\hat{\sigma}_0$ and higher order corrections in α_{QCD} . The latter denotes the physical, not the bare coupling constant, which leads to a dependence on a further scale μ_R . The hard-scattering cross-section itself is a function of the reduced squared center-of-mass energy $s' = x_a x_b s$. It is common to set

³In this equation, international units were used for clarification.

3. Production of Electroweak Gauge Bosons at the Large Hadron Collider

$\mu_F = \mu_R = M$, with M being the mass of the lepton-antilepton pair. The final result is only dependent on μ_F and μ_R because the calculation cannot be performed to all orders in perturbation theory (cf. ref. [32]).

The PDFs have to be obtained from experimental results. The most important input data were obtained through electron-proton scattering as performed for example by the HERA experiment at DESY (cf. ref. [28]). Different collaborations have been formed in order to use the available data sets to produce PDFs. Notable examples are the CTEQ (cf. ref. [33]), MSTW (cf. ref. [34]), ABKM (cf. ref. [35]), GJR (cf. ref. [36]) and NNPDF (cf. ref. [37]) collaborations. The results of these groups differ due to varying approaches taken for example in the selection of experimental data sets and the treatment of possible inconsistencies between those. Moreover, each group uses a certain function for the parametrization of the PDFs⁴, and a fitting approach containing different assumptions which are to a certain extent arbitrary or under discussion. This leads to further differences between the different PDFs.

As an example, the analyses presented in this thesis are based on the CT10 PDF (cf. ref. [38]). In this PDF, results from HERA and Tevatron experiments were used, with the notable exception of the data collected at Tevatron concerning the W lepton asymmetry, since the authors reported tension with the remaining data set. The PDFs are parametrized using 26 free parameters, for example the valence quark PDFs take the form:

$$q_v(x, \mu) = a_0 x^{a_1} (1-x)^{a_2} \exp(a_3 x + a_4 x^2 + a_5 \sqrt{x}) \quad (3.15)$$

In this parametrization, $a_2 \dots a_5$ are free parameters, fitted separately for u and d quarks, while a_1 is set to 0.5 due to theoretical considerations. The uncertainties on the final PDF from each of the 26 parameters are de-correlated and stored as 26 up- and down variations along the new eigenvectors.

An illustration of the content of the aforementioned PDFs for different flavors and their dependence on x_B is shown in Figure 3.4. As can be seen, the distribution for u and d quarks shows a shoulder at values of $x_B \approx 10^{-1}$. This is understandable, since in the naive model each valence quark would carry an equal amount of the proton momentum, corresponding to a value of x_B of 1/3. The remaining quark flavors form the sea, for which no such shoulder is expected nor visible. Gluons also carry only a small fraction of the proton momentum on average.

Given a certain PDF, its dependence on Q^2 can be calculated. This is the reason why PDFs using input data at much lower values of Q^2 than commonly observed at ATLAS can be used. This evolution is performed via the so-called DGLAP evolution (cf. ref. [28]). The kinematic regime in which the PDFs are probed at ATLAS is shown in Figure 3.5.

For the measurement of M_W , the proton structure plays an important role. This can be easily seen in leading order in a simplified case in which only u and d quarks are considered. Here, the production of W bosons can be decomposed into terms corresponding to helicity states $\lambda = +1$ and $\lambda = -1$ (cf. ref. [39]):

$$\sigma_{W^+} \propto u(x_1)\bar{d}(x_2) + \bar{d}(x_1)u(x_2) \quad (3.16)$$

$$\sigma_{W^-} \propto d(x_1)\bar{u}(x_2) + \bar{u}(x_1)d(x_2) \quad (3.17)$$

In this equation, u and d represent the corresponding PDFs for u and d quarks, with x_1 and x_2 denoting the value of x_B for each quark. As can be seen, the helicity of W^+ and W^- , and

⁴An exception is the NNPDF collaboration, which trains a neural net instead of fitting pre-defined functions to obtain PDFs.

therefore the angular distribution of the decay leptons, depends on the contributions of u , \bar{u} , d and \bar{d} quarks. In NLO, states with $\lambda = 0$ can also be produced through gluons in the initial state. Reference [39] expects the systematic uncertainty on M_W due to the PDFs among the leading uncertainties, estimating approximately 10 MeV to 20 MeV, depending on the chosen PDF set.

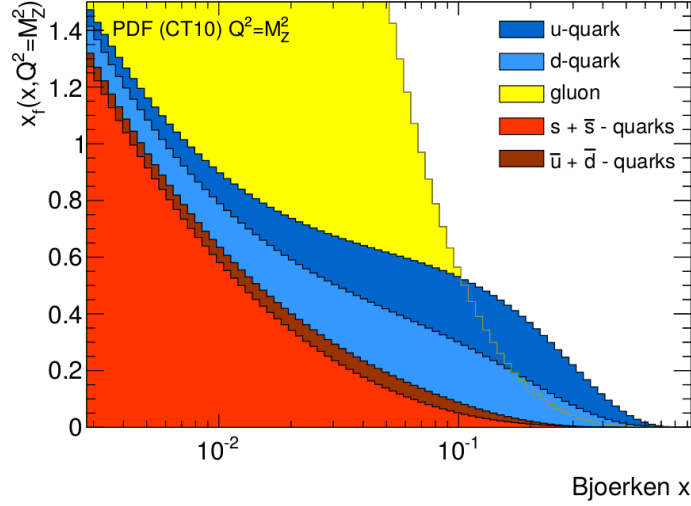


Figure 3.4.: Probability density to find a parton of given flavor as function of x_B . The densities are shown for $Q^2 = M_Z^2$. Taken from ref. [28].

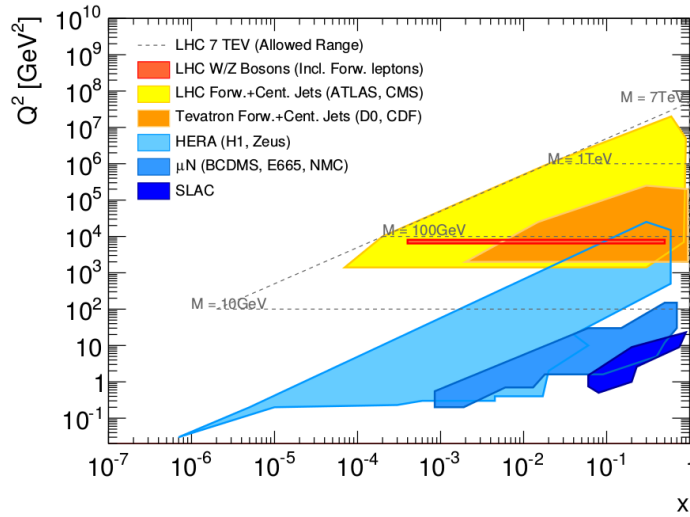


Figure 3.5.: Kinematic plane spanned by Bjorken x and Q^2 with a selection of experiments and their coverage. As noted above, the dependence with respect to Q^2 can be calculated with perturbative methods, while the dependence with respect to x has to be measured. Taken from ref. [28].

3.3. Higher-order effects

As discussed above, the Drell-Yan process is only the leading order contribution to the full production cross-section of W and Z bosons. Higher-order processes can be grouped into QCD and electroweak processes.

The QCD processes can only partly be calculated perturbatively. The running of the strong coupling constant $\alpha_s(Q^2)$ prohibits perturbative calculations in the regime where the momentum transfer Q^2 is small. Currently, the inclusive production cross-section and boson rapidity distributions are known in NNLO (cf. ref. [28]). However, the non-perturbative corrections have a large impact on the measured angular distributions, and therefore on p_T , m_T and E_T^{miss} of the resulting decay leptons. Examples of higher order QCD processes are shown in Figure 3.6.

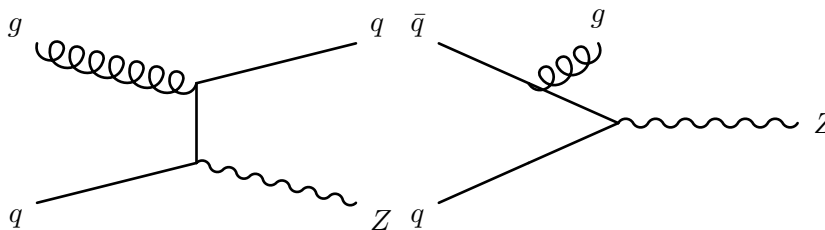


Figure 3.6.: Examples for higher-order QCD contributions to the Drell-Yan process. The left diagram shows the production of Z bosons through reactions of quarks and gluons, the right diagram QCD initial state radiation. Following ref. [28].

The electroweak processes, while small compared to higher-order QCD corrections, have a significant effect on the line shape of the invariant mass of the vector boson. Neglecting these processes would introduce a significant bias of the order of 10 MeV on the resulting measurement (cf. ref. [28]). The largest impact is due to final state radiation (FSR) of photons. A sample of higher order electroweak processes is shown in Figure 3.7.

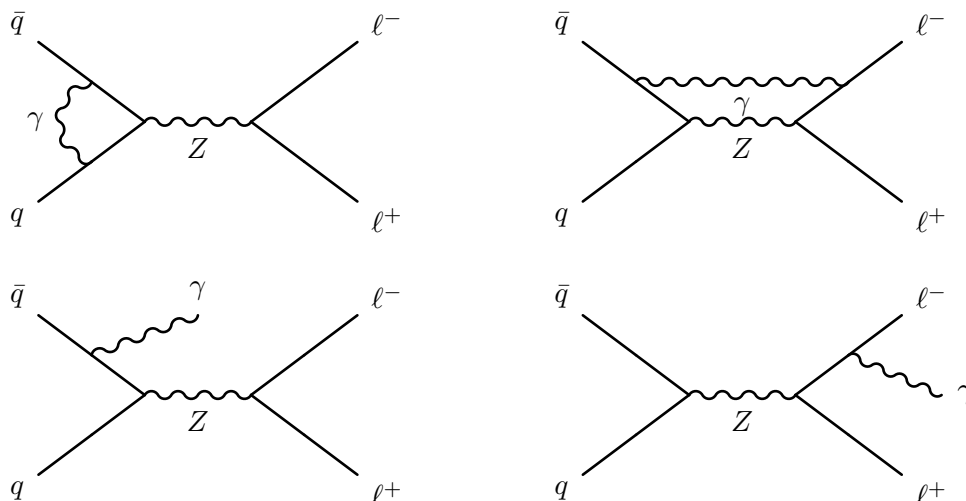


Figure 3.7.: Higher-order electroweak contributions to the Drell-Yan process. The upper histograms show a photon loop and simultaneous Z and γ exchange. The lower histograms show initial and final state radiation, respectively. Following ref. [28].

As can be seen in all these processes, the production of the vector boson is accompanied by further particles, meaning that its momentum transversal to the beam axis will be non-zero. This introduces a broadening of the distributions of the transversal momentum of the decay particles. Producing an accurate model of this distribution is theoretically very challenging, due to the strong interaction and hadronization processes involved. Therefore, detailed studies of this quantity have been performed with Z bosons (cf. for example [40]), with the result transferred to W bosons, as described in Section 5.4.1.

3.4. Underlying Event

After the production of a vector boson via the Drell-Yan process, two color charged proton remnants remain. On its own, none of these remnants are color-neutral, meaning that the partons in both remnants immediately start to interact with each other in order to form colorless particles. In the course of this process, a large number and variety of particles is produced — mesons, baryons, charged leptons and neutrinos. Most of these newly formed particles are unstable and decay within the detector. These processes are called the *underlying event*, and accompany each collision in which Z and W bosons are produced via the Drell-Yan process. Since the energy in the underlying event is spread over a large number of particles, the average momentum is very small compared to the decay of the Z and W bosons. Therefore, the latter is known as the hard scattering. An illustration of this theoretically challenging process is shown in Figure 3.8.

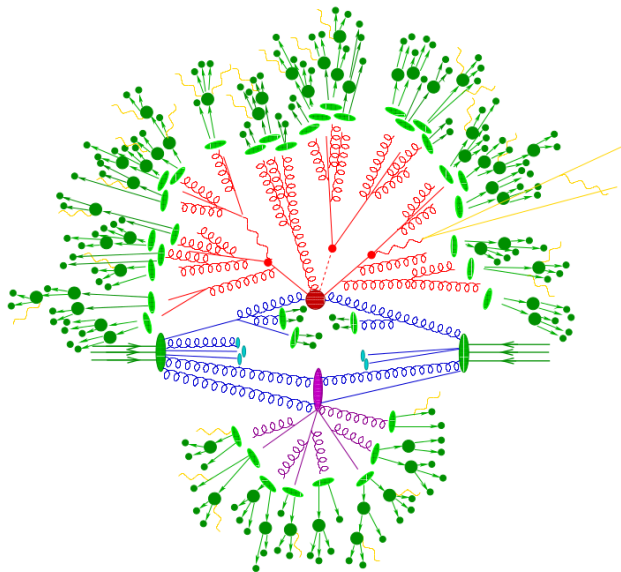


Figure 3.8.: Illustration of a proton-proton collision leading to the production of $t\bar{t}h$. The hard-scattering process is the large red dot. Both quarks and the Higgs decay directly after their production, illustrated by the small red dots. This leads to further hard QCD radiation. The proton remnants interact in the lower half of the illustration, as illustrated by the purple dot. In the end, the final state partons hadronize (light green) and decay (dark green). Photon radiation can be observed at every stage of the process, and is illustrated by the yellow line. Taken from ref. [41].

3.5. Pile-up

At the LHC, the proton beams consist of so-called bunches of protons. In the configuration chosen in 2011, each of these bunches contained approximately $1.5 \cdot 10^{11}$ protons (cf. ref. [42]), which means that generally several protons collide with each other at the same time. This means that, apart from the collision leading to the production of the Z or W boson, several other collisions are observed at the same time. This is called the *in-time* pile-up. Its main effect is a degradation of all energy measurements relying on the calorimeters, since a separation of the energy deposition in the detector into pile-up, underlying event and hard scattering can only be performed approximative. In addition, the tracking efficiency is affected due to the larger number of hits in the tracking system and subsequent ambiguities in the reconstruction. Figure 3.9 shows an overview of the number of interactions per crossing. As can be seen, for the two beam configurations with different β^* , on average 6.3 and 11.6 interactions per crossing were observed.

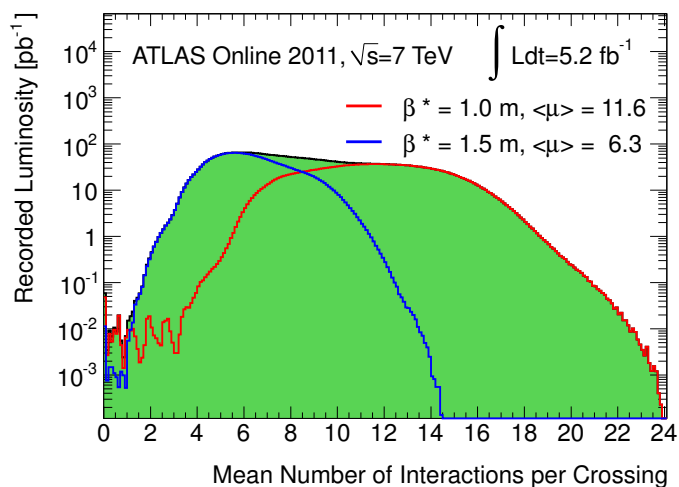


Figure 3.9.: Pile-up distribution for data taken in 2011. The two values of β^* correspond to the beam configuration after and before the September Technical Stop, respectively. Taken from ref. [42].

Apart from the *in-time* pile-up, also a certain amount of *out-of-time* pile-up can be observed. This is due to the fact that several signals in the detector have a time scale much larger than the time between the collisions of the bunches. An example is the rise and fall of the voltage in the LAr calorimeters after a particle has passed through (cf. also Section 4.3.2). These signals have a duration of approximately 700 ns, which greatly exceeds the time frame between two bunch collisions, which was 50 ns in 2011.

3.6. Background Processes

At the LHC, none of the processes above can be observed in isolation. On the contrary, in each measurement an admixture from unwanted physics processes is observed. These processes form the *background*, and usually exhibit properties fully unconnected to the process under study.

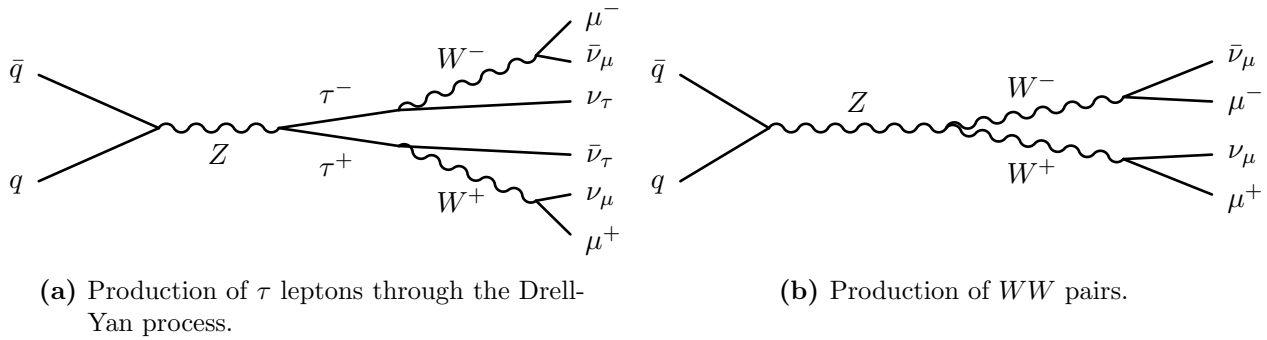


Figure 3.10.: Examples for electroweak background processes.

Therefore, events from these processes have to be suppressed, and the remaining admixture has to be carefully estimated.

In the case of W and Z production with charged leptons in the final state, these background processes can be grouped into three categories: electroweak background processes, top background processes and QCD background processes.

3.6.1. Background from Electroweak Bosons

Background from electroweak bosons, or *electroweak background* in short, originates from decays of W and Z bosons into charged leptons. In the analysis of the decay $Z \rightarrow \mu\mu$, this background is very small, with significant contributions from the decay of τ leptons and the production of pairs of gauge bosons. In the decay of $W \rightarrow \mu\nu$, a significant level of electroweak background is produced through decays of $Z \rightarrow \mu\mu$ in which one muon is not emitted within the detector acceptance.

At the LHC, τ leptons are mostly produced through the Drell-Yan process. The processes $Z \rightarrow \tau\tau$ and $W \rightarrow \tau\nu_\tau$ are the same as described above, except for Z and W bosons decaying into τ leptons instead of muons. The reason why these processes appear as background processes is the short life time of the τ lepton of $(290.3 \pm 0.5) \times 10^{-15}$ s (cf. ref. [8]). This means that the τ will usually decay inside the detector. One of the decay channels for the τ lepton is $\tau \rightarrow \mu\nu_\mu\nu_\tau$. This process has a branching ratio of $(17.41 \pm 0.04)\%$ (cf. ref. [8]) and is depicted in Figure 3.10(a).

Decays of τ leptons usually play a minor role due to the small momentum of the muons in the final state. While the τ has a momentum distribution very similar to the muons from $Z \rightarrow \mu\mu$ or $W \rightarrow \mu\nu$, with the only difference being the larger mass of the τ compared to μ , the neutrinos produced in the τ decay carry a significant part of the momentum on average.

Apart from the production of τ leptons, also the production of pairs of gauge bosons, as illustrated in Figure 3.10(b), can lead to background events passing the selection criteria for the Drell-Yan process. This background is also to a large extent negligible, since its cross-section, multiplied with the branching ratio for muonic decays, is only ~ 10 nb, much smaller than that of the Drell-Yan process with 990 nb.

3.6.2. Top Background

The top is the heaviest fermion known so far. With its mass of $(173.21 \pm 0.51(\text{stat.}) \pm 0.71(\text{sys.}))$ GeV (cf. ref. [8]), a large variety of decay channel are feasible. The large decay

width of $2.00_{-0.43}^{+0.47}$ GeV (cf. ref. [8]) translates into a very short life time of $3.3 \cdot 10^{-25}$ s using $\tau = \hbar/\Gamma$. This means that, even when considering relativistic time dilation, the top quark decays almost instantaneously inside the detector. This also means that the top quark will not form hadrons, i.e. *hadronize*, before its decay. The decays usually progress via W radiation into lighter quarks. The W bosons involved in these decay chains are able to produce muons.

In a process similar to the Drell-Yan process, pairs of top and anti-top quarks can be produced via a triple gluon vertex, as illustrated in Figure 3.11. Another possibility to produce top quarks is via a gluon induced t-channel process (cf. ref. [43]), in which two gluons couple to the $t\bar{t}$ pair.

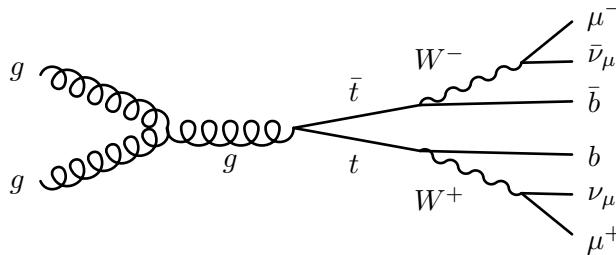


Figure 3.11.: Example for a process producing $t\bar{t}$ pairs.

3.6.3. Multijet Background

Apart from top decays, the production and subsequent decay of the remaining quark flavors also plays a large role. However, contrary to the top quark, the life time of these quarks is long enough for hadronization to occur. Simulating these processes is very challenging due to the amount of strong interactions involved. Moreover, decays in which muons are produced, are rare and only play a role due to large cross sections for quark production. The theoretical uncertainty, as well as the large statistics needed, make it impossible to obtain a good description from Monte Carlo simulations alone. On the contrary, the contribution from these processes is usually estimated via data-driven methods. Detailed descriptions of these strategies can be found in the sections describing the different analyses later in this thesis.

3.7. Overview of Previous Measurements

Since its discovery through the UA1 and UA2 collaborations at CERN in the early 1980s (cf. ref. [14,16]), the mass of the W boson could be measured with ever increasing precision. From values of (81 ± 5) GeV and 80_{-6}^{+10} GeV reported by the UA1 and UA2 collaborations in the references above, towards the current world average of (80.385 ± 0.015) GeV (cf. ref. [8]), an improvement in precision of more than two orders of magnitude could be achieved. An overview of the measurements used by the Particle Data Group in calculating its world average are shown in Table 3.1. Note that, for comparison, the world average of M_Z is (91.1876 ± 0.0021) GeV (cf. ref. [8]), with the uncertainty an order of magnitude smaller. As will become clearer in Part III of this thesis, this is mostly driven by the availability of a second charged lepton in the final state.

Year	Experiment	M_W [GeV]	ΔM_W [GeV]	Reference
2001	CDF (Tevatron)	80.433	0.079	[44]
2002	D0 (Tevatron)	80.483	0.084	[45]
2006	ALEPH (LEP)	80.440	$0.043(\text{stat.}) \pm 0.027(\text{sys.})$	[46]
2006	L3 (LEP)	80.270	$0.046(\text{stat.}) \pm 0.031(\text{sys.})$	[47]
2006	OPAL (LEP)	80.415	$0.042(\text{stat.}) \pm 0.031(\text{sys.})$	[48]
2008	DELPHI (LEP)	80.336	$0.055(\text{stat.}) \pm 0.039(\text{sys.})$	[49]
2012	CDF (Tevatron)	80.387	0.019	[50]
2014	D0 (Tevatron)	80.375	0.023	[51]
2015	World average	80.385	0.015	[8]

Table 3.1.: Overview of previous measurements of M_W and Γ_W . Only the values used by the Particle Data Group for the fit of the world average are shown. Values taken from ref. [8].

As can be seen, the mass of the W boson could be measured with higher precision at the $p\bar{p}$ Tevatron experiments D0 and CDF than those at the e^+e^- collider LEP. This appears to be counter-intuitive at first glance, because lepton colliders generally offer a much cleaner environment for precision studies. This is because the two collision partners are point-like, leading to better constraints on the kinematics of the vector boson exchange than can be accomplished at hadron colliders.

Even though effects of the structure as well as interaction of remnants of the collision partners play no role, the measurement of M_W at lepton colliders is very challenging. This is because the production mechanism for W and Z bosons differ fundamentally at lepton colliders: At hadron colliders, W bosons are produced via the Drell-Yan process, similarly to Z bosons and with comparable cross-sections. At lepton colliders, on the other hand, Z and W bosons are produced through very different processes. While Z bosons can be produced similar to the Drell-Yan process via $e^+e^- \rightarrow Z \rightarrow \ell^+\ell^-$, W bosons are predominantly produced via the exchange of a neutrino and the production of a W boson pair. The latter process has a much smaller cross-section than the former — for example, the ALEPH result for M_W was obtained with only 8692 W boson events, while the D0 result for M_W was obtained with 500 000 W boson events. This illustrates the different strategies pursued at lepton and hadron colliders.

At lepton colliders, in addition to direct reconstruction of the decay particles of the decay of the W boson pair, the sharp turn-on of the cross-section as function of the center of mass energy at $2 \times M_W = 161$ GeV can be used to measure M_W . This was done for all measurements performed at LEP shown in Table 3.1. At hadron colliders, the measurement of M_W is driven by single W boson production close to M_W .

4. Experimental Setup

4.1. Large Hadron Collider

The Large Hadron Collider (LHC) is a particle accelerator located at the European Laboratory for Particle Physics (CERN¹) on the French-Swiss border close to Geneva, Switzerland.

With a circumference of 27 km, the Large Hadron Collider (LHC) is the largest particle accelerator at the time of writing. It uses the tunnel built for its predecessor LEP², an e^+e^- collider aimed at precision measurements of W and Z properties. It can be operated in two modes, accelerating either heavy ions or protons, and supplies four large and several small experiments with high-energetic beams and collisions.

For protons, the LHC was designed for a center-of-mass energy of up to $\sqrt{s} = 14$ TeV. The results discussed in this thesis were obtained on data collected in 2011 and 2012, with a center-of-mass energy of $\sqrt{s} = 7$ TeV in 2011 and $\sqrt{s} = 8$ TeV in 2012. At the beginning of 2013, the LHC was shut down for maintenance work until its restart with $\sqrt{s} = 13$ TeV in 2015.

At the design luminosity of $1 \times 10^{34} \text{ cm}^{-2}\text{s}^{-1}$, two bunches of protons, each containing 1.1×10^{11} protons, are brought into collision each 25 ns, leading to approximately 25 inelastic proton-proton interactions during each collision. In 2011 and 2012, these parameters were not reached. The time between two collisions was increased to 50 ns. In 2011, the luminosity could be steadily increased with an average of $3.6 \times 10^{33} \text{ cm}^{-2}\text{s}^{-1}$. The number of protons per bunch was slightly higher than designed, with 1.5×10^{11} protons per bunch. At the beam parameters chosen, this led to an average of only 9.1 inelastic proton-proton interactions per collision. From the point of view of the measurement of M_W , this is very advantageous, since higher pile-up leads to a degradation of the reconstructed values of E_T^{miss} and thus m_T , as discussed in Section 4.5.5.

The LHC is the last link in a chain of accelerators, as illustrated in Figure 4.1. This chain starts with a Linear Accelerator (LINAC2), from where the protons are accelerated via the BOOSTER, PS and SPS before being injected into the LHC itself. The beam quality and luminosity deteriorates on a time scale of hours, until the beams have to be dumped and the acceleration process starts anew.

¹It should be noted that CERN refers to the organization which operates the European Laboratory for Particle Physics. The origin of this abbreviation is the former name of the organization — *Conseil Européen pour la Recherche Nucléaire*, now the *European Organization for Nuclear Research*. *CERN* is commonly used as shorthand reference for the European Laboratory for Particle Physics and so will be in this thesis.

²Large Electron-Positron Collider

4. Experimental Setup

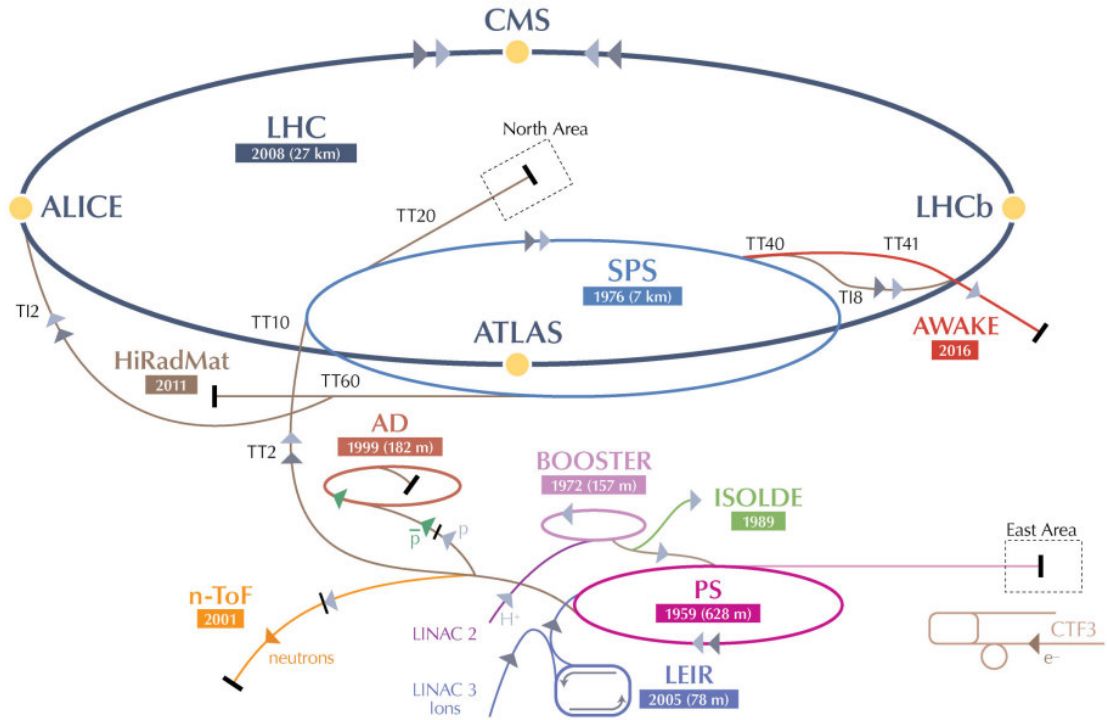


Figure 4.1.: Overview of the CERN accelerator complex. Shown in light grey are the beam lines for protons, in darker grey for ions, in orange for neutrons, green for anti-protons and brown for electrons. The years give the dates of the inauguration for the different accelerators. Taken from ref. [52].

4.2. Overview of Detectors

The four large detectors at the LHC can be divided into two general purpose detectors, ATLAS and CMS, and two detectors with a specialized physics program, ALICE and LHCb.

At the ATLAS³ detector (cf. ref. [53]) as well as the CMS (cf. ref. [54]), a broad physics program is pursued. Apart from studies of the Standard Model, of which this thesis is a part, searches for new particles are performed. A special emphasis is put on the now successful search for the Higgs boson, as well as for particles predicted by extensions of the SM, such as supersymmetry, which predicts yet undetected partners for each particle of the SM, or further exotic particles, such as heavy versions of the W and Z bosons.

The ATLAS and CMS experiments are independently planned and operated, offering a very similar scope and performance. This means that both experiments are able to cross-check their results and validate their discoveries.

ALICE (cf. ref. [55]) was built to address questions in the physics of heavy ion collisions, such as the investigation of quark-gluon plasmas, a state of matter which likely existed shortly after the Big Bang. It can perform measurements similar to those performed at the RHIC collider in Upton, New York (cf. ref. [56]).

LHCb (cf. ref. [57]) is a detector specially designed to investigate the physics of b -quarks and B -mesons, with a special focus on the measurement for CP violation, one of the prerequisites for the existence of the universe in its present form⁴.

In addition to these four large detectors, also two small detectors are built at some distance from the interaction points where the large detectors are located. These are the TOTEM (cf. ref. [59]) and LHCf (cf. ref. [60]). Their goal is the investigation of particles emitted at very small angles to the beam line, which cannot be accessed by the other experiments. TOTEM is specialized in measuring the total proton-proton cross section, while LHCf uses the high energetic pions to study the effect of cosmic rays on detectors. The high-energetic particles for these two small detectors originate from the collisions in the interaction points of CMS and ATLAS, respectively.

³ATLAS was originally an abbreviation for *A Toroidal LHC Apparatus*, a name which is no longer commonly used.

⁴The other prerequisites are a violation of baryon number conservation, breaking of C symmetry and a state out of thermal equilibrium, the so-called Sakharov criteria (cf. ref. [58]).

4.3. ATLAS Detector

Note: The information presented in this chapter is to a large extent based on ref. [53].

Like most modern particle detectors in use at collider experiments, the ATLAS detector is built with cylindrical symmetry around the beam axis, as shown in Figure 4.2. It has a length of approximately 44 m and diameter of 25 m with a weight of 7000 t. The detector is generally divided into the two end-caps on both sides and the so-called barrel between them. Using this design, the ATLAS detector is able to cover the full azimuthal angle φ and almost the full polar angle θ . Only the range of $|\eta| > 4.9$ ⁵ is not fully instrumented⁶, corresponding to $\theta < 0.85^\circ$ and $\theta > 179.15^\circ$, yielding a coverage in solid angle of 12.51 sr, or 99.5% of a full sphere.

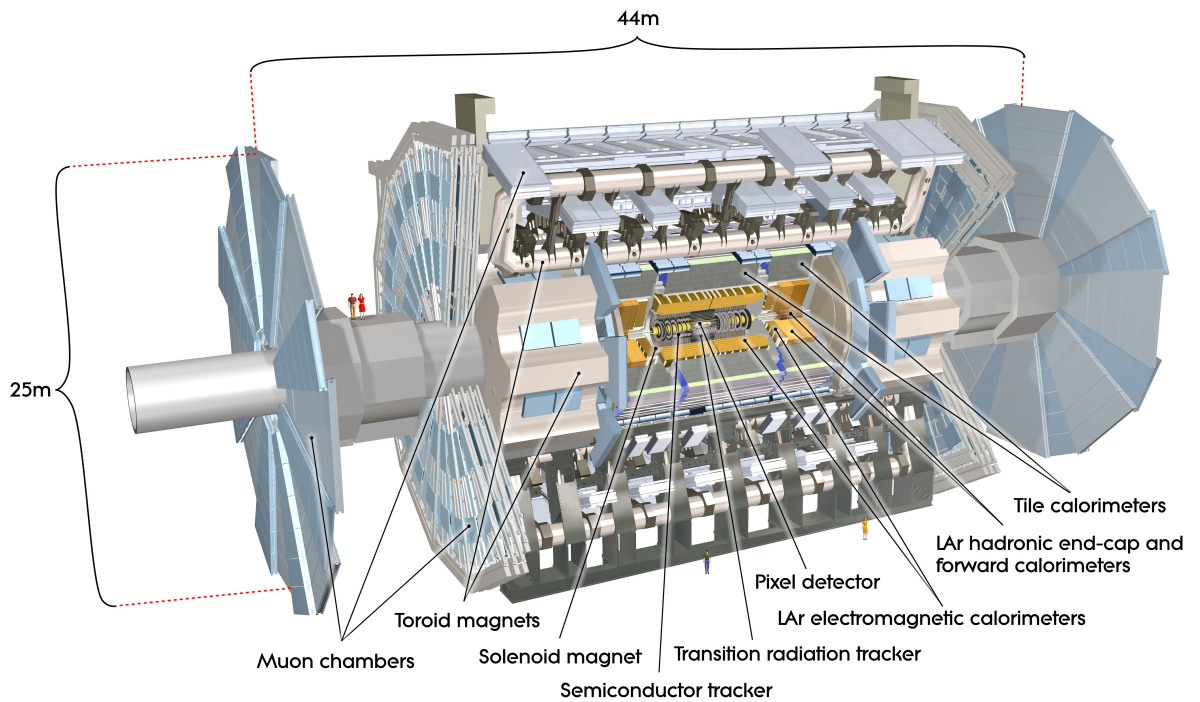


Figure 4.2.: Illustration of the ATLAS detector. As can be seen, the ATLAS detector exhibits a cylindrical symmetry allowing for an almost complete 4π sr coverage. Figure taken from ref. [62].

Following common design principles, it has an onion-like structure. A particle produced in the interaction point and with sufficient energy and life time⁷ will transverse a set of detector layers, each specialized for a specific purpose. This is shown in Figure 4.3.

⁵The pseudorapidity η will be introduced in greater detail later. It is defined as $\eta = -\ln(\tan(\theta/2))$.

⁶With the exception of the ALFA, ZDC and LUCID detectors, mostly aimed at a precise luminosity determination and beam monitoring (cf. ref. [61]).

⁷Apart from stable particles, such as electrons, this includes also muons and neutrons. Due to their high energy, they will generally decay after having traversed the detector first.

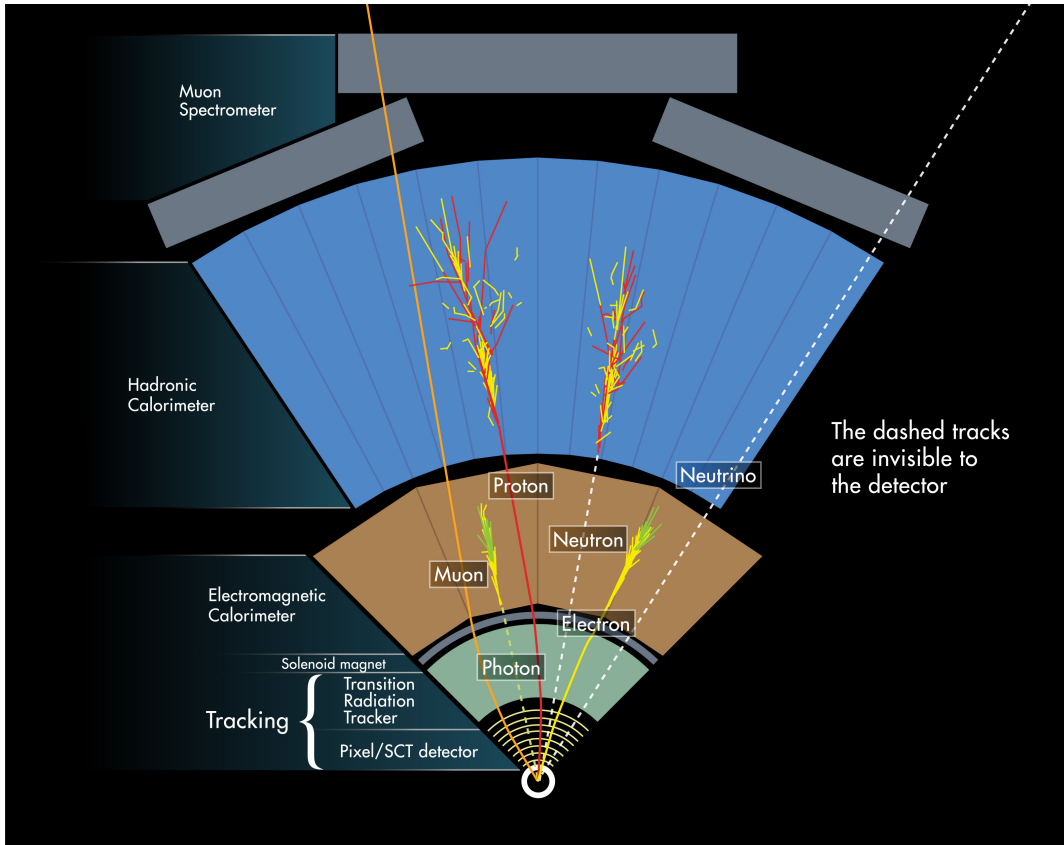


Figure 4.3.: Working principle of the ATLAS detector. The image shows a section of the ATLAS detector with the interaction point at the bottom and the surface of the ATLAS detector at the top. The particle traverses a set of different detector systems specialized for measuring different properties. Figure taken from ref. [63].

From inside out, the systems are:

- **Inner Detector** The inner detector (ID) is used to measure the trajectory of high energetic charged particles originating in the interaction point. This information can be used to infer the type of the particle, its momentum and exact origin. A detailed description is given in Section 4.3.1.
- **Solenoid Magnet** The ID is surrounded by a solenoid magnet producing a magnetic field of 2 T in the ID. This field is needed in order to infer the ratio of charge to momentum q/p via the Lorentz force and its effect on the traversing charged particle.
- **Calorimeters** The purpose of the calorimeter system is the measurement of the energy of the particles produced in the interaction by absorbing them. The electromagnetic calorimeter measures the energy of electrons and photons, while the hadronic calorimeter measures the energy of hadrons produced in the collision. This distinction can be made since electrons and photons interact via the electromagnetic force unlike hadrons, which predominantly interact via the strong force. A detailed description is given in Section 4.3.2.

4. Experimental Setup

- **Muon System** Unlike most other particles, muons can pass through the detector without being absorbed. Therefore, the muon detectors are forming the outer shell using the rest of the detector as shielding against other particles able to mimic a muon signature. The muon system consists of the muon detectors themselves as well as a system of magnetic coils producing a toroidal magnetic field around it. A detailed description is given in Section 4.3.3.

The coordinate system of ATLAS reflects its symmetries. It is a modified cylindrical coordinate system, with the z axis formed by the beam axis. Positive values of z point into the clock-wise direction of the beam pipe. The y axis points upwards and the x axis into the center of the accelerator ring. The azimuth φ is chosen such that $\varphi = 0$ corresponds to the positive x axis. Instead of using the polar angle θ , the pseudo-rapidity η is chosen. It is defined as:

$$\eta = -\ln \left[\tan \left(\frac{\theta}{2} \right) \right] \quad (4.1)$$

For massless particles, this is identical to the rapidity $y = \frac{1}{2} \ln \left(\frac{E+p_z}{E-p_z} \right)$. Strictly speaking, this definition is only valid if $p_x, p_y \ll p_z$, which is usually the case at hadron colliders and therefore a common definition in high energy physics. The rapidity y has the favorable feature that differences in y are invariant under Lorentz boosts along the z -axis. For particles with negligible mass, such as electrons and muons, the same holds true for the pseudo-rapidity η . Distances in $\eta - \varphi$ space are calculated as $\Delta R = \sqrt{\Delta\eta^2 + \Delta\varphi^2}$.

4.3.1. Inner Detector

As described earlier, the purpose of the inner detector is a precise measurement of the trajectories of the particles produced in the interaction point. Apart from the measurement of the particle momentum, the trajectories measured by the ID have to be so precise that an assignment of the particle to the correct production vertex can be made. In 2011, an average of 9.1 inelastic interactions could be reconstructed per bunch crossing. In 2012 this number increased to 20.7 (cf. ref. [64]). These collision vertices are called primary vertices (PV). Usually, only one of these primary vertices produces the particles of interest, e.g. a W or Z boson. The other PV are called pile-up vertices. Apart from these primary vertices, also secondary vertices can appear if relatively long-lived particles, such as τ leptons and b hadrons, decay after some time of flight. This is for example important in the tagging of jets originating from b -quarks.

In order to meet its requirements, the inner detector consists of three specialized sub-detectors, from inside out the Pixel Detector (PIX), consisting of three layers of silicon pixel sensors, the Silicon Strip Detector (SCT), consisting of four layers of silicon strip sensors and the Transition Radiation Tracker (TRT), being a straw tube tracker. An illustration of the ID is shown in Figure 4.4.

In total the ID has a dimension of 6.2 m in length and 2.1 m in diameter. It covers a range in pseudo-rapidity up to $|\eta| = 2.5$. In order to reduce leak currents due to radiation damage, the silicon detectors — PIX and SCT — are kept at a temperature of -5 to -10 °C. The whole ID is placed in a solenoid, providing a homogeneous magnetic field with 2 T, oriented parallel to the beam axis. This means that charged particles will be deflected in the r - φ plane. On average, more than 40 hits are produced per track.

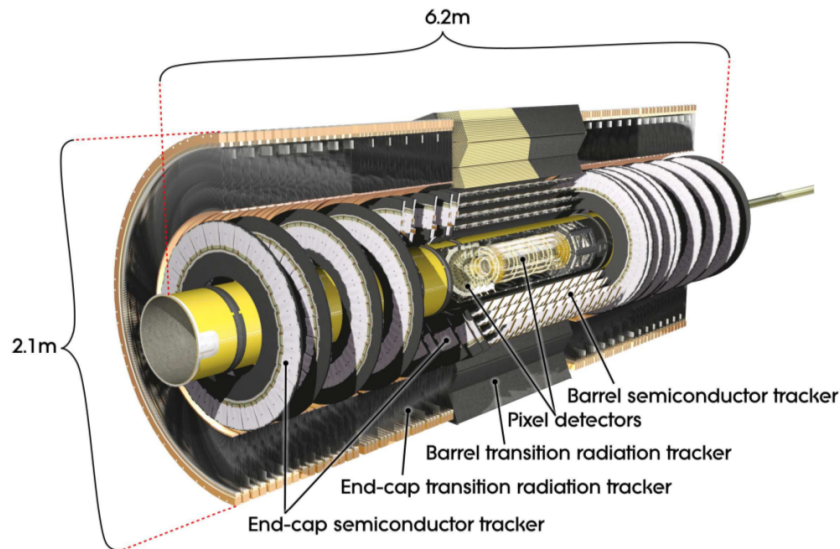


Figure 4.4.: Illustration of the Inner Detector and its components. Taken from ref. [53].

Pixel Detector

As is common at ATLAS, the Pixel detector (PIX) is separated into a barrel and two endcaps. The barrel is formed by three layers of silicon pixel sensors, while the endcaps are formed by three so-called disks on each side. An overview is found in Table 4.1. Each of the 1744 modules contains 47 232 pixels each, forming 46 080 readout channels. In total, this equals approximately 80M readout channels, corresponding to 80% of the total readout channels of ATLAS. Approximately 90% of the pixels have a size of $50\ \mu\text{m} \times 400\ \mu\text{m}$, with the remaining pixels of a size of $50\ \mu\text{m} \times 600\ \mu\text{m}$. This is due to geometry constraints from the readout electronics.

Barrel	Radius [mm]	Modules	Pixels
Layer-0	50.5	286	13.2×10^6
Layer-1	88.5	494	22.8×10^6
Layer-2	122.5	676	31.2×10^6
End-cap (one side)	z [mm]	Modules	Pixels
Disk 1	495	48	2.2×10^6
Disk 2	580	48	2.2×10^6
Disk 3	650	48	2.2×10^6
Barrel and both end-caps		1744	80.4×10^6

Table 4.1.: Overview of the PIX detector. It is separated into a barrel, formed by three layers, and two end-caps formed by three disks each. Almost every pixel has its own read-out channel. Table taken from ref. [53], adapted.

4. Experimental Setup

The pixels offer an accuracy in the position measurement of $10\ \mu\text{m}$ in the $R - \varphi$ plane and $115\ \mu\text{m}$ in the z axis for Layers 0,1 and 2, as well as $10\ \mu\text{m}$ in the $R - \varphi$ plane and $115\ \mu\text{m}$ in the R axis for the disks.

Silicon Strip Detector

The Silicon Strip Detector (SCT) consists of a barrel formed by four layers, and two endcaps, formed by nine disks each. In total, the SCT has 4088 modules, consisting of four sensors each. Two sensors are on the bottom, two on the top side of the module, and are rotated by $\pm 20\ \text{mrad}$ with respect to each other. This stereo angle enables a measurement of $R - \varphi$, as well as R or z , simultaneously. Each barrel module contains 786 strips with $80\ \mu\text{m}$ pitch, aligned along the beam axis. In the endcaps, the strips are oriented radially. On average, eight hits per track are expected. The accuracy of these measurements is $17\ \mu\text{m}$ in the $R - \varphi$ plane and $580\ \mu\text{m}$ in the z axis for the barrel as well as in the R axis for the endcaps.

Transition Radiation Tracker

The Transition Radiation Tracker (TRT) consists of a barrel part and two endcaps, formed by nine wheel-like structures. It consists of approximately 280 k proportional drift tubes (straws) of 4 mm in diameter, which are oriented in the z axis in the barrel and radially in the endcaps. Their diameter was chosen such that the TRT can operate at the high rates. With the chosen design, all charged tracks with $p_T > 0.5\ \text{GeV}$ and $|\eta| < 2.0$ will transverse at least 36 straws, except in the transition region between barrel and end cap ($0.8 < |\eta| < 1.0$), where the minimum is 22 crossed straws. The purpose of the TRT is twofold: Not only do the straws detect the passage of ionizing particles, in addition the material between the straws — polypropylene fibers (barrel) and foils (endcaps) — leads to the production of transition radiation for ultra-relativistic particles. An average of seven to ten hits from transition radiation are expected for electrons with energies above 2 GeV. This information is used to differentiate pions from electrons, since the amount of transition radiation for particles with identical momentum decreases with the mass.

4.3.2. Calorimeters

The main task of the calorimeter system is the energy measurement of all particles — except neutrinos and muons — produced in the interaction. Both neutrinos and muons are not absorbed in the calorimeter. While muons are detected by the muon system surrounding the calorimeter, neutrinos leave ATLAS without interaction. In order to estimate their energy and direction, the so-called missing energy E_T^{miss} is calculated as described in Section 4.5.5. A good estimate can only be found with a large coverage of the detector. For ATLAS, as discussed above, the calorimeters are able to cover 99.5% of a full sphere, thus providing an excellent estimate of E_T^{miss} .

The ATLAS calorimeters are divided into electromagnetic and hadronic calorimeters. The task of the former is an energy measurement of photons and electrons, while the latter is used to measure the energy of hadrons. Similar to the ID, the calorimeters are divided into barrels and endcaps. In addition, a so-called forward calorimeter was added, which is used for electromagnetic as well as hadronic calorimetry. An illustration of the calorimeters is shown in Figure 4.5, while a summary of the coverages of the different systems is shown in Table 4.2.

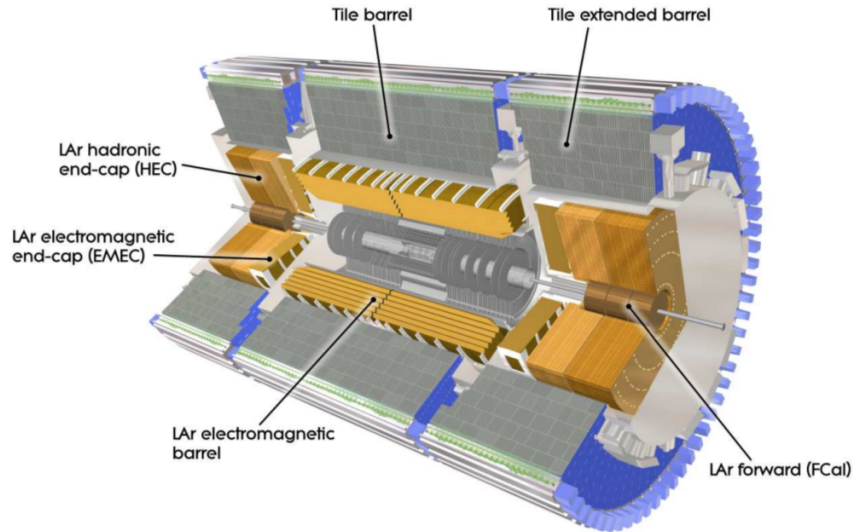


Figure 4.5.: Illustration of the calorimeter system and its components. Taken from ref. [53].

System	Coverage in $ \eta $	Detector medium	Absorber medium
Electromagnetic Barrel	$0.0 < \eta < 1.475$	Liquid Argon	Lead
Electromagnetic Endcap	$1.375 < \eta < 3.2$	Liquid Argon	Lead
Hadronic Tile Barrel	$0.0 < \eta < 1.0$	Plastic	Steel
Hadronic Tile Extended Barrel	$0.8 < \eta < 1.7$	Plastic	Steel
Hadronic Endcap	$1.5 < \eta < 3.2$	Liquid Argon	Copper
Forward Calorimeter	$3.1 < \eta < 4.9$	Liquid Argon	Copper & Tungsten

Table 4.2.: Summary of the different calorimeter sub-systems. Values taken from ref. [53].

The ATLAS electromagnetic calorimeters were built to obtain a relative energy resolution of $\sigma_E/E = 10\%/\sqrt{E[\text{GeV}]} \oplus 0.7\%$. For the hadronic calorimeters, the design goal was a jet energy resolution of $\sigma_E/E = 50\%/\sqrt{E[\text{GeV}]} \oplus 3\%$ in $|\eta| < 3.2$ and $\sigma_E/E = 100\%/\sqrt{E[\text{GeV}]} \oplus 10\%$ in the forward region. All calorimeters are sampling calorimeters, albeit with different choices for the absorber and active detection material. A summary is given in Table 4.2.

Apart from measuring the energies of the electromagnetic and hadronic particles produced in the collision, the calorimeters have an important secondary task: shielding the muon system from these particles by absorbing them. Otherwise a so-called punch-through into the muon system would occur, faking the presence of a real muon. To this end, the calorimeters have a large depth, as measured by the radiation length or interaction length for the electromagnetic and hadronic calorimeter respectively. For the electromagnetic calorimeter, the radiation length⁸ is at least $22 X_0$ in the barrel and $24 X_0$ in the end-caps. For the hadronic

⁸The radiation length X_0 denotes the length after which the energy of the incoming particles has decreased to $1/e$ of the original value.

4. Experimental Setup

calorimeters, the interaction length⁹ is 9.7λ in the barrel and 10λ in the end-caps. Together with 1.3λ from the outer support, a total depth of 11λ could be reached at $\eta = 0$. With this depth, punch-through is negligible at ATLAS.

Electromagnetic Calorimeter

The electromagnetic calorimeter consists of the Electromagnetic Barrel and the Electromagnetic Endcap (EMEC). The former is divided into two halves with a gap of 4 mm at $|\eta| = 0$, while the latter consists of two so-called wheels. The EMEC outer wheel covers from 1.375 to 2.5 in $|\eta|$ and surrounds the inner wheel (EMEC IW), which has a coverage in $|\eta|$ from 2.5 to 3.2. Between the Barrel and Endcap a *transition region* exists, which is usually excluded in analyses performed with electrons due its deviating behavior from the reminder of the calorimeter. Similarly, the region of the transition from the EMEC IW to the Forward Calorimeter is excluded.

The choice of liquid argon (LAr) as the active detector material was motivated by its "intrinsic linear behavior, its stability of response over time and its intrinsic radiation-hardness" (cited from ref. [53]). Due to the usage of LAr as active material, the calorimeters have to be cooled to 87 K (cf. ref. [65]). To this end, the barrel and both endcaps are each housed in cryostats. The endcap cryostats also contain the hadronic end-cap calorimeter (HEC) and the forward calorimeter (FCal).

The electromagnetic calorimeter has an accordion geometry, offering a full coverage with respect to φ without any cracks. Moreover, it allows for a fast extraction of the obtained signal. However, the length of the signal still is on the order of multiple bunch crossings, thereby requiring a careful examination of the energy as a function of in-time and out-of-time pile-up (cf. Section. 3.5). Studies of this kind were performed as a service task as part of this thesis. The structure of the accordion geometry was optimized for large uniformity in terms of linearity and resolution as a function of φ .

The electromagnetic calorimeters consist of several layers with different granularity. An overview is given in Table 4.3. It should be noted that the granularity with respect to φ is usually larger than with respect to η . This is because the inner detector is immersed in a solenoidal magnetic field, which deflects electrons along the φ direction. The bremsstrahlung produced by these electrons will therefore encompass a larger area in φ than η .

Hadronic Calorimeter

The hadronic calorimeters are specialized in the measurement of the energy of the hadrons produced in the collision. It surrounds the electromagnetic calorimeter and inner detector, which together have a depth of $\approx 2 \lambda$, depending on the location in η . This means that the energy measurement of the hadronic calorimeters is almost unaffected by these detector components.

Similar to the electromagnetic calorimeter, the hadronic calorimeter is a sampling calorimeter, using a steel-plastic combination for the tile component, and a copper-LAr combination for the endcap. The latter was chosen to withstand the high particle flux expected in this region.

⁹The interaction length is the mean free path of the hadrons in the detector material.

Sub-system	Coverage in $ \eta $	Granularity in $\Delta\eta \times \Delta\varphi$
Barrel Presampler	$ \eta < 1.52$	0.025×0.1
Barrel 1st layer	$ \eta < 1.40$	$0.025/8 \times 0.1$
	$1.40 < \eta < 1.475$	0.025×0.025
Barrel 2nd layer	$ \eta < 1.40$	0.025×0.025
	$1.40 < \eta < 1.475$	0.075×0.025
Barrel 3rd layer	$ \eta < 1.35$	0.050×0.025
Endcap Presampler	$1.5 < \eta < 1.8$	0.025×0.1
	$1.375 < \eta < 1.425$	0.050×0.1
Endcap 1st layer	$1.425 < \eta < 1.5$	0.025×0.1
	$1.5 < \eta < 1.8$	$0.025/8 \times 0.1$
	$1.8 < \eta < 2.0$	$0.025/6 \times 0.1$
	$2.0 < \eta < 2.4$	$0.025/4 \times 0.1$
	$2.4 < \eta < 2.5$	0.025×0.1
	$2.5 < \eta < 3.2$	0.1×0.1
Endcap 2nd layer	$1.375 < \eta < 1.425$	0.050×0.025
	$1.425 < \eta < 2.5$	0.025×0.025
	$2.5 < \eta < 3.2$	0.1×0.1
Endcap 3rd layer	$1.5 < \eta < 2.5$	0.050×0.025

Table 4.3.: Granularity of the electromagnetic calorimeters. Values taken from ref. [53].

Forward Calorimeter

The forward calorimeter (FCal) covers the range $3.1 < |\eta| < 4.9$. Only with this calorimeter an almost hermetic design of ATLAS could be reached. Due to the vicinity to the beam, a large flux of high-energetic particles had to be expected. For this reason, the FCal was designed to have only very small LAr gaps, using a rod-like structure for the electrodes. The FCal consists of three modules: from the interaction point outwards these are FCal1, FCal2 and FCal3.

FCal1 uses copper as absorber and is mainly used as electromagnetic calorimeter. Copper was chosen to obtain an optimal resolution and heat removal. FCal2 and FCal3 use tungsten as absorber and are used as hadronic calorimeters. They were optimized for high absorption length. In total, 1762 channels are read from each FCal.

4.3.3. Muon System

The muon system (MS) is illustrated in Figure 4.6. It forms the outer shell of the ATLAS detector, with the detector components closer to the interaction point acting as a shield for other species of particles. It is designed to detect muons with $|\eta| < 2.7$, with the ability to trigger on these muons in the region with $|\eta| < 2.4$. The resolution of the transverse momentum is $\sigma_{p_T}/p_T = 10\%$ at $p_T = 1$ TeV. The main components are listed in Table 4.4. As for the other detector systems, the muon system can be divided into a barrel, consisting of MDTs and RPCs, and two endcaps, each consisting of MDTs, CSCs and TGCs.

4. Experimental Setup

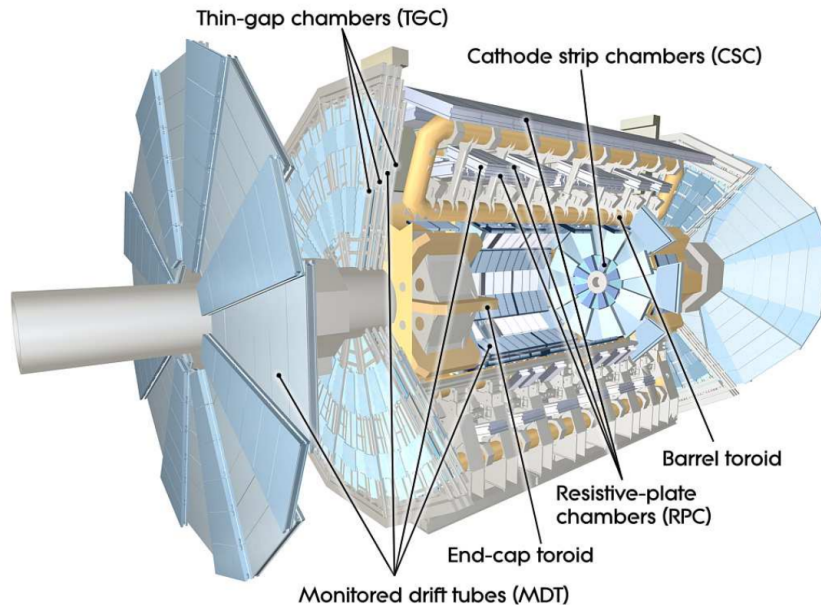


Figure 4.6.: Illustration of the muon system and its components. Taken from ref. [53].

Component	Range in $ \eta $	Main Task
Monitored Drift Tubes (MDT)	$0 < \eta < 2.7$	Precision tracking
Cathode Strip Chambers (CSC)	$2.0 < \eta < 2.7$	Precision tracking
Resistive Plate Chambers (RPC)	$0 < \eta < 1.05$	Triggering, second coordinate
Thin Gap Chambers (TGC)	$1.05 < \eta < 2.7$	Triggering, second coordinate

Table 4.4.: Overview of the different components of the ATLAS muon system. Data taken from ref. [53].

The muon system is located in and around the toroidal magnets after which ATLAS is named. It provides the magnetic field necessary for the measurement of muon momenta, which amounts to 0.5 T in the barrel region and 1 T in the end-cap region. Between those regions, the field is irregular, which poses a challenge for track reconstruction. The toroid magnet system consists of three large air-core toroids — one barrel toroid and two end-cap toroids on each side of the detector.

As can be discerned from Table 4.4, the muon sub-systems can be divided into two sub-systems specialized in tracking and two sub-systems specialized in triggering. The precision tracking is performed by the Monitored Drift Tubes (MDTs) at low values of $|\eta|$, with added Cathode Strip Chambers (CSCs) at larger values of $|\eta|$. The triggering is performed by fast trigger chambers, namely the Resistive Plate Chambers (RPCs) and Thin Gap Chambers (TGCs). The latter provide a signal a few tenths of a nanosecond after being traversed by a charged particle. All sub-systems exist in two widths, large and small, which are installed in alternating order (cf. ref. [13]).

- **Monitored Drift Tubes (MDTs):** The main components of this system are pressurized drift tubes with a diameter of approximately 30 mm. These are filled with an Ar/CO₂ mixture at 3 bar. The main goal of this system is precision tracking with a resolution in the z -axis of 35 μm . Approximately 20 measurements per track are expected.
- **Cathode Strip Chambers (CSCs):** Similar to the MDT, the CSC provides a precision measurement, the difference being the larger values of $|\eta|$ covered by the CSC and the deviating working principle. The CSCs consist of two disks with eight chambers each — eight small chambers and eight large chambers. Each chamber contains four CSC planes, resulting in four independent measurements in η and φ along each track.

The reason for the switch to CSCs at high values of $|\eta|$ lies in the high-rate limit of MDTs. The limit safe operation for MDTs is 150 Hz/cm², which is exceeded in the region of $|\eta| > 2$ in the first layer of the end-cap. CSCs can be safely operated at counting rates of up to 1000 Hz/cm², which is sufficient to reach a value of $|\eta| = 2.7$.

- **Resistive Plate Chambers (RPCs):** The RPCs are gaseous parallel electrode-plate detectors. They consist of two resistive plates, made of plastic laminate, and kept parallel to each other at a distance of 2 mm by insulating spacers. A voltage of 4.9 kV is applied between these plates, leading to avalanches being formed along the ionizing tracks. The resulting signal is read out via capacitive coupling.

The timing resolution of the RPCs is 1.5 ns. Compared to the time span between bunch crossings of 50 ns in the 2011 data taking campaign, this allows for a correct assignment of bunch crossing in almost all cases.

- **Thin Gap Chambers (TGCs):** The TGCs replace the RPCs as trigger system at values of $|\eta| > 1.05$. They are multi-wire proportional chambers, characterized by a wire-to-cathode distance smaller than the wire-to-wire distance (1.4 mm vs. 1.8 mm). The filling consists of highly quenching gas, preventing the formation of streamers.

The muon spectrometer has a non-uniform response in the η - φ space. This is due to transitions between the different muon sub-systems as well as support structures. Among the most pronounced structures are the so-called feet — the structures which carry the ATLAS detector. In this region, the φ -symmetry is broken, because some chambers are missing, leading to a smaller reconstruction efficiency. In η , the region at $|\eta| \approx 0$ has less muon chambers due to space constraints from the services for the calorimeter and ID. At $|\eta| \approx 1.2$, the transition between barrel and end-cap occurs, and only one layer of muon chambers is traversed. This decreases the reconstruction efficiency. Following ref. [13], ten different regions can be defined as shown in Table 4.5. These are illustrated in Figure 4.7.

4. Experimental Setup

Region	Definition
Barrel large	Regions only consisting of large barrel chambers
Barrel small	Regions only consisting of small barrel chambers
Barrel overlap	Overlap between small and large barrel chambers
Feet	Support structures of the detectors, some chambers are missing
Transition	Transition between barrel and end-cap region, most tracks only traversing two instead of three muon stations
End-cap small	Small end-cap sectors, MDTs
End-cap large	Large end-cap sectors, MDTs
BEE	Barrel–End-cap region, specialized MDTs mounted on top of the end-cap cryostat; only part of the azimuthal range covered
CSC small	Small end-cap sectors, CSCs, outside TRT acceptance
CSC large	Large end-cap sectors, CSCs, outside TRT acceptance

Table 4.5.: Different regions of the muon system. This classification follows [13].

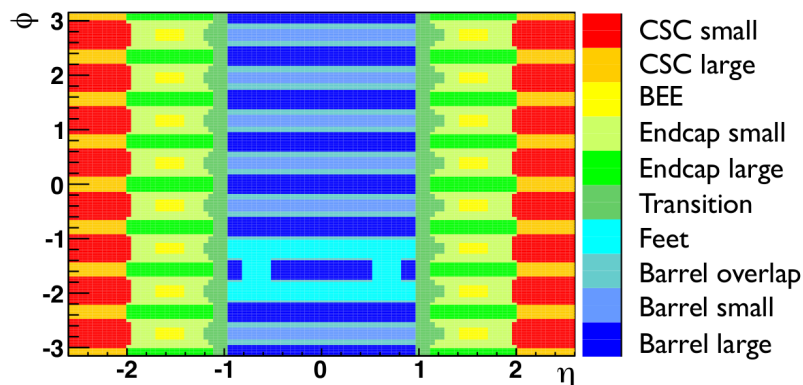


Figure 4.7.: Illustration of the different regions in the muon system. Taken from ref. [13]

4.4. Data Acquisition and Triggering

In 2011, bunches of protons were brought into collision approximately each 50 ns — corresponding to a rate of 20 MHz. On average, each of these bunch crossing produced 9.1 proton-proton interactions (cf. ref. [64]), out of which only a tiny fraction led to the production high-energetic lepton pairs via W or Z bosons¹⁰. The selection and storage of these events — among others of interest to analyses at ATLAS — is the task of the trigger system.

In order to cope with the high rate, which is orders of magnitude larger than the read-out capacity of ATLAS of 300 Hz, a multi-staged trigger is implemented. The first level (L1) operates on very coarse detector information: Only coarse-grained calorimeter information and the RPCs and TGCs of the muon system are used. Using this information, the L1 trigger

¹⁰The cross section for the signal processes $pp \rightarrow Z + X \rightarrow \mu\mu + X$ and $pp \rightarrow W + X \rightarrow \mu\nu_\mu + X$ is on the order of 10 nb (cf. Table 5.2), while the full cross-section for inelastic proton-proton scattering is on the order of 60 mb (cf. ref. [66]). This corresponds to a factor of 6×10^6 .

is able to reduce the rate to 75 kHz with a maximum trigger decision time of 2.5 μ s after the bunch crossing.

The second level trigger (L2) is seeded by the regions of interest (ROIs) detected by the L1 trigger. Using more detailed calorimeter and tracking information, the event rate can be reduced to 3.5 kHz with an event processing time of 40 ms.

The event filter (EF) acts as the last step in the trigger chain. It works on fully reconstructed events and uses analysis procedures similar to those used in physics analysis at ATLAS. With these algorithms, the event rate can be reduced to 200 Hz with an event processing time of 4 s.

At ATLAS, a large number of such trigger chains — combinations of L1, L2 and EF criteria — are tested in parallel. This means that one event can pass several different trigger chains at once. For example, an event can pass the so-called EF_MU18 trigger, which searches for a muon with a transverse momentum of more than 18 GeV, but can pass the EF_E20_MEDIUM trigger at the same time, which searches for an electron with transverse momentum larger than 20 GeV and additional cuts.

Several triggers are prescaled. A prescale of n means that only one of n events passing the trigger is actually stored. This is especially the case for triggers with low momentum threshold. In the analyses presented in this thesis, the triggers with the lowest transverse momentum threshold without prescaling, the so-called *lowest unprescaled triggers*, were chosen.

4.5. Event Reconstruction

Event reconstruction is the task of inferring the identity, trajectory, momentum, energy and charge of all particles produced in the collision. To this end, information from all sub-detectors has to be combined. The relevant particle species and their interactions with the detector were illustrated in 4.3.

4.5.1. Muons

Muons are measured in the ID and the MS, and can be accompanied by a small energy deposition in the calorimeters. Naturally, the possible combinations of these measurements allow for a number of definitions for muon objects, as can be found in ref. [67]:

- **Stand-alone muons:** In this case, the muon trajectory is only reconstructed in the MS. The muon energy has to be corrected for the estimated energy loss in the calorimeters. From the MS, the trajectory is extrapolated back to the beam line.
- **Combined muons:** Here, the measurements from the ID and the MS are combined. The ID information is used to enhance the information on the trajectory compared to stand-alone muons.
- **Segment-tagged muons:** Here the measurement relies mostly on the ID — a track in the ID is selected as muon if it can be matched to straight track segments in the precision muon chambers. All track parameters are reconstructed from the ID measurement alone.
- **Calorimeter-tagged muons:** Similar to segment tagged muons, the measurement relies mostly on the ID. Tracks in the ID are identified as muons if the associated energy deposition in the calorimeters is compatible with that of a muon. This definition has the highest rate of mis-identification and is not commonly used.

4. Experimental Setup

In 2011, two muon chains were used. Each of these chains represents a selection of algorithms to reconstruct each of the muon objects defined above. These two chains are the MUID chain and the STACO chain (cf. ref. [68] and references therein). Both chains differ in their approach to pattern recognition and in the algorithm to combine ID and MS measurements for combined muons.

In the analyses discussed in this thesis, the STACO chain was used. As far as possible, only kinematics from the ID were used. As will be discussed in detail in Section 6, the muon reconstruction efficiency, i.e. the probability of a muon to be reconstructed as such, is to a large extent dominated by the MS efficiency, while the ID efficiency is very close to unity.

4.5.2. Electrons

Electrons are capable of producing showers in the electromagnetic calorimeters as well as tracks in the inner detector. In the *forward region*, i.e. the region of $|\eta| > 2.5$, electron reconstruction can only be performed using calorimeter¹¹ information, while in the *central region*, i.e. the region with $|\eta| < 2.47$, information from both ID and calorimeters can be used. Therefore, electron reconstruction in the central and forward region uses different methods. A detailed description of the reconstruction algorithm can be found in ref. [69].

Electrons produce energy depositions localized in η and φ , so-called clusters, in the electromagnetic calorimeters. Due to their low mass, electrons are very likely to produce bremsstrahlung photons. The cross-section for this process makes it very likely for these photons to be collinear to the electron and to carry only a small momentum. Therefore, these photons are very likely to be added to the cluster under consideration. Only bremsstrahlung photons with large momentum and large acollinearity produce separate clusters.

Due to the solenoidal magnetic field in which the ID is placed, the trajectory of the electron is bent in the φ direction. Therefore, the emitted bremsstrahlung photons, which are unaffected by the magnetic field, will exhibit a larger spread in φ than η .

In the central region, electron reconstruction starts at the electromagnetic calorimeter, in which clusters are searched. To this end, a *sliding window* algorithm is used, with a window size of 3×5 in units of 0.025×0.025 in $\eta \times \varphi$. This algorithm is expected to locate clusters from W or Z decay electrons with $E_T > 20$ GeV with almost full efficiency.

In a second step, a track is searched in the ID which can be matched to the cluster. The matching criteria are $|\Delta\eta| < 0.05$ and $\Delta\varphi < 0.1$ on the side where bremsstrahlung photons are expected and $\Delta\varphi < 0.05$ on the other.

After a successful match, the electron cluster is rebuilt by adding all calorimeter cells in a block of 3×7 in $\eta \times \varphi$ in barrel, or 5×5 in the end-cap, respectively. These values were optimized for the different energy distributions in barrel and end-cap.

In the forward region, calorimeter cells with energy depositions differing significantly from the expected noise are clustered. These topological clusters have a varying number of cells.

Energy depositions in the electromagnetic calorimeter can also be produced by hadrons misidentified as electrons, photons and background electrons (primarily from photon conversions and semileptonic decays of heavy-flavor particles). Since photons do not produce tracks, these can only be mistaken for electrons in the forward or central region through combinatoric background. In any case, the reconstruction of electrons thus has to be accompanied by an electron identification algorithm.

¹¹For the discussion of electron and photon reconstruction, also the first layer of the FCal is counted as an electromagnetic calorimeter.

The goal of the identification algorithm is to assign a probability to each electron candidate of being a true electron. In 2011, the electron identification algorithm was based on a cut-based selection using calorimeter, tracking and combined variables. Three reference sets of cuts were obtained for three different levels of increasing background rejection power: *loose*, *medium* and *tight*. These were defined inclusively, i.e. it is ensured that an electron passing a more stringent identification level will also pass all looser levels. The target signal efficiency for these three cut sets in the central region is 90 %, 80 % and 70 %, respectively, with a background rejection power of approximately 2 500, 25 000 and 50 000, respectively.

Electron identification in the forward region has to rely solely on the shape of the energy deposition in the calorimeter. The forward region offers access to phase space of special importance for studies such as on the PDFs or angular distribution of Z decays. Since studies of these quantities play an important part in the measurement of M_W , an optimized forward electron identification algorithm, obtained for data taken in 2012 at $\sqrt{s} = 8$ TeV was derived as part of this thesis. It will be discussed in Appendix A.

4.5.3. Hadrons and Jets

At ATLAS, several processes, such as the decay of Z or W bosons or the interaction of the proton remnants (cf. Section 3.4), can produce quarks and gluons with significant momentum. Since these particles are not color-neutral, they will immediately hadronize. In the course of this process, a multitude of hadrons, leptons and photons are produced. Due to the momentum of the original quark or gluon, these decay products will be collimated into a so-called jet.

A large fraction of these particles will be absorbed by the calorimeters. The hadronic contribution will produce clusters in the hadronic calorimeter very similar to those discussed for electrons and photons in Section 4.5.2. Jet reconstruction can rely either on these clusters or on the tracks in the ID (cf. ref. [70]). A large number of algorithms to group these energy depositions or ID tracks into jets is available. At ATLAS, an anti- k_T algorithm is used (cf. ref. [71]).

4.5.4. Hadronic Recoil

As discussed in Section 3.4, the hard scattering, in which the W or Z boson is produced from quark-antiquark annihilation, is accompanied by the so-called underlying event — the interaction and hadronization of the color-charged proton remnants. In leading order, this means that a multitude of hadrons will recoil against the produced W or Z boson. In higher order, these are accompanied by QCD initial and final state radiation. The kinematics are illustrated in Figure 4.8 for the production of a Z boson. Here also the projections u_{\parallel}^Z and u_{\perp}^Z of the hadronic recoil parallel to the transverse momentum of the vector boson and perpendicular to it are shown.

Momentum conservation requires the sum of the incoming momenta to equal the sum of the outgoing momenta. If the small boost due to the non-zero crossing angle is neglected, this means that the total momentum of all outgoing particles has to vanish and that the momentum of the hadronic recoil has to be balanced exactly by the momentum of the boson produced in the hard scattering.

At ATLAS, the hadronic recoil is estimated by summing the energy depositions in all calorimeter cells. This assumes that all particles produced as part of the hadronic recoil are fully absorbed by the calorimeter cells.

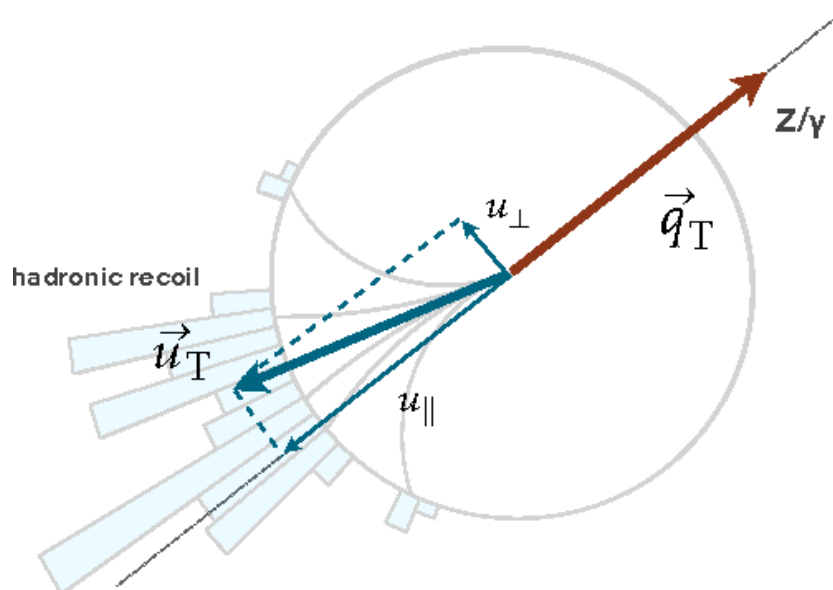


Figure 4.8.: Illustration of the hadronic recoil in the production of a Z boson. In addition to the hadronic recoil (denoted here by \vec{u}_T), the projection onto the transverse momentum of the vector boson $-\vec{q}_T$, $u_{||}^{(Z)}$, and perpendicular to the transverse momentum, $u_{\perp}^{(Z)}$, are shown. Taken from ref. [72].

However, this assumption is not fully correct for several reasons:

- **Incomplete acceptance:** As discussed in Section 4.3, the ATLAS calorimeters are almost hermetic. The area close to the beam axis, however, is not instrumented. Since particles close to the beam axis carry a large momentum along the z axis, the longitudinal momentum of the hadronic recoil can only be estimated with significant uncertainty and is generally not used.
- **Incomplete absorption:** Neutrinos produced as part of the hadronic recoil are not absorbed by the calorimeters, an effect discarded by the algorithm. This leads to an additional uncertainty on the estimated hadronic recoil. In general, also muons pass the detector without absorption. This can only be corrected for if the transverse momentum of the muon is above the detection limit of the muon system of 6 GeV.
- **Pile-up:** In addition to the collision vertex in which the hard scattering takes place, several so-called pile-up vertices exist as discussed in Section 3.5. The energy deposition from these interactions is added to the hadronic recoil, leading to an additional uncertainty, and thus a degradation of resolution.

In general, the difference between the estimated hadronic recoil and the transverse momentum of the boson is on the order of several GeV.

4.5.5. Neutrinos

In the production of W bosons, the decay neutrinos are not visible to the detector. However, their presence can be inferred due to momentum conservation. To this end, the hadronic recoil

and the momentum of the charged decay lepton is used. Momentum conservation requires the muon momentum and the neutrino momentum to exactly balance the hadronic recoil.

Due to the points discussed above, this calculation is in general only performed in the transverse plane. The transverse momentum of the neutrino becomes visible as an imbalance in the total energy deposition of the calorimeters and is therefore called missing transverse energy, or E_T^{miss} . Due to the challenges in the estimation of the hadronic recoil discussed above, the transverse momentum of the neutrino can only be gained with reduced resolution compared to that of the charged decay leptons.

Hadronic recoil and missing energy can be related by assuming the transverse momentum of the center of mass to be negligible through momentum conservation. For the case of the process $pp \rightarrow W + X \rightarrow \mu\nu + X$, the equation reads:

$$-HR = p_T^\mu + MET \quad (4.2)$$

5. Monte Carlo Simulation

Like all high-energy experiments, ATLAS relies heavily on Monte Carlo simulations (MC) for designing the detector as well as its components, estimating detector performance, as well as for the prediction of experimental outcomes (cf. ref. [73]). This is mainly because the physics processes involved are complicated and difficult to calculate analytically, and because the detector response to these processes is challenging to model.

This becomes very obvious in the measurement of the W boson mass. Here, the processes leading to its production are governed by the PDFs discussed in Section 3.2. The dependence of these functions on Q^2 and x_B plays a large role, and has a huge impact on the distribution of the transverse momentum of the charged decay lepton. The same holds true for initial and final state radiation, both through QED and QCD processes. The impact of these processes on the observables used for the measurement of M_W has to be well modeled.

The shape of the observables is also significantly impacted by the characteristics of the detector. Such detector effects, for example cut efficiencies depending on the transverse momentum, are very common, and can significantly distort the observed spectrum of the transverse momentum.

These two facets of MC simulations are mirrored in the two-step approach taken at ATLAS. First of all, the physics process is modeled using one or several combined MC generators, with a resulting list of particles in the final state, including their momenta and charges. This is called the truth record. It is used as input for the detector simulation, which uses a very detailed model of the detector, and which simulates the response of all sub-systems to these particles. Part of the second step is also the reconstruction of these particles, i.e. the inference from the response of the ATLAS detector to the trajectory, momentum, charge and flavor of the original particles. In Monte Carlo simulations, these reconstructed particles can be compared to their counterparts in the truth record, yielding information on the expected reconstruction efficiency and quality.

5.1. Event Generators

A wide range of MC generators is available at ATLAS. An overview of the generators used for the analyses discussed in this thesis is given in Table 5.1.

Following ref. [28], these generators can be characterized by the extent to which they are able to simulate the full proton-proton interaction and by the order $\mathcal{O}(\alpha_s)$ to which the hard scattering is calculated.

Generators able to simulate the full proton-proton interaction are known as multi-purpose generators. These programs offer an interface to PDFs, initial-state showering models, a simulation of the hard scattering, final-state showering, hadronisation and further particle decays. Examples for such multi-purpose generators used at ATLAS are PYTHIA (cf. ref. [29, 30]), HERWIG (cf. ref. [74, 75]) and SHERPA (cf. ref. [76]). All these generators offer an extensive library of leading-order Standard Model processes.

5. Monte Carlo Simulation

The results from these generators can be improved by replacing the routines calculating the hard scattering process. To this end, specialized programs such as ALPGEN and MADGRAPH are used. While not providing an NLO matrix element calculation, these programs are nevertheless able to give an estimation of NLO effects by adding up to six (ALPGEN) or four (MADGRAPH) additional partons in the final state. In this way, the additional partons are treated as real instead of virtual.

The occurrence of additional partons poses a problem: A significant overlap exists between the showers predicted by the initial- or final-state showering algorithms and the showers predicted by taking additional partons in the hard scattering into account. Therefore, the results from both calculations have to be matched in order to avoid double-counting. To this end, several algorithms were devised, such as the Catani-Krauss-Kuler-Webber (CKKW) algorithm (cf. ref. [77, 78]) and the Mangano (MLM) algorithm (cf. ref. [79]). Alternatively, merging algorithms can also be used, which reweight the parton showers through weights from the matrix element. Notable examples for this approach are PYTHIA and HERWIG. It should be noted that it is very difficult to model higher jet multiplicities in this approach.

The measurement of M_W requires the incorporation of higher orders due to their effect on the spectra of the observables used. Therefore, the hard scattering has to be calculated in NLO. However, the matching algorithms described above only work for LO matrix element calculations. More sophisticated methods are needed for the match between the NLO matrix element from the dedicated program, and the parton shower algorithm from the multi-purpose generator. The two approaches used at ATLAS are the MC@NLO approach (cf. ref. [80]) and the POWHEG approach (cf. ref. [81]). The latter is also implemented in PYTHIA.

Apart from these event generators, three specialized generators were used in the analyses presented in this thesis. RESBOS (cf. ref. [82]), a generator based on a resummation approach, was used to obtain a very accurate prediction of the transverse momentum of the W or Z boson. PHOTOS (cf. ref. [83]) was used to improve the description of QED final state radiation, which is especially important with regard to electrons in the final state. When using PHOTOS, the production of QED final state radiation in the multi-purpose generator is switched off to avoid double-counting (cf. ref. [73]). A further event generator is DYNNLO (cf. ref. [84, 85]), which is able to take NNLO effects into account, thereby providing an excellent description of the angular distribution of the decay leptons of W and Z bosons. This generator was used to improve the results obtained from the standard POWHEG+PYTHIA simulation.

Commonly, these event generators contain processes which can currently not be calculated from first principles. This is especially the case in the realm of non-perturbative QCD processes, which govern for example parton showering, hadronization and multiparton interactions. The models describing these processes, used in the event generators presented here, are typically either approximations to high-multiplicity QCD calculations, or phenomenological attempts to address non-perturbative physics (cf. ref. [86]). Therefore, these event generators contain free parameters, governing the description of these processes. These free parameters cannot be calculated from first principles, are interconnected and must be chosen, such that these generators produce a reasonable description of these processes. The optimization of these parameters is known as *tuning*. Due to the freedom of choice in this optimization process, a range of tunes were derived for the ATLAS experiment. An overview for the PYTHIA event generator is given in ref. [86].

Program	Matrix element $\mathcal{O}(\alpha_s)$	Full Event Generator	Merging/Matching
PYTHIA	LO	yes	matrix-element correction for first branching
HERWIG	LO	yes	matrix-element correction for hardest branching
MC@NLO	NLO	yes (interface to HERWIG)	PS matching
POWHEGBOX	NLO	yes (interface to PYTHIA or HERWIG)	PS matching
ALPGEN	LO	no (but interface to PYTHIA or HERWIG)	MLM (all parton multiplicities)
MADGRAPH	LO	no (but interface to PYTHIA)	n.a. (all parton multiplicities)
SHERPA	LO	yes	CKKW (all parton multiplicities)
RESBOS	Resummation	no (only boson kinematics)	n.a.
PHOTOS	n.a.	no (only QED FSR)	n.a.
DYNNLO	NNLO	no (only boson and decay lepton kinematics)	n.a.

Table 5.1.: Overview of the different Monte Carlo generators used at ATLAS. Taken from ref. [28], adapted.

5.2. Detector Simulation

The interaction between the particles produced by the event generator and the ATLAS detector is simulated with a dedicated detector simulation. This simulation is based on the GEANT4 (cf. ref. [87]) package, which is able to simulate the interaction between final-state particles and the detector on the microscopic level. To this end, the GEANT4 package contains a large set of models for particle-material interactions across a wide energy range.

In the GEANT4 simulation, each particle produced by the event generator is tracked step-by-step through the simulated detector. In each step, physics processes such as decays and interactions with material are simulated. If the interaction takes place in a part of the detector marked as sensitive in the simulation, a *hit* is recorded. From these hits, the simulated response of the sub-detector is calculated in a process called digitization. The output of this process are so-called Raw Data Objects (RDOs). These represent the detector output, for example counts from an analog-to-digital converter (ADC) or a time-to-digital converter (TDC).

Naturally, this form of simulation is very time-consuming. In order to reduce the processing time per event, several simulation algorithms with less detailed interactions have been developed (cf. ref. [73]). For example, in the so-called *fast G_4 simulation*, the showering in the electromagnetic calorimeters is simulated via a mixture of parametrization (as proposed for example in ref. [88]), a library of pre-defined showers and full simulation, depending on the energy.

5. Monte Carlo Simulation

These digitized hits are then passed through the ATLAS reconstruction software in the same way signals obtained from real data taking would be. This way, it can be made sure that simulated and actually observed events are treated as similar as possible. Both the reconstruction software and the simulation software are part of the ATHENA framework (cf. ref. [89]). The main goal of the reconstruction algorithms is the inference from the digitized hits to the momentum, trajectory, charge and flavor of the particle which has produced these hits.

5.3. Overview of Monte Carlo Samples

An overview of the Monte Carlo samples used in this thesis is given in Table 5.2. The first three samples are the MC signal samples for the production and subsequent decay of W and Z bosons, while the following samples represent the MC samples used to estimate the electroweak and top background, as introduced in Section 6.2. The r and p tags quoted in the table represent the version of the software used to produce and reconstruct these Monte Carlo simulations. The last column represents the cross section, corrected by the branching ratio, with its accompanying uncertainty.

Process	Generator	Dataset ID	r/p tags	$\sigma \times BR[\text{pb}]$
Signal Samples				
$W^+ \rightarrow \mu^+ \nu_\mu$	POWHEG+PYTHIA8	147401	r4982_p1731	6160 (5%)
$W^- \rightarrow \mu^- \bar{\nu}_\mu$	POWHEG+PYTHIA8	147404	r4982_p1731	4300 (5%)
$Z \rightarrow \mu^+ \mu^-$	POWHEG+PYTHIA8	147407	r4982_p1731	990 (5%)
Background Samples				
$W^+ \rightarrow \tau^+ (\rightarrow e^+, \mu^+) \nu$	POWHEG+PYTHIA8	147412	r4982_p1731	930.04 (5%)
$W^- \rightarrow \tau^- (\rightarrow e^-, \mu^-) \nu$	POWHEG+PYTHIA8	147415	r4982_p1731	603.63 (5%)
$Z \rightarrow \tau^+ \tau^- (\rightarrow e, \mu)$	POWHEG+PYTHIA8	147418	r4982_p1731	260.42 (5%)
WW	HERWIG	105985	r4982_p1731	20.86 (7%)
ZZ	HERWIG	105986	r4982_p1731	1.54 (7%)
WZ	HERWIG	105987	r4982_p1731	6.97 (7%)
$t\bar{t}$	MC@NLO	105200	r4982_p1731	137.30 (6.2%)
Single top t-channel $e\nu$	MC@NLO	108340	r4982_p1731	6.83 (12%)
Single top t-channel $\mu\nu$	MC@NLO	108341	r4982_p1731	6.82 (12%)
Single top t-channel $\tau\nu$	MC@NLO	108342	r4982_p1731	6.81 (12%)
Single top s-channel $e\nu$	MC@NLO	108343	r4982_p1731	0.46 (12%)
Single top s-channel $\mu\nu$	MC@NLO	108344	r4982_p1731	0.46 (12%)
Single top s-channel $\tau\nu$	MC@NLO	108345	r4982_p1731	0.46 (12%)
Single top Wt	MC@NLO	108346	r4982_p1731	14.37 (7%)

Table 5.2.: Overview of the MC samples used for the analyses performed on 2011 data. Cross sections are normalized to NNLO. Relative uncertainties on the cross-sections are shown in brackets. Data taken from ref. [90], uncertainties follow ref. [91].

5.4. Additional Corrections

The simulated events, obtained by the methods above, cannot be used directly in the measurement. Instead, further corrections are needed. The reasons for these corrections can be grouped into two categories:

- **Physics corrections:** Examples for this group of corrections are the modeling of processes not included in the event generator, or known differences between observations and the generator prediction.
- **Detector corrections:** The simulation is based upon several assumptions about the performance of the LHC and ATLAS, which were shown not to be fully correct. Enhancing the description through detailed studies and obtaining associated corrections plays a large role in the measurement of M_W . Work to this end will be presented in Part II of this thesis.

5.4.1. Physics Corrections

In order to enhance the description of the measured observables, a large number of physics corrections was applied. A detailed overview of these corrections can be found in ref. [90].

Resonance Parametrization and Corrections

In general, the Monte Carlo generators used include higher order QCD corrections, but only leading order electroweak expressions. Since higher-order electroweak corrections have a significant impact on the line shape of the W and Z bosons (cf. Section 3.3), these corrections have to be added for a precise determination of M_W . To this end, the shape of the W and Z resonance in the signal MC samples is reweighted to match the improved Born approximation (IBA) as developed at LEP (cf. ref [92]). This is performed with the standard ATLAS package `LINESHAPE TOOL-00-00-04`.

Boson Rapidity and Transverse Momentum

The transverse momentum of the boson has a direct impact on the three observables used for the measurement of the W boson mass — lepton p_T , m_T and E_T^{miss} . Therefore, it has to be modeled with high precision. As an additional challenge, p_T^W cannot be measured independently of the hadronic recoil, contrary to the case of p_T^Z . In the latter case, both leptons can be reconstructed independently of the hadronic recoil, while in the former the kinematic configuration of the neutrino has to be extracted using the measured hadronic recoil. This means, that an improvement of the simulation output, using a comparison to the measured distribution of p_T^W , is not feasible.

Instead, as discussed in ref. [93], the distribution of p_T^W has to be modeled using p_T^Z . This can be performed relying solely on perturbative QCD, or, as was done for the analyses presented in this thesis, through tuning. Here, the correction is achieved by using the PYTHIA AZ tune, which in turn relies to a large extent on the measured p_T^Z distribution at ATLAS (cf. ref. [40]).

Angular Coefficients

As discussed in Section 3.1, the angular coefficients play a large role in the transfer from the distribution of the transverse momentum to the full momentum of the decay leptons. A mis-modeling of these coefficients would therefore introduce a bias in the measured value of M_W . In ref. [90], it could be shown that DYNNLO is able to reproduce the observed dependence of the angular coefficients A_i on the boson p_T much better than POWHEG+PYTHIA8, except in the case of A_4 in Z boson production. Therefore, in the $W \rightarrow \mu\nu$ MC samples, A_i ($i = 0 - 4$) are reweighted to match the DYNNLO prediction; while in the $Z \rightarrow \mu\mu$ MC sample, only A_i , ($i = 0 - 3$) are reweighted.

5.4.2. Detector Corrections

The following corrections were applied due to mis-modeling of the detector or the accelerator parameters.

Pile-up Reweighting

The number of interactions per bunch crossing is a function of the number of protons per bunch, as well as the dimension of the beam spot and geometry of the beams. Moreover, it is a function of time, since after the fill, the number of protons per bunch steadily decreases until the beams are dumped. However, the MC was only simulated for a discrete number of pile-up conditions. Therefore, the MC simulation has to be reweighted to describe the observed pile-up conditions, which was performed with the ATLAS tool PILEUPREWEIGHTING-00-02-05.

Vertex Reweighting

The distribution of interaction vertices along the z axis was not correctly modeled in Monte Carlo. Instead, the distribution is much wider in the simulation than in data, a fact which can influence kinematic measurements. Therefore, the simulated distribution is reweighted with the ATLAS tool VERTEXRWTOOL from the tool collection EGAMMAANALYSISUTILS-00-04-31.

Muon Momentum Correction

The muon momentum simulated in the MC samples has to correspond precisely to the momentum distribution observed in data, since the transverse momentum of the decay lepton is used to infer the mass of the W boson. In first order, the measured value of M_W depends linearly on p_T^μ . Any mis-modeling of p_T^μ would therefore introduce a bias in M_W . Therefore, the MC simulation has to be calibrated through comparison with real data, for which the decay of Z bosons can be used. In this decay, both leptons can be reconstructed, and the corresponding background level is low.

As described in ref. [94], the correction of the muon momentum consists of three parts: the muon scale and resolution correction as well as the sagitta bias correction. In all three cases, the goal is an improved agreement between the values of muon p_T from simulation and subsequent reconstruction, and those obtained in direct measurements.

The muon scale correction remedies mis-modeling of the detector along its the radial dimension, of the magnetic field in the ID and of the material distribution. These effects can be parametrized via:

$$p_T^{\text{meas}} = p_T^{\text{reco}}(1 + \alpha) \quad (5.1)$$

The muon resolution remedies imperfect modeling of the processes leading to a finite resolution of the detector: fluctuations of the energy loss, multiple scattering as well as other effects producing a deviation in the angle of the trajectory, and, finally, finite spacial resolution of the detector. These effects can be parametrized by:

$$\frac{\sigma(p_T)}{p_T} = \frac{a}{p_T} \oplus b \oplus c \times p_T \quad (5.2)$$

In this correction, only the last two terms are corrected, while multiple scattering is neglected due to the small material upstream to the ID.

The third correction is the sagitta bias correction, which takes into account possible charge-dependent mis-modelings, as can be introduced by mis-alignment of the detector. In this way, the trajectories for positive and negative muons, which are bent into opposite directions by the ID solenoid field, may exhibit a bias in the measured radius and therefore in the measured transverse momentum.

Muon Efficiency Correction

The efficiency of the ATLAS detector to reconstruct and trigger muons, as well as the probability of these muons to pass a detector-based isolation requirement, differs in part significantly from the values used in the simulation. Most importantly, a dependence on the transverse momentum of the decay leptons would be able to introduce a large bias in the resulting value of M_W . Therefore, a precise determination of these efficiencies and their dependence on the kinematics of the decay leptons has been performed as part of this thesis. The results of this study are presented in Part II of this thesis, where it will be shown that a precise determination of these efficiencies could be performed.

Hadronic Recoil Correction

The hadronic recoil was introduced in Section 4.5.4. Since it is the foundation upon which the missing energy E_T^{miss} and transverse mass m_T are built, it is important to calibrate this quantity with great care. To this end, the process $pp \rightarrow Z + X \rightarrow \mu^+ \mu^- + X$ was selected, as described in ref. [95]. In this process, an independent estimation of the hadronic recoil via p_T^Z , in addition to the reconstructed hadronic recoil itself, is feasible. This is because momentum conservation forces the transverse momentum of the Z boson in this process to balance the hadronic recoil.

The transverse momentum of the Z boson can be measured with a high precision of 1-2 GeV compared to the typical precision of the hadronic recoil of ~ 15 GeV. Therefore, a precise calibration of the latter with the former is possible.

In a first step, a correction of the distribution of the vertex multiplicity between data and Monte Carlo is performed. This is followed by a correction of the distribution of $\sum E_T$, the scalar sum of the transverse energies of all clusters from which the hadronic recoil is calculated. This is performed using a Smirnof transform (cf. ref. [96]).

5. Monte Carlo Simulation

As a final step, remaining differences between the hadronic recoil in data and Monte Carlo are corrected, using a set of correction factors for the component of the hadronic recoil parallel u_{\parallel} , and perpendicular u_{\perp} , to the Z boson momentum.

The resulting equations for the u_{\parallel} and u_{\perp} components read:

$$u'_{\parallel} = b \left(p_T, \left(\sum E_T - u \right)^{\text{tr}} \right) + \langle u_{\parallel} \rangle_{\text{Data}} + (u_{\parallel} - \langle u_{\parallel} \rangle_{\text{Data}}) \times r \left(p_T, \left(\sum E_T - u \right)^{\text{tr}} \right) \quad (5.3)$$

$$u'_{\perp} = u_{\perp} \times r \left(p_T, \left(\sum E_T - u \right)^{\text{tr}} \right) \quad (5.4)$$

In these equations, b is obtained from the means of $u_{\parallel} + p_T^Z$ on data and Monte Carlo according to:

$$b = \langle u_{\parallel} + p_T^Z \rangle^{\text{Data}} - \langle u_{\parallel} + p_T^Z \rangle^{\text{MC}} \quad (5.5)$$

The value of r is obtained from the spread of the distribution of u_{\perp} in data and Monte Carlo:

$$r = \frac{\sigma_{u_{\perp}}^{\text{Data}}}{\sigma_{u_{\perp}}^{\text{MC}}} \quad (5.6)$$

Crossing Angle Correction

Since the beams of the LHC must only be brought into collision at the defined interaction points, a certain crossing angle to separate them before and after each interaction point was chosen. At Interaction Point 1 (IP1), where the ATLAS detector is located, the full crossing angle θ between the colliding beams is $240 \mu\text{rad}$ according to ref. [97]. A simple calculation shows the resulting size of the motion of the center-of-mass system with respect to the detector system. With the four-momenta of the protons given by:

$$p_1 = \begin{pmatrix} E_1 \\ \vec{p}_1 \end{pmatrix}, \quad p_2 = \begin{pmatrix} E_2 \\ \vec{p}_2 \end{pmatrix} \quad (5.7)$$

Using the following relations

$$(5.8)$$

$$E_1^2 \sim \vec{p}_1^2, \quad E_2^2 \sim \vec{p}_2^2 \quad (5.9)$$

$$p_{1,x} = p \sin(\theta/2), p_{1,y} = 0, p_{1,z} = p \cos(\theta/2) \quad (5.10)$$

$$p_{2,x} = p \sin(\theta/2), p_{2,y} = 0, p_{2,z} = -p \cos(\theta/2) \quad (5.11)$$

leads to

$$p = p_1 + p_2 = \begin{pmatrix} E_1 + E_2 \\ 2p \sin(\theta/2) \\ 0 \\ 0 \end{pmatrix} \quad (5.12)$$

Using $p = 3.5 \text{ TeV}$ and $\theta = 240 \mu\text{rad}$

$$p = \begin{pmatrix} 7000 \text{ GeV} \\ 0.840 \text{ GeV} \\ 0 \\ 0 \end{pmatrix} \quad (5.13)$$

$$(5.14)$$

The center-of-mass energy \sqrt{s} is not influenced by this Lorentz boost, as it is a Lorentz scalar. However, the center-of-mass system has a momentum in positive x-direction of 0.840 GeV, which is not modeled in the Monte Carlo simulations used. This can be corrected by either performing the Lorentz boost on Monte Carlo in order to describe the movement of the center of mass in data, or by performing the Lorentz boost on data. The latter has the advantage of leading to a φ -symmetric situation, and was therefore chosen.

For the decay leptons, this introduces a shift in the momentum on the scale of 10 MeV, which has a different sign in the upper and lower half of the detector, thus canceling out almost completely. However, for the hadronic recoil, introduced in Section 4.5.4, the effect is much more significant and on the order of 1 GeV. Moreover, the effect on the hadronic recoil depends on the number of pile-up vertices and the ability of the hadronic recoil reconstruction algorithm to suppress contributions from these vertices. Unfortunately, for the purpose of the analyses presented in this thesis, the full four-momentum information needed for the correction is only available for the decay leptons and not for the hadronic recoil. Therefore, only the lepton momentum could be corrected, indicating a point for further study.

Part II.

Muon Performance

6. Overview of Muon Efficiency Corrections

Note: The results presented in this part of the thesis form the basis of an internal ATLAS note as part of the W boson mass measurement effort, cf. ref. [98]

A precision measurement always acts as a benchmark for how well the characteristics of the detector — to be precise, its response to incoming particles — have been understood and modeled. While several measurements and calibrations had been performed before ATLAS was assembled¹, a detailed understanding can only be gained with in-situ measurements, i.e. measurements performed while the detector is in operation. This is of special importance in regard to the measurement of the mass of the W boson. This is because, as was shown in Chapter 3.1, the spectrum of the transversal momentum of the decay lepton is both the variable most sensitive to the mass of the W boson, but also very sensitive to physics and detector modeling effects. Hence, the kinematic dependence of the muon reconstruction, trigger and isolation efficiency has to be well understood. The reconstruction efficiency is the efficiency of a muon already reconstructed as a track in the inner detector to be reconstructed as a combined STACO muon. The trigger efficiency is the probability for a muon, having passed the offline reconstruction and isolation requirements, to also fire the trigger. The isolation cut efficiency is the efficiency of a signal muon to pass a detector-based isolation requirement. In particular, it is important to evaluate how the reconstruction, trigger and isolation efficiencies differ between data and Monte Carlo simulations. Using this information, correction factors — the so-called scale factors — can be derived according to:

$$SF(\eta, \varphi, p_T, u_{\parallel}^l) = \frac{\varepsilon_{\text{D}}(\eta, \varphi, p_T, u_{\parallel}^l)}{\varepsilon_{\text{MC}}(\eta, \varphi, p_T, u_{\parallel}^l)} \quad (6.1)$$

As stated explicit in this equation, up to four kinematic variables were considered in this analysis: Apart from the pseudo-rapidity η , azimuth φ and transverse momentum p_T of the decay leptons, a possible dependence on u_{\parallel}^l was also investigated. The latter variable, already introduced in the previous part of this thesis, is defined as the parallel component of the projection of the hadronic recoil onto the transverse momentum of the decay lepton. Similarly, the quantity u_{\perp}^l is defined as the perpendicular projection of this quantity. For the sake of brevity, the explicit dependence of both scale factors and efficiencies is suppressed in the following. The variables η and φ are merged into a combined binning — the *detector region* variable, defined in Figure 6.1.

Apart from the full three-dimensional dependence on *region*, p_T and u_{\parallel}^l , two- and one-dimensional projections onto the single variables are supplied with a finer binning². Naturally, the total number of bins increases considerably with the number of dimensions involved, thereby decreasing the statistical precision. After careful consideration, the two-dimensional correction factors with respect to the *region* and lepton p_T were chosen since these usually give

¹See for example the measurements described in the ATLAS Technical Design Report (ref. [53], Chapter 10).

²This means, that the two-dimensional combinations are (*region*, p_T), (*region*, u_{\parallel}^l) and (p_T , u_{\parallel}^l).

6. Overview of Muon Efficiency Corrections

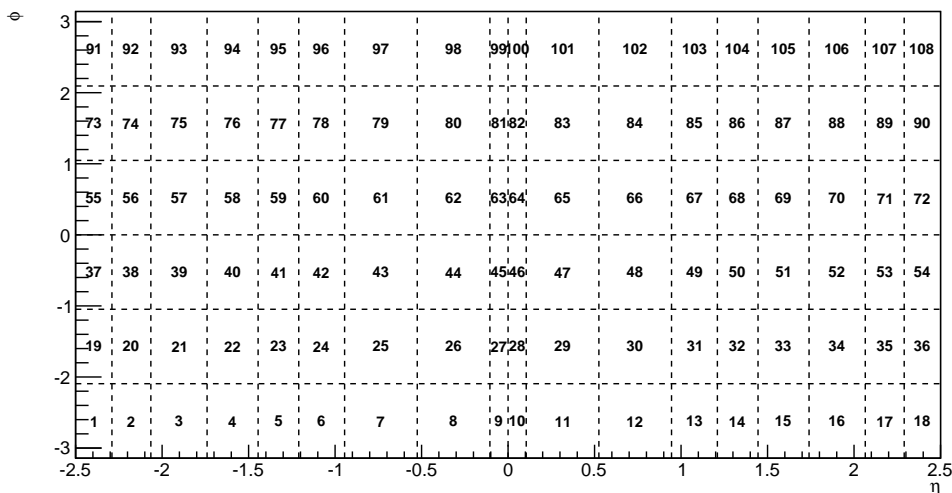


Figure 6.1.: Definition of the *region*, the combined η - φ binning used in this study.

Dimensionality	Observable	Binning
1-D	(η, φ)	<i>Region</i> binning, cf. Figure 6.1
	p_T	20...80 GeV in bins of 5 GeV
	u_{\parallel}^l	-80...80 GeV in bins of 4 GeV
2-D	(η, φ)	<i>Region</i> binning, cf. Figure 6.1
	p_T	20...80 GeV in bins of 5 GeV
	u_{\parallel}^l	-80..80 GeV in bins of 13 GeV
3-D	(η, φ)	<i>Region</i> binning, cf. Figure 6.1
	p_T	{20,25,30,35,40,45,50,60,70,80} GeV
	u_{\parallel}^l	-80..80 GeV in bins of 20 GeV

Table 6.1.: Bin definitions for the 1-D, 2-D and 3-D scale factors.

the best trade-off between statistical precision and accuracy of the modeling. Therefore, this binning is used for the W boson mass fit. The binning for all variables is shown in Table 6.1.

A priori, the muon isolation, trigger and reconstruction efficiencies depend on each other, mostly because the amount of background expected in each bin depends on all three efficiencies. The studies presented in this part of the thesis are very clean with only little background. However, due to the high precision aimed for, the remaining small effect of cross-talk is considered and minimized by calculating the efficiencies iteratively. This means that all scale factors were first calculated without correcting for the reconstruction, trigger and isolation efficiencies. In a second iteration, these efficiency corrections were applied to obtain the final efficiency corrections. The uncertainties obtained in the first iteration were propagated into the second iteration. After the second iteration, the results remained stable, as tested by performing a third iteration.

The muon reconstruction efficiency consists of three separate efficiencies — the efficiency for muons to produce inner detector tracks, the efficiency for muons to be reconstructed in the muon system and the efficiency for the tracks in the inner detector to be matched to corresponding muon objects in the muon system. In this analysis, the two latter efficiencies are combined, and the efficiency of inner detector tracks to result in a combined muon is calculated. The former efficiency is expected to be very close to unity in data and Monte Carlo. This assumption was tested in Appendix C and found to hold. All studies were performed using the STACO muon reconstruction algorithm.

The muon trigger efficiency was obtained for the two triggers used in the measurement of the W boson mass — EF_MU18 and EF_MU18_MEDIUM — depending on the period of the data taking: all periods up to period J use EF_MU18, while those following use EF_MU18_MEDIUM. Data corresponding to 1.4 fb^{-1} were collected using EF_MU18, the remaining data correspond to 3.1 fb^{-1} . In order to cover differences in the detector performance observed in 2011, both periods were divided into two sub-periods each. This will be discussed in more detail in Chapter 8.

The analysis of the muon isolation efficiency was performed for the variable $p_T^{\text{cone20}}/p_T < 0.1$, with p_T^{cone20} defined as the scalar sum of the transverse momenta of all tracks within a cone of $\Delta R < 0.2$ surrounding the track under investigation. This requirement acts as a countermeasure against muons originating from the decay of quarks, since these are generally accompanied by a jet of high energetic particles.

This part of the thesis is structured as follows: the next section deals with the Tag and Probe method, central to the selection of lepton candidate and the measurement of efficiencies. In Section 6.2, the event selection and the basic principle of the background determination is described. The method to evaluate systematic and statistical uncertainties is documented in Chapter 6.3. The evaluation of the muon reconstruction efficiency is summarized in detail in Chapter 7. Here, details of the event selection specific to this measurement as well as the scale factor determination, including uncertainties, is discussed. A similar discussion for the trigger scale factors is given in Section 8 and for the isolation scale factors in Chapter 9. In Appendix C a study on the ID track efficiency, very similar to the aforementioned studies, is described. A closure test of the obtained results can be found in Chapter 10.

In Appendix A, an excursus is presented: if methods very similar to those described in this chapter are used in combination with multivariate analysis methods to identify electrons as the final state, a much wider range in pseudorapidity can be used. Instead of $|\eta| \leq 2.7$ for muons, values of $|\eta| \leq 4.9$ can be reached by including the forward calorimeters in the electron reconstruction. These extend the acceptance of the central calorimeters, which reaches up to $|\eta| < 2.47$ by the range $2.5 < |\eta| < 4.9$. Using this region of the detector, a much broader range of Bjorken- x can be sampled, thereby testing different regions of the used PDFs. It has to be noted that this region cannot be used to study the decay $W \rightarrow e\nu$, because events with the electron in the forward calorimeter are not triggered. However, in the study of the decay $Z \rightarrow ee$, important insights into the PDFs can be gained and used as indirect input for the W boson mass measurement. Appendix A therefore presents an optimized electron identification algorithm and a measurement of its efficiency for electrons, obtained as part of the 2012 measurement campaign.

6.1. Tag and Probe method

The main challenge in this study lies in obtaining a clean sample of lepton candidates. Consider for example the case of measuring the reconstruction efficiency: in order to perform this measurement, the true nature of the lepton candidate has to be established before the offline identification, which relies on the reconstruction algorithm under study, is applied. In order to obtain sufficient certainty on the true nature of the lepton candidates without relying on the reconstruction algorithm, the Drell-Yan process $pp \rightarrow Z/\gamma^* + X \rightarrow \ell^+ \ell^- + X$ can be used: if a pair of two lepton candidates is found, with one passing very tight selection criteria, and the pair having an invariant mass close to the Z mass, it can be assumed that the other lepton candidate has a high probability of also being a true lepton. This is the key idea of the Tag and Probe method, as illustrated in Figure 6.2. In this method, the first lepton candidate, passing the tight selection criteria, is called the *Tag*, while the second candidate, only required to pass very loose criteria, is called the *Probe*. Naturally, a small rate of mis-identifications will be observed and has to be corrected. Its size and dependence on the kinematic variables has to be estimated with Monte Carlo and data-driven methods.

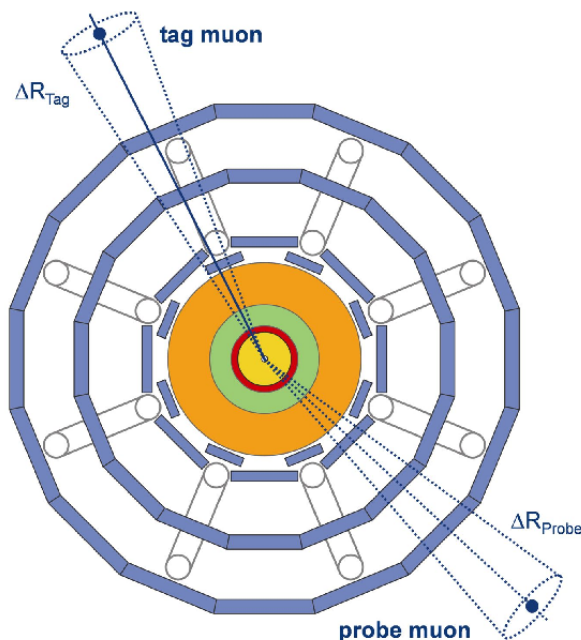


Figure 6.2.: Illustration of the Tag and Probe method used for the detector studies discussed in this chapter. Figure taken from ref. [99].

6.2. Event Selection and Background Subtraction

6.2.1. Event Selection

The detailed event selections differ for the determination of the muon reconstruction, trigger and isolation efficiencies and are described in detail in Section 7.1, Section 8.1 and Section 9.1. However, the basic selection is similar: two tracks are required, each with a transverse momen-

tum of $p_T > 20$ and $|\eta| < 2.4$, and with an invariant mass of $81 < m_{\text{pair}} < 101$. The study of the muon reconstruction efficiency requires only one muon track to be a combined muon, while the other muon track only needs to be reconstructed in the inner detector without any further muon-based requirements. Both tracks have to appear isolated in the detector. The study of the trigger efficiency is based on two combined muon tracks, both fulfilling an isolation requirement. The study of the isolation efficiency is based on two combined muon tracks, of which only one has to fulfill the isolation requirement under study. In all three cases, the tag is required to be matched to a muon trigger object. As will be shown, all three selections lead to clean signal samples.

The studies are based on data corresponding to 4.6 fb^{-1} of the 2011 data set³. The Monte Carlo samples used were already introduced in Table 5.2. It has to be noted that the samples listed in this table are so-called SMLIGHT samples. This means that, in order to reduce the file size of these samples, only information sufficient for a standard W/Z selection has been kept. In this way, all information concerning the ID tracks in the events is lost. However, this information is required to measure the muon reconstruction efficiency (cf. Chapter 7) as well as the ID track reconstruction efficiency (cf. Appendix C). Therefore, so-called SMWZ samples had to be used for these two analyses. These samples differ not only in terms of contained information, but also in terms of the software version used. In Chapter 10 it is shown that the results obtained on these samples are also valid for SMLIGHT samples. Note also, that the samples describing the process $W \rightarrow \mu\nu$ were not used in this part of the thesis, since the contribution from these processes were estimated data-driven, as described below. A full overview of the samples used is given in Table 6.2. The NNLO cross-sections quoted in the table are used to normalize predicted event counts for the various samples. The relative uncertainties on the production cross-sections are shown in brackets.

³The data used for this analysis was selected with a so-called Good Run List (GRL), in which the *lumi-blocks*, i.e. data blocks corresponding to approximately two minutes of data-taking, with sufficient data quality are stored (cf. ref. [100]). In the case of this analysis, the GRL used was `DATA11.7TeV.PERIODALL-YEAR.DETSTATUS-V36-PRO10_COOLRUNQUERY-00-04-08_WZJETS_ALLCHANNELS_DTOM.XML`. The integrated luminosity quoted here was calculated considering this GRL.

Process	Generator	Dataset ID	r/p tags (SMLIGHT)	r/p tags (SMWZ)	$\sigma \times BR[\text{pb}]$
Signal Sample					
$Z \rightarrow \mu\mu$	POWHEG+PYTHIA8	147407	r4982_p1731	r4982_p1486	990 (5%)
Background Samples					
$W^+ \rightarrow \tau^+(\rightarrow e^+, \mu^+)\nu$	POWHEG+PYTHIA8	147412	r4982_p1731	r4982_p1486	930.04 (5%)
$W^- \rightarrow \tau^-(\rightarrow e^-, \mu^-)\nu$	POWHEG+PYTHIA8	147415	r4982_p1731	r4982_p1486	603.63 (5%)
$Z \rightarrow \tau^+\tau^-(\rightarrow e, \mu)$	POWHEG+PYTHIA8	147418	r4982_p1731	r4982_p1486	260.42 (5%)
WW	HERWIG	105985	r4982_p1731	r4982_p1486	20.86 (7%)
ZZ	HERWIG	105986	r4982_p1731	r4982_p1486	1.54 (7%)
WZ	HERWIG	105987	r4982_p1731	r4982_p1486	6.97 (7%)
$t\bar{t}$	MC@NLO	105200	r4982_p1731	r2993_p1035	137.30 (6.2%)
Single top t-channel $e\nu$	MC@NLO	108340	r4982_p1731	r2993_p1035	6.83 (12%)
Single top t-channel $\mu\nu$	MC@NLO	108341	r4982_p1731	r2993_p1035	6.82 (12%)
Single top t-channel $\tau\nu$	MC@NLO	108342	r4982_p1731	r2993_p1035	6.81 (12%)
Single top s-channel $e\nu$	MC@NLO	108343	r4982_p1731	r2993_p1035	0.46 (12%)
Single top s-channel $\mu\nu$	MC@NLO	108344	r4982_p1731	r2993_p1035	0.46 (12%)
Single top s-channel $\tau\nu$	MC@NLO	108345	r4982_p1731	r2993_p1035	0.46 (12%)
Single top Wt	MC@NLO	108346	r4982_p1731	r2993_p1035	14.37 (7%)

Table 6.2.: Overview of the MC samples used for the Tag and Probe analyses performed on 2011 data. Cross sections are normalized to NNLO. Relative uncertainties on the cross-sections are shown in brackets. Data taken from ref. [90], uncertainties follow ref. [91].

In all analyses, quality cuts on the ID track are enforced. These consist of a minimal number of hits in the silicon detectors, as well as a veto against TRT hits far away from the fitted track. These so-called outliers can originate either from drift tube signals without a nearby track, or drift tube hits which cannot be reconciled with the trajectory measured in the Pixel and SCT detectors. In this way, fake tracks, as well as signals produced by hadrons, can be suppressed. These quality cuts are summarized in Table 6.3.

Sub-Detector	Requirement
Pixel	at least two pixel hits if pixels not dead
SCT	at least six SCT hits if channels not dead
Pixel + SCT	at most two holes
TRT ($ \eta < 1.9$)	$n_{\text{hits}} + n_{\text{outliers}} > 5$ and $\frac{n_{\text{outliers}}}{n_{\text{hits}} + n_{\text{outliers}}} < 0.9$
TRT ($ \eta \geq 1.9$)	for $n_{\text{hits}} + n_{\text{outliers}} > 5$: $\frac{n_{\text{outliers}}}{n_{\text{hits}} + n_{\text{outliers}}} < 0.9$

Table 6.3.: Quality cuts enforced on the track segment in the inner detector. As described in the text, the purpose of these cuts is a safeguard against fake tracks and tracks originating from hadrons.

6.2.2. Background Subtraction

As mentioned before, all three analyses are performed on clean samples with only small background admixtures. Concerning the relevant background processes, it is important to note that several of these produce isolated muons quite similar to those originating in Z decays. This means that their admixture has only a minor effect on the observed efficiencies. On the other hand, muons originating from QCD processes — for example from the decays of hadrons containing b or c quarks — are seldom isolated, and can bias the efficiencies significantly, if not subtracted correctly. An overview of the main background processes is given in Section 3.6.

For the reconstruction, trigger and isolation efficiency studies, the EW and top background processes were estimated using corresponding MC samples, scaled by the data luminosity. Uncertainty on this estimation stems from the limited statistics of the MC samples and the MC cross-section uncertainties.

Only part of the background originating from QCD-related processes can be estimated with Monte Carlo-driven methods. This includes the decay of top quarks into lighter quarks, associated with the production of W bosons decaying into muons. The remaining processes, e.g. the production and decay of b and c -hadrons mentioned above, however, could not be assessed with Monte Carlo simulations, since no sample with sufficient statistics and precision exists. Therefore, as it is common, only this data-driven background is denoted QCD background. By construction, it contains also the process $W \rightarrow \mu\nu$ in association with the production of a further muon candidate. Two methods were used to obtain this QCD background: a fit to the isolation distribution and the so-called ABCD method. The fit method was performed on a background-enriched sample, in which the isolation requirement on the probe (for the trigger and reconstruction efficiencies) or the tag (for the isolation efficiencies) was dropped. The distribution of the isolation is dominated by QCD background towards high values — this was chosen as the background control region. In this fit, signal MC was considered as a signal template, while a selection with same-signed muon candidates was taken as a background

6. Overview of Muon Efficiency Corrections

template. From this background template, all EW and top contributions described by the Monte Carlo samples shown in Table 6.2 were subtracted.

The fitting procedure (template fits) consisted of the determination of signal and background normalization factors S_{sig} and S_{bkg} in order to describe the distribution of data in the signal region with EW and top backgrounds subtracted, $N_{\text{data-EW}}$:

$$N_{\text{data-EW}} = S_{\text{sig}}N_{\text{sig}} + S_{\text{bkg}}N_{\text{bkg}}, \quad (6.2)$$

where N_{sig} is the number of signal MC events, scaled by data luminosity. The quantity N_{bkg} is the number of background events in the template used. The factor S_{sig} is used as a small correction to the luminosity normalization, which has a value close to unity and is within the cross-section uncertainties. This method is similar to that performed in ref. [91]. Examples for these fits are shown separately for each scale factor determination in Section 7.1, Section 8.1 and Section 9.1.

In the ABCD method, four different selections, defining four different sub-samples, were performed, as illustrated in Figure 6.3. Events A are signal dominated events, used for efficiency calculations. The goal of the method is to estimate the QCD background in sub-sample A, using only sub-samples B, C and D since the latter are dominated by background and the corrections due to the admixture of signal are small.

Isolation \ Charge μ_1, μ_2	Opposite sign	Same sign
Tag isolated	A	B
Tag anti-isolated	C	D

Figure 6.3.: Illustration of the four possible selections in the ABCD-method for the estimation of the QCD background. The two cuts are assumed to be independent of each other.

The cut on the charge of the muon candidate pair is assumed to be independent of the cut on the tag isolation. Given this assumption, the relations shown in Eq. 6.3, where N is a number of QCD background events in a given sub-sample, can be obtained.

$$\frac{N_A}{N_C} = \frac{N_B}{N_D}, \quad \frac{N_A}{N_B} = \frac{N_C}{N_D} \quad (6.3)$$

Sub-samples B, C and D are dominated by QCD background. The remaining signal contamination, as well as EW and top contributions, can be estimated with corresponding MC samples (see Table 6.2) and subtracted. After this subtraction, the obtained distributions — for example for η , φ , lepton p_T and u_{\parallel}^l — are considered background templates, which can be used to describe the QCD background in the corresponding distributions from sub-sample A.

However, since high positive values of u_{\parallel}^l are correlated to a low isolation efficiency of both the tag and probe muon (cf. Section 9.2), QCD templates C and D are expected to insufficiently describe the QCD background in this important variable in sub-sample A. Therefore, the QCD background in sub-sample A was taken from QCD template B, scaled with the ratio N_C/N_D .

The systematic uncertainties for the QCD background come from the statistical uncertainty of the ABCD factor and the difference between the normalization obtained in the fit method and the ABCD method, which is usually larger by a factor of two. The normalization factor was obtained once for each analysis. The values for the isolation and anti-isolation definitions are shown in Table 6.4.

Analysis	Isolation variable	Signal cut	QCD cut (ABCD)	QCD cut (Fit)
Reconstruction	$p_T^{\text{trkcone40}} / p_T^{\text{trk}}$	< 0.1	> 0.1	> 0.5
Trigger	$p_T^{\text{cone20}} / p_T$	< 0.1	> 0.1	> 0.5
Isolation	$p_T^{\text{cone20}} / p_T$	< 0.1	> 0.1	> 0.5

Table 6.4.: Overview of the isolation definitions used to obtain the muon efficiency scale factors.

6.3. Treatment of Uncertainties

6.3.1. Estimation of Uncertainties

Muon reconstruction, trigger and isolation efficiency SFs are used to correct MC samples for differences in efficiency to data and are calculated as a ratio of data efficiency ε_{Data} to MC efficiency ε_{MC} (cf. Eq. 6.4). The efficiency is calculated as a ratio of probes passing the selection $N_{\text{probe after cut}}$ under study (reconstruction, trigger or isolation) to the number of all probes $N_{\text{all probe}}$. In the case of the data efficiency calculation, the estimated background is first subtracted from both numerator and denominator:

$$SF = \frac{\varepsilon_{Data}}{\varepsilon_{MC}}, \text{ where} \quad (6.4)$$

$$\varepsilon_{Data} = \frac{N_{\text{probe after cut}} - N_{\text{probe after cut}}^{\text{bkg}}}{N_{\text{all probe}} - N_{\text{all probe}}^{\text{bkg}}}, \quad \varepsilon_{MC} = \frac{N_{\text{probe after cut}}}{N_{\text{all probe}}}$$

For the statistical uncertainty, the uncertainties from the data sample, the signal Monte Carlo sample and all background Monte Carlo samples were combined. For the resulting statistical uncertainty, the same approach as in ref. [101] was used, with the resulting equation reading:

$$\Delta\varepsilon = \sqrt{\frac{(1 - 2\varepsilon)\Delta N_{\text{probe after cut}}^2 + \varepsilon^2\Delta N_{\text{all probe}}^2}{N_{\text{all probe}}}} \quad (6.5)$$

Since on data a background subtraction was performed, the value ΔN , denoting the statistical uncertainty of the entries per bin, has to be calculated via error propagation from the statistical uncertainty of each sample, assumed to be Poissonian distributed.

For the cases where $N_{\text{all probe}} = 0$, ε is set to 0.5 and $\Delta\varepsilon$ to $1/\sqrt{12}$. The uncertainties on the data and Monte Carlo efficiencies were propagated into the statistical uncertainty on the Scale Factor. This was performed assuming no correlation between the data and Monte Carlo efficiencies using Gaussian error propagation.

Different sources for the systematic uncertainty were studied, namely:

- **Muon momentum scale uncertainty:** For this analysis, muon momentum scales, obtained in the dedicated analysis described in ref. [94], were used. The influence of the momentum scale uncertainty was assessed by propagating the scale and smearing up and down variations into the MC signal sample and the MC background sample.
- **Hadronic recoil correction:** The effect of the hadronic recoil correction was estimated by extracting the scale factors without the correction, and taking the difference as additional systematic uncertainty.

6. Overview of Muon Efficiency Corrections

- **Monte-Carlo corrections:** As described in detail in Sections 7.1, C.1, 8.1 and 9.1, several weights were used in the study of the muon reconstruction, trigger and isolation efficiencies. These weights are accompanied with uncertainties, which were estimated by shifting the values of these weights by $\pm 1\sigma$. The difference to the nominal result was used as systematic uncertainty due to reweighting.
- **Background subtraction uncertainty:** The background contamination is overall small. The uncertainties on the background subtraction (discussed in Sec. 6.2) contribute to the uncertainties of the efficiency SFs. The estimation of the SFs (reconstruction, trigger and isolation) was performed multiple times with a variation of $\pm 1\sigma^{\text{bkg}}$ and the resulting uncertainties were counted as independent uncertainty sources.

The systematic uncertainties were assessed by calculating the difference between the nominal scale factors and the scale factors obtained in the variation. The systematic uncertainties listed here are assumed to be fully bin-by-bin correlated. Methods to perform a variety of combinations of the obtained uncertainties are provided. For the bin-by-bin correlated uncertainties, a signed value was chosen, where the sign signifies if the variations lead to higher or lower values for the scale factors than the nominal selection.

For the control plots shown in the following sections, the uncertainties were grouped as shown in Table 6.5.

Group	Grouped sources of uncertainty
Statistical	Combined statistical uncertainty from data and all background sources
Weights	Uncertainty due to the application of the remaining other two scale factors
Scale	Combined muon momentum and hadronic recoil scale uncertainty
Cross-Section	Theoretical uncertainty on the cross-sections of the used Monte Carlo samples
QCD Template	Uncertainty on the QCD template normalization

Table 6.5.: Groups of uncertainties as used in the control plots in the following sections.

7. Muon Reconstruction Efficiency

7.1. Methodology, Event Selection and Corrections

The reconstruction efficiency of muons in the ATLAS detector depends on the reconstruction of inner detector tracks, on the reconstruction of muons in the muon spectrometer and their subsequent combination. Since the tracking efficiency of the inner detector for high energetic muons with $p_T > 15$ is close to unity¹, it is sufficient to study the muon reconstruction efficiency of combined muon tracks with respect to inner detector tracks. The predicted MC reconstruction efficiency for MC Truth muons² vs η and p_T for $W \rightarrow \mu\nu$ and $Z \rightarrow \mu\mu$ events is shown in Figure 7.1. The reconstruction efficiencies are very similar for both samples, which confirms the assumption that the determined reconstruction efficiencies in Z -boson data can also be applied to the W boson samples³. In addition, only a very weak dependence on the transverse momentum of the muon can be observed, with a change of only 4 ‰ over the whole spectrum.

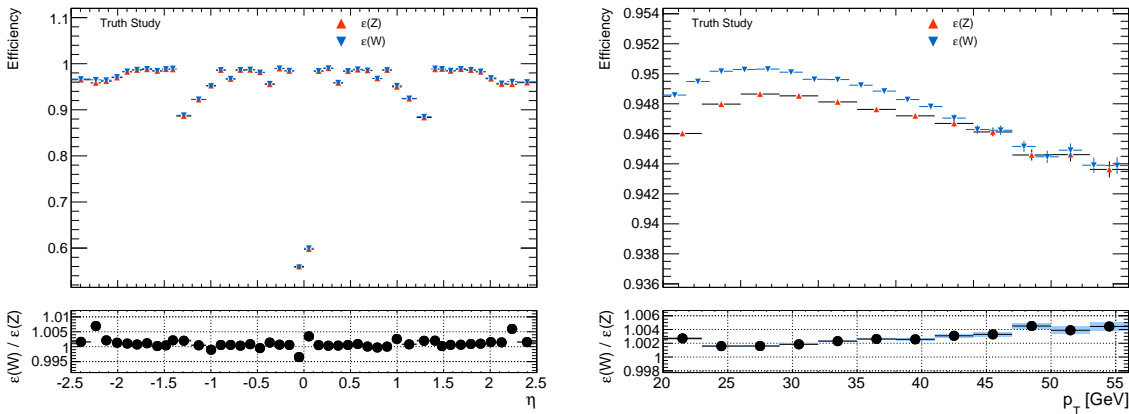


Figure 7.1.: Reconstruction efficiency of muons in $W \rightarrow \mu\nu$ and $Z \rightarrow \mu\mu$ MC samples vs. η (left) and p_T (right). The uncertainties shown are purely statistical.

The determination of the muon reconstruction efficiency in data is based on the ‘tag-and-probe’ method. The ‘tag’-object in this case is an isolated combined muon, the ‘probe’-object is an isolated inner detector track, which leads — together with the tag-kinematics — to an invariant mass close to the Z boson. Since the background contribution to this process is low, the reconstruction efficiency of combined muon tracks can be precisely determined.

¹See Appendix C

²All truth muons with $p_T > 20$ GeV and $|\eta| < 2.4$ are considered.

³Remaining differences can be explained by the difference in the underlying p_T or η distribution of the decay leptons from W and Z bosons.

7. Muon Reconstruction Efficiency

The selection criteria for the tag and probe object selection are summarized in the following:

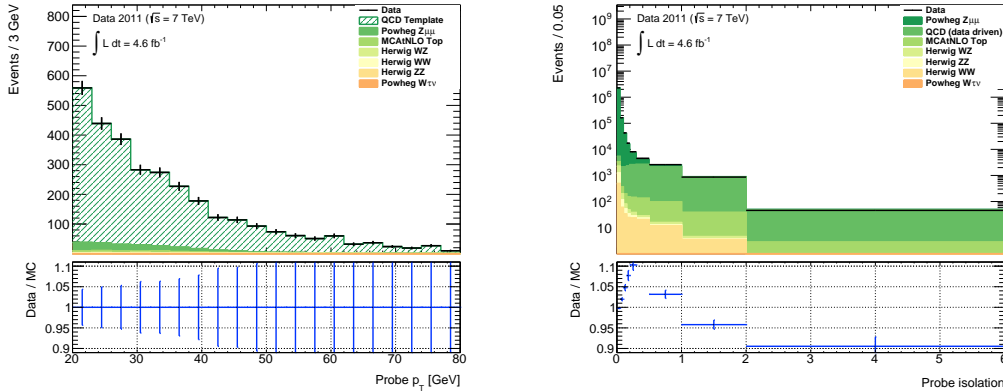
- Event cuts:
 - Trigger: EF_MU18 up to period J, EF_MU18_MEDIUM from period J inclusive
 - At least three tracks from primary vertex
- Tag track:
 - Quality cuts summarized in Table 6.3
 - $|\eta| \leq 2.4$
 - $p_{T,ID} \geq 20 \text{ GeV}$
 - $|z_{0,PV}| < 10 \text{ mm}$
 - Trigger matched with $\Delta R < 0.01$
 - Isolated with $p_T^{trkcone40}/p_T < 0.1$
- Probe track:
 - Quality cuts summarized in Table 6.3
 - $|\eta| \leq 2.4$
 - $p_{T,ID} \geq 20 \text{ GeV}$
 - $|z_{0,PV}| < 10 \text{ mm}$
- Pair:
 - $|z_{0,PV,1} - z_{0,PV,2}| < 3 \text{ mm}$
 - $|M_{\mu\mu} - M_Z| \leq 10 \text{ GeV}$
 - Opposite charge
 - Exactly one pair per event

The muon reconstruction efficiency is determined in the binning defined in Table 6.1. On average, several thousand probe-tracks per bin are found for the full 2011 data-set in the three-dimensional binning, with a subsequently higher number in the one- and two-dimensional binnings.

Technically, the efficiencies are represented by two sets of histograms, one representing the kinematics of probe-tracks, the other representing the kinematics of those probe-tracks which could be matched to a combined muon. A probe muon (= inner detector track) is defined as matched to a muon track if a muon track is found within $\Delta R = 0.05$. It is defined as combined muon, if the ISCOMBINED flag is set by the reconstruction algorithm. The final reconstruction efficiencies are obtained by dividing the histograms from both sets, after backgrounds are subtracted.

The background determination was already described in Section 6.2. As discussed, two methods for the estimation of the QCD background were used: the ABCD method and a fit in the isolation distribution of a control selection with skipped isolation requirement on the probe. A same-sign selection — corresponding to selection *B* in the ABCD method — was used to obtain QCD templates for all histograms. An example is shown in Figure 7.2(a) for the distribution of the transverse momentum of the probe candidates. Here, the discrepancy

between Monte Carlo and data corresponds to the background template obtained for this variable. Figure 7.2(b) shows the result of the fit approach. A good description of data by the combined Monte Carlo and QCD template can be observed.



(a) Shape of the QCD template in probe p_T . (b) Result of the fit approach in the probe isolation.

Figure 7.2.: Control plots from the QCD background estimation. Figure (a) shows the shape of the QCD template in the same-signed selection. Figure (b) shows the result of the fit performed in the isolation distribution of the probe.

An overview of the selected inclusive number of events in the numerator and denominator, including the background estimations, is given in Table 7.1.

Sample	Numerator			Denominator		
	N	Δ_{stat}	Δ_{syst}	N	Δ_{stat}	Δ_{syst}
Data	2 299 373	1 516	0	2 466 222	1 570	0
POWHEG $Z\mu\mu$ (147407)	2 322 274	576	116 113	2 457 768	593	122 888
MC@NLO $t\bar{t}$ (105200)	554	4	34	1 411	7	87
HERWIG WW (105985)	208	2	14	471	3	33
HERWIG ZZ (105986)	757	4	53	808	4	56
HERWIG WZ (105987)	1 100	5	77	1 194	5	83
PYTHIA $Z\tau\tau$ (106052)	183	27	9	656	51	32
MC@NLO Single Top (108340)	0	0	0	0	0	0
MC@NLO Single Top (108341)	0	0	0	16	1	1
MC@NLO Single Top (108342)	0	0	0	1	0	0
MC@NLO Single Top (108343)	0	0	0	0	0	0
MC@NLO Single Top (108344)	0	0	0	0	0	0
MC@NLO Single Top (108345)	0	0	0	0	0	0
MC@NLO Single Top (108346)	56	2	3	137	3	9
QCD (data driven)	74	9	8	3 754	68	430

Table 7.1.: Overview of selected events in the numerator and denominator for data and all background contributions.

7. Muon Reconstruction Efficiency

Several things should be noted. First of all, events which contain two tag-muons — i.e. two inner detector tracks that are matched to combined muons — are used twice. First with the positive lepton as tag candidate and the negative as probe candidate, then vice versa. The efficiencies are calculated separately for both cases. This ensures a correct treatment of the combinatorics. Secondly, only the tag muons are required to trigger the events and no similar requirement is applied to the probe-object. Hence, the determined efficiencies are independent from trigger requirements.

Several kinematic distributions of probe tracks are shown in Figures 7.3 and 7.4, where all MC corrections except the reconstruction efficiency scale factors have been applied. Since this is the first time such control plots are presented in this thesis, it is worthwhile to discuss the shapes of these distributions one-by-one:

- **Invariant Mass:** This plot shows the invariant mass of the selected Tag and Probe muon candidate, $m_{\mu\mu}$. As can be seen, this distribution is dominated by the Z boson peak, with the position of its center corresponding to the Z boson mass of 91.1876 GeV (cf. ref. [8]). Moreover, almost full agreement with the prediction from the Monte Carlo simulation of the process $pp \rightarrow Z + X \rightarrow \mu\mu + X$ can be observed. This shows that background plays a negligible role, as well as that the peak is very well described. The distribution of the invariant mass is in general very robust against physics and detector mis-modeling.
- **Probe p_T :** Here, the so-called Jacobian shape discussed in Section 3.1 can be observed, with an edge at $p_T \sim M_Z/2$. As was also discussed in Section 3.1, the distribution is washed out by the non-vanishing transverse momentum of the intermediary Z boson.
- **Probe η :** The angular distribution of the decay lepton was also discussed in Section 3.1. If transformed from the $\cos\theta$ dependence chosen in this discussion into the η dependence, the angular distribution of the decay muon close to the Z peak has a shape similar to that of a normal distribution centered at zero. This corresponds to the distribution visible in the sub-plot in Figure 7.3.
- **Probe φ :** This distribution can a priori assumed to be flat. However, effects due to inefficiencies in the detector can easily produce structures in this plot, such as the dip between 1 rad and 2 rad. This can be attributed to a drop in the reconstruction efficiency between -1.1 and -1 rad and -2 rad. In this region, as discussed in Section 4.3.3, the so-called feet of the muon spectrometer are located, with a sparser instrumentation and subsequent decrease in the reconstruction efficiency. Since a reconstruction requirement is enforced on the tag muon candidate and tag and probe appear almost fully back-to-back with respect to φ , this is mirrored in the distribution of the azimuth φ of the probe.
- **u_{\parallel}^l :** This variable is centered at zero, since the correlation between probe p_T and HR is not very strong. The value of u_{\parallel}^l can be seen as a proxy for the distance ΔR between probe and hadronic recoil. If hadronic recoil and probe transverse momentum are parallel, u_{\parallel}^l can reach large positive values, whereas in the case of both being anti-parallel, the sign of u_{\parallel}^l flips and very negative values can be reached. If the hadronic recoil was projected onto p_T^Z , a bias towards small values would be expected. The modeling of u_{\parallel}^l is a part of the modeling of the hadronic recoil, and therefore depends on a number of kinematic cuts, as

well as the modeling of other quantities, such as p_T^Z . The slight mis-modeling observed here is expected, since the HR correction applied here was tuned for the settings used in the W boson selection, especially the hadronic recoil used in the SMLIGHT samples.

- u_{\perp}^l : For this variable the same remarks as for the associated variable u_{\parallel}^l hold. Also here a mis-modeling is visible, and also in this case it can be attributed to a selection different from that used for the Z and W boson mass measurement. The variable u_{\perp}^l is centered at zero. This is because the hadronic recoil is on average expected to be small and does not show a strong correlation with lepton p_T .

In general, a good data/MC agreement can be observed, except for the two variables associated with the modeling of the hadronic recoil. The remaining differences are expected to vanish after the correct application of the reconstruction efficiency scale factors determined in this chapter.

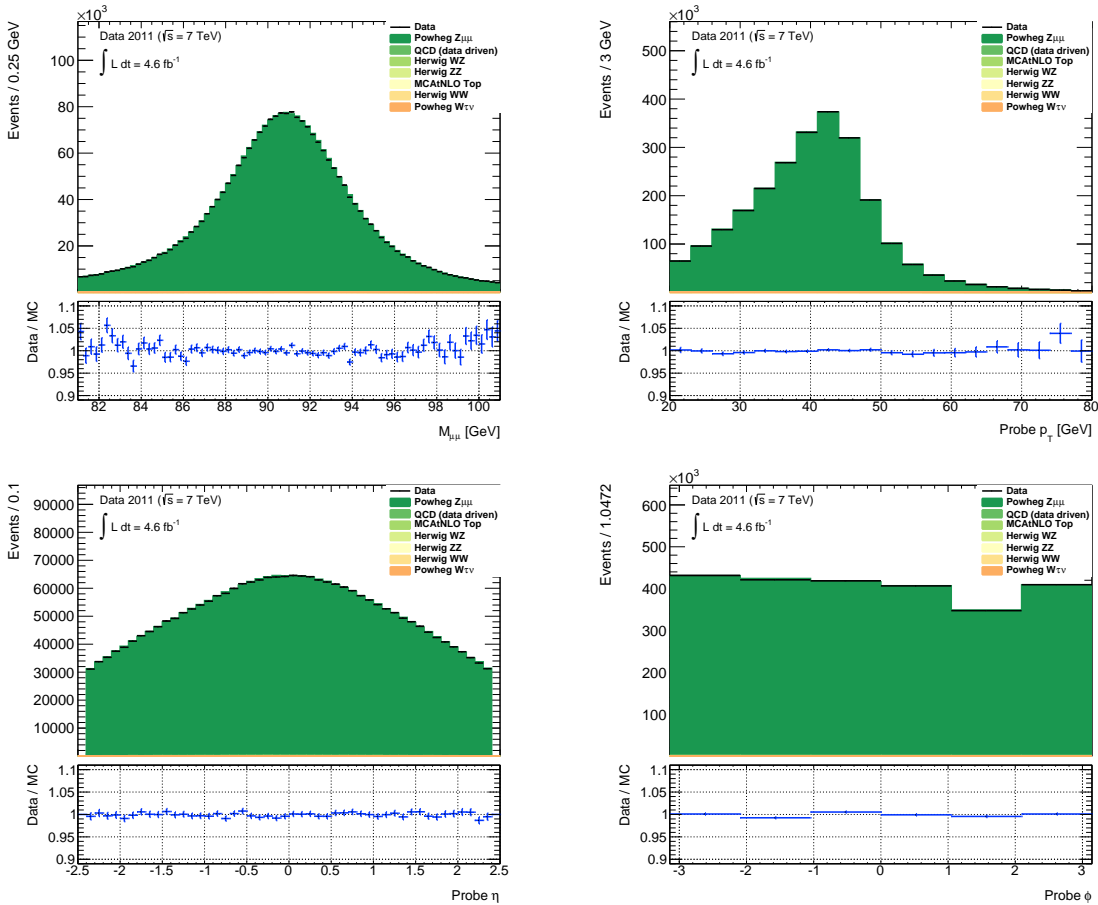


Figure 7.3.: Kinematic distributions of probe-tracks comparing data to the combined signal and background prediction. From left to right, top to bottom: Invariant mass of the selected $\mu\mu$ pair, probe p_T , η , ϕ .

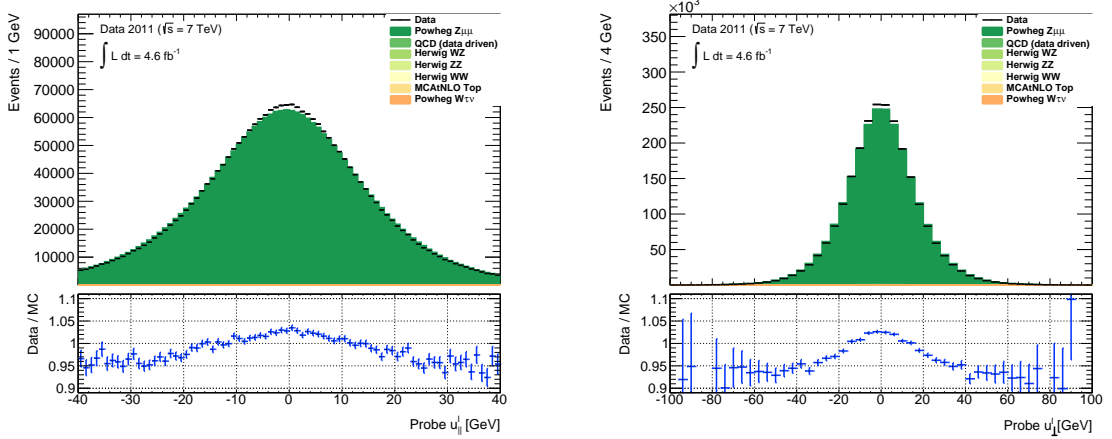


Figure 7.4.: Kinematic distributions of probe-tracks comparing data to the combined signal and background prediction. The plots show $u_{||}^l$ (left) and u_{\perp}^l (right). As discussed in the text, the mis-modeling observed here is likely due to the usage of SMWZ samples.

7.2. Efficiency and Scale Factor Determination

The resulting efficiencies are shown in Figure 7.5 in one-dimensional projections with a higher granularity, where the tag and probe method has been applied on both data and the POWHEG $Z \rightarrow \mu\mu$ sample. For clarity, instead of presenting the *region*, i.e. the combined η - φ binning, separate results for η and φ are shown in two separate histograms. Overall, a shift of the muon reconstruction efficiency can be seen. The general dependence on the studied variables is very similar between data and Monte Carlo.

As can be seen, three pronounced drops exist with respect to η . These can be associated with the structures of the muon system: At $|\eta| \approx 1$, the transition between barrel and end-cap takes place, with sparser instrumentation and subsequent decrease in the reconstruction efficiency. A similar effect can be seen at $|\eta| = 0$, where a gap between the two barrel parts of the muon system exists.

With regards to lepton p_T , a structure with a dip around ~ 20 GeV is visible. This structure alone cannot be taken as indicating that the reconstruction efficiency depends on p_T . On the contrary, it has to be kept in mind that, in essence, the momentum of all probe muons is close to $M_Z/2$, and that lepton p_T can therefore be regarded as a direct function of lepton η . In this way, inefficiencies in η are directly propagated to lepton p_T . This will be investigated in larger detail below.

With respect to $u_{||}^l$, a drop in the efficiency is visible. The almost identical drop in data and signal MC shows that the effect is expected and cannot be due to background effects. Its appearance could be explained by the following consideration: a corrected value of the hadronic recoil was used, via the ATLAS algorithm HR_CORRRECOIL_20. In this algorithm, calorimeter activity associated to signal muons is subtracted. In the case where the muon fails to be reconstructed, it is likely that the algorithm fails to correct for the additional activity produced by the muon. Subsequently, the resulting hadronic recoil will be biased towards the non-reconstructed muon, and $u_{||}^l$ will be overestimated.

To cross-check this hypothesis, studies of the reconstruction efficiency with respect to $u_{||}^l$ and to a similar quantity obtained from the projection of $-p_T^Z$ onto the probe instead of the

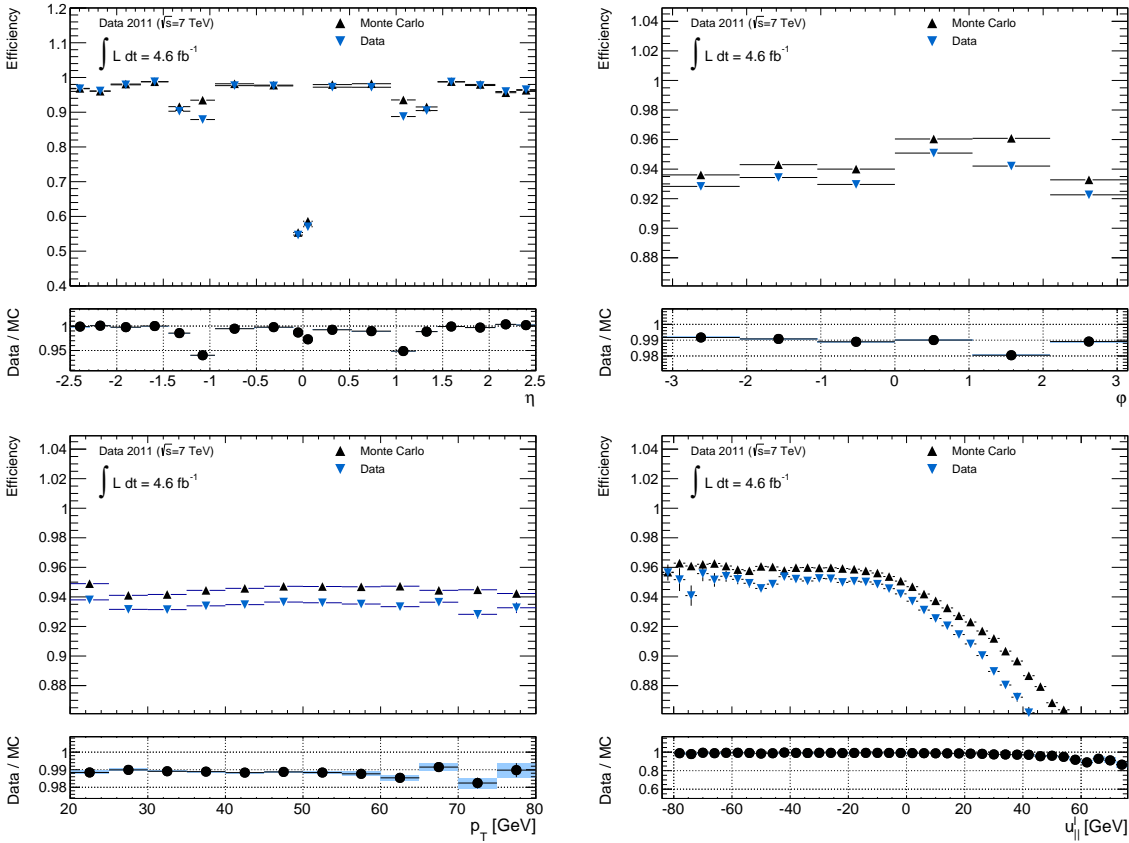


Figure 7.5.: Determined reconstruction efficiency by the tag and probe method for data and MC. From left to right, top to bottom: $\eta, \varphi, p_T, u_{\parallel}^l$. Only statistical uncertainties are shown.

hadronic recoil, were performed. In these studies, only the truth information from Signal Monte Carlo was used. If the effect was due to increased activity around the probe, a drop at large values should appear in both cases. The results are shown in Figure 7.6, where it is clearly visible that no such drop exists when replacing the hadronic recoil with $-p_T^Z$. This can be assumed to be further evidence that the calculation of the hadronic recoil introduces this bias. The effect is well-modeled in Monte Carlo and therefore does not play a large role in the extraction of M_W .

Figure 7.7 shows the resulting efficiencies for each of the four η regions used in the measurement of the W boson mass. As can be seen, region 1 is influenced by the crack at $|\eta| \approx 0$, which influences mostly the low- p_T probes due to the fact that $|\eta|$ and p_T are correlated. Region 2 covers the crack region at $|\eta| \approx 1$, where the efficiency also drops.

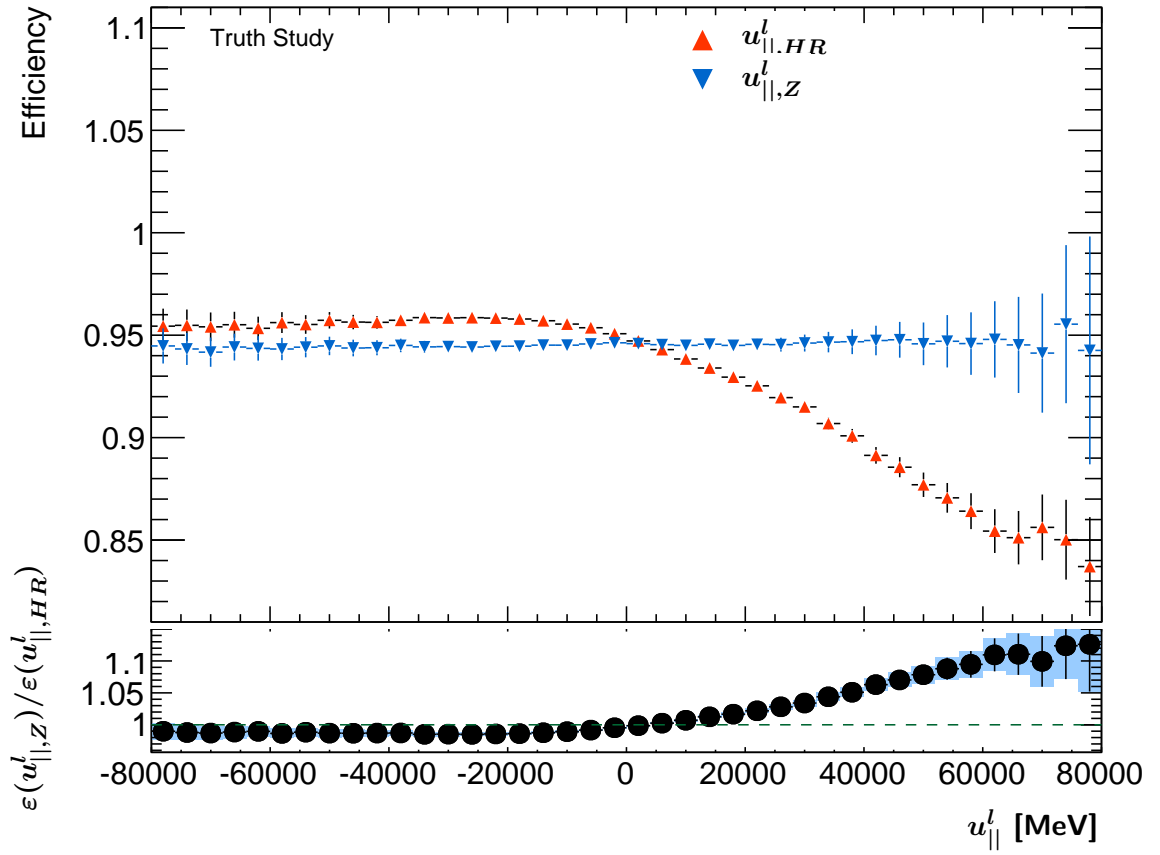


Figure 7.6.: Comparison of reconstruction efficiencies as a function of $u_{||}^l$, calculated from the hadronic recoil, and from p_T^Z . As can be seen, the efficiencies are flat with respect to p_T^Z , while a clear drop with respect to the hadronic recoil is visible.

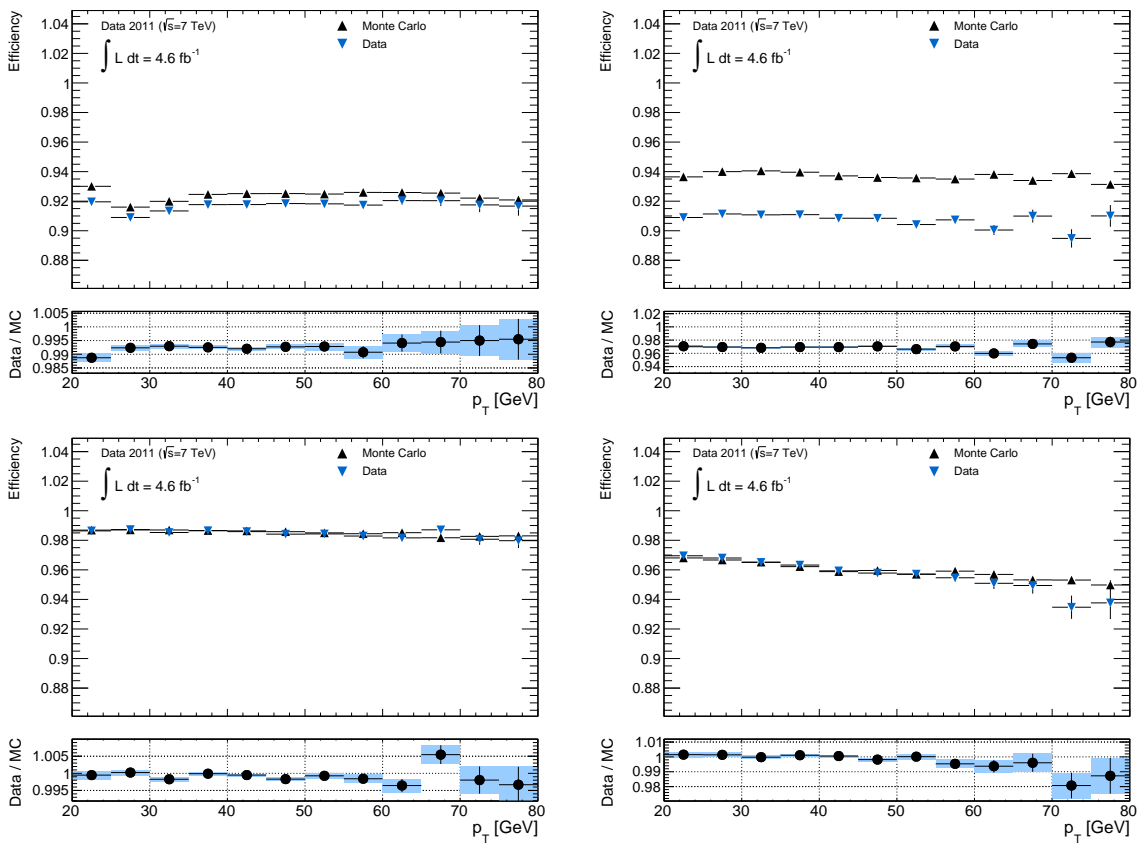


Figure 7.7.: Determined reconstruction efficiency using the tag and probe method for Data and MC as a function of p_T . From left to right, top to bottom: Region 1 ($0 < |\eta| \leq 0.8$), Region 2 ($0.8 < |\eta| \leq 1.4$), Region 3 ($1.4 < |\eta| \leq 2.0$) and Region 4 ($2.0 < |\eta| \leq 2.4$). Only statistical uncertainties are shown.

7. Muon Reconstruction Efficiency

In order to correct the differences between data and MC, scale factors are defined via the ratio of the reconstruction efficiency in data and MC, $SF := \varepsilon_{Data}/\varepsilon_{MC}$. These scale factors have to be applied to the MC sample, in order to model the muon reconstruction efficiency correctly. The resulting scale factors are shown in Figure 7.8. As it could already be assumed from the good description of the data efficiencies by Monte Carlo, the resulting scale factors are relatively flat and close to unity. Towards high values of $u_{||}^l$, the scale factors drop down, albeit with large uncertainties. This might in part be due to a possible mis-modeling of this background-dominated tail of the signal distribution, also visible in the Figure 7.3. The uncertainties shown are the total uncertainties obtained by combining statistical and systematic uncertainties.

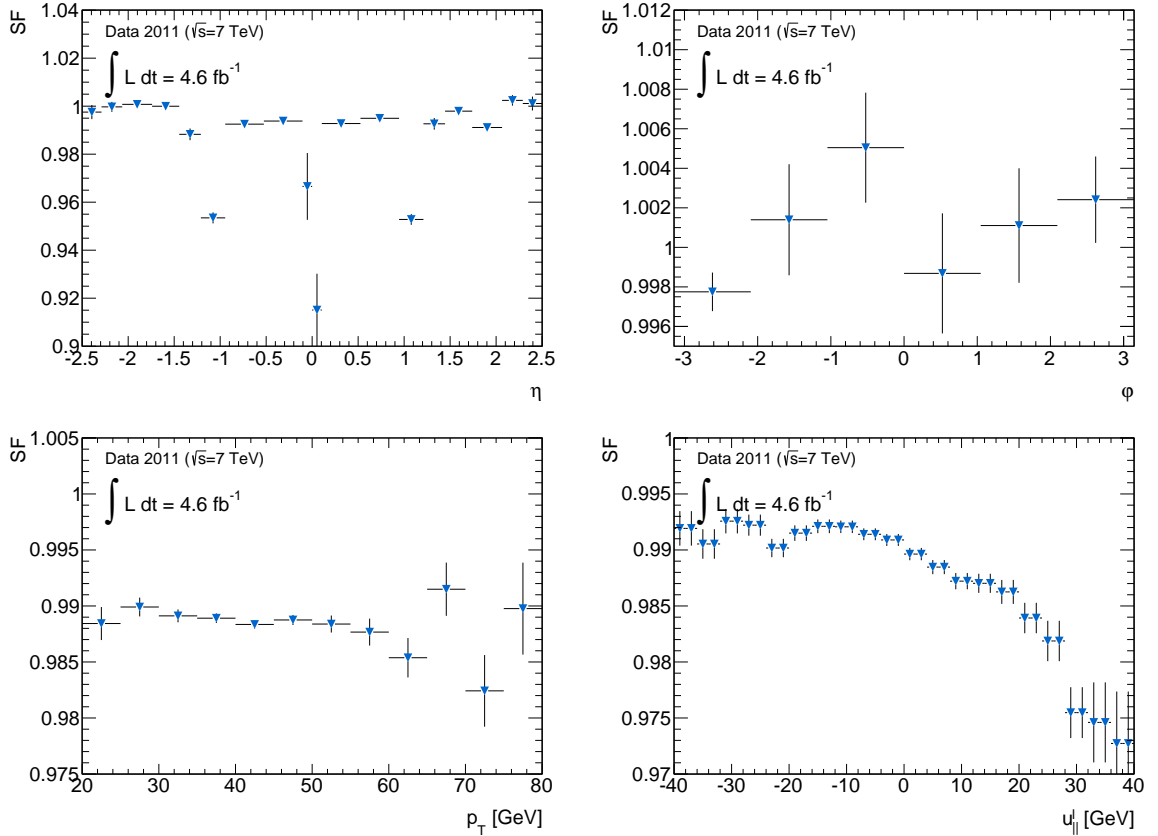


Figure 7.8.: Reconstruction scale factors determined for the POWHEG MC simulation. From left to right, top to bottom: η , p_T , $u_{||}^l$. Uncertainties shown are the full systematic and statistical uncertainties.

The general approach for the treatment and estimation of uncertainties is described in Section 6.3. Figure 7.9 shows the different contributions to the uncertainty on the one-dimensional scale factors. The statistical uncertainty is dominant in all distributions in these specific plots. The largest systematic uncertainties are due to the QCD background estimation. The uncertainties due to the corrections applied to Monte Carlo are usually very small. As expected, the uncertainties grow larger in regions where the background becomes larger: at high and low values of u_{\parallel}^l and p_T . As a reminder, towards high values of u_{\parallel}^l data is almost fully background-dominated.

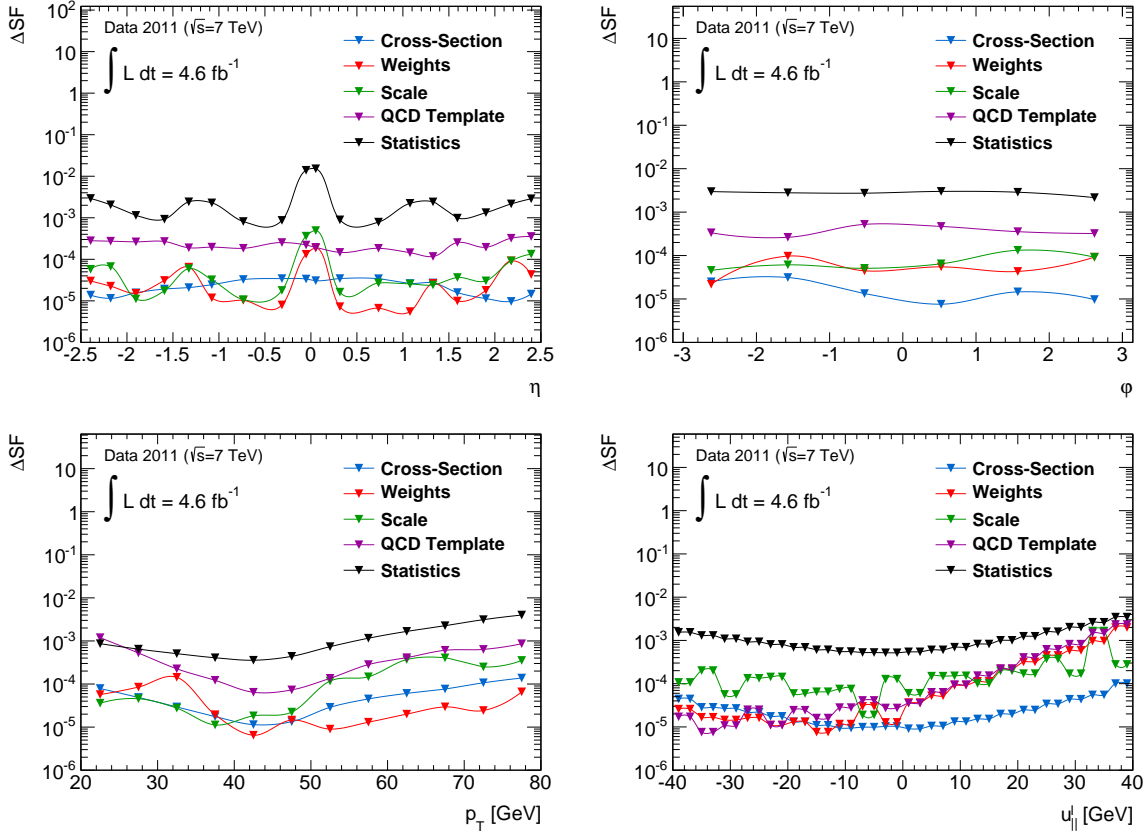
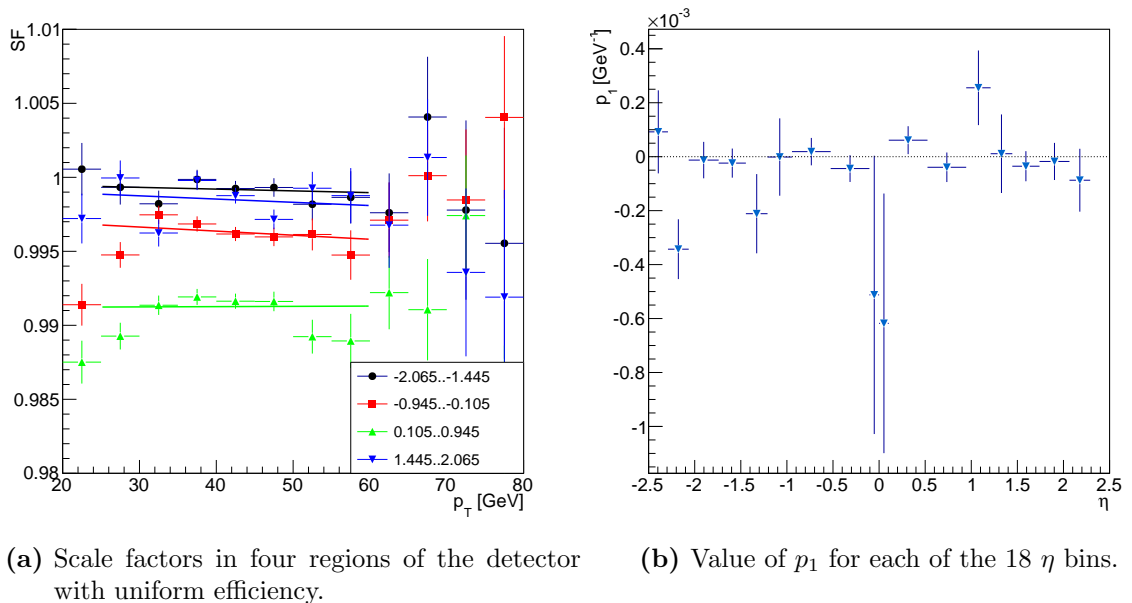


Figure 7.9.: Uncertainties on the reconstruction scale factors for the POWHEG MC prediction. From left to right: η , p_T , u_{\parallel}^l . Table 6.5 gives details on the categories shown in the plot.

7. Muon Reconstruction Efficiency

As mentioned before, it is possible that the fluctuations in p_T can be fully explained by the structures in η and their effect on the p_T distribution. To test this hypothesis, the detector was divided into four bins in η , which have a relatively uniform reconstruction efficiency. These regions are $-2.065 \leq \eta \leq -1.445$, $-0.945 \leq \eta \leq -0.105$, $0.105 \leq \eta \leq 0.945$ and $1.445 \leq \eta \leq 2.065$, thereby excluding the crack regions between the endcaps and the barrel at $|\eta| \approx 1.05$ and the gap at $|\eta| = 0$. The resulting scale factors in p_T for these four regions can be seen in Figure 7.10(a). In this figure, the results from a fit for each of the distributions with a polynomial of the form $p_0 + p_1 \cdot p_T$ in the range of 25 to 60 GeV is shown. The slope p_1 for all 18 bins in η is shown in Figure 7.10(b). The associated significance $p_1/\Delta p_1$ is summarized in Table 7.2. As can be seen, the distribution of the scale factors is compatible with a flat distribution in all four regions, as well as in all 18 bins in which the scale factors were originally derived. In this study, only statistical uncertainties were used, since these are the dominating source of uncertainty.



(a) Scale factors in four regions of the detector with uniform efficiency. (b) Value of p_1 for each of the 18 η bins.

Figure 7.10.: Test of the flatness of the reconstruction scale factors. The left plots shows the reconstruction scale factors in four regions of the detector with uniform efficiency defined in the text. The corresponding fit values are shown in Table 7.2. In this plot, only the statistical uncertainty is shown. The right plot shows the values of the fitted slope p_1 in each of the 18 η bins in which the scale factors were obtained.

η	χ^2/dof	p_1 [GeV $^{-1}$]	Δp_1 [GeV $^{-1}$]	$p_1/\Delta p_1$
-2.065..-1.445	3.2/5	$-1.19 \cdot 10^{-5}$	$4.21 \cdot 10^{-5}$	-0.28
-0.945..-0.105	8.5/5	$-2.76 \cdot 10^{-5}$	$3.55 \cdot 10^{-5}$	-0.78
0.105..0.945	11.9/5	$1.82 \cdot 10^{-6}$	$3.76 \cdot 10^{-5}$	0.05
1.445..2.065	16.2/5	$-2.19 \cdot 10^{-5}$	$4.33 \cdot 10^{-5}$	-0.51

Table 7.2.: Resulting fit values for the fits shown in Figure 7.10(a).

7.2. Efficiency and Scale Factor Determination

As mentioned earlier, charge-dependent scale factors were also obtained. Figure 7.11 shows the comparison between the scale factors obtained for positive and negative probes. As can be observed, the scale factors are, in general, very similar. However, there are some deviations: With respect to η it is notable that the two transition regions at $\eta=-1.05$ and $\eta=1.05$ exhibit significantly different scale factors for positive and negative probes. While the transition region in the C side shows higher scale factors for μ^- than μ^+ , this flips around for the transition region at the A side. Apart from this no significant differences can be observed, as is also expected since the reconstruction efficiency should be charge independent.

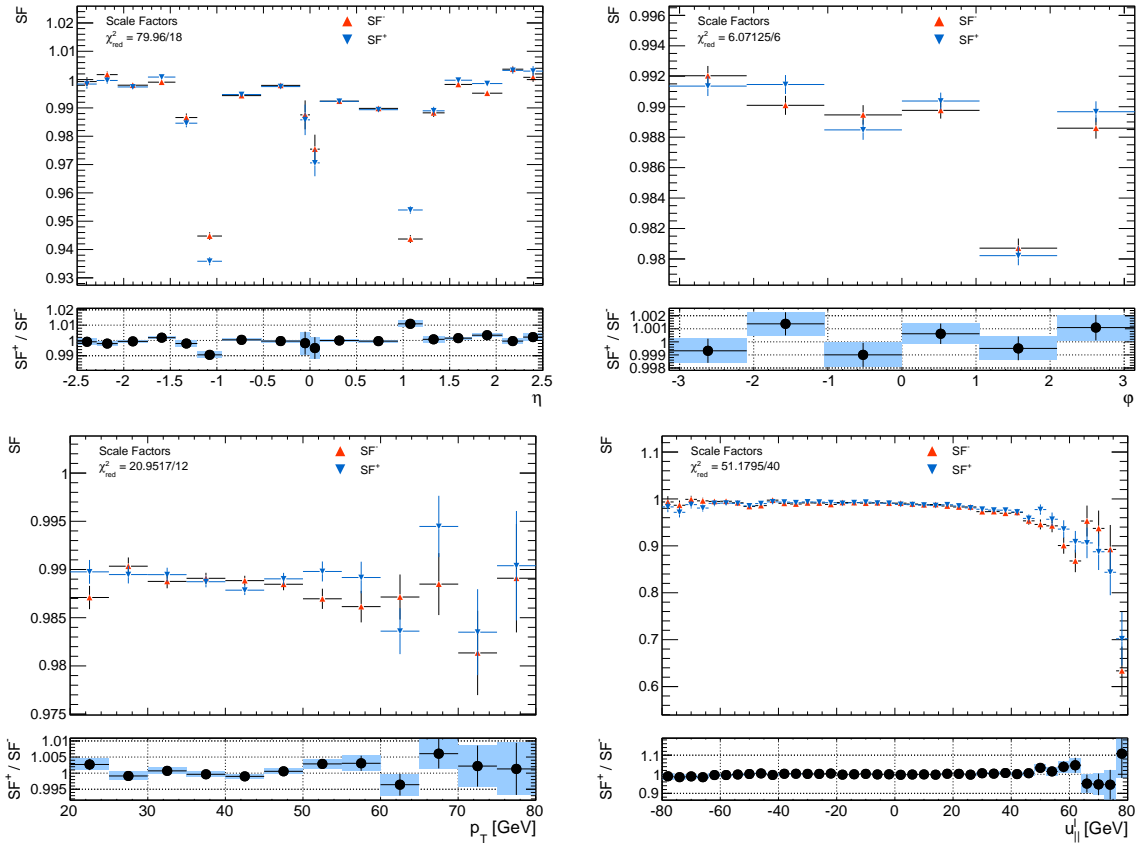


Figure 7.11.: Comparison of Reconstruction scale factors obtained for negative and positive probes. From left to right: η , p_T , $u_{||}^l$. The uncertainties shown are only statistical.

7.3. Comparison with Previous Results

In order to check for consistency with earlier measurements, these results were compared with the scale factors from the recommended version of the official ATLAS package⁴. A detailed description of the tag and probe method used to obtain these scale factors can be found in ref. [102]. Scans in the variable η were performed. In the official scale factors, no dependence on lepton p_T , φ or $u_{||}^l$ was modeled. The scale factors shown in Figure 7.12 were obtained. An overall shift of approximately 5 % can be observed, which could be traced back to the change from MC11C to MC11D. This, as well as the fact that the official scale factor were not supplied as function of φ , p_T or $u_{||}^l$, shows the value of the re-assessment performed as part of this thesis.

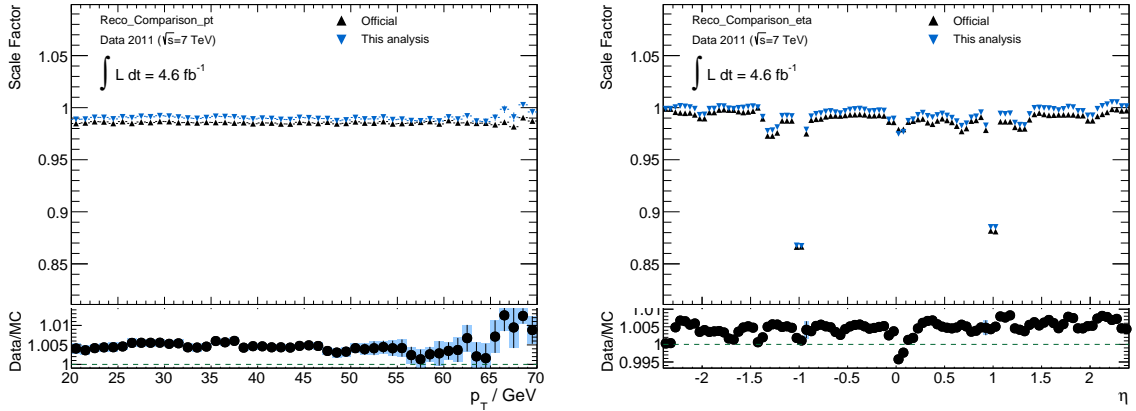


Figure 7.12.: Comparison of the reconstruction scale factors obtained with the official ATLAS package and from this analysis in dependence of η . The official scale factors were not supplied as function of lepton φ , p_T or $u_{||}^l$.

⁴MUONEFFICIENCYCORRECTIONS-02-01-20

8. Muon Trigger Efficiency

8.1. Methodology, Event Selection and Corrections

In this analysis, the trigger efficiency is defined as the probability of an isolated, combined muon to also fire the triggers used in this analysis. For the data taken in 2011 in period B-I, EF_MU18 was the lowest unrescaled trigger, while for period J-M, EF_MU18_MEDIUM was the lowest unrescaled trigger¹. The data taken in 2011 was further divided into four sub-periods, as shown in Table 8.1. This follows ref. [91], where a significant charge-dependence was observed in periods B-G5. In addition, the efficiencies in period L3 and L4 were significantly influenced by a timing problem in the RPCs. These deviations, not modeled in MC, make this separation in a total of four disjunct trigger periods necessary. In the following, the focus will be laid onto the results obtained for EF_MU18_MEDIUM_STD, since this period contains about half of the total integrated luminosity. Reference to the other three settings will only be made to stress significant differences. The plots for the three other settings — EF_MU18_BG5, EF_MU18_G6I and EF_MU18_MEDIUM_L3L4 — may be found in Appendix B.

Sub-period	Trigger	Period	Luminosity [fb ⁻¹]
EF_MU18_BG5	EF_MU18	B-G5	0.76
EF_MU18_G6I	EF_MU18	G6-I	0.73
EF_MU18_MEDIUM_L3L4	EF_MU18_MEDIUM	L3,L4	0.48
EF_MU18_MEDIUM_STD	EF_MU18_MEDIUM	J-M except L3,L4	2.61

Table 8.1.: Definition of the four sub-periods for which dedicated trigger scale factors were obtained. The sub-periods were chosen such that the data efficiency within each sub-period is similar.

The predicted MC trigger efficiency for MC Truth muons vs η and p_T for $W \rightarrow \mu\nu$ and $Z \rightarrow \mu\mu$ events are shown in Figure 8.1. Note that a large zoom on the y axis was necessary to make the differences with respect to p_T visible. The trigger efficiencies are very similar for both samples and differ by only around 5 %, which confirms the assumption that the determined trigger efficiencies in Z-boson data can also be applied for the W boson samples². The results for the three other settings are very similar and shown in Figures B.1 in Appendix B.

The determination of the muon trigger efficiency in data is also based on the tag and probe method. The tag object in this case is an isolated, combined and triggered muon, the probe object is an isolated, combined muon which leads — together with the tag-kinematics — to an invariant mass close to the Z boson. Since the background contribution to this process

¹The term *lowest unrescaled trigger* denotes the trigger with the loosest selection criteria without prescaling factor. Obtaining the maximum number of events is ensured by choosing these triggers for the analysis.

²Remaining differences can be explained by the difference in the underlying p_T or η distribution of the decay leptons from W and Z bosons.

8. Muon Trigger Efficiency

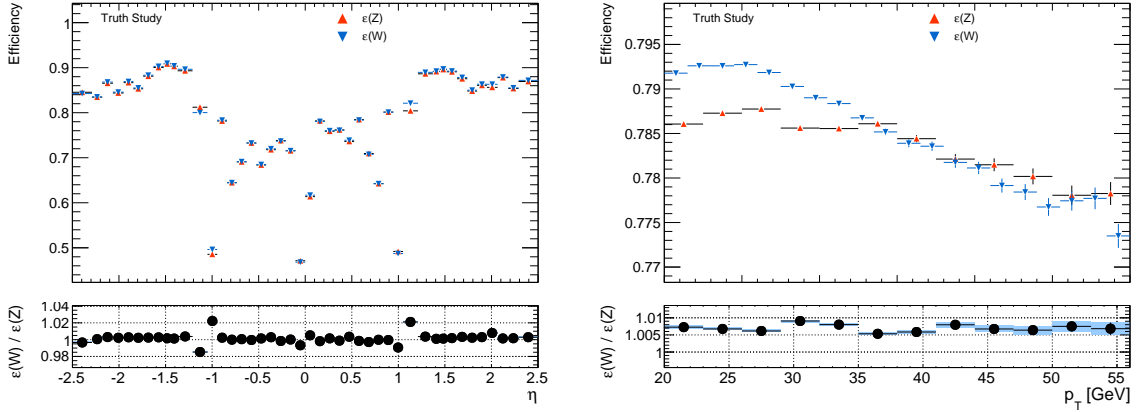


Figure 8.1.: Trigger efficiency of muons in $W \rightarrow \mu\nu$ and $Z \rightarrow \mu\mu$ MC samples vs. η (left) and p_T right. The results are shown for EF_MU18_MEDIUM_STD. The uncertainties shown are purely statistical.

is the lowest of all three analyses discussed in this part of the thesis, the trigger efficiency of combined muons can be precisely determined. The selection criteria for the tag- and probe-object selection are summarized in the following.

Pairs of STACO muons were selected according to these selection criteria:

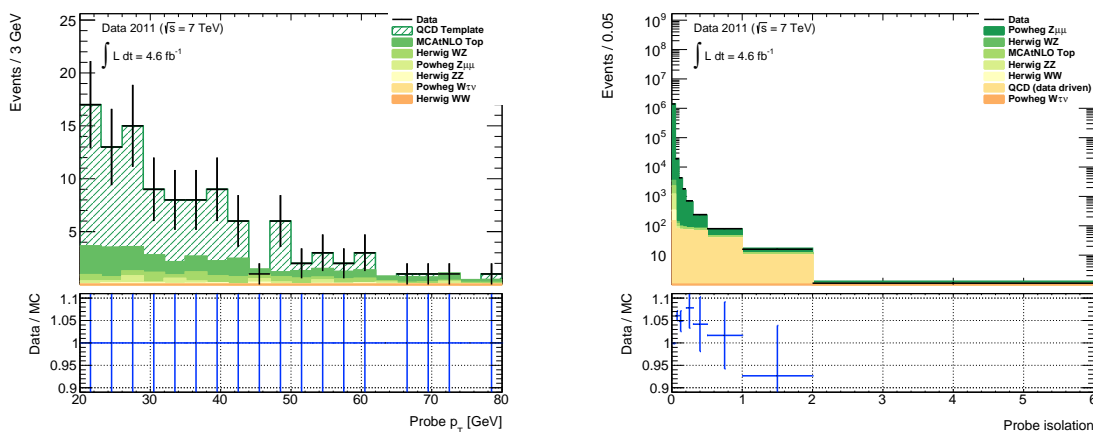
- Event cuts:
 - Trigger: EF_MU18 up to period J, EF_MU18_MEDIUM from period J inclusive
 - At least three tracks from primary vertex
- Muon selection:
 - Quality cuts summarized in Table 6.3
 - Combined (CB) muon
 - $|\eta| \leq 2.4$
 - $p_{T,ID} \geq 20 \text{ GeV}$
 - Isolated with $p_T^{\text{cone20}}/p_T < 0.1$
 - $|z_{0,PV}| < 10 \text{ mm}$
- Pair selection:
 - $|z_{0,PV,1} - z_{0,PV,2}| < 3 \text{ mm}$
 - $|M_{\mu\mu} - M_Z| \leq 10 \text{ GeV}$
 - Opposite charge
 - Exactly one pair per event
- Tag trigger matched

The muon trigger efficiency is also determined in three dimensions, using the binning shown in Table 6.1 for the transverse momentum of the muon p_T , $u_{||}^l$ and also the detector region, which is a combined η - φ -binning. On average, several thousand probe muons per bin for the full 2011

data-set were found. Technically, the efficiencies are represented by two sets of histograms, one representing the kinematics of probe muons, the other representing the kinematics of those probe muons that could be matched to a trigger object. A probe muon is defined as matched to a trigger object if a trigger object is found within $\Delta R = 0.10$. The final trigger efficiencies are obtained by dividing the number of probes passing the trigger matching requirement with the total number of probes for any given bin.

The background determination was already described in Section 6.2. As discussed, two methods for the estimation of the QCD background were used: the ABCD method and a fit in the isolation distribution of a control selection with skipped isolation requirement on the probe. A same-sign selection — corresponding to selection *B* in the ABCD method — was used to obtain QCD templates for all histograms. An example is shown in Figure 8.2(a) for the distribution of the transverse momentum of the probe candidates. Here, the discrepancy between Monte Carlo and data corresponds to the background template obtained for this variable. Figure 8.2(b) shows the result of the fit approach. A satisfying description of data by the combined Monte Carlo and QCD template can be observed.

An overview of the selected inclusive number of events in the numerator and denominator including the background estimations for the EF_MU18_MEDIUM_STD trigger is given in Table 8.2. The results for the other three trigger configurations are similar and shown in Appendix B.



(a) Shape of the QCD template in probe p_T . (b) Result of the fit approach in the probe isolation.

Figure 8.2.: Control plots from the QCD background estimation. Figure (a) shows the shape of the QCD template in the same-signed selection — the QCD template corresponds to the difference between data and Monte Carlo stack. Figure (b) shows the result of the fit performed in the isolation distribution of the probe. As can be seen from the comparison of data to the QCD shape in the upper half of this plot, the tail of the isolation is described by the QCD template. Results shown are for EF_MU18_MEDIUM_STD.

The selection is run twice: In the first run, only positive muons are considered as tags, in the second only negative candidates. This ensures a correct treatment of the combinatorics.

Several kinematic distributions of probe tracks are shown in Figure 8.3, where all MC corrections except the trigger efficiency scale factors have been applied. In general, a good data/MC can be observed. The remaining differences are expected to vanish after the correct application

8. Muon Trigger Efficiency

Sample	Numerator			Denominator		
	N	Δ_{stat}	Δ_{syst}	N	Δ_{stat}	Δ_{syst}
Data	1095512	1046	0	1412170	1188	0
POWHEG $Z\mu\mu$ (147407)	1102230	395	55111	1409405	447	70470
MC@NLO $t\bar{t}$ (105200)	557	4	34	740	5	45
HERWIG WW (105985)	121	1	8	155	2	10
HERWIG ZZ (105986)	546	3	38	698	3	48
HERWIG WZ (105987)	756	4	52	978	4	68
PYTHIA $Z\tau\tau$ (106052)	65	16	3	87	18	4
MC@NLO Single Top (108340)	0	0	0	0	0	0
MC@NLO Single Top (108341)	0	0	0	2	0	0
MC@NLO Single Top (108342)	0	0	0	0	0	0
MC@NLO Single Top (108343)	0	0	0	0	0	0
MC@NLO Single Top (108344)	0	0	0	0	0	0
MC@NLO Single Top (108345)	0	0	0	0	0	0
MC@NLO Single Top (108346)	45	1	3	57	2	4
QCD (data driven)	162	21	0	227	25	0

Table 8.2.: Overview of selected events in the numerator and denominator for data and all background contributions for the determination of the EF_MU18_MEDIUM_STD trigger scale factors.

of the trigger efficiency scale factors that will be determined. Compared to the plots shown in Figure 7.3, several differences are notable: first of all, in the distribution of the probe η , two dips at $|\eta| \approx 1$ are visible. This is because, contrary to the selection for the measurement of the reconstruction efficiency, the probe is now required to additionally fulfill the reconstruction requirement. Subsequently, it is affected by the lower reconstruction efficiency in the transition between barrel and end-cap. Second of all, the description of u_{\parallel}^l and u_{\perp}^l is enhanced. This is because the samples used for the measurement of the trigger efficiencies are the same as those for the W boson and Z boson mass measurement. Therefore, the description of the hadronic recoil, as well as the derived quantities u_{\parallel}^l and u_{\perp}^l , is improved. The results for the three remaining settings are found in Appendix B.

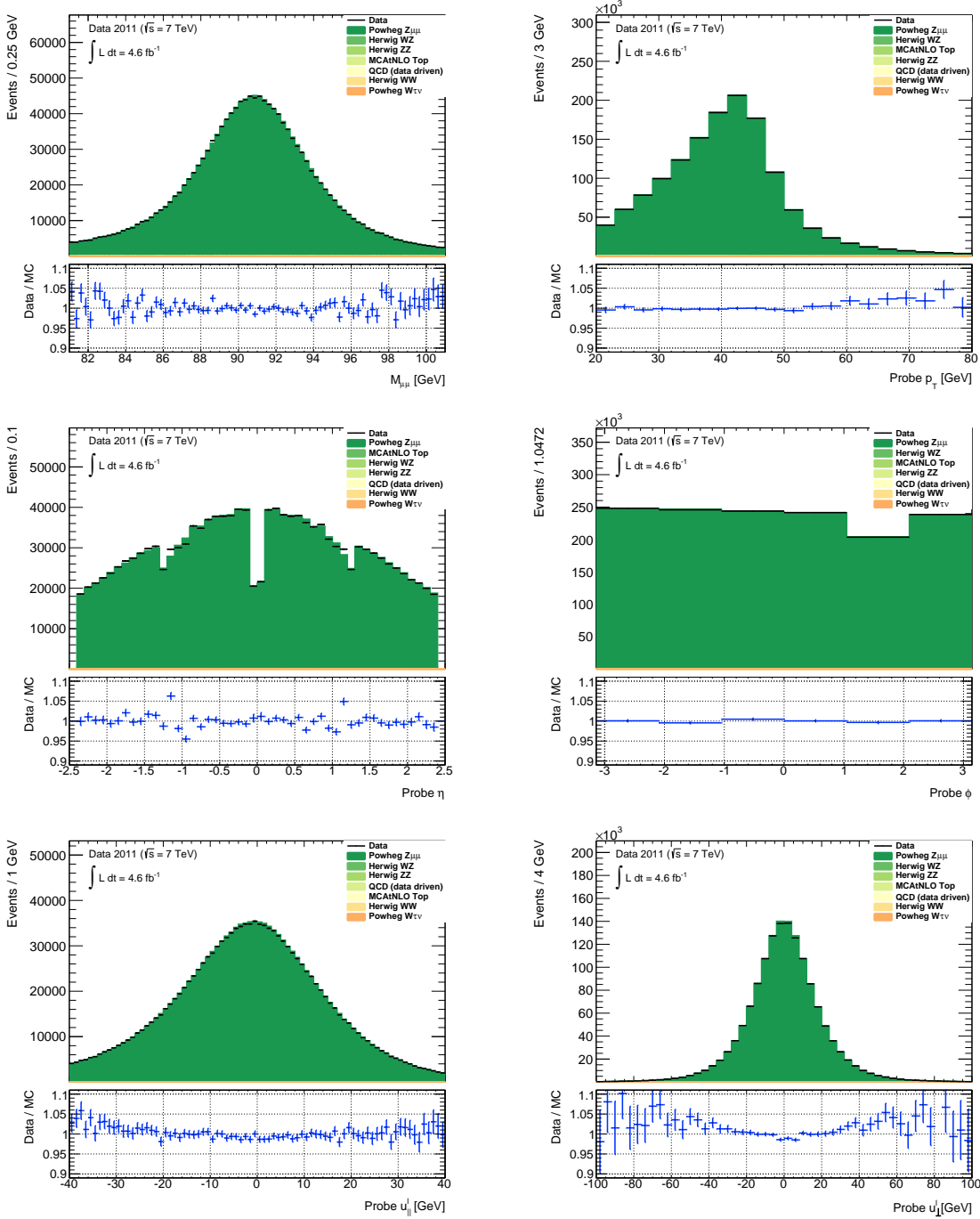


Figure 8.3.: Kinematic distributions of probe-tracks comparing data to the combined signal and background prediction. From left to right, top to bottom: invariant mass of the selected $\mu\mu$ pair, probe p_T , η , φ , $u_{||}^l$ and u_{\perp}^l . The control plots shown are for EF_MU18_MEDIUM_STD.

8.2. Efficiency and Scale factor Determination

The resulting efficiencies for EF_MU18_MEDIUM_STD are shown in Figure 8.4 in one-dimensional projections with a higher granularity. For clarity, instead of presenting the *region*, i.e. the combined η - φ binning, separate results for η and φ are shown in separate histograms. It can be observed that the trigger efficiencies fluctuate much more than the reconstruction efficiencies. With respect to φ , a significant, but well-modeled, inefficiency can be seen in the region of the feet. In η , it may be observed that the transition from barrel to end-cap at $|\eta| \sim 1$, as well as the structures at $|\eta| = 0$, lead to significantly lower trigger efficiencies. These general characteristics can also be observed for the three remaining settings, shown in Appendix B.

As mentioned in the introduction, the division into four trigger periods was necessary because of two reasons: in periods L3 and L4, the trigger efficiencies were significantly influenced by a timing problem in the RPCs; and in periods G6-I, a significant charge dependence was observed in several regions in η . In both cases, the inefficiencies in η have a direct impact on the p_T spectrum. This can be understood by keeping in mind that the muon candidates used here originate from Z boson decays, and are therefore produced with only a small spread in their momentum $|\vec{p}|$, with $|\vec{p}| \sim M_Z/2$. The value of p_T can therefore be understood as a function only of $|\eta|$, with $p_T = |\vec{p}|/\cosh(\eta) \sim M_Z/(2 \cosh(\eta))$. In this way, it becomes clear that the inefficiencies in η affect p_T , as shown in Figure 8.5.

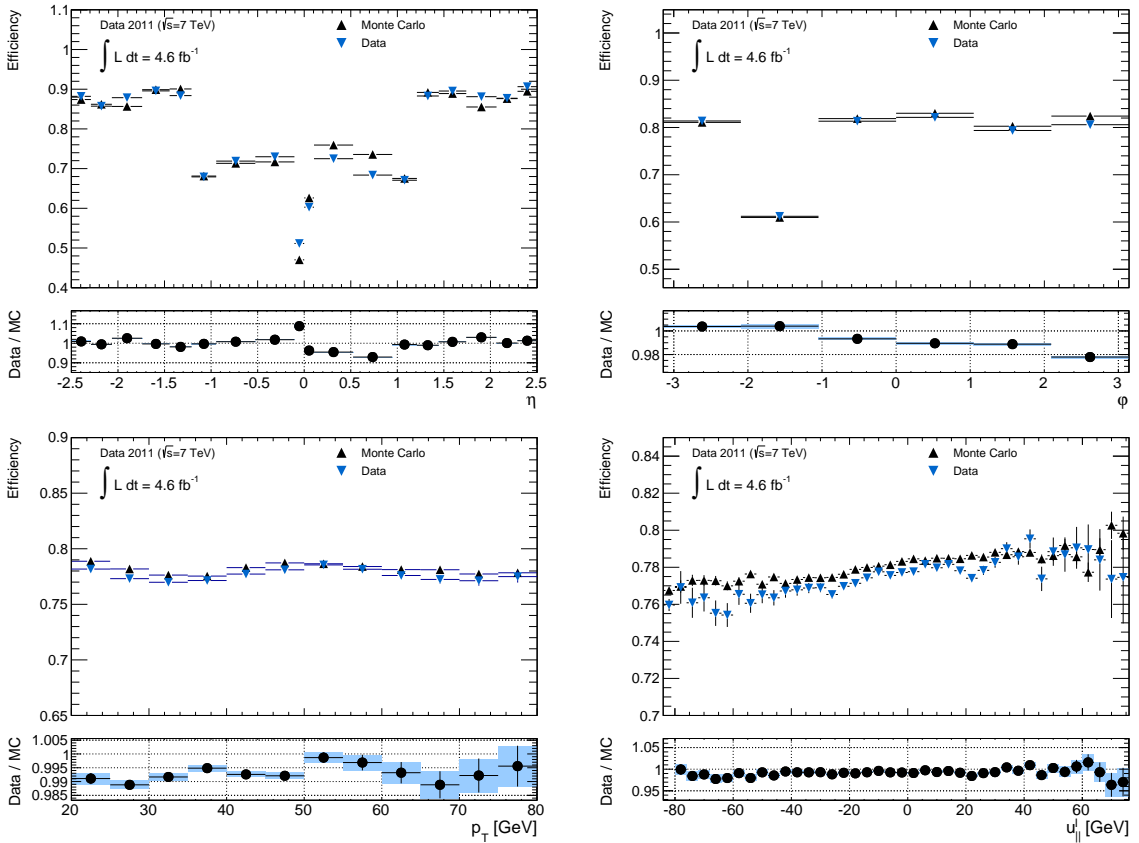


Figure 8.4.: Determined trigger efficiency by the tag and probe method for data and MC. From top to bottom, left to right: η , φ , p_T , $u_{||}^l$. Results are only shown for EF_MU18_MEDIUM_STD. Only statistical uncertainties are shown.

8.2. Efficiency and Scale factor Determination

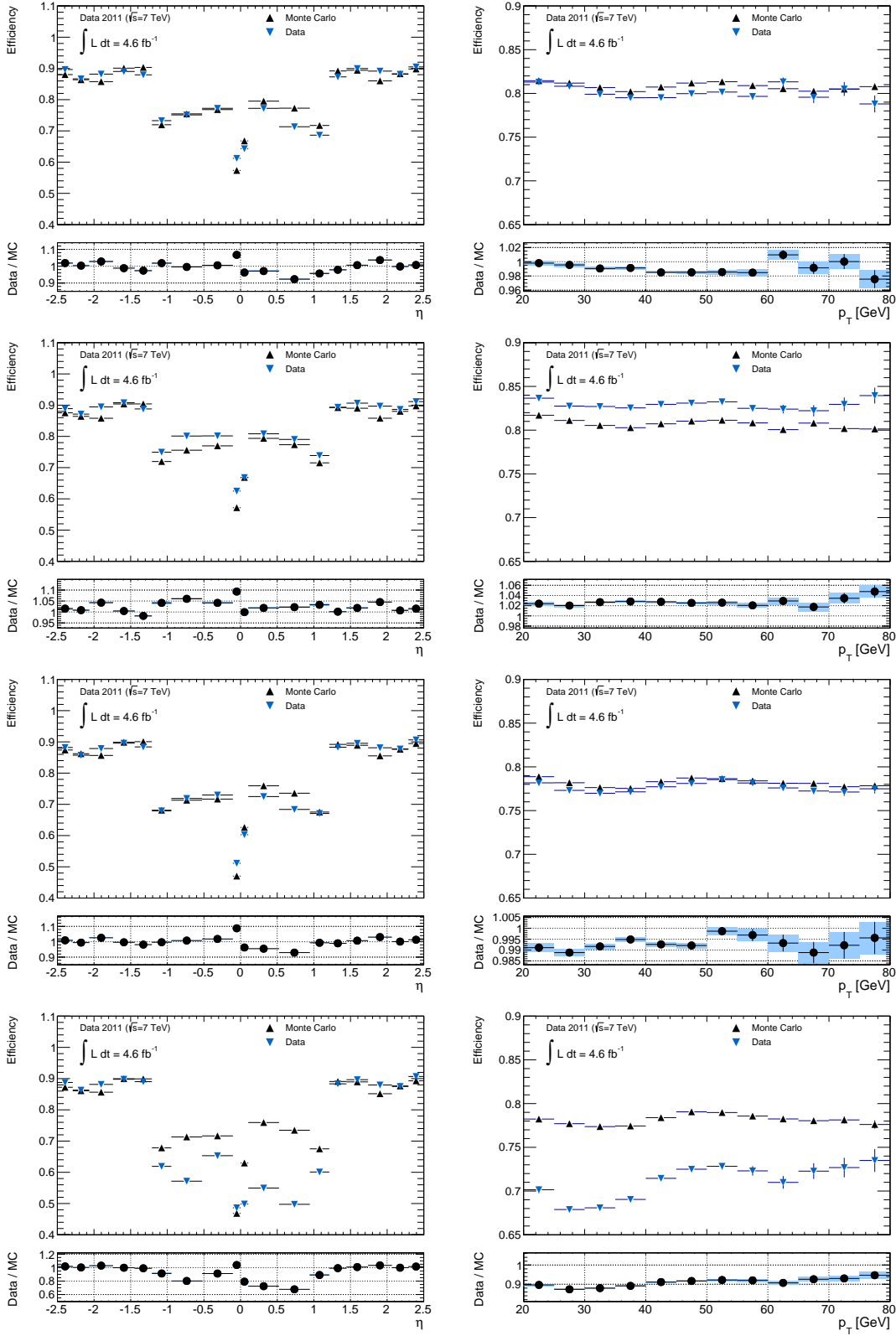


Figure 8.5.: Determined trigger efficiency by the tag and probe method for data and MC. From top to bottom, EF_MU18_BG5, EF_MU18_G6I, EF_MU18_MEDIUM_STD, EF_MU18_MEDIUM_L3L4. In each row, the dependence on η is shown on the left, and on p_T on the right. Only statistical uncertainties are shown.

8. Muon Trigger Efficiency

In order to correct for the differences between data and MC, scale factors are defined as the ratio of the trigger efficiencies in data and MC, $SF := \varepsilon_{Data}/\varepsilon_{MC}$. These scale factors have to be applied on the MC sample, in order to model the muon trigger efficiency correctly. The resulting scale factors are shown in Figures 8.6-8.9. As it could already be assumed from the fluctuations of the data efficiencies and their mis-modeling by Monte Carlo, the resulting scale factors show significant deviations from unity. This has already been observed in ref. [103]. With respect to $u_{||}^l$, the scale factors are quite flat, whereas a trend with respect to p_T is discernible. This slope would influence the measured value of M_W if not corrected. The uncertainties shown are the total uncertainties obtained by combining statistical and systematic uncertainties.

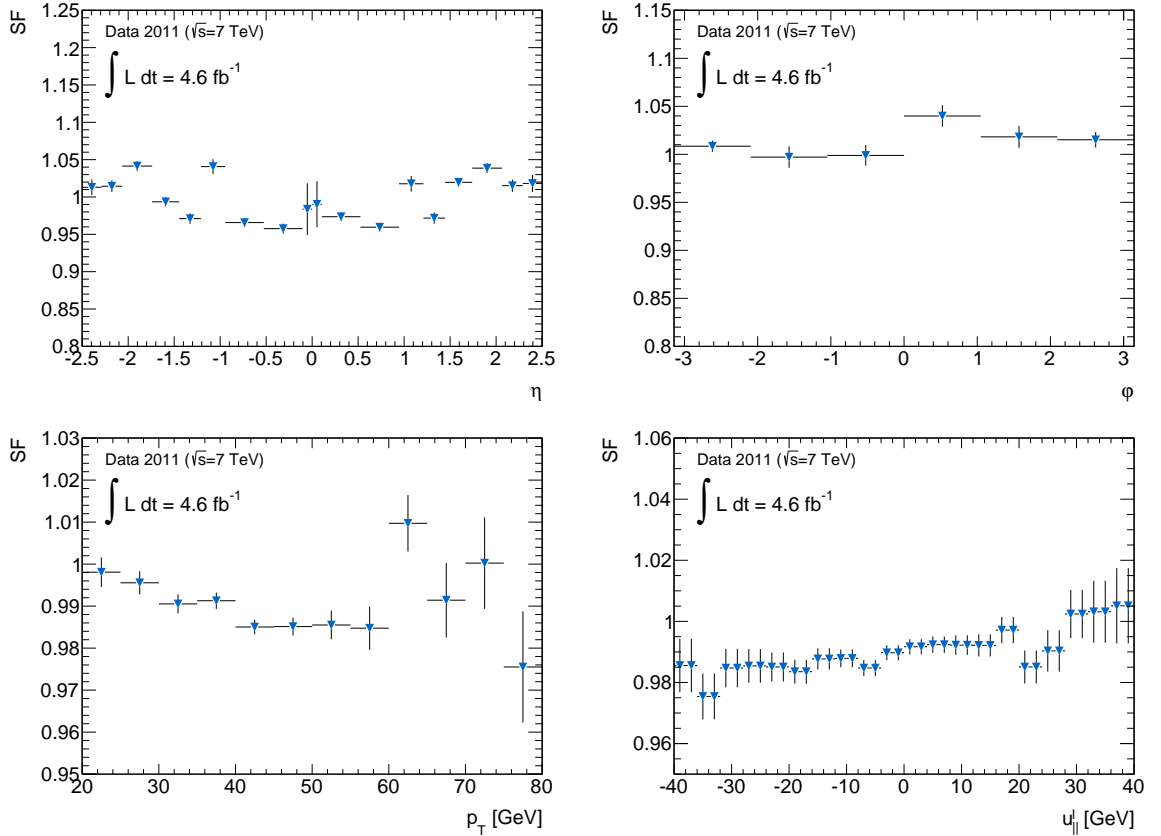


Figure 8.6.: Resulting trigger scale factors for the trigger EF_MU18_BG5. From left to right, top to bottom: η , φ , p_T , $u_{||}^l$. Uncertainties shown are the full systematic and statistical uncertainties.

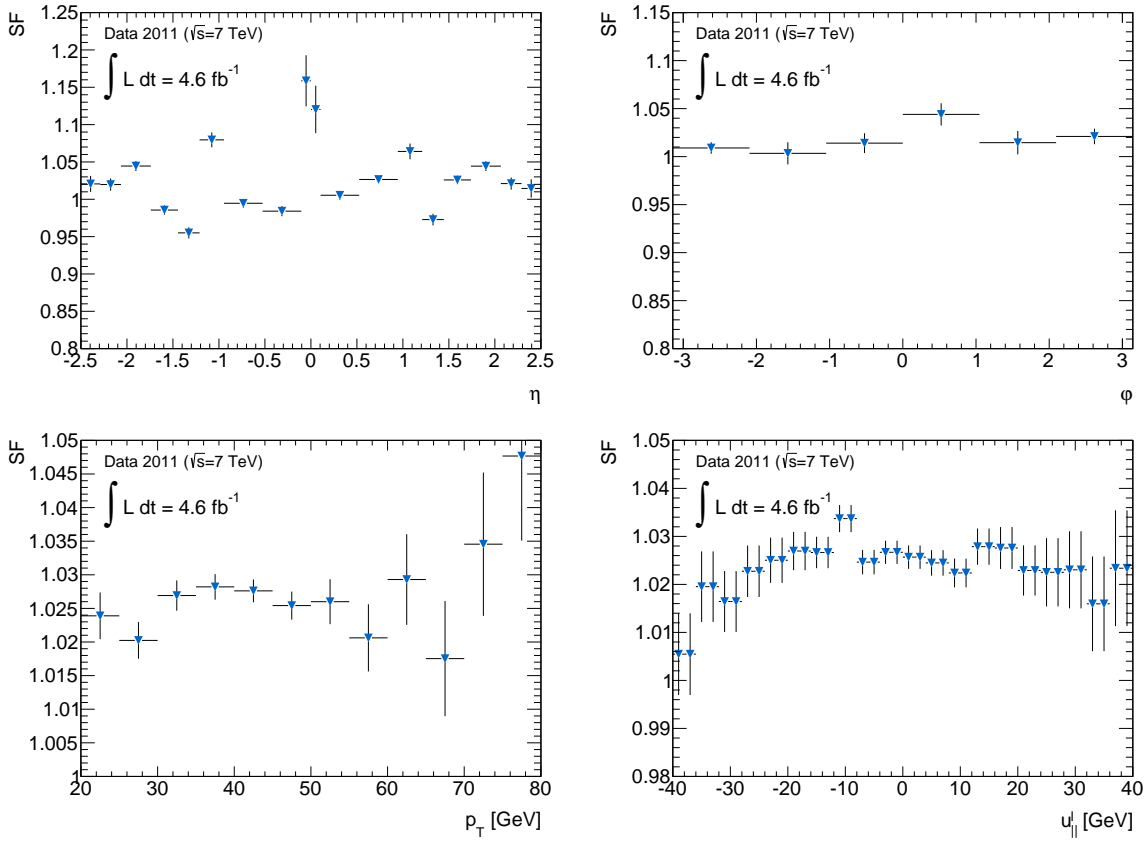


Figure 8.7.: Resulting trigger scale factors for the trigger EF_MU18_G6I. From left to right, top to bottom: η , ϕ , p_T , $u_{||}^l$. Uncertainties shown are the full systematic and statistical uncertainties.

8. Muon Trigger Efficiency

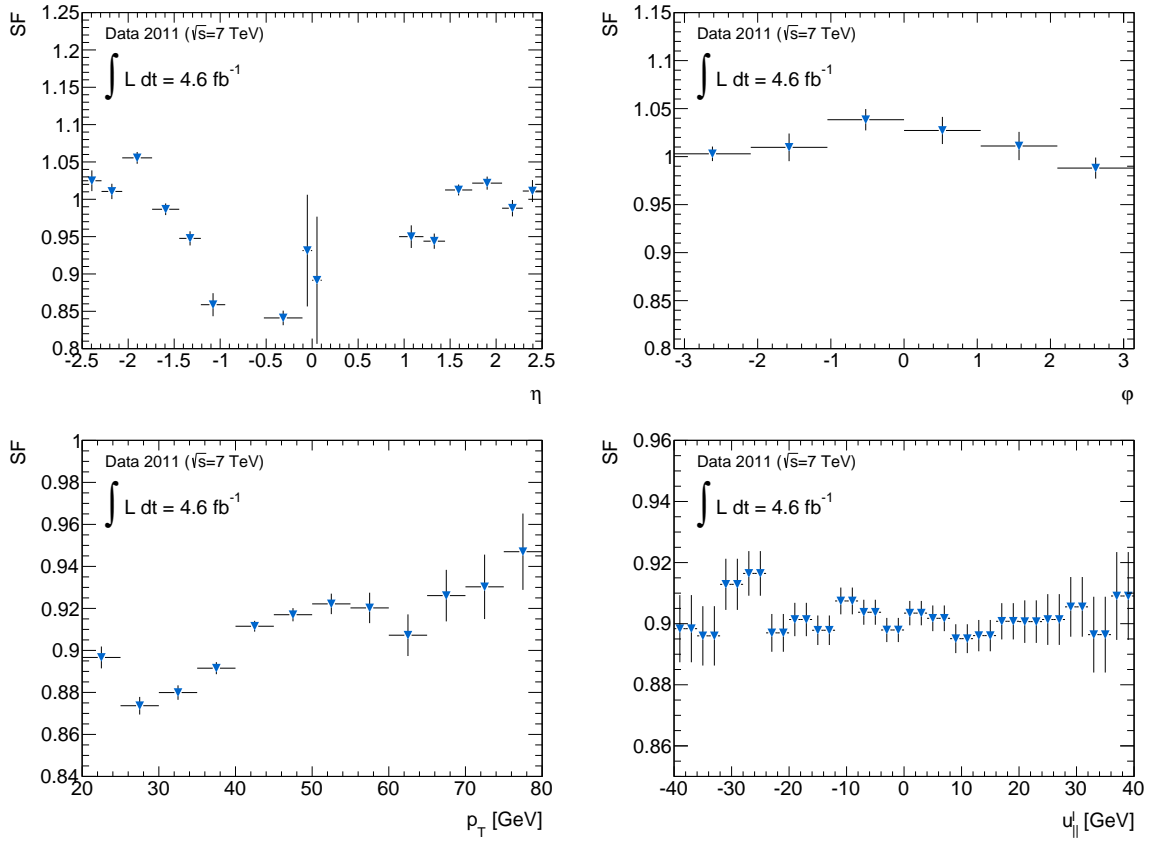


Figure 8.8.: Resulting trigger scale factors for the trigger EF_MU18_MEDIUM_L3L4. From left to right, top to bottom: η , ϕ , p_T , u_{\parallel}^i . Uncertainties shown are the full systematic and statistical uncertainties.

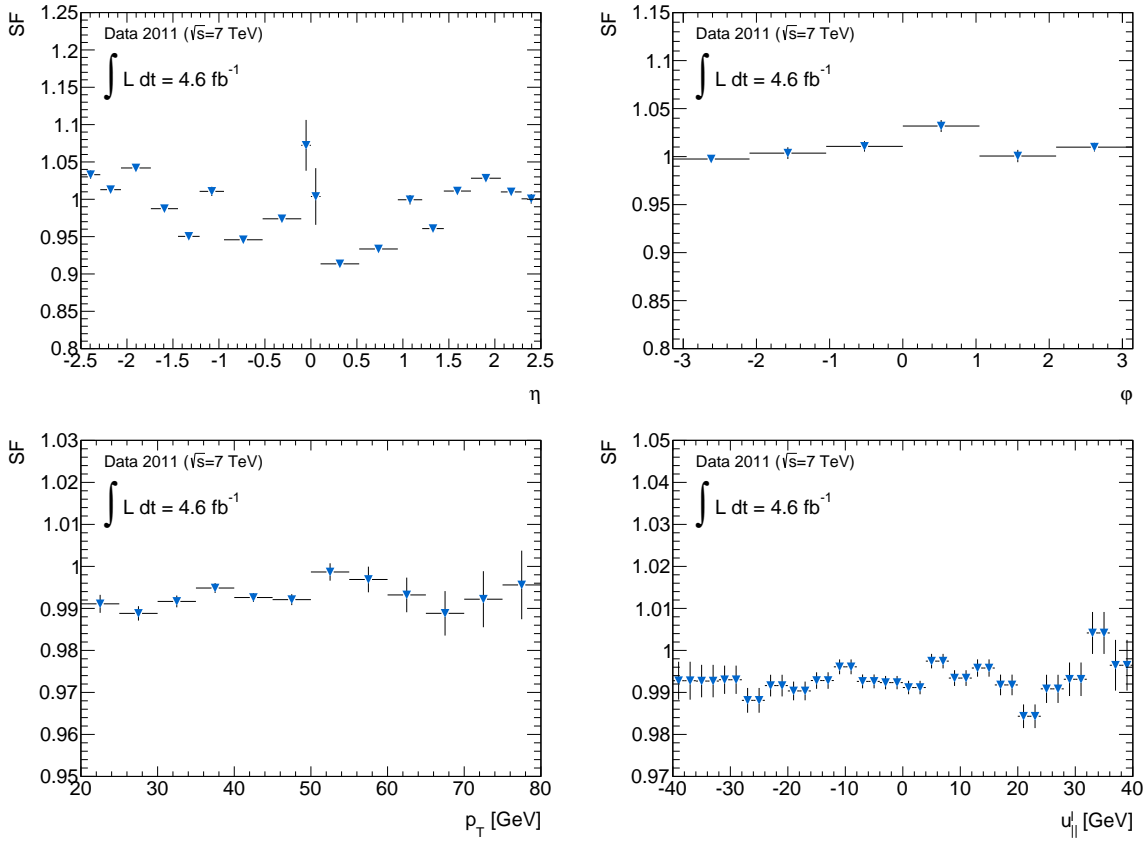


Figure 8.9.: Resulting trigger scale factors for EF_MU18_MEDIUM_STD. From left to right, top to bottom: η , ϕ , p_T , $u_{||}^l$. Uncertainties shown are the full systematic and statistical uncertainties.

8. Muon Trigger Efficiency

The general approach for the treatment and estimation of uncertainties is described in Section 6.3. Figure 8.10 show the different contributions to the uncertainty on the one-dimensional scale factors for EF_MU18_MEDIUM_STD. The statistical uncertainty is dominating in all distributions in these specific plots. The largest systematic uncertainty is due to the scale corrections, which includes the p_T and hadronic recoil correction. This is most probably due to the p_T dependence of the scale factors. Two other major sources of systematic uncertainty are the reconstruction and isolation scale factors. The uncertainties due to imperfect detector simulations are usually very small. Even though most uncertainties can be treated as fully correlated among all bins, a somewhat larger impact on the W-boson mass fit is expected due to the trend in lepton p_T . The results for the three remaining trigger settings are very similar and can be found in Appendix B.

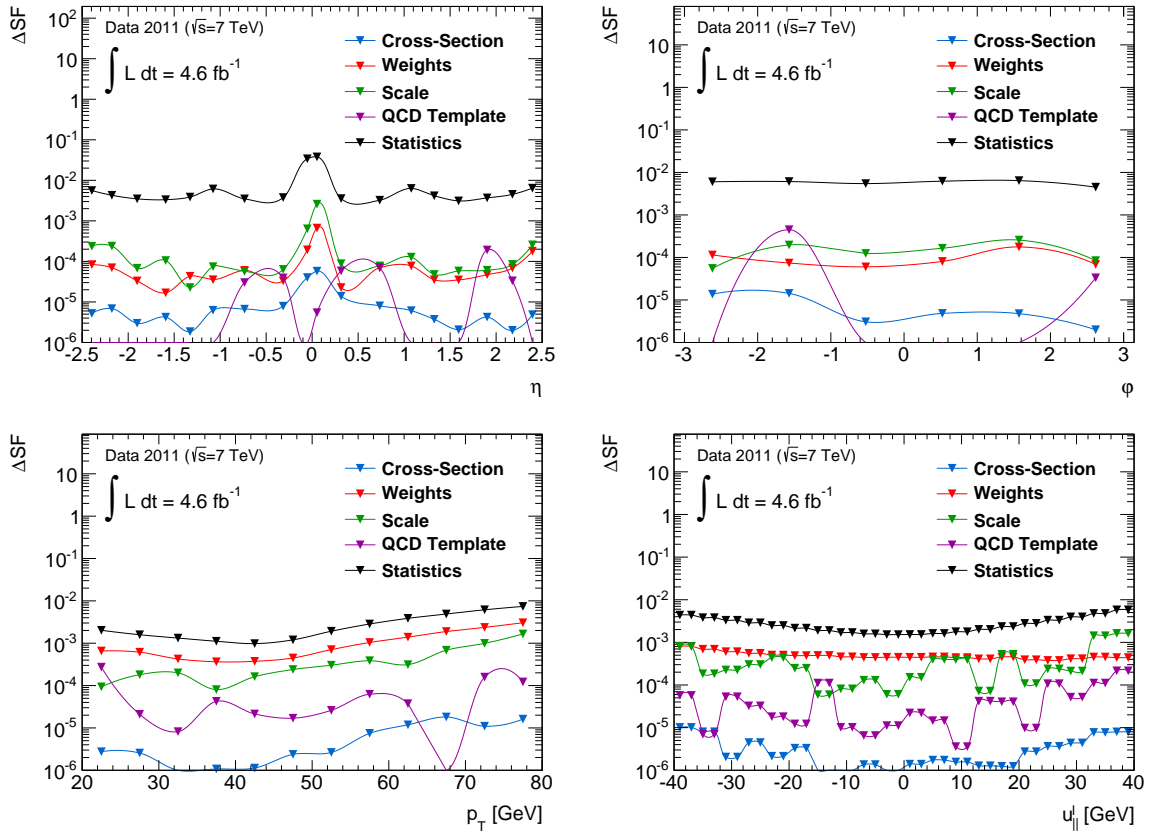


Figure 8.10.: Uncertainties on the obtained trigger scale for the trigger EF_MU18_MEDIUM_STD. From left to right: η , p_T , $u_{||}$. Table 6.5 gives details on the categories shown in the plot.

Similar to the approach in the analysis of the reconstruction scale factors, possible slopes in p_T were investigated by dividing the detector into four regions. These regions are $-2.065 \leq \eta \leq -1.445$, $-0.945 \leq \eta \leq -0.105$, $0.105 \leq \eta \leq 0.945$ and $1.445 \leq \eta \leq 2.065$, thereby excluding the crack regions between the end-caps and the barrel at $\eta \approx 1.05$ and the gap at $\eta = 0$. The resulting scale factors in p_T for these four regions can be seen in Figure 8.11. In this figure, the results from a fit for each of the distributions with a polynomial of the form $p_0 + p_1 \cdot p_T$ in the range of 25 to 60 GeV are also shown. In this fit, only the statistical uncertainty on the scale factors was taken into account, because it is the dominating source of uncertainty. In Table 8.3 the significance $p_1/\Delta p_1$ is shown. A full overview of all fitted values for all 18 bins is shown in Figure 8.12. As can be seen, several regions exhibit significant dependencies on p_T . This indicates the importance of the trigger scale factors for the measurement of the mass of the W boson, but it also indicates that the uncertainty on these scale factors will play an important role in the precision achievable in the final measurement. It has to be noted, that except for some bins in EF_MU18_G6I and EF_MU18_MEDIUM_STD a good description of the scale factors by the polynomial function could be achieved.

Trigger	η	χ^2/dof	p_1 [GeV $^{-1}$]	Δp_1 [GeV $^{-1}$]	$p_1/\Delta p_1$
EF_MU18_BG5	-2.065..-1.445	3.9/5	$-5.26 \cdot 10^{-4}$	$2.47 \cdot 10^{-4}$	-2.13
	-0.945..-0.105	3.1/5	$-4.38 \cdot 10^{-4}$	$2.79 \cdot 10^{-4}$	-1.57
	0.105..0.945	5.1/5	$-1.77 \cdot 10^{-3}$	$2.73 \cdot 10^{-4}$	-6.48
	1.445..2.065	4.8/5	$1.66 \cdot 10^{-4}$	$2.42 \cdot 10^{-4}$	0.68
EF_MU18_G6I	-2.065..-1.445	7.6/5	$1.75 \cdot 10^{-5}$	$2.477 \cdot 10^{-4}$	0.71
	-0.945..-0.105	5.8/5	$-2.20 \cdot 10^{-5}$	$2.74 \cdot 10^{-4}$	-0.80
	0.105..0.945	2.6/5	$9.65 \cdot 10^{-5}$	$2.63 \cdot 10^{-4}$	0.37
	1.445..2.065	16.1/5	$4.77 \cdot 10^{-4}$	$2.47 \cdot 10^{-4}$	1.93
EF_MU18_MEDIUM_L3L4	-2.065..-1.445	7.2/5	$-1.01 \cdot 10^{-4}$	$3.13 \cdot 10^{-4}$	-0.32
	-0.945..-0.105	7.3/5	$-3.10 \cdot 10^{-4}$	$4.20 \cdot 10^{-4}$	-0.74
	0.105..0.945	1.5/5	$3.69 \cdot 10^{-4}$	$4.06 \cdot 10^{-4}$	0.91
	1.445..2.065	6.5/5	$5.86 \cdot 10^{-4}$	$3.23 \cdot 10^{-4}$	1.81
EF_MU18_MEDIUM_STD	-2.065..-1.445	7.3/5	$1.66 \cdot 10^{-4}$	$1.33 \cdot 10^{-4}$	1.24
	-0.945..-0.105	4.2/5	$-3.60 \cdot 10^{-4}$	$1.69 \cdot 10^{-4}$	-2.13
	0.105..0.945	12.9/5	$-1.04 \cdot 10^{-4}$	$1.62 \cdot 10^{-4}$	-0.64
	1.445..2.065	4.2/5	$4.68 \cdot 10^{-4}$	$1.34 \cdot 10^{-4}$	3.49

Table 8.3.: Values obtained in the fit to the trigger scale factors shown in Figure 8.11.

8. Muon Trigger Efficiency

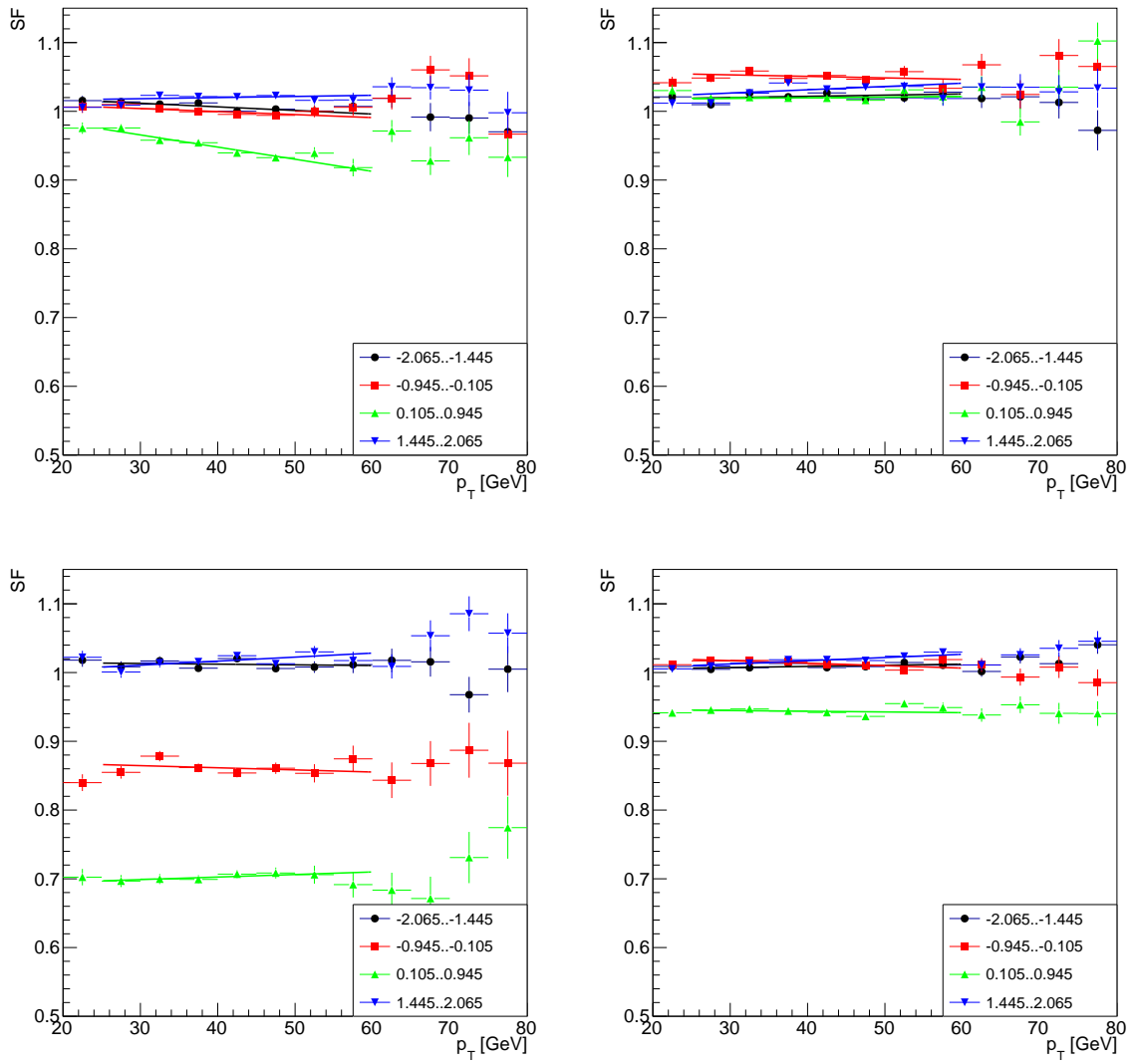


Figure 8.11.: Trigger scale factors in four regions of the detector. As can be seen, several regions exhibit significant dependencies on p_T . From left to right, top to bottom: EF_MU18_BG5, EF_MU18_G6I, EF_MU18_MEDIUM_L3L4, EF_MU18_MEDIUM_STD. Resulting fit values are shown in Table 8.3.

8.2. Efficiency and Scale factor Determination

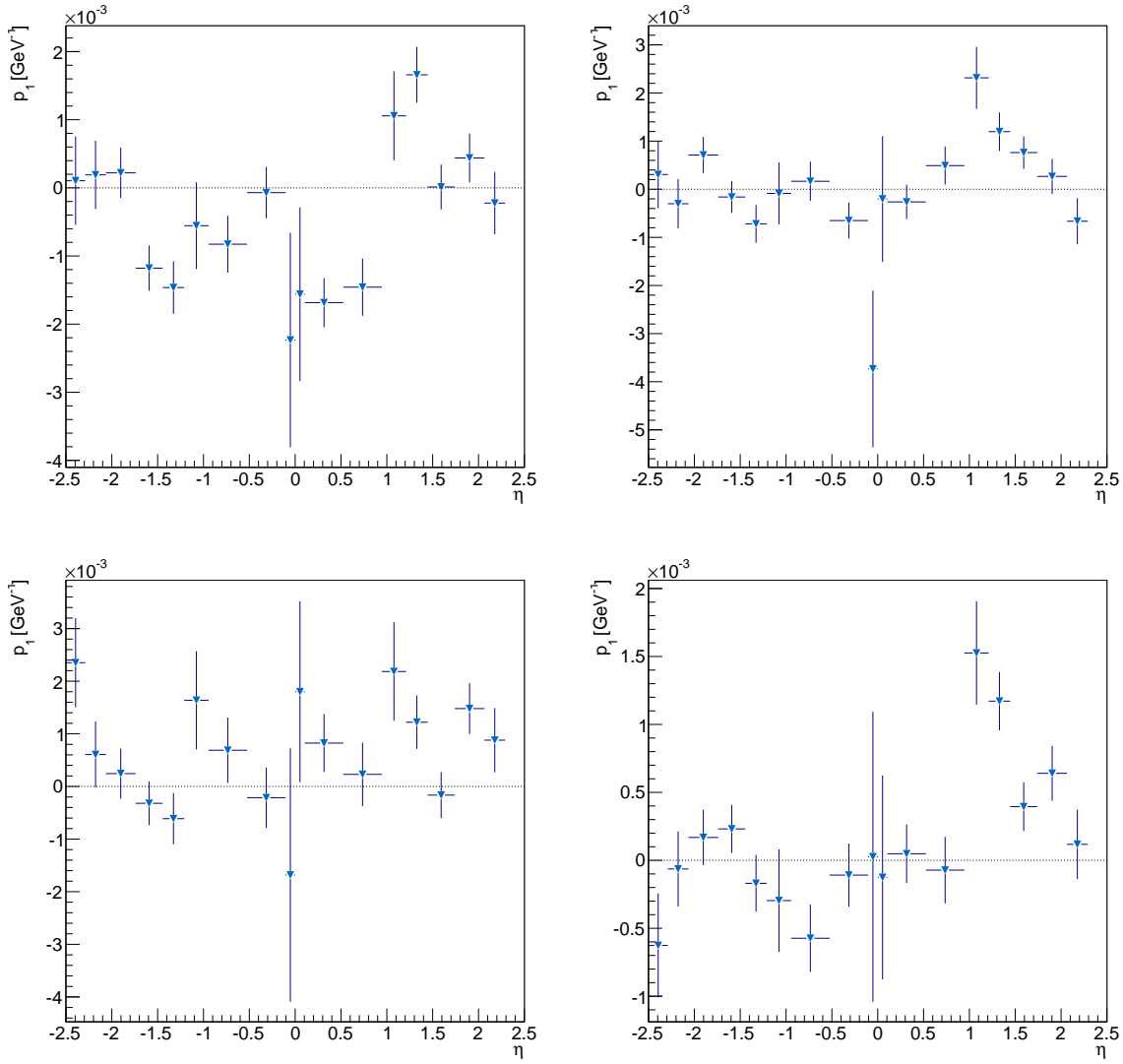


Figure 8.12.: Value of p_1 for each of the 18 η bins. From left to right, top to bottom: EF_MU18_BG5, EF_MU18_G6I, EF_MU18_MEDIUM_L3L4, EF_MU18_MEDIUM_STD.

8. Muon Trigger Efficiency

Apart from the inclusive scale factors, scale factors were also obtained as a function of the charge of the probe. Figures 8.13 - 8.16 show the results for the triggers under investigation. While the scale factors for positive and negative charge show a reasonable agreement in general, notable features can be discerned: the χ^2 tests of these histograms are often quite large, hinting at differences. A visible discrepancy can be seen in the region $0 \leq \eta \leq 1$ for the trigger EF_MU18_BG5, where the scale factors for negative probes are significantly higher than for positive probes. This was already observed in [91] and is one of the reason for the chosen binning in the run number.

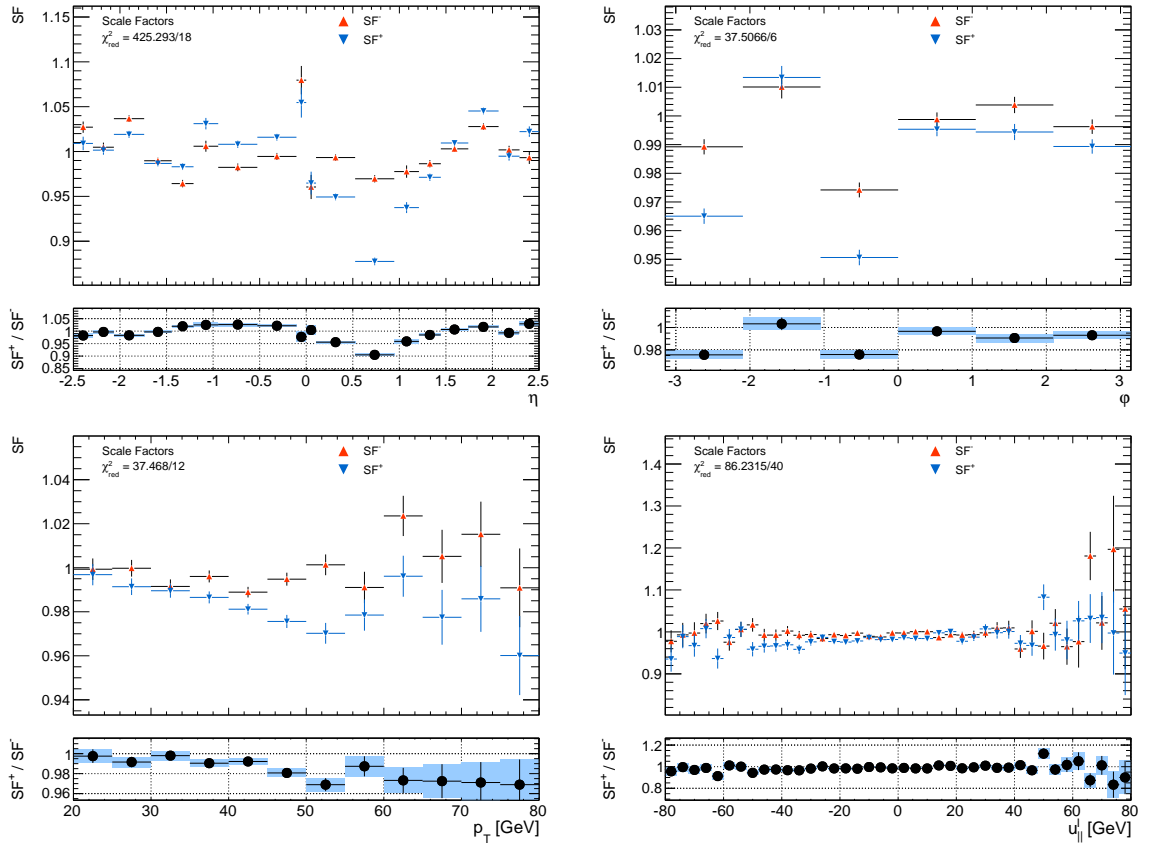


Figure 8.13.: Comparison of trigger scale factors obtained for negative and positive probes for the trigger EF_MU18_BG5. From left to right: η , p_T , u_{\perp}^l . The uncertainties shown are only statistical.

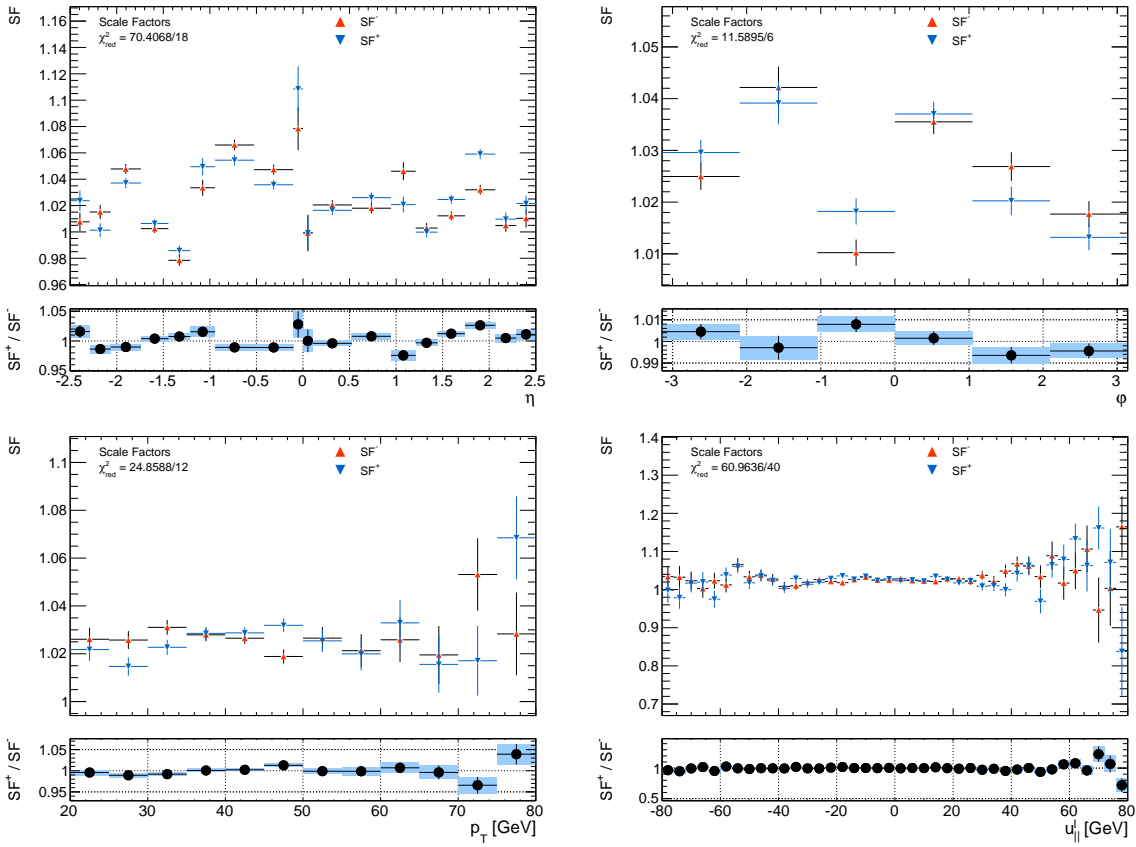


Figure 8.14.: Comparison of trigger scale factors obtained for negative and positive probes for the trigger EF_MU18_G6I. From left to right: η , p_T , u_T . The uncertainties shown are only statistical.

8. Muon Trigger Efficiency

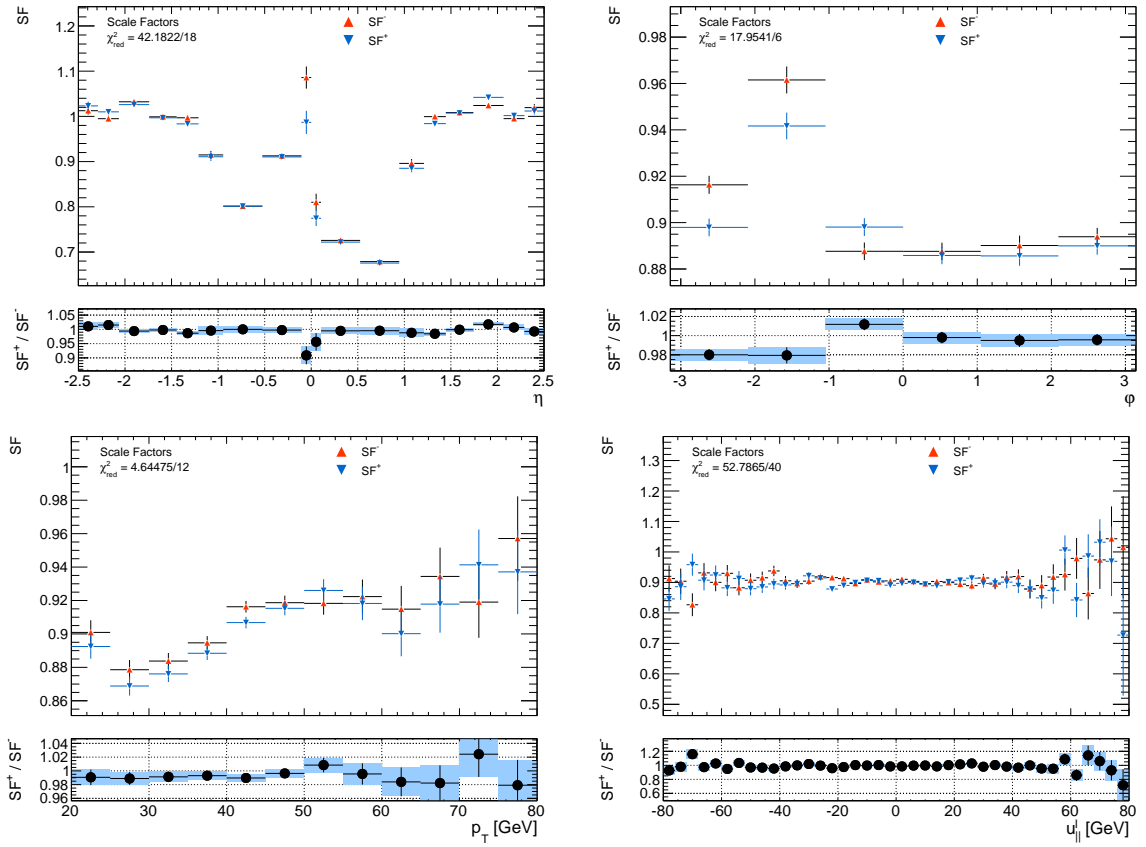


Figure 8.15.: Comparison of trigger scale factors obtained for negative and positive probes for the trigger EF_MU18_MEDIUM_L3L4. From left to right: η , p_T , $u_{||}^l$. The uncertainties shown are only statistical.

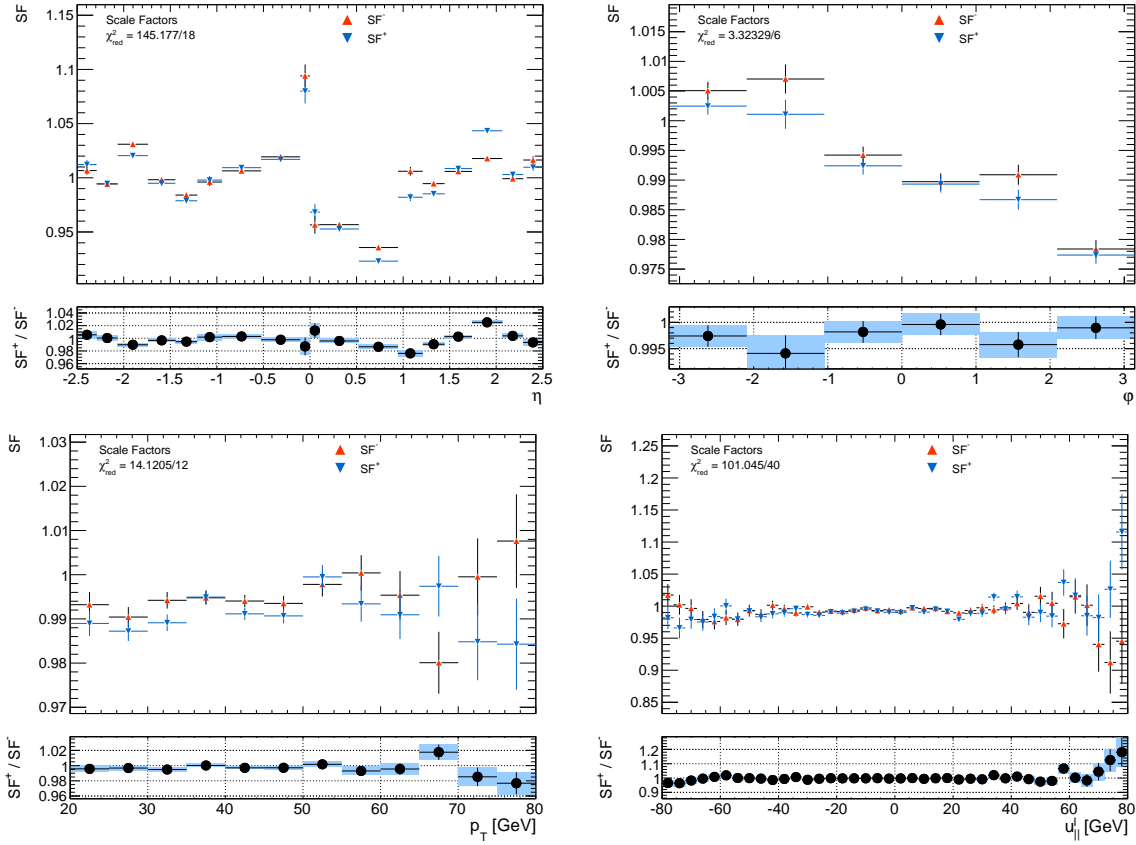


Figure 8.16.: Comparison of trigger scale factors obtained for negative and positive probes for the trigger EF_MU18_MEDIUM_STD. From left to right: η , p_T , u_{\perp}^l . The uncertainties shown are only statistical.

8.3. Comparison with Previous Results

In order to check for consistency with earlier measurements, the results were compared with the scale factors obtained in a previous analysis (cf. ref. [91]). A detailed description of the tag and probe method used to obtain these scale factors can be found in ref. [103]. Scans were performed in the variable η . In the previous scale factors, no dependence on lepton p_T or $u_{||}^l$ was modeled, leading to the scale factors shown in Figure 8.17. A shift with respect to previous values is notable. As was the case concerning the muon reconstruction scale factors, the reason for this shift might also lie in changes of the underlying simulation between MC11C and MC11D.

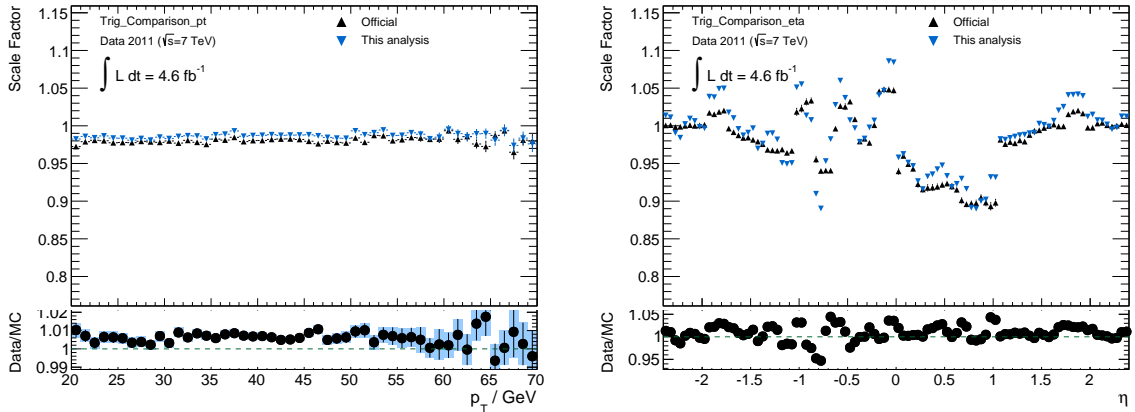


Figure 8.17.: Comparison of the trigger scale factors obtained with the official ATLAS package and from this analysis in dependence of η and p_T . The official scale factors were not supplied as function of lepton p_T or u^l .

9. Muon Isolation Efficiency

9.1. Methodology, Event Selection and Corrections

Decay muons of vector bosons mostly appear isolated in the detector, i.e. without further activity in the calorimeter or the inner tracker within a narrow (η, φ) cone around the signal lepton. This is different from muons which stem from purely QCD related interactions, where the resulting jets contain b - or c -hadrons, whose subsequent decay leads to muons. Muons from the latter processes usually appear in a very active environment, i.e. are accompanied by a larger number of other particles that leave energy or track signatures around the reconstructed muons. Hence, several observables that quantify the isolation of a muon have been introduced to suppress jet-induced backgrounds.

The most common one is defined as:

$$p_T^{\text{cone20}} = \sum_{i \in (\text{tracks in cone with } 0.2)} p_T^{i, \text{track}} \quad (9.1)$$

This isolation variable is the scalar p_T sum of all inner detector tracks around the signal lepton within a cone-radius of 0.2 (where the muon itself is not taken into account). This quantity is usually normalized to the transverse momentum of the muon and required to fulfill

$$p_T^{\text{cone20}}/p_T < 0.1$$

for vector boson decay muons in order to suppress large fractions of the jet-induced background. In this case, the isolation cut efficiency is defined as the fraction of signal events which pass this cut. Since the underlying event and the hadronisation modeling in the signal MC plays a major role in the expected p_T^{cone20} behavior, this efficiency has to be determined in a data-driven way.

As already discussed in Chapter 6, the currently available scale factors are not evaluated as functions of the crucial observables for the W boson mass measurement. Hence, a reevaluation has to be performed. The predicted MC isolation-cut efficiency for MC signal muons vs. p_T and η for $W \rightarrow \mu\nu$ and $Z \rightarrow \mu\mu$ events is shown in Figure 9.1. The isolation efficiencies are very similar for both samples, which confirms the assumption that the determined reconstruction efficiencies in Z -boson data can also be applied to the W boson samples.

9. Muon Isolation Efficiency

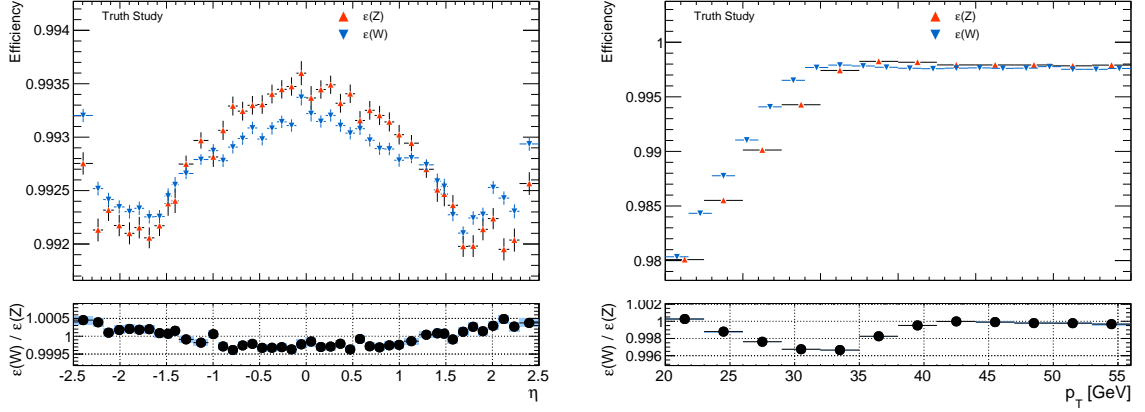


Figure 9.1.: Isolation efficiency of muons in $W \rightarrow \mu\nu$ and $Z \rightarrow \mu\mu$ MC samples vs. η (left) and p_T (right). The uncertainties shown are purely statistical.

The basic approach is similar to the determination of the reconstruction and trigger scale factors, described in the previous sections, and is based on a tag and probe method. The tag object in this case is an isolated combined muon, the probe object is a combined muon without any further isolation requirements, but which leads to an invariant mass close to the Z boson when combined with the tag. The background was estimated as discussed in Section 6.2. An overview of the selected inclusive number of events in the numerator and denominator, including the background estimations, is given in Table 9.1.

Sample	Numerator			Denominator		
	N	Δ_{stat}	Δ_{syst}	N	Δ_{stat}	Δ_{syst}
Data	1 936 606	1 391	0	1 949 633	1 396	0
POWHEG $Z\mu\mu$ (147407)	1 933 951	528	96 697	1 944 284	530	97 214
MC@NLO $t\bar{t}$ (105200)	958	6	59	1 149	6	71
HERWIG WW (105985)	220	2	15	225	2	15
HERWIG ZZ (105986)	953	4	66	966	4	67
HERWIG WZ (105987)	1 324	5	92	1 339	5	93
Pythia $Z\tau\tau$ (106052)	146	24	7	151	25	7
Single Top (108340)	0	0	0	0	0	0
Single Top (108341)	3	0	0	29	2	3
Single Top (108342)	0	0	0	0	0	0
Single Top (108343)	0	0	0	0	0	0
Single Top (108344)	0	0	0	1	0	0
Single Top (108345)	0	0	0	0	0	0
Single Top (108346)	80	2	5	93	2	6
QCD (data driven)	204	20	59	1 390	52	404

Table 9.1.: Overview of selected events in the numerator and denominator for data and all background contributions.

Since the background contribution to this process is low, the isolation efficiency of combined muon tracks can be precisely determined. The selection criteria for the tag and probe object selection is summarized in the following.

Tag and probe pairs were selected according to the following selection criteria:

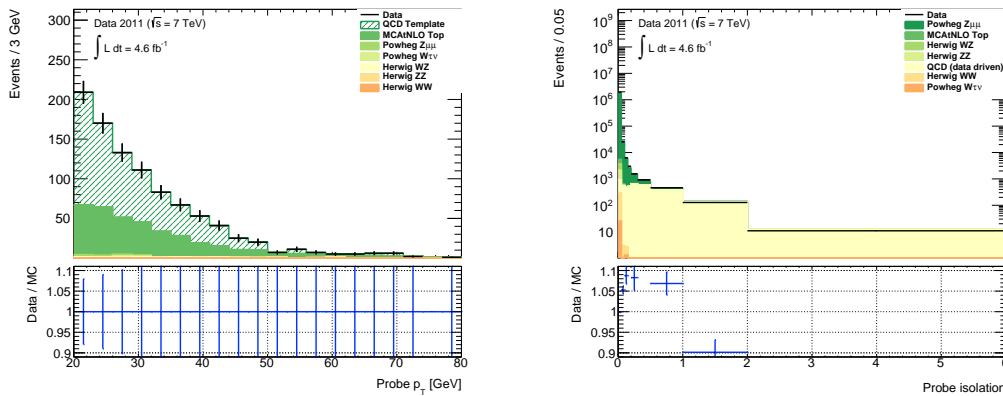
- Event cuts
 - Trigger: EF_MU18 up to period J, EF_MU18_MEDIUM from period J inclusive
 - At least 3 tracks from primary vertex
- Muon tag selection:
 - Quality cuts summarized in Table 6.3
 - Combined (CB) muon
 - $|\eta| \leq 2.4$
 - $p_{T,ID} \geq 20 \text{ GeV}$
 - Isolated with probed isolation definition
 - $|z_{0,PV}| < 10 \text{ mm}$
- Muon probe selection:
 - Quality cuts summarized in Table 6.3
 - Combined (CB) muon
 - $|\eta| \leq 2.4$
 - $p_{T,ID} \geq 20 \text{ GeV}$
 - $|z_{0,PV}| < 10 \text{ mm}$
- Pair selection:
 - Opposite charge
 - $|M_{\mu\mu} - M_Z^{\text{PDG}}| \leq 10 \text{ GeV}$
 - Exactly one pair per event

The muon isolation efficiency is determined in three dimensions as described in Table 6.1. On average, several thousand probe-tracks per bin are found for the full 2011 data-set.

The background determination was already described in Section 6.2. As discussed, two methods for the estimation of the QCD background were used: the ABCD method and a fit in the isolation distribution of a control selection with skipped isolation requirement on the tag. A same-sign selection — corresponding to selection B in the ABCD method — was used to obtain QCD templates for all histograms. An example is shown in Figure 9.2(b) for the distribution of the transverse momentum of the tag candidates. Here, the discrepancy between Monte Carlo and data corresponds to the background template obtained for this variable. Figure 9.2(a) shows the result of the fit approach. A good description of data by the combined Monte Carlo and QCD template can be observed.

The same technical procedure as described in Section 7.1 is used. In Figure 9.3, several kinematic distributions for the selected muon pairs are shown. Compared to the corresponding plots for the muon reconstruction efficiencies (Figure 8.3), the distribution of probe η and φ

9. Muon Isolation Efficiency



(a) Shape of the QCD template in probe p_T . (b) Result of the fit approach in the probe isolation.

Figure 9.2.: Control plots from the QCD background estimation. Figure (a) shows the shape of the QCD template in the same-signed selection. Figure (b) shows the result of the fit performed in the isolation distribution of the tag.

now show a multitude of additional structures. In both cases, these structures originate from inefficiencies in the trigger matching localized in the η - φ space and showing their effect on the control distributions. This is very pronounced in the case of probe φ : As was described earlier, muon candidates in the feet region of the muon system ($-2 \text{ rad} < \varphi < -1 \text{ rad}$) have a significantly reduced probability to pass the tag requirement, visible as a decrease in the number of probes between $\varphi = 1 \text{ rad}$ and 2 rad due to the back-to-back configuration of tag and probe. In addition, in the measurement of the isolation efficiency the probe candidates are now also affected directly, leading to two dips located at the position of the feet region and opposite to it.

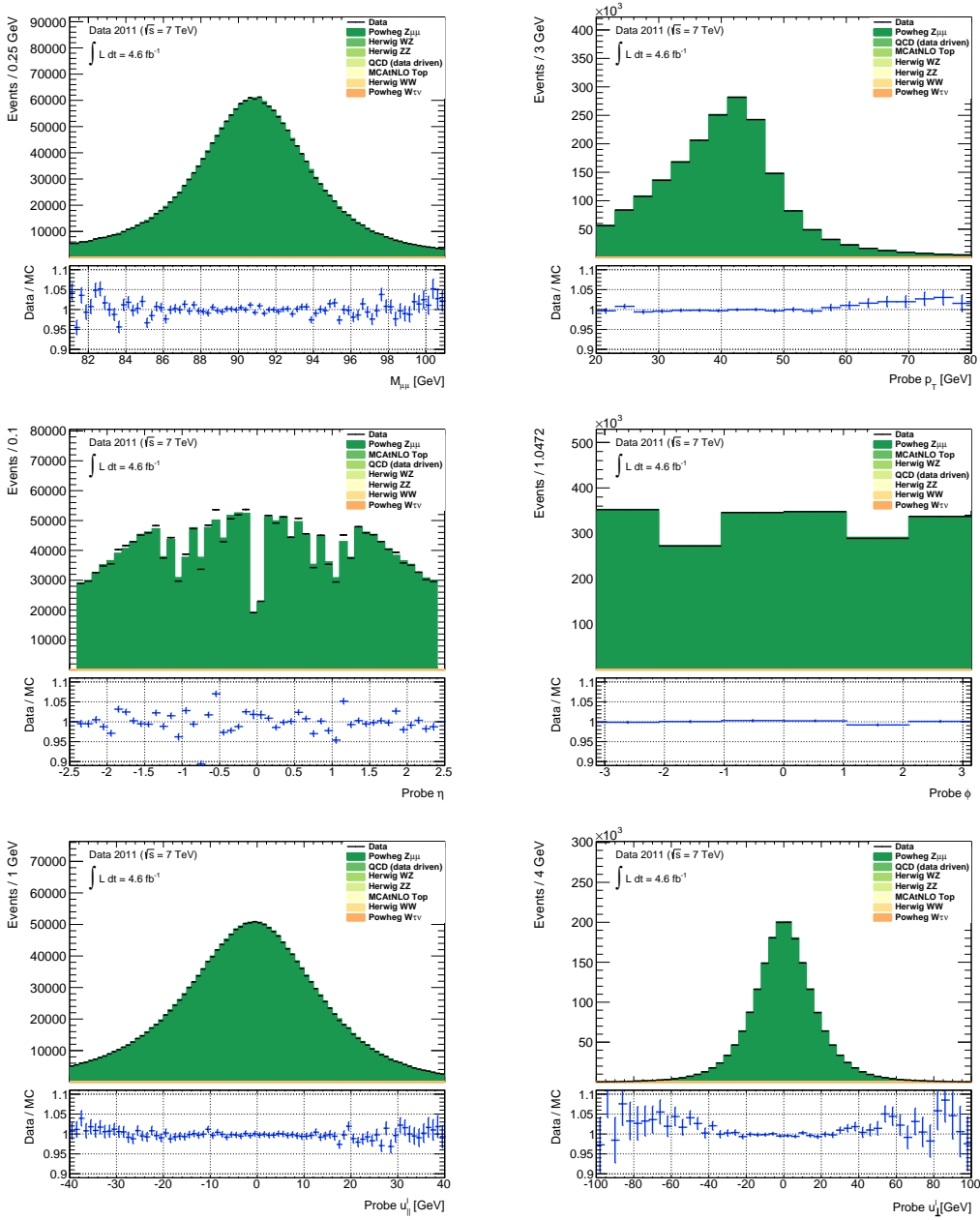


Figure 9.3.: Kinematic distributions of probe-tracks comparing data to the combined signal and background prediction. From left to right, top to bottom: Invariant mass of the selected $\mu\mu$ pair, probe p_T , η , ϕ , u_{\parallel}^l and u_{\perp}^l .

9.2. Efficiency and Scale Factor Determination

The resulting isolation-cut efficiencies are shown in Figure 9.4 in one-dimensional projections with a higher granularity. For clarity, instead of presenting the *region*, i.e. the combined η - φ binning, separate results for η and φ are shown in different histograms. Especially when compared to the corresponding results in the study of the trigger and reconstruction efficiencies, the agreement between data and Monte Carlo is excellent. The drop with respect to high values of u_{\parallel}^l is expected since high values of u_{\parallel}^l correspond to the hadronic recoil being closer to the probe muon. The additional activity in the vicinity of the probe decreases its isolation efficiency — an effect well modeled by Monte Carlo. In a similar fashion, the turn-on with respect to the transverse momentum of the probe can be explained: the activity surrounding the muon originates partly from the muon itself, i.e. through bremsstrahlung, and can be expected to rise with the transverse momentum of the muon. However, part of the activity is fully independent of the transverse momentum of the muon and forms a baseline. This baseline is sufficient to make the chosen isolation requirement fail at adequately low levels of muon p_T , leading to a decrease in efficiency. Ideally, the isolation requirement would be linear in p_T for high-energetic muons, and absolute for low-energetic muons.

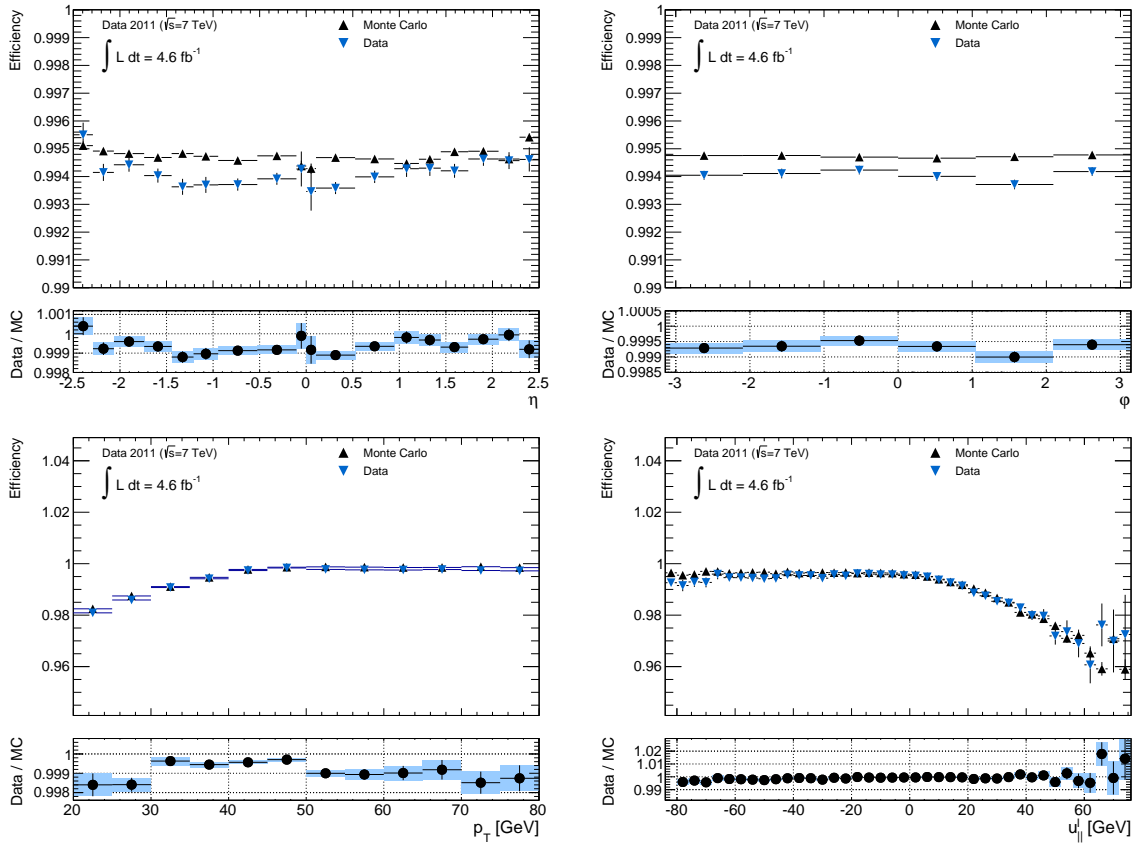


Figure 9.4.: Isolation efficiencies for $p_T^{\text{cone}20}/p_T < 0.1$. From left to right, top to bottom: η , φ , p_T , u_{\parallel}^l .

Figure 9.5 shows the resulting efficiencies for each of the four η regions used in the measurement of the W boson mass.

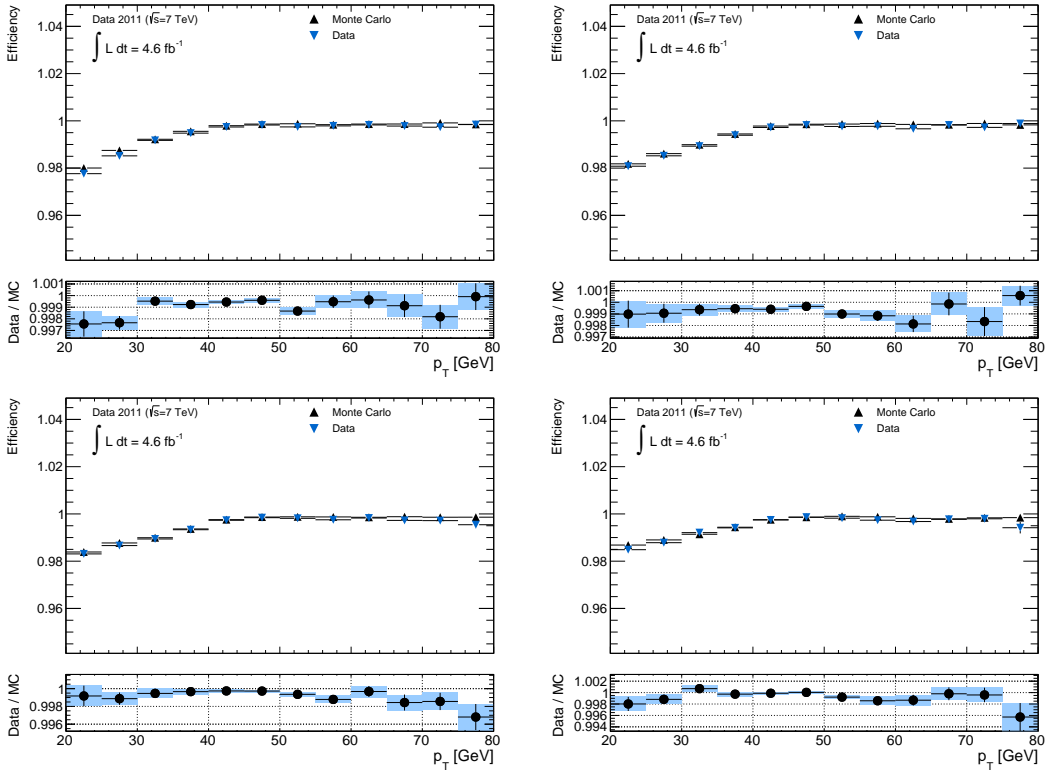


Figure 9.5.: Determined isolation efficiency using the tag and probe method for Data and MC as a function of p_T . From left to right, top to bottom: Region 1 ($0 < |\eta| \leq 0.8$), Region 2 ($0.8 < |\eta| \leq 1.4$), Region 3 ($1.4 < |\eta| \leq 2.0$) and Region 4 ($2.0 < |\eta| \leq 2.4$). Only statistical uncertainties are shown.

9. Muon Isolation Efficiency

Analogous to the reconstruction and trigger efficiencies, isolation scale factors are defined as the ratio of the isolation efficiency in data and MC, $SF := \varepsilon_{Data}/\varepsilon_{MC}$. These scale factors have to be applied on the MC sample, in order to model the muon isolation efficiency correctly. The resulting scale factors are shown in Figure 9.6. As could be expected from the efficiency plots shown above, the resulting scale factors are very flat and close to unity. The remaining drops and rises are well covered by the uncertainties shown, which are the full uncertainties.

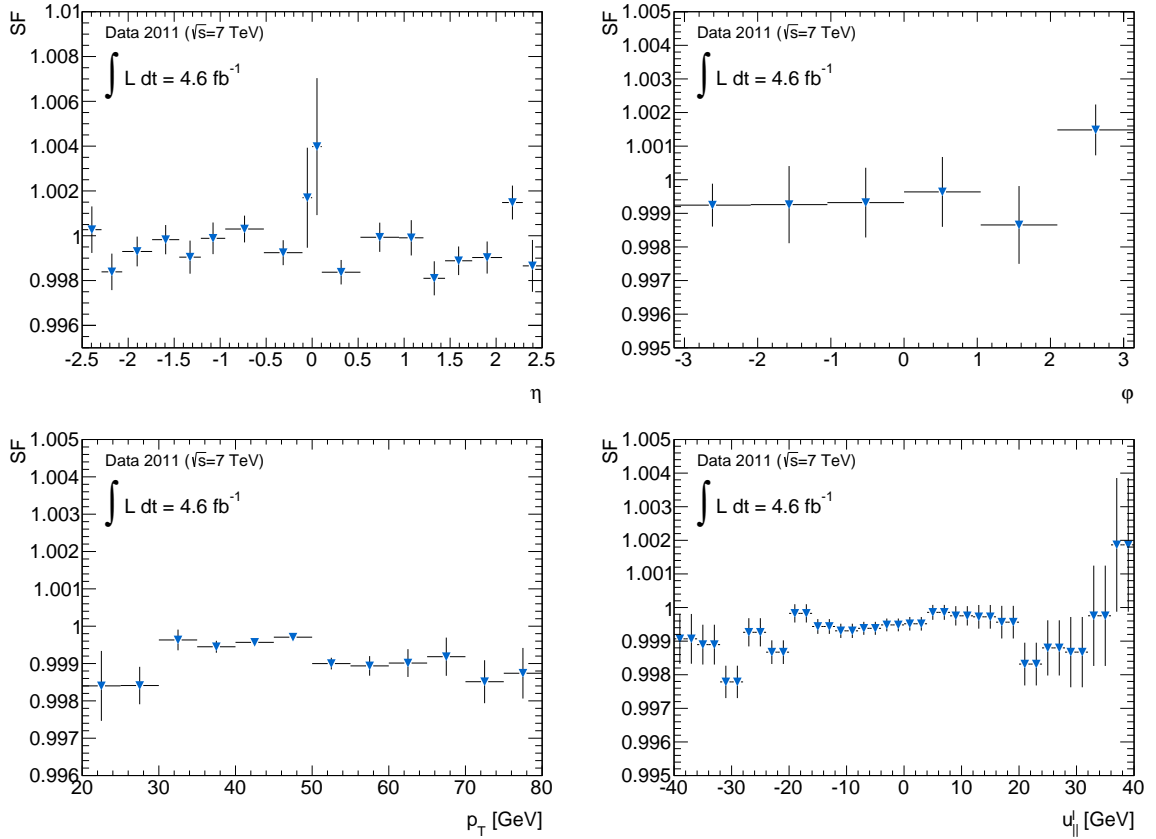


Figure 9.6.: Isolation scale factors determined as a function η , p_T , $u_{||}^l$. Uncertainties shown are the full systematic and statistical uncertainties.

The treatment and estimation of uncertainties for the isolation scale factors follows also Section 6.3. Figure 9.7 shows the different contributions to the uncertainty on the one-dimensional scale factors. The statistical uncertainty is dominating in all distributions in these specific plots.

In comparison to the reconstruction scale factors, the uncertainties are significantly reduced. This is mainly due to smaller background contributions and also the higher cut-efficiency. Systematic and statistical uncertainties are of similar order of magnitude. Since the signal is centered at $u_{\parallel}^l = 0$ and $p_T \sim 45$ GeV, the highest precision is expected at this point. This is highly relevant for the W -boson mass measurement, since in this measurement, the highest statistical precision is also expected in this region.

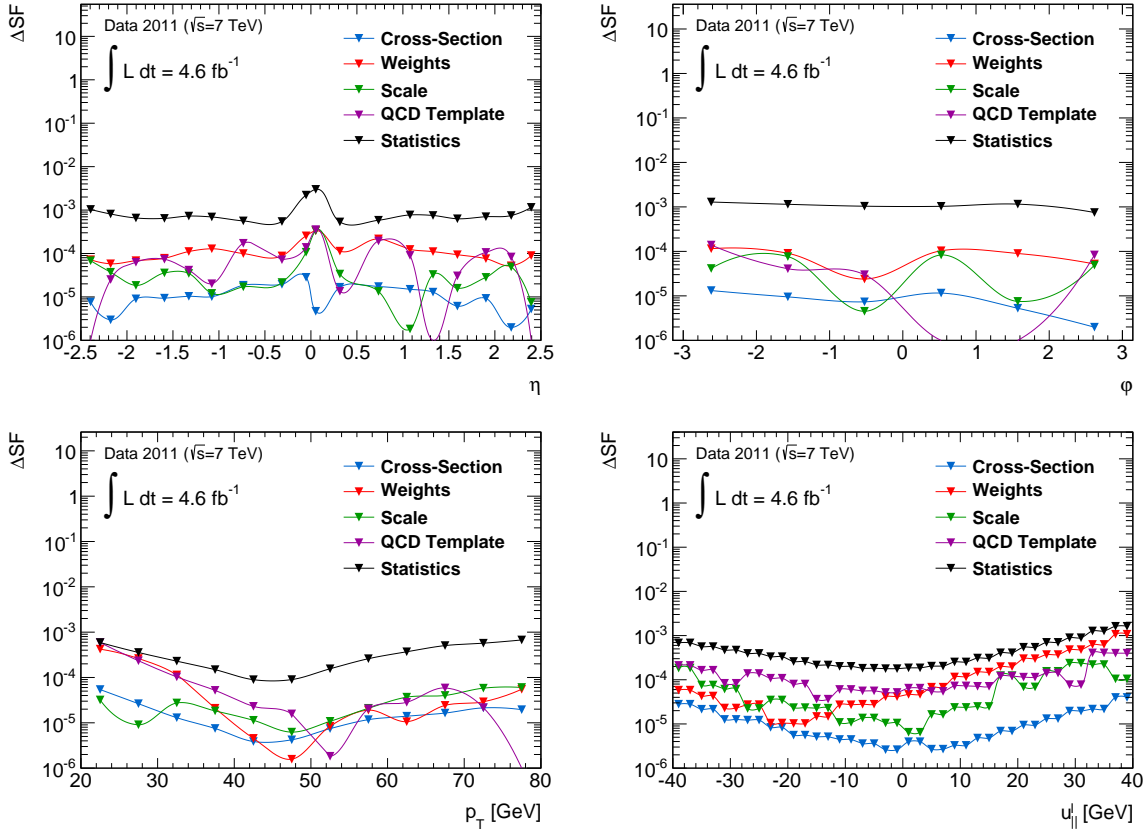
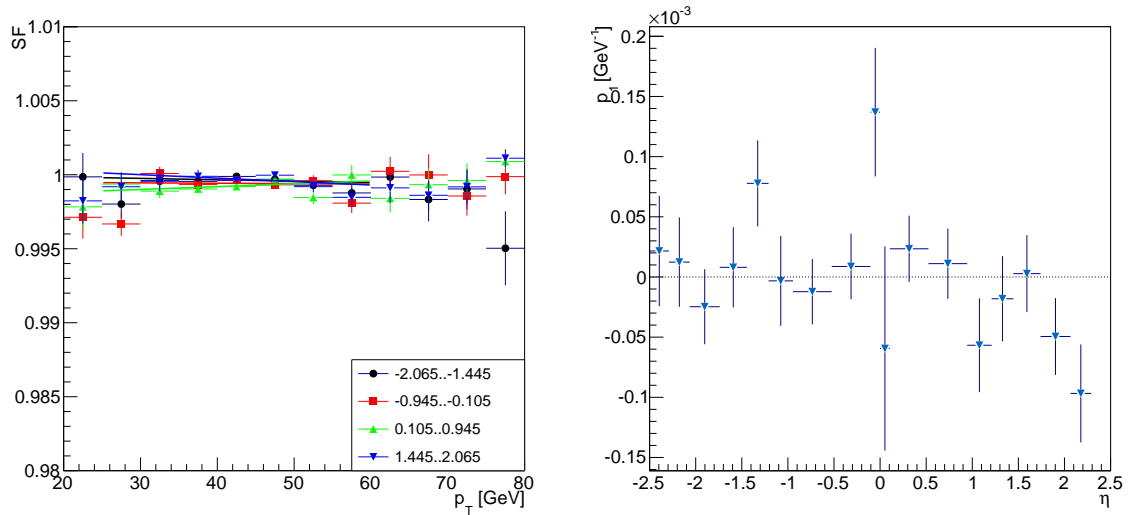


Figure 9.7.: Uncertainties on the isolation scale factors. From left to right: η , p_T , u_{\parallel}^l . Table 6.5 gives details on the categories shown in the plot.

9. Muon Isolation Efficiency

Similar to the approach in the analysis of the reconstruction scale factors, possible slopes in p_T were investigated by dividing the detector into four regions. These regions are $-2.065 \leq \eta \leq -1.445$, $-0.945 \leq \eta \leq -0.105$, $0.105 \leq \eta \leq 0.945$ and $1.445 \leq \eta \leq 2.065$, thereby excluding the crack regions between the end-caps and the barrel at $\eta \approx 1.05$ as well as the gap at $\eta = 0$. The resulting scale factors in p_T for these four regions can be seen in Figure 9.8(a). In this figure, the results from a fit for each of the distributions with a polynomial of the form $p_0 + p_1 \cdot p_T$ in the range of 25 to 60 GeV are shown. Table 9.2 shows the significance $p_1/\Delta p_1$. As can be seen, the isolation scale factors are almost flat with respect to lepton p_T . A full overview of the fitted slopes for all 18 bins in η is shown in Figure 9.8(b). For this study, only statistical uncertainties were used, since these are the dominating source of uncertainty.



(a) Scale factors in four regions of the detector with uniform efficiency. (b) Value of p_1 for each of the 18 η bins.

Figure 9.8.: Test of the flatness of the isolation scale factors. The left plots shows the isolation scale factors in four regions of the detector with uniform efficiency defined in the text. The corresponding fit values are shown in Table 7.2. In this plot, only the statistical uncertainty is shown. The right plot shows the values of the fitted slope p_1 in each of the 18 η bins in which the scale factors were obtained.

η	χ^2/dof	p_1 [GeV $^{-1}$]	Δp_1 [GeV $^{-1}$]	$p_1/\Delta p_1$
-2.065..-1.445	6.5/5	$-9.38 \cdot 10^{-6}$	$2.28 \cdot 10^{-5}$	-0.41
-0.945..-0.105	19.5/5	$-2.60 \cdot 10^{-6}$	$1.91 \cdot 10^{-5}$	-0.14
0.105..0.945	8.1/5	$1.92 \cdot 10^{-5}$	$2.00 \cdot 10^{-5}$	0.96
1.445..2.065	6.3/5	$-2.34 \cdot 10^{-5}$	$2.26 \cdot 10^{-5}$	-1.04

Table 9.2.: Overview of the fitted values obtained in the fits shown in Figure 9.8(a).

Figure 9.9 shows a comparison of the scale factors obtained for positive and negative probes. As can be seen, both scale factors show no significant deviations and agree very well within their uncertainties. This can also be seen in the resulting values of χ^2 , except for the distribution in $u_{||}^l$. The systematic uncertainty is not included in these plots.

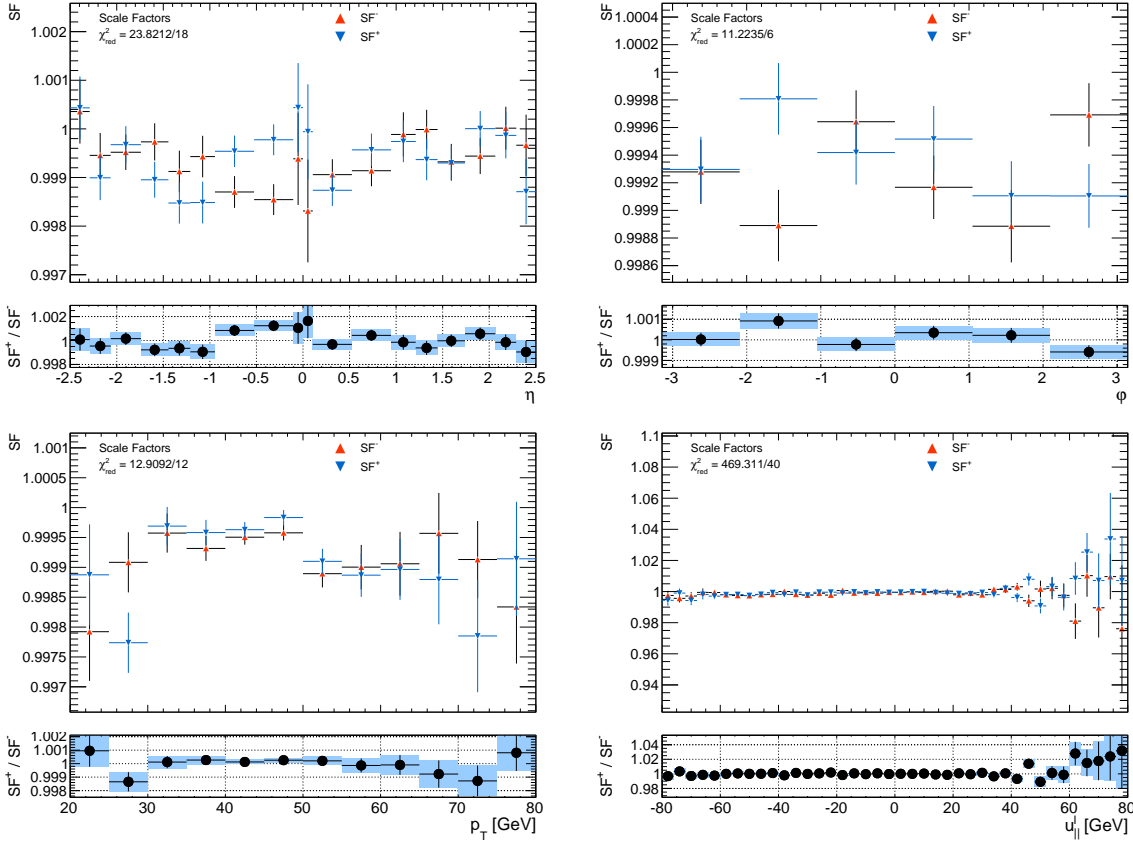


Figure 9.9.: Comparison of isolation scale factors obtained for negative and positive probes. From left to right: η , p_T , $u_{||}^l$. The uncertainties shown are only statistical.

10. Closure Test of the Obtained Scale Factors

10.1. Closure Test for the Z Boson Selection

As was described earlier, the scale factors were obtained as a function of *region*, lepton p_T and $u_{||}^l$, the former being a combined η - φ mapping. Apart from the dependence on all variables, the scale factors can also be used as a function of only a sub-set of those. Since the number of bins increases exponentially in the number of dimensions used, a fact only somewhat mitigated by merging bins, reducing the number of dimensions is advantageous in terms of stability and precision. Therefore, it was chosen to drop the dependence on $u_{||}^l$ in the following, since it has no direct impact on the kinematic variables η , φ and p_T , which are of largest importance for the measurement of M_W .

To cross-check the obtained SFs, a clean signal selection analogous to the selections used in the determination of the isolation and trigger scale factors was performed. Here, both muons are required to be isolated and trigger-matched. The latter requirement poses a challenging test for the quality of the extracted trigger scale factors. Strictly speaking, it would suffice if only one muon was matched to a trigger object since the triggers under consideration are single muon triggers. However, in this case, the resulting weight for the Monte Carlo event would read:

$$w = \frac{1 - (1 - \varepsilon_1^{\text{Data}})(1 - \varepsilon_2^{\text{Data}})}{1 - (1 - \varepsilon_1^{\text{MC}})(1 - \varepsilon_2^{\text{MC}})} \quad (10.1)$$

With the selection outlined above, this simplifies to $w = SF_1 \cdot SF_2$. The associated cut on both triggers leads to a lower cut efficiency with a higher impact of possible mis-modeling.

In summary, the selection criteria used were:

- Event cuts:
 - Trigger: EF_MU18 up to period J, EF_MU18_MEDIUM from period J inclusive
 - At least 3 tracks from primary vertex
- Muon selection:
 - Quality cuts summarized in Table 6.3
 - Combined (CB) muon
 - $|\eta| \leq 2.4$
 - $p_{T,ID} \geq 20 \text{ GeV}$
 - $|z_{0,PV}| < 10 \text{ mm}$
 - Isolated with $p_T^{\text{cone20}}/p_T < 0.1$
- Pair selection:
 - $|z_{0,PV,1} - z_{0,PV,2}| < 3 \text{ mm}$

10. Closure Test of the Obtained Scale Factors

- $|M_{\mu\mu} - M_Z| \leq 10 \text{ GeV}$
- Opposite charge

- Both muons trigger-matched

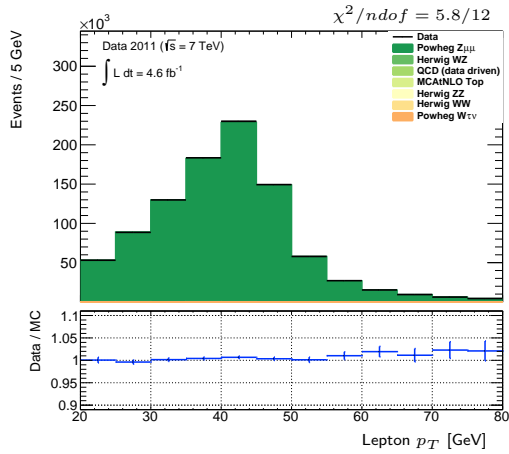
The different SFs were switched on one by one, starting with the trigger SFs, which are expected to play the largest role. This is followed by the reconstruction SFs and the isolation SFs. The resulting χ_{red}^2 values¹ for a sample of control distributions are shown in Table 10.1. The associated control distributions can be seen in Figures 10.1 to 10.5. As can be seen, with each step Monte Carlo describes data better. The values of the reduced χ^2 even fall below unity, indicating that the derived scale factors capture some statistical fluctuations in the data and Monte Carlo samples used. The notable exception from this picture is the $u_{||}^l$ distribution, for which no scale factors were applied in this test. The central distribution in these comparisons is the η distribution of the muons, since it is not affected by physics modeling, M_W or the detector resolution. The mis-modeling of the η distribution in Monte Carlo before corrections is almost exclusively due to the mis-modeling of the muon reconstruction, trigger and isolation efficiencies.

Observable	$M_{\mu\mu}$	Lepton p_T	Lepton η	Lepton φ	$u_{ }^l$
No weights	82.0 / 80	8.7 / 12	708.0 / 18	50.0 / 6	52.3 / 80
Trigger	70.7 / 80	6.7 / 12	141.4 / 18	16.4 / 6	50.5 / 80
Trigger + Reconstruction	70.6 / 80	7.4 / 12	7.5 / 18	9.9 / 6	50.9 / 80
Reconstruction + Isolation	77.4 / 80	11.5 / 12	507.0 / 18	46.1 / 6	52.1 / 80
Trigger + Isolation	70.7 / 80	6.3 / 12	144.0 / 18	16.0 / 6	50.5 / 80
Full weight	69.6 / 80	7.2 / 12	7.6 / 18	9.3 / 6	50.9 / 80

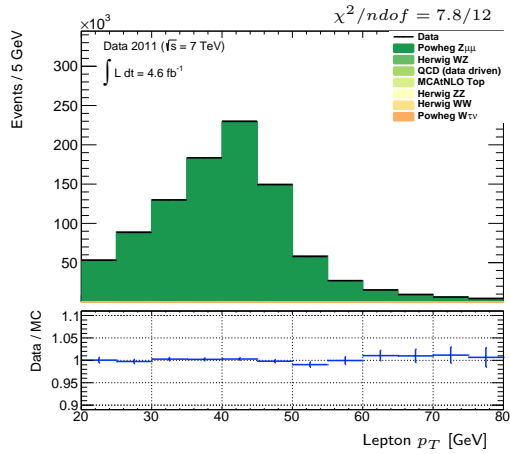
Table 10.1.: χ_{red}^2 for a sample of control distributions. Shown are the values for no application of the scale factors, with corrections for the trigger efficiencies, additional reconstruction and isolation efficiencies.

¹Each χ_{red}^2 value is obtained by performing a χ^2 test only taking statistical uncertainties into account.

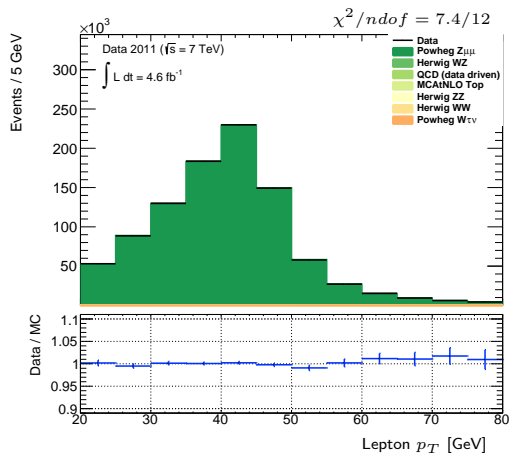
10.1. Closure Test for the Z Boson Selection



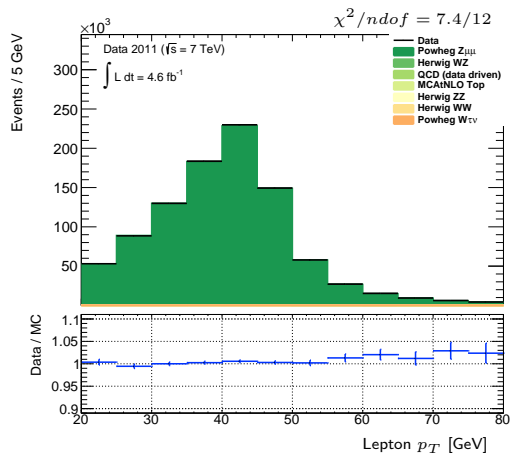
(a) No Weights



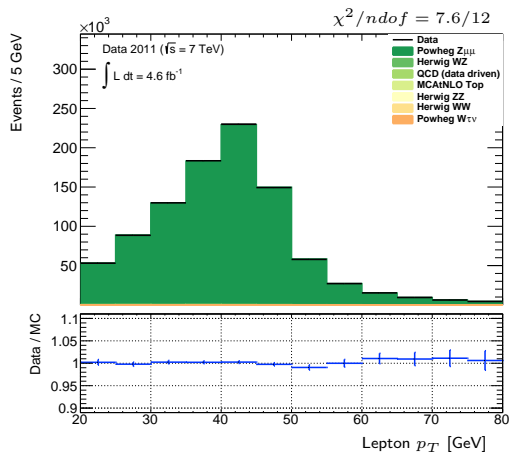
(b) Trigger SF



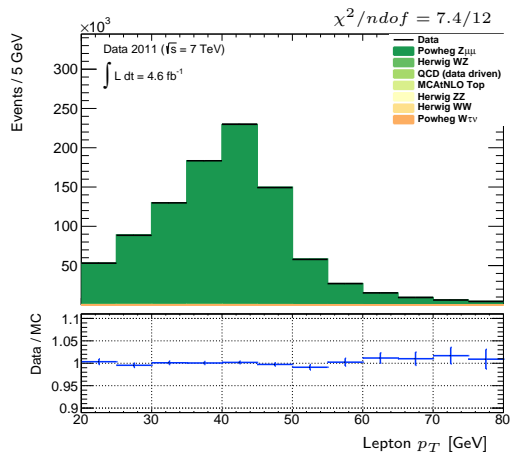
(c) Trigger+Reconstruction SF



(d) Reco+Iso



(e) Trigger+Iso



(f) Trigger+Reconstruction+Isolation SF

Figure 10.1.: Distributions of lepton p_T for different settings of the scale factors.

10. Closure Test of the Obtained Scale Factors

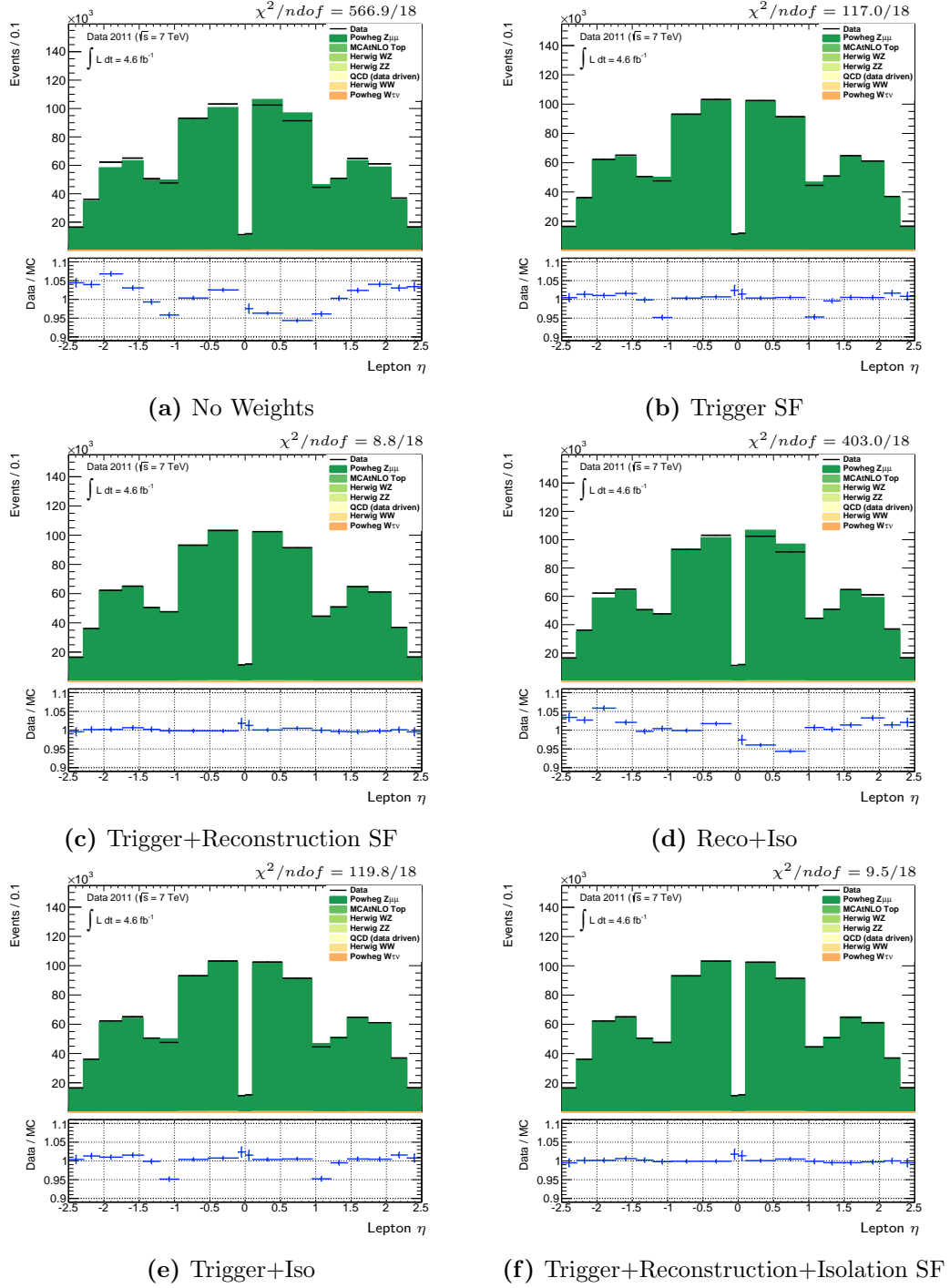


Figure 10.2.: Distributions of lepton η for different settings of the scale factors.

10.1. Closure Test for the Z Boson Selection

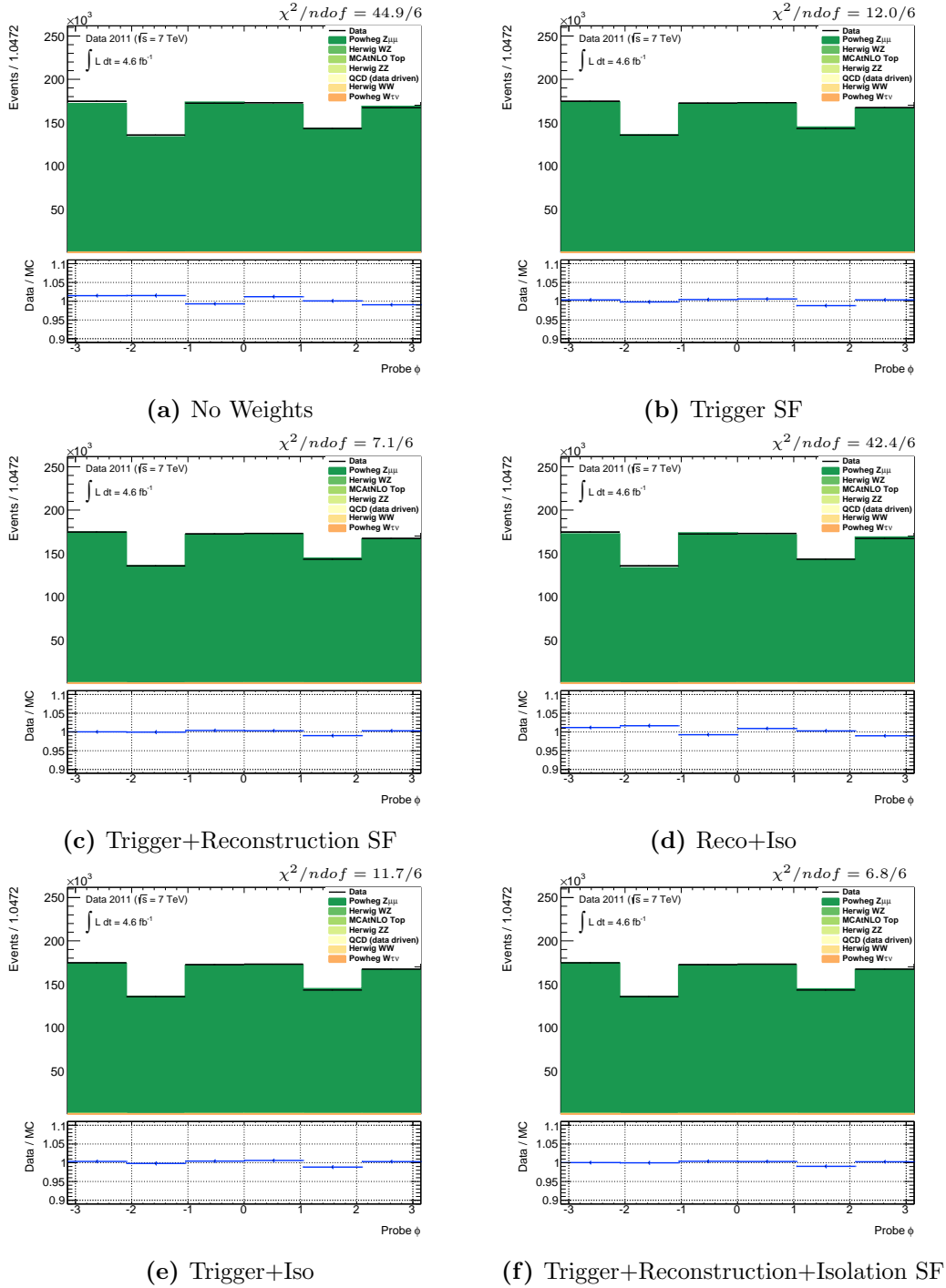


Figure 10.3.: Distributions of lepton η for different settings of the scale factors.

10. Closure Test of the Obtained Scale Factors

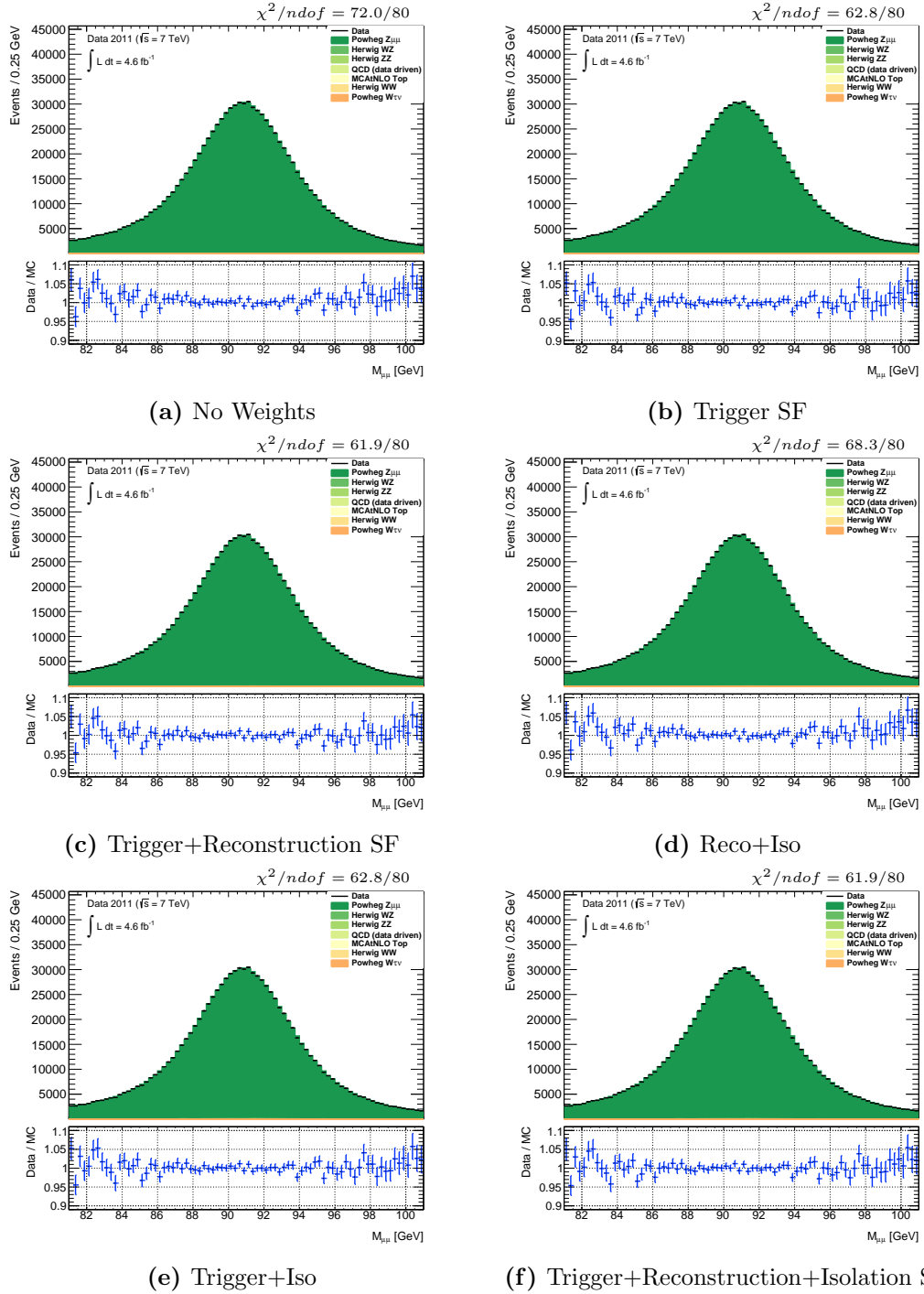


Figure 10.4.: Distributions of the invariant mass for different settings of the scale factors.

10.1. Closure Test for the Z Boson Selection

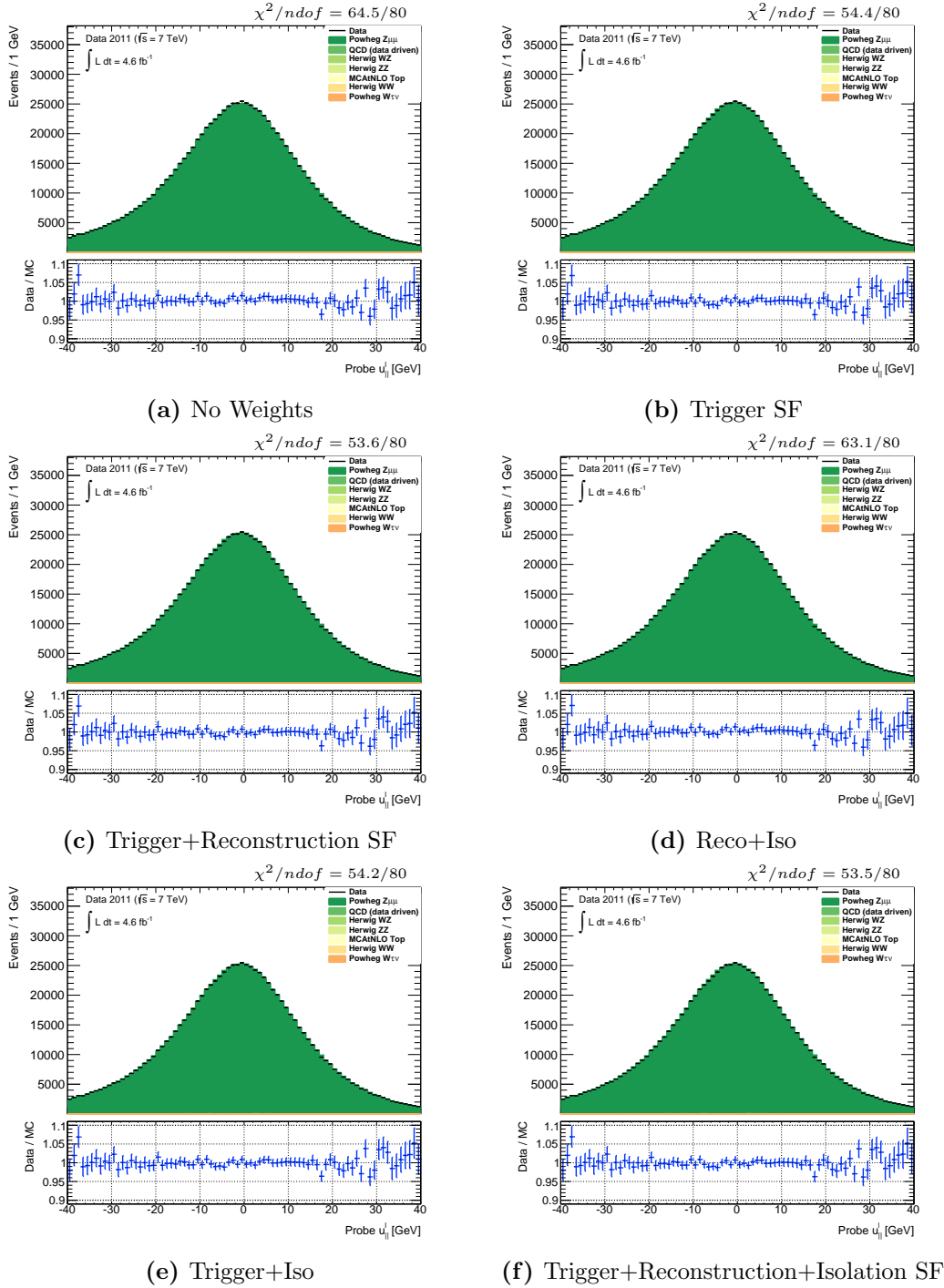


Figure 10.5.: Distributions of $u_{||}^l$ for different settings of the scale factors.

10.2. Closure Test for the W Boson Selection

In addition to the selection described above, where both muons were forced to be trigger-matched, it is also useful to test the closure of the SFs for a selection similar to that used for the measurement of the W boson mass. As a reminder, the W boson selection assumes one signal lepton, which can be either μ^+ or μ^- , and which has to be matched to the trigger. If this is to be simulated with the Z boson selection discussed in this chapter, the selection has to be modified as follows:

- **Positive muon trigger matched:** In this case, only the μ^+ candidate is required to be trigger-matched. The status of the trigger matching on the μ^- is disregarded, and the event weight subsequently reads:

$$w = SF_{\text{reco}}^+ \times SF_{\text{reco}}^- \times SF_{\text{iso}}^+ \times SF_{\text{iso}}^- \times SF_{\text{trigger}}^+ \quad (10.2)$$

- **Negative muon trigger matched:** Analogous to the case above, only the μ^- candidate is required to be trigger-matched. The status of the trigger matching on the μ^+ is disregarded, with the event weight subsequently reading:

$$w = SF_{\text{reco}}^+ \times SF_{\text{reco}}^- \times SF_{\text{iso}}^+ \times SF_{\text{iso}}^- \times SF_{\text{trigger}}^- \quad (10.3)$$

Figures 10.6 and 10.7 show the distribution of η and φ of the μ^+ and μ^- , respectively, because these distributions are most sensitive to mis-modeling of the reconstruction, trigger and isolation efficiency. Additionally, the effect on lepton p_T is also shown, since this is the most sensitive variable for the measurement of the W boson mass. Table 10.2 gives an overview of the values of χ_{red}^2 obtained in the different settings.

	Variable	All weights except trigger	Full weight
μ^+ matched	η^+	722 / 18	18 / 18
μ^- matched	η^-	514 / 18	11 / 18
μ^+ matched	φ^+	38 / 6	6 / 6
μ^- matched	φ^-	53 / 6	10 / 6
μ^+ matched	p_T^+	25 / 20	20 / 20
μ^- matched	p_T^-	13 / 20	13 / 20

Table 10.2.: Overview of the values of χ_{red}^2 for the W -like selection.

As can be seen, the trigger scale factors lead to a large improvement in the description of lepton η , φ and p_T . In η and φ , the reduced value of χ^2 becomes consistent with unity after application of the scale factors. In lepton p_T , which is also very susceptible to physics mis-modeling as well as detector mis-modeling, the effect is not as pronounced. However, a small improvement can be observed also here.

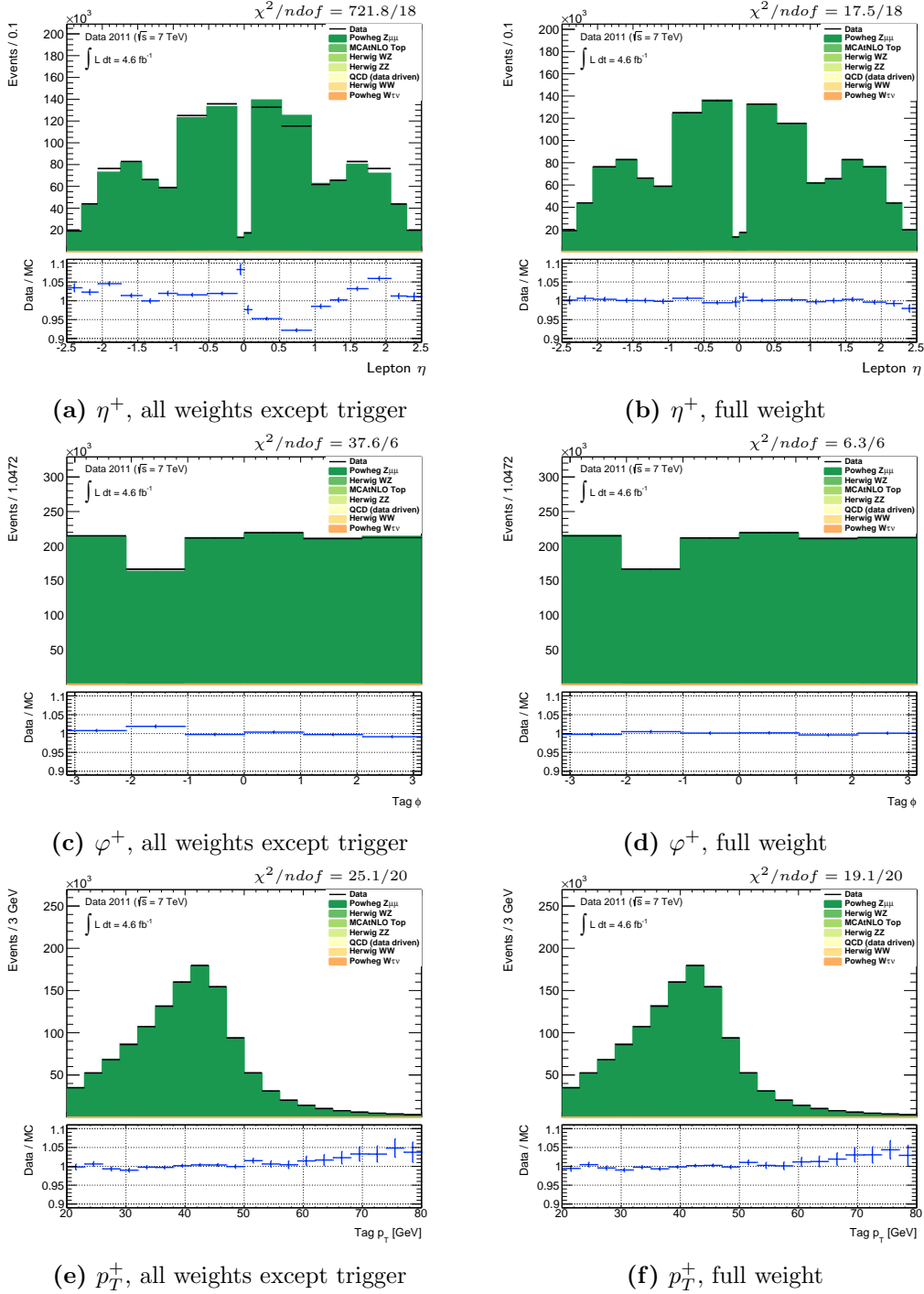


Figure 10.6.: Distributions for η^+ , φ^+ and p_T^+ in the case of the W -like selection. The left column shows the distribution with only reconstruction and isolation scale factors applied, the right column with the full event weight as defined in the text.

10. Closure Test of the Obtained Scale Factors

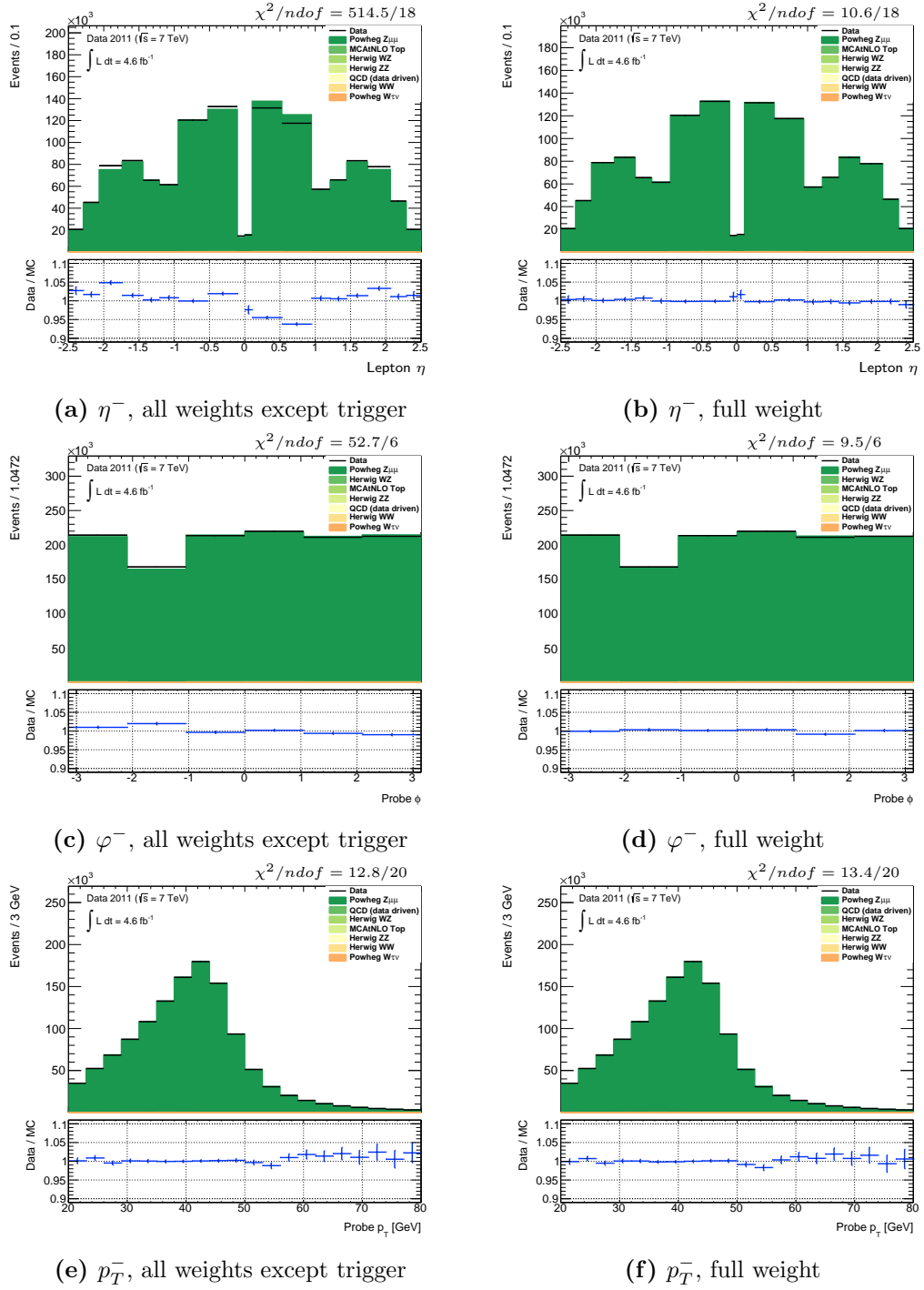


Figure 10.7.: Distributions for η^+ , φ^+ and p_T^+ in the case of the W -like selection. The left column shows the distribution with only reconstruction and isolation scale factors applied, the right column with the full event weight as defined in the text.

10.2. Closure Test for the W Boson Selection

Part III.

Towards a First Measurement of the Mass of the W-Boson

11. Overview of the Measurement

Building on the discussions in Part I, it is now possible to lay out the full strategy to measure the mass of the W boson at ATLAS. As was shown in Chapter 3, three observables can be used as proxy for the W boson mass:

- **Transverse momentum of the lepton:** The transverse momentum of the decay lepton p_T offers direct access to the mass of the W boson. It can be measured with very high precision and, in the case of muons in the final state, is almost unaffected by pile-up. On the other hand, the shape of the spectrum is very sensitive to physics and detector mis-modeling.
- **Missing transversal energy:** The missing transversal energy E_T^{miss} acts as a proxy for the decay neutrino p_T . However, since the reconstruction of E_T^{miss} is a challenging task including several sources of uncertainty, a smaller sensitivity to M_W compared to that using the lepton p_T is expected. Moreover, since an estimation of the contribution from pile-up vertices is challenging, the precision decreases with larger pile-up as observed towards the end of the 2011 data taking campaign.
- **Transverse mass:** The transverse mass m_T is built from the information on the lepton and the E_T^{miss} size and direction. Therefore, it can be seen as a compromise between both observables. In principle, the transverse mass is less sensitive to mis-modelings than lepton p_T (cf. ref. [104]).

As discussed in Chapter 3 and Chapter 5, external variables, such as pile-up and hadronic recoil, as well as detector effects, such as efficiencies depending on the value of p_T , have a significant impact on the shape of these distributions. Therefore, the value of M_W cannot be directly extracted from these distributions. Instead, a technique commonly known as forward folding is used.

In this approach, a Monte Carlo simulation is used to produce predictions for all three observables at different values of M_W . These predictions are stored as histograms called *templates*, are merged with the background prediction and are finally compared to the observed distributions in data. This comparison is performed using a χ^2 test, leading to a set of different χ^2 values for different, simulated values of M_W . The value of M_W leading to the minimal value of χ^2 is used as estimator for the true value of M_W .

The measurement of M_W was performed blinded. This means, that in each measurement a fixed, but unknown shift was applied to the final result¹. In this way, a possible bias towards the current world average (cf. ref. [8]) was prevented. In the final measurement, after the analysis is fixed, this blinding will be removed.

However, at the time of writing, not all corrections discussed in Section 5.4, which are needed for the final measurement, were finalized. This means that, in order to prevent the authors of

¹In practice, this is performed by using a random number generator, placing it in a defined state by fixing the so-called *seed*, and using the first random number produced by the generator to define the shift.

these corrections to be biased, the blinding could not yet be removed for the results presented in this thesis. Instead, it was chosen to present results on a limited set of data, corresponding to an integrated luminosity of 100 pb^{-1} . This means that only $\sim 2\%$ of the full data set were used. In this way, the statistical uncertainty is enlarged by a factor of approximately seven². Thus, a proof of principle of the measurement, as well as a first result, can be presented without endangering the remaining work towards the publication of the final result.

Since the mass of the W boson is very sensitive to physics modeling effects, a cross-check was performed by using the fitting package to measure the mass of the Z boson. This approach has the advantage that the mass of the Z boson is very well-known, with an uncertainty of 2.1 MeV (cf. ref. [8]) – well beyond the reach of this analysis. In this way, it can serve as an excellent benchmark for both the fitting package and the current state of the corrections. However, it has to be noted that a certain amount of correlation is introduced. This is due to the fact that part of the corrections, namely the muon momentum scale and the muon efficiencies, were obtained using $Z \rightarrow \mu\mu$ events. This means that the significance of the deviations of the measured values from the world average is to some extent underestimated.

In the remainder of this chapter, the topics common to both the measurement of the mass of the W and the Z boson are discussed. The following chapters will then discuss the points specific to the measurement of the mass of the Z boson and the W boson in turn.

11.1. Reweighting

Since the generation and reconstruction of $\sim 10^8$ events with the full ATLAS analysis framework is a very performance-intensive task, it is impossible to perform a full simulation for each possible value of M_W . Instead, a reweighting approach is chosen. In this approach, only events for a fixed value of M_W are produced. Then these events are weighted according to a theoretical description of the W and Z resonances, such that the line shape for values of M_W other than the original value can be obtained. To this end, the official ATLAS tool `LINESHAPE TOOL` was used, which is based on the improved Born approximation (IBA) (cf. Section 5.4). In this way, predictions for all possible values of M_W were feasible.

11.2. Fitting Procedure

As mentioned earlier, each Monte Carlo template is first merged with the background prediction³, yielding a prediction template h_{MC} , and then compared to the distribution observed in data h_{Data} using a χ^2 test. This test is performed after both histograms are normalized. In this case, χ^2 is defined as:

$$\chi^2 = \sum_{i=1}^N \frac{(f_{\text{MC},i} - f_{\text{Data},i})^2}{\Delta_{f_{\text{MC},i}}^2 + \Delta_{f_{\text{Data},i}}^2} \quad (11.1)$$

²A detailed calculation, performed in Chapter 13, yields a factor of 6.77.

³Note that the background prediction is not reweighted to different values of M_W or M_Z , respectively. This is because in the case of M_Z , background can be neglected, and because in the case of M_W , the leading background contributions originate from $Z \rightarrow \mu\mu$, which can be treated as independently of M_W . In the measurement of M_W , the sub-leading contribution originates from the multi-jet background, which is data-driven and therefore already includes the true value of M_W by construction. A remaining dependence of the background on M_W plays only a negligible role.

Here, $f_{\text{MC},i}$ and $f_{\text{Data},i}$ represent the uncertainties in bin i of h_{MC} and h_{Data} , respectively. The quantities $\Delta_{f_{i,\text{MC}}}$ and $\Delta_{f_{i,\text{Data}}}$ represent the uncertainties on $f_{i,\text{MC}}$ and $f_{i,\text{Data}}$, respectively. These uncertainties were estimated with Gaussian error propagation under the assumption of Poissonian-distributed uncertainties on the original distributions.

With allowing for up to two-dimensional histograms, the number of degrees of freedom can be calculated as:

$$n_{\text{dof}} = n_{\text{bins},x} \times n_{\text{bins},y} - 1 \quad (11.2)$$

One degree of freedom is lost due to normalization.

Since the templates are only produced for disjunct points in parameter space, interpolation has to be used to find the global minimum of the χ^2 curve, as shown in Figure 11.1. For this interpolation, the fact is used that the χ^2 curve can be approximated by a parabola close to its minimum. The equation used is shown in Equation (11.3).

$$\chi^2 \approx a + U_{11}(x - x_0)^2 \quad (11.3)$$

In this equation, the coefficient $U_{ij} = U_{ji}$ is the entry of the inverse of the covariance matrix $U_{ij} = (V^{-1})_{ij}$, and a denotes the minimum value of χ^2 and x_0 the values of x where the minimum is reached.

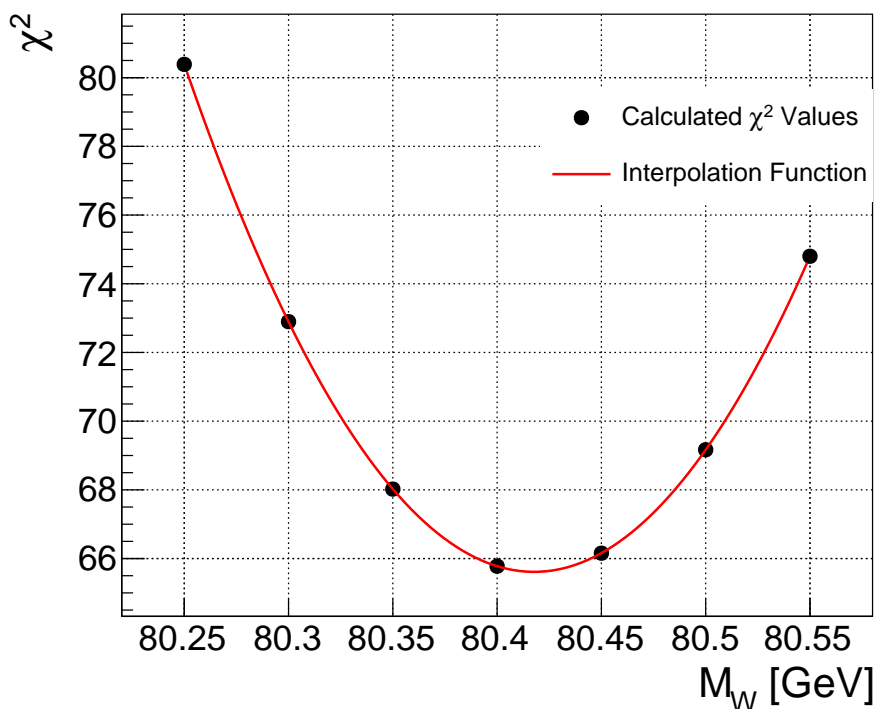


Figure 11.1.: Example of the interpolation used to obtain the global minimum of the χ^2 parabola. The plot shows the actual result from the fit of the W boson mass in the observable p_T^μ .

11.3. Estimation of Uncertainties

11.3.1. Propagation of Uncertainties

Systematic uncertainties can be assessed by their effect on MC and background templates. Some uncertainties only affect background templates, such as the QCD background estimation; others affect both, such as the momentum scales; and some are only applied to the Signal MC, such as the PDF uncertainties.

The propagation of the uncertainties from background templates is performed by replacing the nominal background template with varied background templates and assessing the effect on the fit result.

The propagation of the uncertainties from the MC templates can be performed in two ways, illustrated in Figure 11.2:

- *Full Template method*: In the full template method, for each uncertainty source, a new set of MC templates is produced. The fitting is then performed for each combination of data template and combined signal plus background template.
- *Pseudo-Data method*: In this method, pseudo-data templates are produced from MC for each uncertainty source. In the fitting package, the fit is performed for each combination of the pseudo-data set and the nominal MC template set.

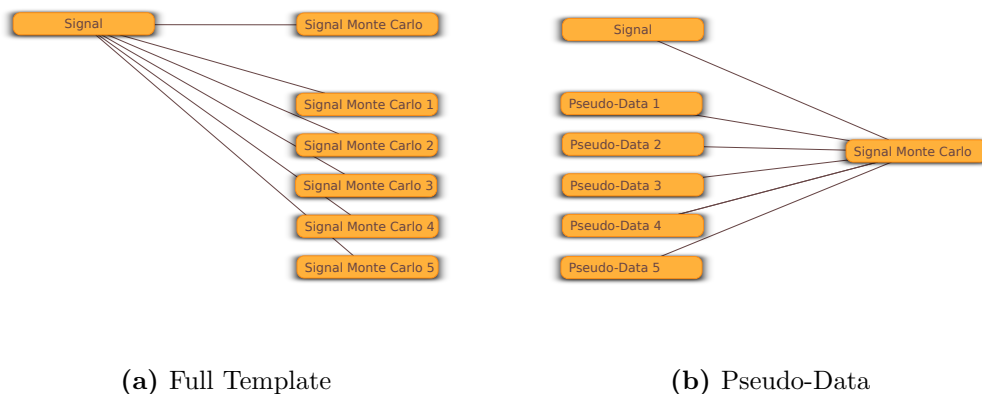


Figure 11.2.: Illustration of the two methods available to obtain MC systematic uncertainties.

In this analysis, the pseudo-data approach was chosen. This is because it is purely MC-based, meaning that the estimation of the systematic uncertainty is fully independent of statistical fluctuations in the data sample. Apart from this, it is clear that this approach is only valid if the Monte Carlo prediction describes the observed data well, a point fulfilled in both the measurement of M_W as well as M_Z .

There are different classes of systematic uncertainties which are treated differently in the calculation of the full uncertainty:

- *Paired*: Paired systematics consist of associated up and down variations. There are cases in which several paired systematics have to be combined for a total paired systematic. For example, the total uncertainty for the PDFs consists of several eigenvector uncertainties.

In general, several paired systematics are combined following ref. [105]. The resulting equations read as:

$$\Delta^+ = \sqrt{\sum_{i=1}^N \max(X_{up,i} - X_{base}, X_{down,i} - X_{base}, 0)^2} \quad (11.4)$$

$$\Delta^- = \sqrt{\sum_{i=1}^N \max(X_{base} - X_{up,i}, X_{base} - X_{down,i}, 0)^2} \quad (11.5)$$

$$\Delta = \frac{1}{2} \sqrt{\sum_{i=1}^N (X_{up,i} - X_{down,i})^2} \quad (11.6)$$

In this analysis, the symmetric form (Equation 11.6) is used.

- *Shifts*: In some cases, a number of shifts with respect to the baseline setting is supplied. The resulting uncertainty for the error source is combined by quadratical addition of the different shifts according to:

$$\Delta = \sqrt{\sum_{i=1}^N (X_{s,i} - X_{base})^2} \quad (11.7)$$

- *Toy MCs*: Uncertainties can be estimated with Toy MCs. Consider for example a correction with a set of scale factors (SF) for each bin. The connected uncertainty can be estimated by performing an up and down-variation with $\widetilde{SF} = SF \pm 1\sigma$. A superior approach is to produce combined Toy Monte Carlos, where in each Toy Monte Carlo i , the scale factors for each bin k are modified as shown in Equation (11.8):

$$\widetilde{SF}_i^k = SF^k + \Delta SF_{\text{stat+uncorr}}^k \cdot g_i^k + \sum_{s=1}^S \Delta SF_{\text{cor},s}^k \cdot g_{i,s} \quad (11.8)$$

Here, g is defined with $g \in \text{Gauss}(0, 1)$, i.e. g is taken from a normal distribution with $\mu = 0$ and $\sigma = 1$. Note that $g_{i,s}$ is the same random number for all bins k in a given Toy Monte Carlo i . In this way, bin-to-bin correlated and uncorrelated uncertainties are correctly taken into account. The resulting uncertainty stemming from the scale factors on the parameter is now estimated using the empirical standard deviation:

$$\Delta = \sqrt{\frac{1}{N-1} \sum_{i=1}^N (X_{s,i} - \overline{X}_s)^2} \quad (11.9)$$

Naturally, the empirical standard deviation has to be interpreted as an estimator for the true standard deviation, $\Delta = \hat{\sigma}$. This also means that Δ will scatter around the true value of the standard deviation σ , a fact which has to be considered in the assessment of the resulting uncertainties. The uncertainty $\Delta(\hat{\sigma})$ on the resulting uncertainty can be

11. Overview of the Measurement

estimated by assuming $\hat{\sigma}$ to follow a normal distribution. Then the empirical standard deviation of the sample is distributed like (cf. ref. [106]):

$$\hat{\sigma}^2 \sim \frac{\sigma^2}{N} \chi_{N-1}^2 \quad (11.10)$$

From this the standard deviation of the sample standard deviation $\Delta\sigma$ can be computed as:

$$\frac{\Delta\hat{\sigma}}{\hat{\sigma}} = \frac{1}{\sqrt{2(N-1)}} \quad (11.11)$$

In this equation, n corresponds to the number of Toy Monte Carlos. Table 11.1 shows a small overview of a range of values for n . As can be seen, for the common cases of $n = 20$ and $n = 100$, the uncertainty is on the order of 10% and can only be decreased significantly with significant computing effort.

n	$\Delta\hat{\sigma}/\hat{\sigma}$ [%]
5	35.4
10	23.6
20	16.2
50	10.1
100	7.1

Table 11.1.: Overview of the relative uncertainty on the uncertainty obtained via Toy MCs.

Different uncertainty sources can always be combined using the quadratic sum if no correlations exist and the uncertainties are distributed following a normal distribution:

$$\Delta_{ij} = \sqrt{\Delta_i^2 + \Delta_j^2} \quad (11.12)$$

11.3.2. Sources of Uncertainties

A number of possible sources of uncertainty were investigated in the measurement of the W and Z boson mass. These uncertainties can be grouped into statistical and systematic uncertainties. Statistical uncertainties would be different for each experiment and decrease with the number of observed events. This plays a large role in the measurement of M_W , were only a fraction of the full data set is used, leading to an artificial increase of the statistical uncertainty. In contrast to the statistical uncertainty, the systematic uncertainty is fixed for the experiment. The uncertainties investigated in the measurement of M_Z and M_W are summarized in Table 11.2. It has to be noted, that two additional sources of uncertainty have to be accounted for in the final measurement: these are the uncertainties connected with the modeling of boson p_T (cf. Section 5.4.1), and with the reweighting of the angular coefficients (cf. Section 5.4.1). In both cases, no full estimation of the uncertainty was available, and no propagation of the uncertainty to M_Z and M_W could be performed.

Source	Method for Estimation
Muon Momentum Scale	Estimated using ref. [107]
Hadronic Recoil	Estimated using ref. [107]
Statistical	Toy Monte Carlos
PDF	Variation of the PDF uncertainty set
Reconstruction Efficiency	Combination of Toy Monte Carlos and shifts
Trigger Efficiency	Combination of Toy Monte Carlos and shifts
Isolation Efficiency	Combination of Toy Monte Carlos and shifts
Angular coefficients	No propagation feasible
Boson p_T modeling	No propagation feasible

Table 11.2.: Uncertainties investigated in the measurement of M_W and M_Z .

Muon Momentum and Hadronic Recoil Correction

As mentioned before, not all corrections were published at the time of writing. This means that, for the estimation of the systematic uncertainty associated with the hadronic recoil and the muon momentum scale, only published estimations will be shown. These estimations are taken from ref. [107], in which the size and impact of these uncertainties on M_W at the ATLAS detector were studied for an integrated luminosity of 10 fb^{-1} at a center of mass energy of $\sqrt{s} = 14 \text{ TeV}$.

The relative uncertainties quoted in this reference are assumed to be driven by statistical uncertainties. In the calibrations performed for the measurement discussed in this thesis, a smaller number of events was available. This is due to the fact that the actual center of mass energy was $\sqrt{s} = 7 \text{ TeV}$, leading to a decrease of the cross section for the production of Z bosons by a factor of 2.14 (cf. ref. [108]), and a reduced integrated luminosity⁴ of $\int L dt = 4.58 \text{ fb}^{-1}$.

⁴This integrated luminosity was calculated using the Good Run List data11-7TeV.periodAllYear_DetStatus-v36-pro10_CoolRunQuery-00-04-08_WZjets_allchannels.DtoM.xml, created for the selection of events for the measurement of M_W and M_Z .

11. Overview of the Measurement

Therefore, the smaller number of $Z \rightarrow \mu\mu$ calibration events available in the 2011 data-set has to be taken into account through an additional factor, calculated as shown in Equation 11.13.

$$s = \sqrt{\frac{N_{exp}}{N_{obs}}} = 2.17, \text{ with } N = \int Ldt \times \sigma_{pp \rightarrow Z+X \rightarrow \mu\mu+X} \quad (11.13)$$

In summary, the values for the muon scale and smearing uncertainty, as well as for the hadronic recoil scale and smearing uncertainty are shown in Table 11.3.

Uncertainty source	$\Delta a/a(14 \text{ TeV}, 10 \text{ fb}^{-1})$	$\Delta a/a(7 \text{ TeV}, 4.58 \text{ fb}^{-1})$
Muon momentum scale	2×10^{-5}	4×10^{-5}
Muon momentum resolution	2×10^{-4}	4×10^{-4}
Hadronic Recoil scale	5×10^{-5}	11×10^{-5}
Hadronic Recoil resolution	6×10^{-4}	13×10^{-4}

Table 11.3.: Estimations for the relative uncertainty $\Delta a/a$ on the muon scale and resolution, as well as for the hadronic recoil scale and resolution. Values taken from ref. [107] and scaled to the observed center-of-mass energy and integrated luminosity in 2011.

These uncertainties are propagated to the final measurement of M_W through a set of up and down shifts. Using ref. [107], the uncertainty on M_W in the p_T^μ fit can be estimated to be on the order of 9 MeV for the muon momentum scale and 2 MeV for the muon momentum resolution. Moreover, the uncertainty on M_W in the fit to m_T , due to the hadronic recoil scale and resolution, can be expected to be on the order of 2 MeV for the scale and 3 MeV for the resolution.

Statistical Uncertainties

In this analysis, three uncertainty sources of statistical origin play a role. These are due to the finite number of events in the Signal MC, Data and Background samples.

At this point, a careful distinction has to be made: the statistical uncertainty due to the finite data sample leads to a true statistical uncertainty on M_W . That means that, hypothetically speaking, if the 2011 data-taking campaign could be repeated n times and no additional uncertainties would exist, an analysis performed for each of these repetitions would yield a different value of M_W , scattered around the true value of M_W with a standard deviation equal to the statistical uncertainty of M_W .

For the MC statistical uncertainty, this is not the case. Here, the same Monte Carlo sample would be used each time. This means that the effect of the finite size of this sample will lead to a difference between the measured and true value of M_W , which would be equal for each of the aforementioned hypothetical repetitions. In this way, while the MC statistical uncertainty originates from statistical effects, the result on M_W is of systematic nature. Therefore, it is counted as one of the sources of systematic uncertainty on the measured value of M_W , and not among the statistical uncertainties.

The background statistical uncertainty is more challenging to categorize, since it consists of both data-driven and Monte Carlo samples. While the data-driven contribution will lead to a true statistical uncertainty on M_W , i.e. it would change in each of the hypothetical repetitions,

the Monte Carlo contribution will lead to a fully systematic contribution. The background statistical uncertainty plays only a minor role, and will be counted as systematic uncertainty on M_W in the following. This is because it is expected to be dominated by Monte Carlo contributions if the full data-set can be used.

The total uncertainty on the measured mass due to these sources can in principle be estimated from the width of the χ^2 parabola. Unfortunately, in this way the size of the three different contributions is lost. Therefore, the three different contributions are estimated separately with Toy MCs. For this N variations of the original MC, Data and Background samples were produced, with N being on the order of 100.

In general, the supplied Monte Carlo samples for the signal and background simulation are sufficiently larger than the data sample. Moreover, the data-driven background contribution considered in the case of the measurement of M_W is sufficiently small, such that the only significant contribution to the total uncertainty is expected to arise from the uncertainty on the data sample itself. Using the estimation performed in ref. [107], and including the aforementioned corrections for the reduced center of mass energy and luminosity, this uncertainty can be estimated to be on the order of 5 MeV.

Interpolation Uncertainty

As described above, a limited number of prediction templates, i.e. combined signal and background templates, is produced for different values of M_W , and is then compared to data using a χ^2 test. From the different χ^2 values obtained, the position of the minimum of the χ^2 parabola is found by interpolation. The interpolating function is a parabola, fitted using a χ^2 fit. This interpolation yields a further uncertainty, since the position of the minimum can only be estimated with a given precision. This uncertainty is taken directly from the χ^2 fit result.

PDF uncertainty

The PDF uncertainty is estimated from the set of uncertainties supplied with the CT10 PDF used. These uncertainties are given as 90% confidence intervals along 26 eigenvectors. Subsequently, these uncertainties have to be scaled by $1/1.64485$ to obtain uncertainties at the Gaussian 1σ level, corresponding to a 68% confidence level. The uncertainty on M_W is obtained by performing up and down-shifts along the 26 eigenvectors, and adding the uncertainties in quadrature as described above.

Reference [39] gives an overview of the expected uncertainties on M_W . In the case of fitting in p_T^μ , an uncertainty of 16 MeV is expected. If separated into $p_T^{\mu+}$ and $p_T^{\mu-}$, the uncertainty is expected to be even larger, ranging up to 22 MeV for the chosen PDF set. This uncertainty is mostly due to the fact that the polarization of the W boson, and therefore the shape of p_T^μ , depends to a large extent on the composition of the incoming protons, as discussed in Section 3.2. A further impact originates from the uncertainties of the charm quark PDFs due to the non-negligible mass of the charm quark and its effect on the spectrum of p_T^W .

It has to be noted that, in the generator output used, no gluon information is stored. This means that the uncertainty on M_W due to the uncertainties on the gluon PDFs could not be assessed. This will have to be remedied for the final measurement, a task which can be performed by either reweighting the current Monte Carlos, or alternatively by producing new Monte Carlo samples.

Muon efficiency uncertainty

The uncertainty on the efficiencies for muon reconstruction, isolation and triggering were obtained as part of this thesis. The uncertainties discussed in Section 6 were propagated through 20 Toy Monte Carlos for the statistical uncertainty, and eight histograms representing the systematic, bin-to-bin correlated uncertainties. The resulting uncertainty will be discussed in detail in Section 13.6.

Boson p_T modeling uncertainty & Angular Coefficients

As discussed in Section 5.4.1, the transverse momentum of the decay leptons is strongly influenced by the transverse momentum of the intermediary vector boson. The uncertainties associated with the modeling of boson p_T , however, were not yet finalized at the time of writing and could therefore not be propagated to the final result of M_Z and M_W , respectively. Reference [39] gives a first estimation of these uncertainties on M_W in the fit in p_T^μ . In this reference, the uncertainty associated with the modeling of p_T^W is found to be on the order of 6 MeV. For M_Z , the effect can be assumed to be smaller, since the knowledge of p_T^Z is much better through the availability of direct measurements. In both cases, the modeling of boson p_T can be expected to play a minor role.

The same is true for the angular coefficients. As discussed in Section 5.4.1, corrections to these factors were obtained by comparing the output of the POWHEG+PYTHIA simulation used to obtain the signal samples for $pp \rightarrow Z + X \rightarrow \mu\mu + X$ as well as for $pp \rightarrow W + X \rightarrow \mu\nu + X$ to the output of the DYNNLO generator. For these corrections, no uncertainties were supplied at the time of writing. However, it is expected that these uncertainties play only a minor role.

12. Validation with Z Bosons

Before performing the fit of M_W , it is important to validate the full analysis chain, including all corrections. To this end, the process $pp \rightarrow Z + X \rightarrow \mu^+\mu^- + X$ is chosen. Since the world average of M_Z is already used in the calibration of the muon momentum corrections, a measurement of M_Z can be expected to reproduce the world average within its uncertainty.

The choice of $Z \rightarrow \mu\mu$ as validation process has several advantages: the mass of the Z boson is very well known, with a world average of (91.1876 ± 0.0021) GeV (cf. ref. [8]), with the uncertainty well beyond the reach of this analysis. A further advantage of the decay of the Z boson is the low level of background observed in this analysis. Moreover, the topologies of Z and W decays are very similar: in principle, muonic decays of W and Z bosons differ only by the replacement of a neutrino as partner of the decay muon in the decay $W \rightarrow \mu\nu$ by a muon of opposite charge in the decay $Z \rightarrow \mu\mu$.

This allows for constructing observables that mimic those used for the measurement of M_W by treating one of the decay muons of the Z boson as a neutrino, adding it to the missing energy of the event. In this way, W -like observables such as m_T and E_T^{miss} can be constructed. Due to the ambiguity as to which decay muon is treated as neutrino, these W -like observables can be constructed either for the case of only μ^+ being treated as a neutrino, or only μ^- being treated as neutrino, or both.

The measurement was performed inclusively as well as in several bins in order to test for internal consistency. These bins were chosen to match those of the measurement of M_W and are summarized in Table 12.1. Apart from two bins in p_T^Z and four bins in η^+ and η^- , also three bins in pile-up μ were defined.

Observable	Bin borders				
p_T^Z	0 GeV	15 GeV	30 GeV		
η^{μ^+}	0	0.8	1.4	2.0	2.4
η^{μ^-}	0	0.8	1.4	2.0	2.4
μ	2.5	6.5	9.5	16	

Table 12.1.: Bin definitions for the measurement of M_Z . Note that μ is the standard ATLAS notation for the average number of interactions per bunch crossing.

12.1. Selection

The selection used for the measurement of M_Z is very similar to that for the Tag and Probe analyses discussed in Chapter 6. The following criteria were used:

- **Good Run List:** The Good Run List used for this analysis was `data11.7TeV.periodAll-Year_DetStatus-v36-pro10_CoolRunQuery-00-04-08_WZjets_allchannels_DtoM.xml`, corresponding to 4.58 fb^{-1} of integrated luminosity.

- **Vertex:** At least three tracks are required to originate from the primary vertex.
- **Trigger:** The triggers applied are the single muon triggers EF_MU18 for data period B-I, and EF_MU18_MEDIUM for period J-M.
- **Muon selection:** Exactly two pre-selected muons are required, with the preselection criteria reading:
 - **Combined muons:** Only staco muons flagged as combined by the muon reconstruction algorithm are considered.
 - **Quality:** Several quality criteria, concerning for example the number of hits in the TRT, were applied. These criteria follow the recommendations from the ATLAS muon combined performance working group and are summarized in Table 6.3.
 - **Distance from primary vertex:** A cut was performed of the longitudinal distance of the track from the primary vertex, $|z_0|$, with $|z_0| < 10$ mm.
 - **Acceptance:** The muons were required to lie well within the acceptance of the ID, with $|\eta| < 2.4$.
 - **Isolation:** All muons are required to appear isolated, by requiring $p_T^{\text{cone20}}/p_T < 0.1$.
 - **Momentum:** The minimal momentum required by the pre-selection is $p_T > 25$ GeV.
- **Invariant Mass:** The selected pair of muons must fulfill the ATLAS definition for on-shell Z bosons, with $66 \text{ GeV} < m_{\mu\mu} < 116 \text{ GeV}$.
- **Trigger matching:** At least one of the muons has to be associated with a trigger object, with $|\eta| < 0.1$.¹
- **Jet veto:** Events are vetoed if a jet fulfilling the LooseBad jet selection criteria are found within a cone of $\Delta R < 0.3$ around one of the muon candidates.
- **LAr hole:** Events are vetoed if one of the jets in the event is close to the so-called LAr hole, a region in the calorimeter experiencing technical problems during the 2011 data taking.
- **Lar error:** Events are vetoed if a noise burst in the liquid argon calorimeter occurred.

The resulting cut flows for data, Signal and Background MC are shown in Table 12.2 and 12.3. These cut flows are already normalized to the integrated luminosity, and therefore give an impression of the low level of background observed. In total, only ~ 5000 background events are expected from the relevant background samples shown here.

¹Note that this cut, while in agreement with the standard analysis cuts chosen by the W boson analysis group, might in principle lead to a case in which a muon failing the trigger matching might be used as signal muon in the construction of the W -like observables p_T^μ , m_T and E_T^{miss} . This might lead to small differences between the Z boson cross-check and the W boson analysis.

	Data	$Z \rightarrow \mu\mu$	Single Top	$t\bar{t}$	$W^- \rightarrow \mu^- \bar{\nu}_\mu$	$W^+ \rightarrow \mu^+ \nu_\mu$	$W \rightarrow \tau\nu_\tau$	Diboson	$Z \rightarrow \tau\tau$
All	110 286 232	5 401 536.4	21 593.4	188 294.8	8 612 386.4	13 522 764.8	1 023 703.3	48 346.5	203 747.0
Combined	109 904 747	5 092 134.5	21 131.6	183 686.4	8 439 526.2	13 246 160.5	1 003 300.7	46 926.3	199 065.6
Quality	108 021 836	5 024 862.1	20 885.4	181 230.3	8 354 220.2	13 114 291.4	993 293.5	46 378.2	197 010.9
z_0	106 891 770	5 009 194.4	20 841.2	181 201.3	8 268 215.4	12 973 805.3	978 269.5	46 281.5	195 446.8
η	105 611 707	4 870 062.7	20 694.5	180 201.3	8 126 038.7	12 740 107.6	961 497.2	45 602.7	192 179.8
Isolation	45 404 748	4 834 746.2	18 984.3	154 278.2	8 068 135.1	12 646 569.1	952 434.3	44 271.0	190 423.9
$p_T > 20$ GeV	29 117 317	4 397 656.9	16 354.9	138 067.0	7 144 958.4	10 757 495.0	544 052.1	39 292.2	115 750.6

Table 12.2.: Number of pre-selected muons per cut for each sample used in the measurement of M_Z . All numbers are scaled to the integrated luminosity of data. *Single top* consists of all seven single top samples (production 108340-108346), while *Diboson* consists of the WW , WZ and ZZ samples.

	Data	$Z \rightarrow \mu\mu$	Single Top	$t\bar{t}$	$W^- \rightarrow \mu^- \bar{\nu}_\mu$	$W^+ \rightarrow \mu^+ \nu_\mu$	$W \rightarrow \tau\nu_\tau$	Diboson	$Z\tau\tau$
All	125 341 170	4 534 200.0	100 027.2	628 834.0	19 694 000.0	28 212 800.0	7 024 208.6	134 514.6	1 192 723.6
GRL	114 016 724	4 534 200.0	100 027.2	628 834.0	19 694 000.0	28 212 800.0	7 024 208.6	134 514.6	1 192 723.6
Vertex	113 823 231	4 507 678.5	99 951.3	628 603.2	19 599 094.0	28 050 741.8	6 989 081.3	134 262.6	1 188 545.1
Trigger	107 690 309	3 299 559.7	22 703.7	180 372.6	9 006 683.8	14 386 243.0	1 319 410.6	45 014.2	248 138.2
Veto	1 561 047	1 542 467.8	11.3	6 369.2	75.9	73.4	12.6	3 467.8	1 784.9
$m_{\mu\mu}$	1 500 034	1 504 250.9	6.8	2 352.1	34.0	41.0	7.8	2 599.8	811.6
Matching	1 499 962	1 504 158.6	6.8	2 346.0	34.0	41.0	7.8	2 597.8	811.6
Jets	1 491 297	1 485 021.3	6.8	2 313.7	33.4	40.7	7.8	2 560.5	801.1
Lar Hole	1 489 574	1 483 680.1	6.8	2 290.4	33.4	40.4	7.8	2 547.7	800.3
Lar Error	1 485 494	1 483 680.1	6.8	2 290.4	33.4	40.4	7.8	2 547.7	800.3

Table 12.3.: Number of selected events per cut for each sample used in the measurement of M_Z . All numbers are scaled to the integrated luminosity of data. *Single top* consists all seven single top samples (production 108340-108346), while *Diboson* consists of the WW , WZ and ZZ samples.

12.2. Background Estimation

Similar to the Tag and Probe analyses performed to obtain the muon trigger, reconstruction and isolation efficiency (cf. Part II), the background can be split into two groups. The first group consists of the electroweak and top background, which is described by Monte Carlo. The second group is the multijet — or QCD — background, which has to be obtained from data since no sample with sufficient statistical precision exists. Moreover, Monte Carlo predictions of QCD background admixtures always carry a large theoretical uncertainty.

The method to obtain the estimation of the QCD background consists of two steps: in a first step, a background-enriched template for the QCD background in all kinematic distributions is obtained. In a second step, the correct normalization factor for this template is obtained. However, in this analysis, QCD background plays only a negligible role, as no event was selected for the QCD template. From studies with dedicated $b\bar{b}$ and $c\bar{c}$ samples, as performed in ref. [109], the number of events in the QCD background is expected to be compatible with zero.

The small role of the QCD background is to a large extent due to the jet veto cut. Given the fact that almost all hadrons and leptons except muons are absorbed in the hadronic and electromagnetic calorimeters of the ATLAS detector, essentially only true muons can produce signals in the muon system. The jets from which these muons originate are easily detectable, even if the muons fulfill the isolation requirement.

12.3. Control Plots

In Figure 12.1, the control distributions for the selection are shown. As can be seen, the background admixture is invisible in all plots. The Signal Monte Carlo offers a very good description of the shown distributions. As expected, the distribution of the invariant mass peaks around the value of M_Z , reflecting the Breit-Wigner resonance in the cross-section formula. Compared to the invariant mass, the transverse momentum of the $\mu^+\mu^-$ system is very difficult to model due to QCD effects. This is reflected by the value of χ^2 shown in this plot: with $\chi_{red}^2 = 119/60$, the value is almost twice as large as for the invariant mass.

The modeling of the transverse momentum of the decay muons is excellent, with values of χ_{red}^2 below unity. The distributions are shaped as expected: a peak at $p_T \sim 45$ GeV, reflecting half of the value of M_Z , and a long tail towards lower values, produced by muons with $|\eta| > 0$. This corresponds to the expectation discussed in Section 3.1. Note that in the distribution of $p_{T,-}$ a hint of a dip can be seen around 55 GeV.

The distribution of η is very sensitive to detector effects. Due to the differences in the selections, the results shown here are not directly comparable with the results presented in Section 6. This is mostly due to the trigger matching, which is here only required on one of both muons.

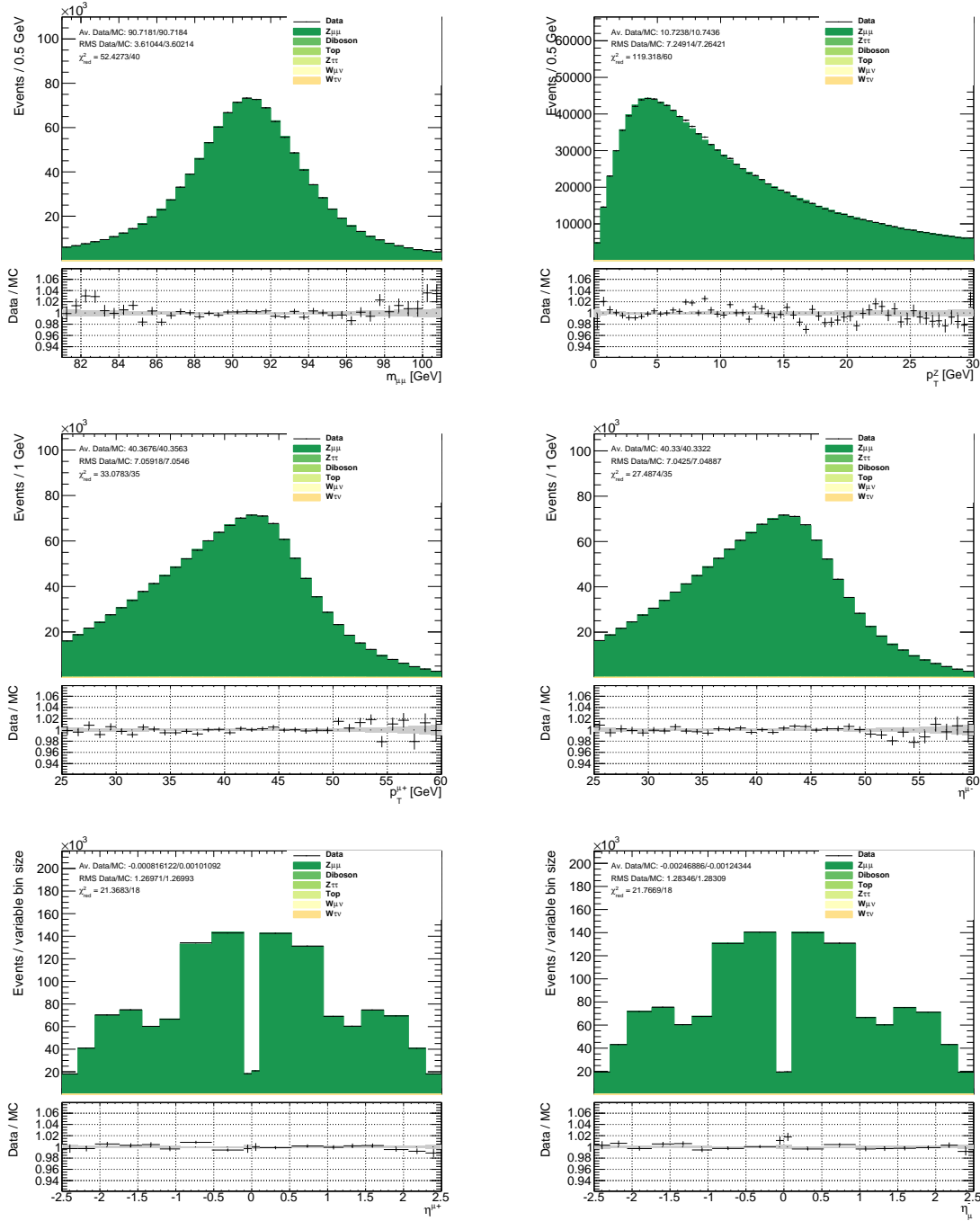


Figure 12.1.: Control Plots for $Z \rightarrow \mu\mu$. From left to right, top to bottom: $M_{\mu\mu}$, $y_{\mu\mu}$, $p_{T,+}$, $p_{T,-}$, η_+ , η_- . In the ratio, the gray band denotes the statistical uncertainty from the combined Monte Carlo and background stack, while the error bars denote the uncertainty from data. Only the statistical uncertainty is shown and used for the χ^2 test shown in each control plot. This test shows the compatibility of the observation and prediction for each distribution.

12.4. Monte Carlo-based Cross-Checks

Before performing the final fit, the stability of the fitting approach, as well as the accuracy of the estimation of the three different sources of statistical uncertainty, were tested by performing a pure Monte Carlo study. To this end, the data was replaced by pseudo-data obtained from signal Monte Carlo. In this way, the internal consistency of the fitting package could be tested.

12.4.1. Numerical Stability

The additional uncertainty due to the interpolation discussed in Chapter 11.2 is estimated by replacing the data template with a Monte Carlo template. In this way, the fit is expected to yield exactly the injected value of 91.1876 GeV. Any deviation from this value can be seen as inaccuracy. As can be seen in Figure 12.2(a), these deviations are below 1 MeV and therefore do not play a role in this analysis. Moreover, the observed deviations are larger in observables and regions in which less sensitivity to the mass of the Z boson is expected, since these settings are connected with flatter χ^2 parabolas. This leads to a larger uncertainty on the interpolated minimum.

Interestingly, a small bias towards positive values is discernible. This might be due to the interpolation method, where each point is treated with equal weight. Essentially, this overestimates the weight of points with larger distance to the minimum of the χ^2 parabola, and might lead to larger biases if the chosen distance between the sampling points is too large. This underlines the importance of performing the test discussed here.

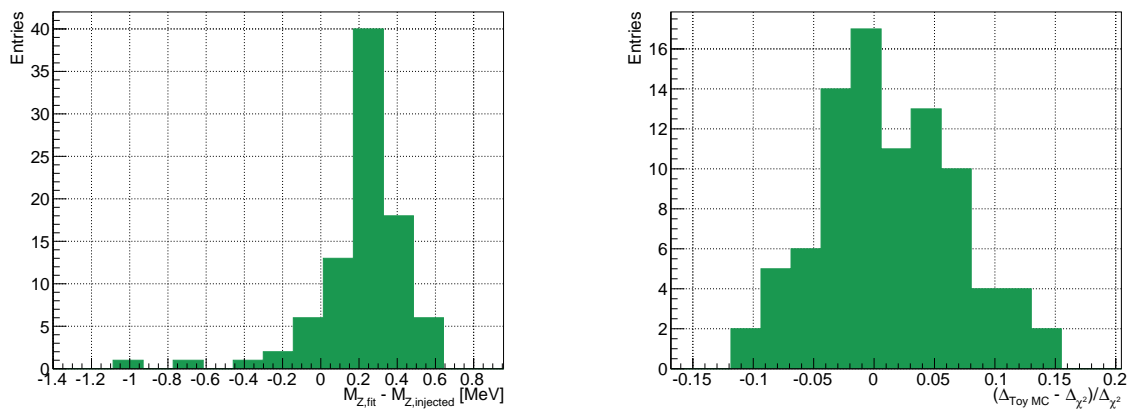
12.4.2. Estimation of Statistical Uncertainty

As discussed above, the statistical uncertainty can, in principle, be obtained from the width of the χ^2 parabola. Since this approach leads to a loss of all information concerning the contributions from data, Signal MC and background estimation, a Toy MC method was applied.

The following four quantities are obtained:

- Δ_{χ^2} : uncertainty estimated from the width of the χ^2 parabola
- $\Delta_{\text{ToyMC}}^{\text{Data}}$: statistical uncertainty from data, estimated with the Toy MC method
- $\Delta_{\text{ToyMC}}^{\text{Bkg}}$: statistical uncertainty from background, estimated with the Toy MC method
- $\Delta_{\text{ToyMC}}^{\text{MC}}$: statistical uncertainty from Signal MC, estimated with the Toy MC method

In a cross-check, the three Toy MC uncertainties are added in quadrature and compared to the total uncertainty estimated from the width of the χ^2 parabola. This is shown in Figure 12.2(b). The regions cited in this plots are defined as in Table 12.1. It can be observed that the statistical uncertainties from both methods differ by less than 10% on average.



(a) Comparison of the nominal values and the values obtained by the fit to pseudo-data in the measurement of M_Z .

(b) Distribution of total statistical uncertainty obtained with the Toy MC method and from the width of the χ^2 parabola. For the definition of the regions see Table 12.1.

Figure 12.2.: Results from the Monte Carlo-based cross-checks.

12.5. Data-based Cross-Checks

Figure 12.4 shows a sample of fit results obtained in the inclusive region. As can be seen, the distribution of the invariant mass of the $\mu^+\mu^-$ pair offers an excellent observable for the measurement of M_Z . This is clearly visible in the values of χ^2 shown in the right figure: Even small deviations from the nominal mass lead to a large increase in the obtained values of χ^2 .

The lower rows show results for fits in the W -like observables p_T , m_T and E_T^{miss} , constructed as described above, by treating one decay muon as neutrino and adding it to the missing energy. The Jacobian peak distribution of lepton p_T was discussed before. As can be seen, its sensitivity to changes in M_Z is significantly reduced compared to the distribution of the invariant mass. This can be clearly deduced from the increased width of the χ^2 parabola. The transverse mass has a very broad peak around M_Z , smeared out by the E_T^{miss} resolution. The missing energy E_T^{miss} itself also shows a smeared-out peak at $M_Z/2$. This behavior will carry over to the measurement of M_W .

The resulting values for the inclusive region are shown in Figure 12.3. Also here, the extreme sensitivity obtainable in the observable $m_{\mu\mu}$ is visible. In E_T^{miss} , only a weak dependence on M_Z can be observed, with the largest uncertainty of all observables. The transverse mass is more sensitive, with the transverse masses obtained with discarding the positive and negative muons being compatible with each other. The transverse momentum of the muon is the most sensitive variable of all three W -like observables. Also here, the results obtained using the transverse momentum of μ^+ and μ^- are compatible. In summary, all results are compatible with the world average (cf. ref. [8]), with a resulting value of $\chi_{\text{red}}^2 = 9.58/8$ and probability of 0.30.

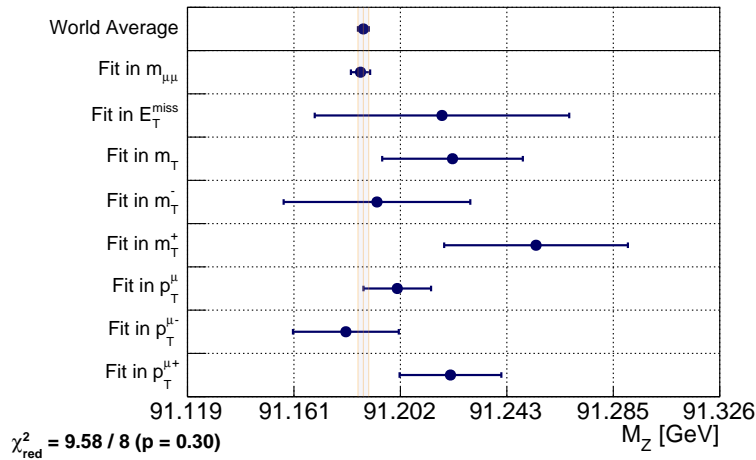


Figure 12.3.: Overview of the fit results for all observables in the *Inclusive* region. For comparison, the current value and uncertainty of the world average (cf. ref. [8]) is also shown. In addition, the resulting value of χ_{red}^2 and the probability of a χ^2 test comparing the obtained results and the world average are shown. For this test, only the statistical uncertainties, without any possible correlations, were considered.

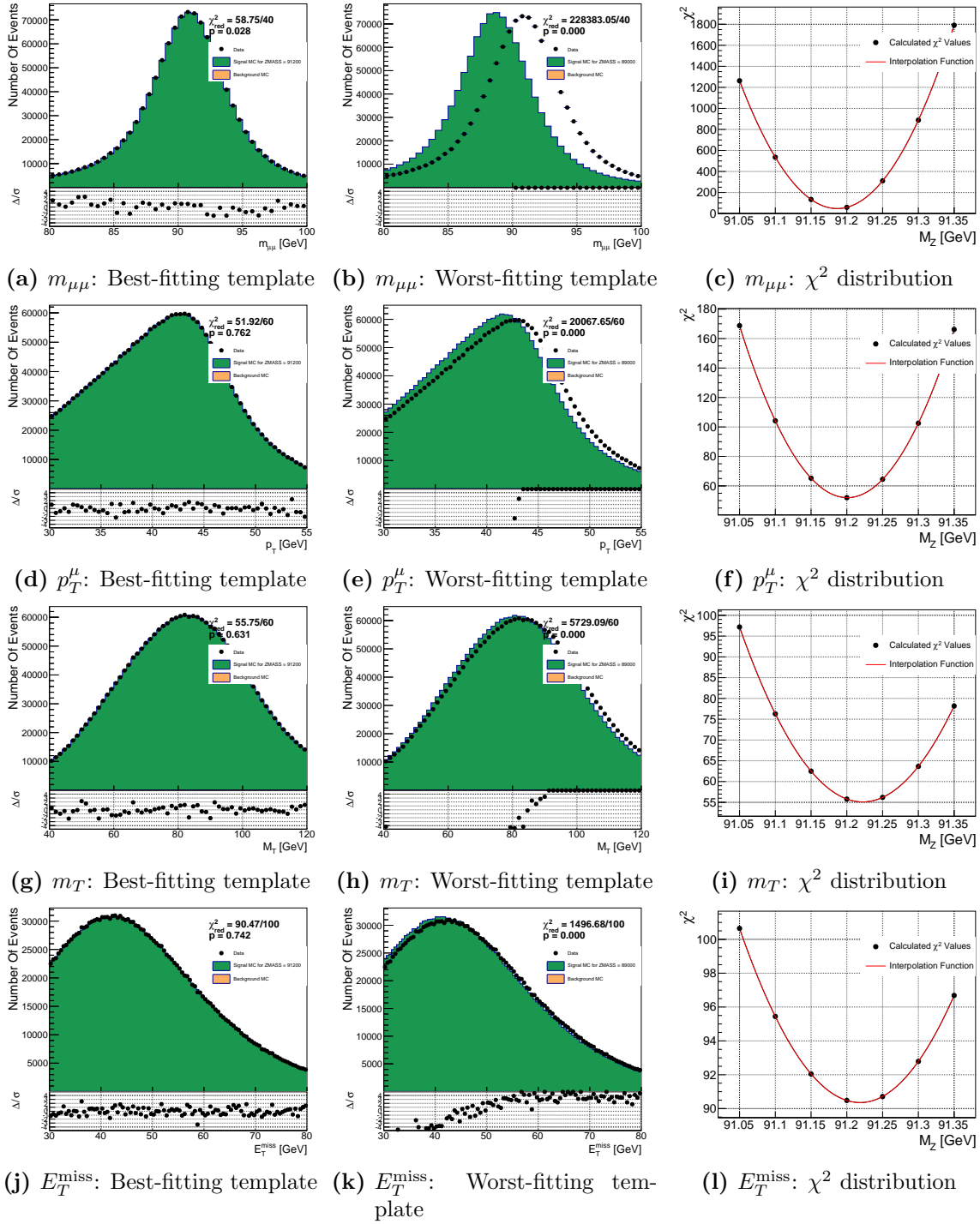


Figure 12.4.: Selected control plots from the consistency tests. Each row shows the template with the lowest value of χ^2 when compared to data, the template with the highest value of χ^2 when compared to data, and the resulting distribution of values of χ^2 for each template. From top to bottom, the fit in the invariant mass of the $\mu^+\mu^-$ pair is shown, followed by observables constructed to match those in which M_W will be measured: lepton p_T , transverse mass m_T and missing transverse energy E_T^{miss} .

12. Validation with Z Bosons

Figure 12.5 shows an overview of the fit results obtained in the observable $m_{\mu\mu}$. The two results obtained in the two different bins in p_T^Z are very similar, with a reduced χ^2 of $0.07/2$, translating into a test probability of 0.96. In the three pile-up bins, the results are also compatible with the world average, with a χ^2 test probability of 0.76. If the fit results are investigated separately for the four $\eta^{\mu-}$ bins, it may be observed that the results for $1.4 < |\eta^{\mu-}| < 2.4$ differ from the world average. This leads to an increase of the value of the χ^2 test, with a fit probability of 0.10. For $\eta^{\mu+}$ no such effect is visible. Overall, the deviation in $\eta^{\mu-}$ is not significant, especially when weighted against the results obtained when separated by p_T^Z , pile-up or $\eta^{\mu+}$.

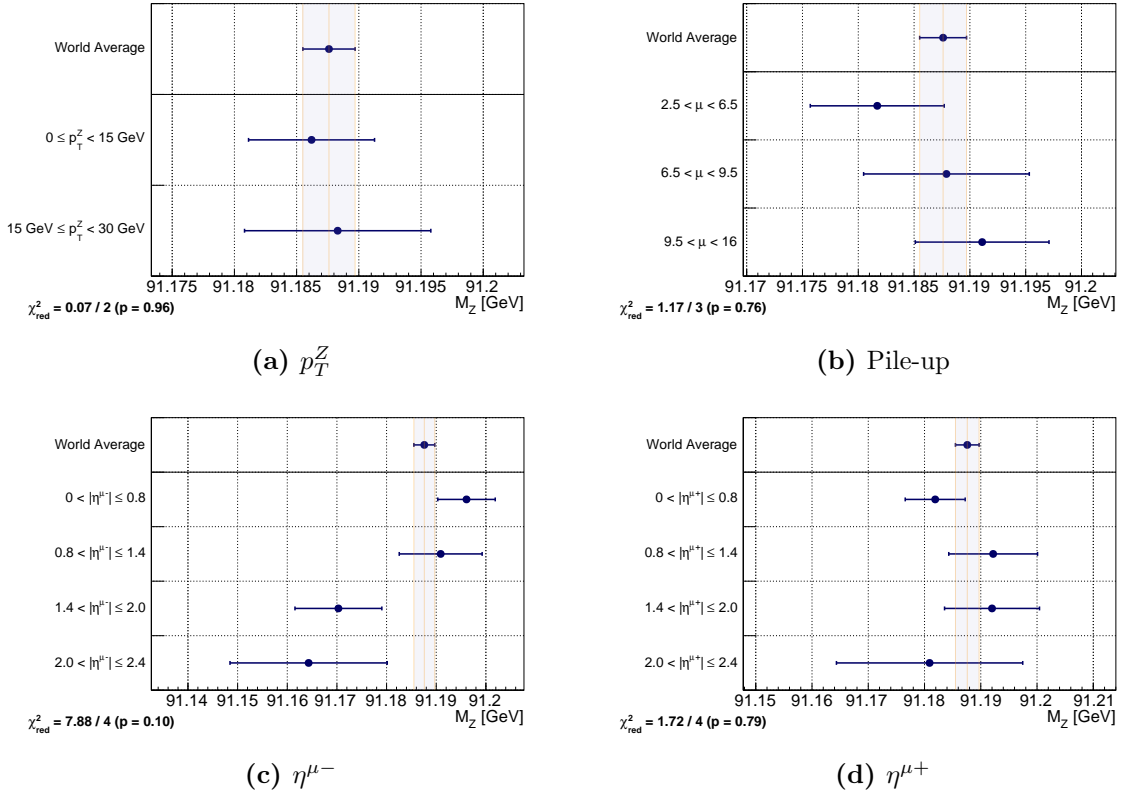


Figure 12.5.: Overview of the fit results obtained in the observable $M_{\mu\mu}$. For comparison, the current value and uncertainty of the world average (cf. ref. [8]) is also shown. In addition, the resulting value of χ_{red}^2 and the probability of a χ^2 test comparing the obtained results and the world average are shown. For this test, only the statistical uncertainties, without any possible correlations, were considered. From left to right, top to bottom, results separated for the two regions of p_T^Z , three regions of pile-up, four regions of $\eta^{\mu-}$ and $\eta^{\mu+}$ are shown.

Figure 12.6 shows fit results obtained in the observables p_T^+ and p_T^- . If separated into bins of p_T^Z , it is clearly visible that the low p_T^Z bin has a much smaller uncertainty than the high p_T^Z bin. This can be understood by recalling the discussion in Section 3.1, where it was shown that the distribution of the lepton transverse momentum is broadened through a non-zero transverse momentum of the Z boson. Thus, the spectrum of p_T^μ is more sensitive to M_Z if p_T^Z is close to zero. With a χ^2 test probability of 0.70, all obtained fit values are compatible. In the three pile-up bins, this holds also true with a probability of 0.75. Also here, no clear structures are visible. If separated into the four η^+ and η^- bins, the test probabilities read 0.88 and 0.28, showing no significant deviations or structures.

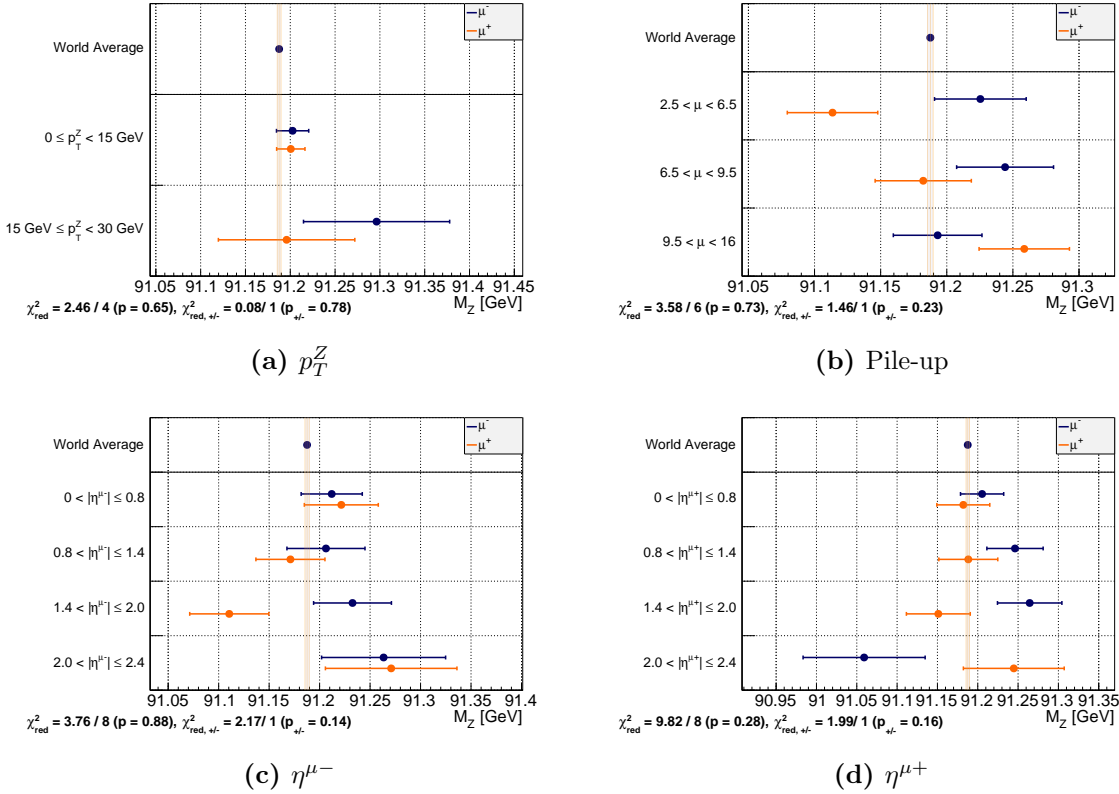


Figure 12.6.: Overview of the fit results obtained in the observable p_T^+ (orange) and p_T^- (blue). For comparison, the current value and uncertainty of the world average (cf. ref. [8]) is also shown. In addition, the resulting value of χ_{red}^2 and the probability of a χ^2 test comparing the obtained results and the world average are shown. Additionally, the result of a χ^2 test comparing the results for μ^+ and μ^- is also shown. For these tests, only the statistical uncertainties, without any possible correlations, were considered. From left to right, top to bottom, results separated for the two regions of p_T^Z , three regions of pile-up, four regions of η^{μ^-} and η^{μ^+} are shown.

12. Validation with Z Bosons

Figure 12.7 shows the fit results obtained in the observable m_T . If separated into the two p_T^Z bins, the same pattern already observed in lepton p_T appears again. As was also the case there, this pattern can be traced back to the decreased smearing of m_T with increased p_T^Z and the subsequently increased sensitivity to M_Z . Here, as well as in the remaining three binnings into pile-up, η^{μ^+} and η^{μ^-} , all obtained fit values are compatible with the world average, with χ^2 test probabilities of 0.38, 0.75, 0.89 and 0.66.

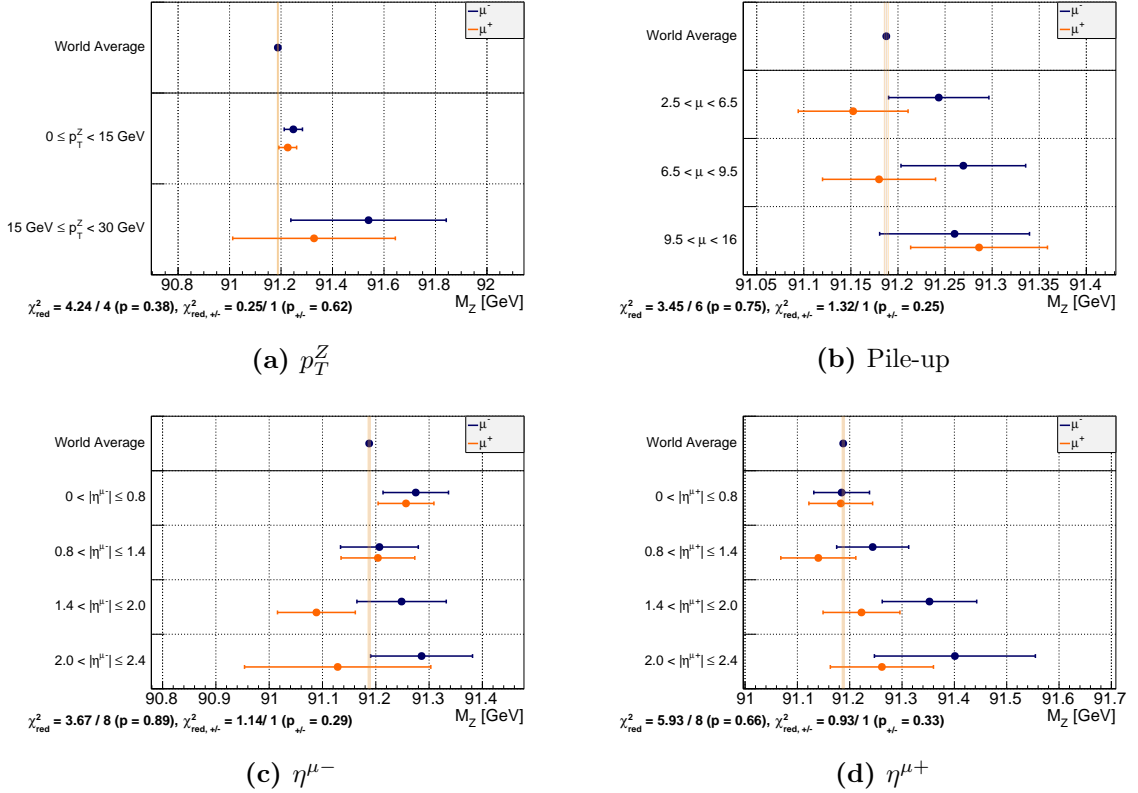


Figure 12.7.: Overview of the fit results obtained in the observable m_T^+ (orange) and m_T^- (blue). For comparison, the current value and uncertainty of the world average (cf. ref. [8]) is also shown. In addition, the resulting value of χ_{red}^2 and the probability of a χ^2 test comparing the obtained results and the world average are shown. Additionally, the result of a χ^2 test comparing the results for μ^+ and μ^- is also shown. For these tests, only the statistical uncertainties, without any possible correlations, were considered. From left to right, top to bottom, results separated for the two regions of p_T^Z , three regions of pile-up, four regions of η^{μ^-} and η^{μ^+} are shown.

Figure 12.8 shows the fit results obtained in the variable E_T^{miss} . Due to the low sensitivity in this variable, a split into μ^+ and μ^- was not feasible. As can be seen, the results obtained are in excellent agreement with the world average, with χ^2 test probabilities of 0.36, 0.69, 0.37 and 0.78. This shows that in this variable no mis-modelings are discernible, either. As can also be seen here, the results for the low p_T^Z and high p_T^Z differ significantly in their uncertainty. With respect to the other variables pile-up, η^{μ^+} and η^{μ^-} , no significant structures can be observed. Only a hint at a rise with $|\eta^{\mu^+}|$ might be discerned. However, this is well within the statistical uncertainties.

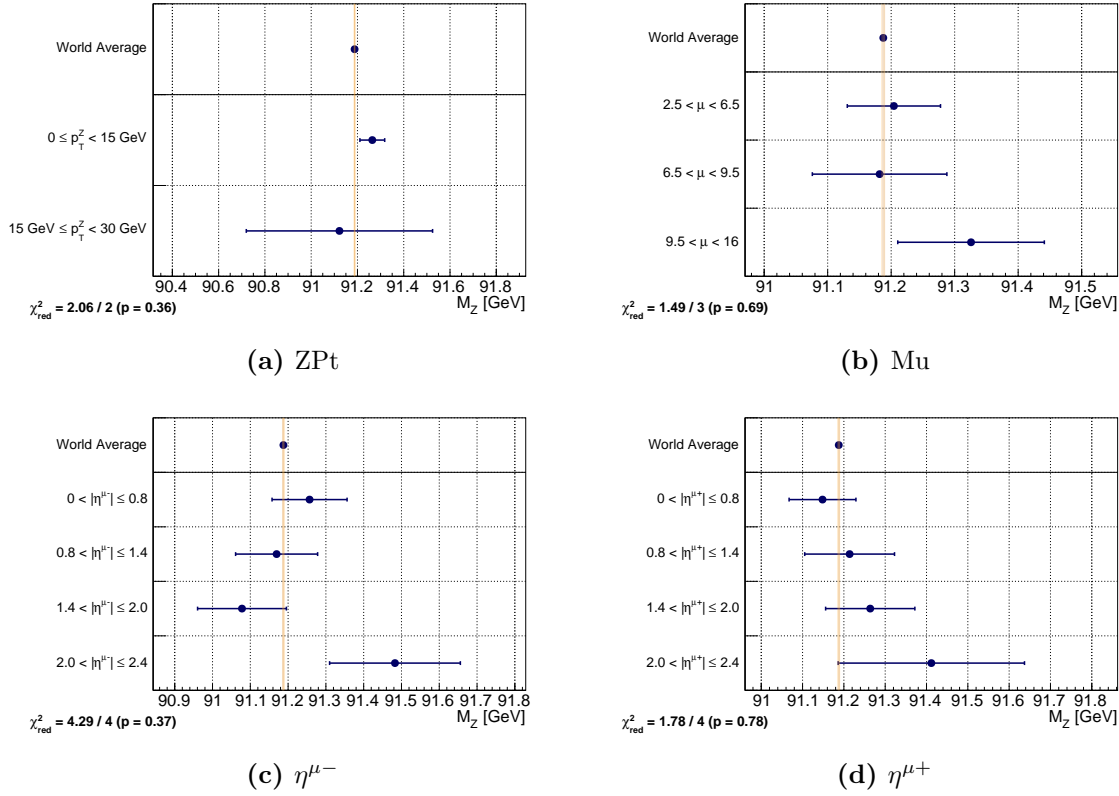


Figure 12.8.: Overview of the fit results obtained in the observable E_T^{miss} . For comparison, the current value and uncertainty of the world average (cf. ref. [8]) is also shown. In addition, the resulting value of χ_{red}^2 and the probability of a χ^2 test comparing the obtained results and the world average are shown. For this test, only the statistical uncertainties, without any possible correlations, were considered. From left to right, top to bottom, results separated for the two regions of p_T^Z , three regions of pile-up, four regions of η^{μ^-} and η^{μ^+} are shown.

12.6. Results

Table 12.4 shows the full result, including the statistical and systematic uncertainties. As can be seen, the data statistical uncertainty is one of the leading contributions to the final uncertainty. The Monte Carlo statistical uncertainty is smaller by a factor of approximately two, as is expected since the Monte Carlo simulation contains approximately six times more events than the data sample. Assuming a Poissonian process, this leads to a decrease in uncertainty by a factor of $\sqrt{6} = 2.4$. The uncertainty due to the background subtraction is very small, since the selection leads to an almost background-free sample. Note that both the Monte Carlo as well as background statistical uncertainty is treated as a systematic uncertainty on the final result, since it will not change with any new data measured.

One of the remaining sources of systematic uncertainty is the uncertainty on the cross-sections used in the background subtraction. Also here, the uncertainties are negligible due to the small levels of background observed in the analysis. Naturally, the uncertainty due to the correction of the hadronic recoil can only play a significant role in the observables in which the hadronic recoil is used — these are the W -like observables m_T and E_T^{miss} . However, judging from the results, also here the uncertainty on the hadronic recoil plays only a minor role.

The uncertainty on the muon momentum scale calibration can, in principle, have a large impact on M_Z , because in all cases p_T^μ enters the observed mass directly. However, since these values could be obtained with high precision, the uncertainty is leading only in the case of the measurement through the invariant mass of the muon pair, since this observable is essentially unaffected by modeling effects. Mis-modeling of the muon momentum smearing, on the other hand, plays no significant role.

The uncertainty connected to the application of the muon trigger, reconstruction and isolation scale factors, which were obtained as part of this thesis, plays a significant role in the W -like observables, which are sensitive to detector modeling effects. Since the Z boson selection requires one muon to be matched to the trigger, the effect of the trigger scale factors is weaker than has to be expected in the measurement of M_W . This is because the uncertainty on the scale is a function of the cut efficiency.

This can be understood by making the following approximation: the scale factor uncertainty is in general dominated by the statistical uncertainty on the data efficiency. Whether one muon will pass or fail a given cut can be seen as a Bernoulli experiment, which gives rise to a binomial distribution $\mathcal{B}(k; N, p)$. In this model, k corresponds to the number of candidates passing the cut N_{acc} , N to the total number of candidates N_{all} and p the cut efficiency ε . The uncertainty on the estimation of ε can then be approximated as:

$$\Delta\varepsilon = \sqrt{\frac{\varepsilon(1-\varepsilon)}{N}} \quad (12.1)$$

In the measurement of M_Z , the cut efficiency of the trigger requirement is on the order of 100 %, while for the measurement of M_W , it is on the order of 70 %. Therefore, the uncertainty of the trigger scale factors will play a much larger role in the measurement of M_W . Of all three sets of scale factors, the muon reconstruction scale factors have the largest impact on the total uncertainty of M_Z . This can be understood by keeping in mind that the muon reconstruction efficiency is significantly smaller than the isolation efficiency.

M_Z [MeV], Fit in ...	$m_{\mu\mu}$	p_T^μ	$p_T^{\mu-}$	$p_T^{\mu+}$	m_T	m_T^-	m_T^+	E_T^{miss}
Nominal	91186.5	91200.8	91180.9	91221.5	91222.3	91193.0	91254.8	91218.2
Interpolation	< 1	< 1	< 1	< 1	< 1	< 1	< 1	< 1
StatData	3.4	12.1	19.3	17.7	25.4	32.7	31.7	43.5
StatMC	1.7	5.1	7.2	9.0	10.2	15.8	16.5	23.7
StatBkg	< 1	< 1	< 1	< 1	< 1	< 1	< 1	< 1
CS	< 1	< 1	< 1	< 1	< 1	< 1	< 1	< 1
HRScale	< 1	< 1	< 1	< 1	< 1	< 1	< 1	4.3
IsolationEfficiency	< 1	1.2	1.5	1.6	2.1	2.7	2.5	1.8
MuonScale	3.7	3.7	3.6	3.7	3.7	3.7	3.8	3.9
MuonSmearing	< 1	< 1	< 1	< 1	< 1	< 1	< 1	< 1
PDF	< 1	15.7	15.4	15.9	26.6	26.2	26.7	24.8
RecoEfficiency	< 1	3.4	4.1	5.4	5.2	5.9	7.4	4.5
TriggerEfficiency	< 1	1.1	1.8	2.0	1.8	2.2	2.3	1.7
Tot. Sys. Unc.	4.1	17.3	18.0	19.6	29.3	31.6	32.7	35.2
Tot. Unc.	5.3	21.1	26.4	26.3	38.8	45.5	45.6	55.9

Table 12.4.: Fit results for M_Z in the inclusive fit region.

12. Validation with Z Bosons

The dominating uncertainty originates from the PDFs. This can be understood by considering the so-called forward-backward asymmetry (cf. ref. [110]). This asymmetry in the polar angle distribution of the decay muons arises due to the mixture of vector and axial-vector couplings in the process $q\bar{q} \rightarrow Z/\gamma^* \rightarrow \mu^+\mu^-$. This effect depends on the flavor and charge of the incoming particle, and therefore on the PDFs.

From Table 12.4, the deviations between the fit results and the world average of M_Z can be calculated. This is performed in Table 12.5. As can be seen, no significant deviations could be detected. Note that in this comparison, several observables show a strong correlation. Since the overall agreement is excellent, no attempt at a combination of significances was performed.

Observable	M_Z [MeV]	ΔM_Z [MeV]	Deviation from world average [MeV]	Significance
$m_{\mu\mu}$	91186.50	5.31	-1.1	-0.19
p_T^μ	91200.82	21.12	13.2	0.62
$p_T^{\mu-}$	91180.85	26.42	-6.8	-0.26
$p_T^{\mu+}$	91221.49	26.34	33.9	1.28
m_T	91222.33	38.77	34.8	0.90
m_T^-	91192.95	45.48	5.3	0.17
m_T^+	91254.83	45.55	67.2	1.47
E_T^{miss}	91218.19	55.92	30.6	0.55

Table 12.5.: Overview of the deviations between the fit results and the world average (cf. ref. [8]) of M_Z .

13. First Measurement of the Mass of the W Boson

As already discussed in Section 6.3, the analysis was performed on a limited data-set of 100 pb^{-1} , since not all corrections have been finalized at the time of writing¹. This increases the statistical uncertainty from data by a factor s , which can be calculated assuming a Poissonian distribution via:

$$s = \sqrt{\frac{L_{\text{sel}}}{L_{\text{full}}}} = \sqrt{\frac{0.10 \text{ fb}^{-1}}{4.58 \text{ fb}^{-1}}} = \frac{1}{6.77} \quad (13.1)$$

This means that the statistical uncertainty using the full data set would be smaller by a factor of 6.77.

As in the measurement of M_Z , the measurement of M_W was performed several bins in order to test for internal consistency. These bins are summarized in Table 13.1. Note that, unlike in the case of M_Z , the transverse momentum of the vector boson cannot be measured directly. Instead, it is estimated via momentum conservation from the size of the hadronic recoil, i.e. $p_T^W = -HR$. This introduces a significant decrease in the resolution of p_T^W with respect to p_T^Z .

Observable	Bin borders				
p_T^W	0 GeV	15 GeV	30 GeV		
η^μ	0	0.8	1.4	2.0	2.4
μ	2.5	6.5	9.5	16	

Table 13.1.: Bin definitions for the measurement of M_W . Note that μ is the standard ATLAS notation for the average number of interactions per bunch crossing.

13.1. Selection

The event selection for the measurement of M_W is very similar to that of the cross-check measurement of M_Z . As was the case there, the selection consists of an event selection and a selection of suitable muon candidates. Out of the events passing the following selection criteria, a representative sub-sample corresponding to 100 pb^{-1} was selected. Selecting a representative sub-sample is of special importance, since significant differences between certain periods in data could be observed (cf. Section 8).

- **Good Run List:** As in the cross-check measurement of M_Z , the GRL applied was `DATA11_7TeV.PERIODALLYEAR_DETSTATUSV36PRO10_COOLRUNQUERY-00-04-08_WZJETS_ALLCHANNELS_DTOM.XML`, corresponding to an integrated luminosity of 4.58 fb^{-1} .

¹A fully unblinded analysis using the full 2011 data-set is currently under preparation.

13. First Measurement of the Mass of the W Boson

- **Vertex:** The primary vertex was required to have at least three tracks originating from it.
- **Trigger:** The triggers used are the single muon triggers EF_MU18 for period D-I, and EF_MU18_MEDIUM for periods J-M.
- **Muon selection:** Exactly one pre-selected muon is required, with the pre-selection criteria reading:
 - **Combined muons:** Only staco muons flagged as combined by the reconstruction algorithm are selected.
 - **Object quality:** Several quality criteria, concerning for example the number of hits in the TRT, were applied. These criteria follow the recommendations from the ATLAS muon combined performance working group and are summarized in Table 6.3.
 - **Distance from primary vertex:** A cut was performed on the longitudinal distance of the track from the primary vertex, $|z_{0,PV}|$, with $|z_{0,PV}| < 10$ mm.
 - **Acceptance:** The muons were required to lie well within the acceptance of the ID, with $|\eta| < 2.4$.
 - **Isolation:** All muons were required to appear isolated, using the requirement $p_T^{\text{cone20}}/p_T < 0.1$.
 - **Momentum:** The minimal momentum required by the pre-selection is $p_T > 20$ GeV.
- **Trigger matching:** The selected muon has to be matched to a trigger object, with $\Delta R < 0.1$.
- **Jet veto:** Events are vetoed if a jet fulfilling the LOOSEBAD selection criteria is found within a cone of $\Delta R < 0.3$ around the selected muon.
- **LAr hole:** Events are vetoed if one of the jets in the event is close to the so-called LAr hole, a region in the calorimeter experiencing technical problems during the 2011 data taking.
- **Lar error:** Events are vetoed if a noise burst in the liquid argon calorimeter occurred.
- **Final cut muon momentum:** After all selection criteria are applied, a final cut on the transverse momentum of the muon was performed, with a cut at 30 GeV.
- **Final cut HR :** Events were vetoed if the size of the hadronic recoil in the event was larger than 30 GeV.
- **Final cut E_T^{miss} :** Events were vetoed if the size of the missing energy was smaller than 30 GeV.
- **Final cut m_T :** Events were vetoed if the size of the transverse mass was smaller than 60 GeV.

The resulting cut-flows for data, signal and background samples are shown in Table 13.2 for the muon pre-selection and in Table 13.3 for the event selection. As can be seen, the level of background observed in the W boson selection is much larger than compared to the Z boson selection. Especially the background admixture from $Z \rightarrow \mu\mu$ events plays a dominant role².

²Note that these estimates were obtained by performing the analysis on the full 2011 data-set before the selection of the 100 sub-sample was performed, and then scaled to the integrated luminosity of the sub-sample.

	Data	$W^- \rightarrow \mu^- \bar{\nu}$	$W^+ \rightarrow \mu^+ \nu$	Single Top	$t\bar{t}$	$W \rightarrow \tau\nu$	Diboson	$Z \rightarrow \mu\mu$	$Z \rightarrow \tau\tau$
All	2 346 511.6	188 043.4	295 250.4	712.0	4 111.2	22 351.6	1 055.6	117 937.5	4 448.6
Combined	2 338 404.3	184 269.1	289 212.3	696.2	4 010.6	21 906.1	1 024.6	111 182.0	4 346.4
Quality	2 298 340.4	182 406.6	286 333.1	687.6	3 957.0	21 687.6	1 012.6	109 713.1	4 301.5
z_0	2 274 297.9	180 528.7	283 264.4	686.5	3 956.4	21 359.6	1 010.5	109 371.1	4 267.4
η	2 247 063.8	177 424.4	278 161.8	682.0	3 934.5	20 993.4	995.7	106 333.2	4 196.1
Isolation	966 057.4	176 160.2	276 118.8	610.6	3 368.5	20 795.5	966.6	105 562.1	4 157.7
$p_T^\mu > 20$ GeV	947 974.5	175 482.9	274 739.5	608.2	3 357.6	20 388.6	963.0	105 267.0	4 085.5

Table 13.2.: Number of pre-selected muons per cut for each sample used in the measurement of M_W . All numbers are scaled to the integrated luminosity of the analyzed data sample. *Single top* consists of all seven single top samples (production 108340-108346), while *Diboson* consists of the WW , WZ and ZZ samples.

	Data	$W^- \rightarrow \mu^- \bar{\nu}$	$W^+ \rightarrow \mu^+ \nu$	Single Top	$t\bar{t}$	$W \rightarrow \tau\nu$	Diboson	$Z \rightarrow \mu\mu$	$Z \rightarrow \tau\tau$
Before Selection	2 666 829.8	430 000.0	616 000.0	3 621.0	13 730.0	153 367.0	2 937.0	99 000.0	26 042.0
GRL	2 425 893.6	430 000.0	616 000.0	3 621.0	13 730.0	153 367.0	2 937.0	99 000.0	26 042.0
Vertex	2 421 766.0	427 927.8	612 461.6	3 618.9	13 725.0	152 600.0	2 931.5	98 420.9	25 950.8
Trigger	2 291 276.6	196 652.5	314 103.6	732.2	3 938.3	28 808.1	982.8	72 042.8	5 417.9
Veto	871 810.6	175 476.3	274 733.1	586.6	3 008.8	20 387.4	771.7	29 858.7	3 895.1
Matching	869 495.7	175 438.5	274 675.3	582.3	2 964.2	20 381.8	767.9	28 863.8	3 883.8
Jets	864 817.0	173 274.1	271 269.3	574.4	2 924.6	20 129.7	757.5	28 447.3	3 830.5
LAr Hole	863 100.0	173 121.5	271 061.0	570.0	2 880.0	20 107.4	753.6	28 420.0	3 819.5
LAr Error	860 691.5	173 121.5	271 061.0	570.0	2 880.0	20 107.4	753.6	28 420.0	3 819.5
$p_T^\mu > 30$ GeV	379 610.6	126 937.2	182 294.5	428.5	2 283.6	6 065.1	571.8	19 049.4	1 336.3
$HR < 30$ GeV	328 655.3	115 467.9	166 961.4	169.9	618.5	4 682.8	335.8	16 990.0	961.4
$E_T^{\text{miss}} > 30$ GeV	220 491.5	84 387.8	120 907.2	117.3	448.4	2 420.6	237.9	11 474.5	283.8
$m_T > 60$ GeV	216 812.8	83 238.2	119 027.8	112.5	433.8	2 279.8	231.7	11 291.5	261.3

Table 13.3.: Number of selected events per cut for each sample used in the measurement of M_W . All numbers are scaled to the integrated luminosity of the analyzed data sample. *Single top* consists of all seven single top samples (production 108340-108346), while *Diboson* consists of the WW , WZ and ZZ samples.

13.2. Background Estimation

13.2.1. Multi-Jet Background

Unlike in the measurement of M_Z , the background from QCD processes plays a significant role in the measurement of M_W . As was the case in the analyses discussed in Chapter 6, the multi-jet, or QCD, background has to be estimated through data-driven methods. This is because the existing samples have a large intrinsic theoretical uncertainty, and because the number of simulated events is too small for the purpose of this analysis.

The estimation of the QCD background consists of two steps: as a first step, a background-enriched template has to be generated from data. Since only part of the full data set is used, this template only contains a fraction of the full 2011 data-set. The template was obtained by inverting the isolation cut to $p_T^{\text{cone20}}/p_T > 0.2$, and by dropping the cut on E_T^{miss} , m_T and p_T^W . In this way, the amount of background could be sufficiently increased. From the QCD template, all contributions already described by the electroweak and top Monte Carlo were subtracted.

The second step is the calculation of the correct normalization factor. This normalization factor is obtained through a fit in E_T^{miss} , where special care has been taken that the estimation of the normalization factor is independent of the final fit of M_W . This is achieved by selecting a control region for the fit of $0 \leq E_T^{\text{miss}} \leq 30$ GeV, whereas the fit to obtain the M_W mass ranges from $30 \text{ GeV} \leq E_T^{\text{miss}} \leq 80$ GeV. The normalization factor was obtained for each fit region independently, where each region was defined in Table 13.1. The uncertainty associated with this normalization factor was obtained by shifting the lower and upper border of the control region in steps of 1 GeV from 0 GeV to 15 GeV, and from 30 GeV to 15 GeV, respectively. The largest deviation with respect to the nominal control region was taken as uncertainty. Figure 13.1 shows the result of the fit performed in the *Inclusive* region.

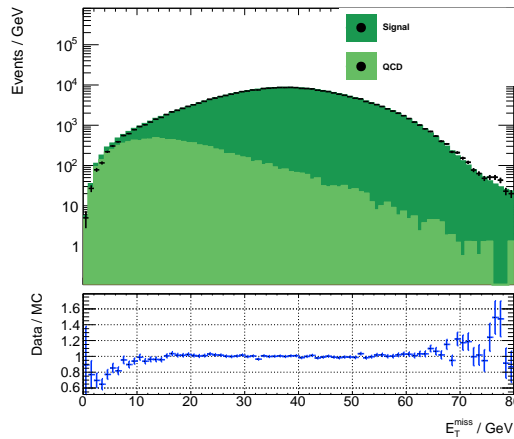


Figure 13.1.: Example of the E_T^{miss} spectrum, used to estimate the amount of QCD background events. In this plot, *QCD* refers to the QCD template obtained as described in the text, while *Signal* refers to the contributions estimated via Monte Carlo, including the signal process and the electroweak and top background processes. As can be seen, the QCD background is expected to have a smaller value of E_T^{miss} than the signal events.

As can be seen, the description of the E_T^{miss} spectrum by the combined QCD template and remaining Monte Carlo contributions is in general very good, with the exception of the region close to $E_T^{\text{miss}} \sim 0$. Here, the description worsens significantly and might hint at insufficiencies in the QCD template in this kinematic region. Similar deviations have to be expected in a data-driven method, since the selection for obtaining the QCD template has to differ from the default selection. This means that regions in which the background composition for the QCD and default selection differ, will be challenging to model. In this case, this might be the case in the region of $E_T^{\text{miss}} \sim 0$, a region in which background events containing W bosons are suppressed. However, the contribution of this region to the total number of events in the fit region is small.

The resulting fraction of the QCD background is summarized in Table 13.4. As can be seen, the level of QCD background admixture is in general on the level of 5%, with a relative uncertainty fluctuating largely between 2% and 22%. This shows that the QCD background estimation is challenging, especially when working with a limited data set. The uncertainty was estimated by varying the fitting range, with its lower value scanning the range 0 GeV to 15 GeV, and the upper value the range 30 GeV to 15 GeV, as well as taking the maximum deviation from the result obtained in the nominal fit range.

In the final measurement, in addition to the uncertainty on the multi-jet background normalization, an additional uncertainty on the shape of the multi-jet background should be considered. This uncertainty can, in principle, be estimated through a modified selection of the multi-jet background template. In the case of the limited data sample used here, this shape uncertainty can be neglected. An additional upgrade of this method is also the estimation of different background for the μ^+ and μ^- case. Both cases are not symmetric, since the production cross section for W^+ at ATLAS is significantly larger than for W^- (cf. Table 5.2) due to the fact that proton-proton interactions are used.

Region	$N_{QCD}/N_{Data}[\%]$	$\Delta_{rel} [\%]$
Inclusive	5.48	3.6
Eta1	4.62	7.9
Eta2	8.24	5.9
Eta3	5.37	4.5
Eta4	4.66	6.9
Mu1	5.32	5.1
Mu2	4.53	1.9
Mu3	5.69	4.1
WPt1	6.23	21.7
WPt2	6.44	4.1

Table 13.4.: Overview of the estimated fraction of QCD background events in each fit region.

13.3. Control Plots

The control plots for the selection discussed above are shown in Figure 13.3. As can be seen, the distributions are dominated by the $W^+ \rightarrow \mu^+ \nu_\mu$ and $W^- \rightarrow \mu^- \bar{\nu}_\mu$ signal contributions, with a visible admixture of background, especially from the $Z \rightarrow \mu\mu$ process. As can also be seen, the uncertainty in the ratio is on the order of one percent and more, which will be reduced when using the full data set.

Overall, a good description of data can be achieved, as can also be seen through the value of χ_{red}^2 , which is generally on the order of unity. A notable exception is the transverse momentum of the W -boson. This is very similar to the case of the Z boson, and is caused by the challenges connected to simulating the transverse momentum of the exchange boson. Note that the value of p_T^W has to be measured indirectly from the size of the hadronic recoil. This means that the uncertainty in the measurement of the hadronic recoil leads to a decrease of the resolution of p_T^W . The transverse mass m_T peaks around M_W and shows a low resolution stemming from the resolution of E_T^{miss} , a fact also visible when comparing the distribution of p_T and E_T^{miss} . On truth levels, both distributions are equal, but due to the challenges connected with measuring E_T^{miss} (cf. Section 4.5.5), the resolution is much worse. Lepton η is the distribution most sensitive to detector mis-modeling effects. As can be seen, the muon efficiency scale factors obtained as part of this thesis lead to an excellent description of this variable. In the case of lepton φ , the description is significantly worse. The difference, however, is well within the full systematic uncertainty. A control plot containing the latter is shown in Figure 13.2. The estimate of the systematic uncertainty in this plot is obtained by combining all systematic uncertainties bin-by-bin.

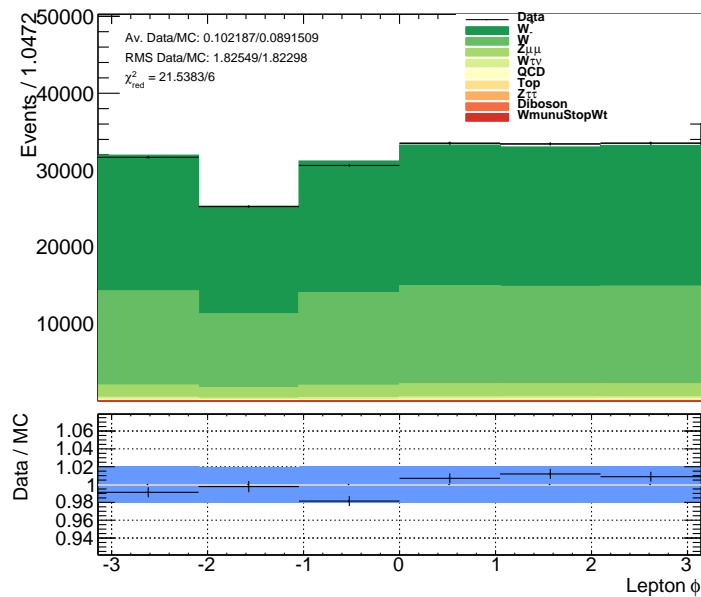


Figure 13.2.: Control plot for lepton φ , including the full systematic uncertainty. In addition to the plots shown in Figure 13.3, the additional systematic uncertainty is shown as a blue band in the ratio.

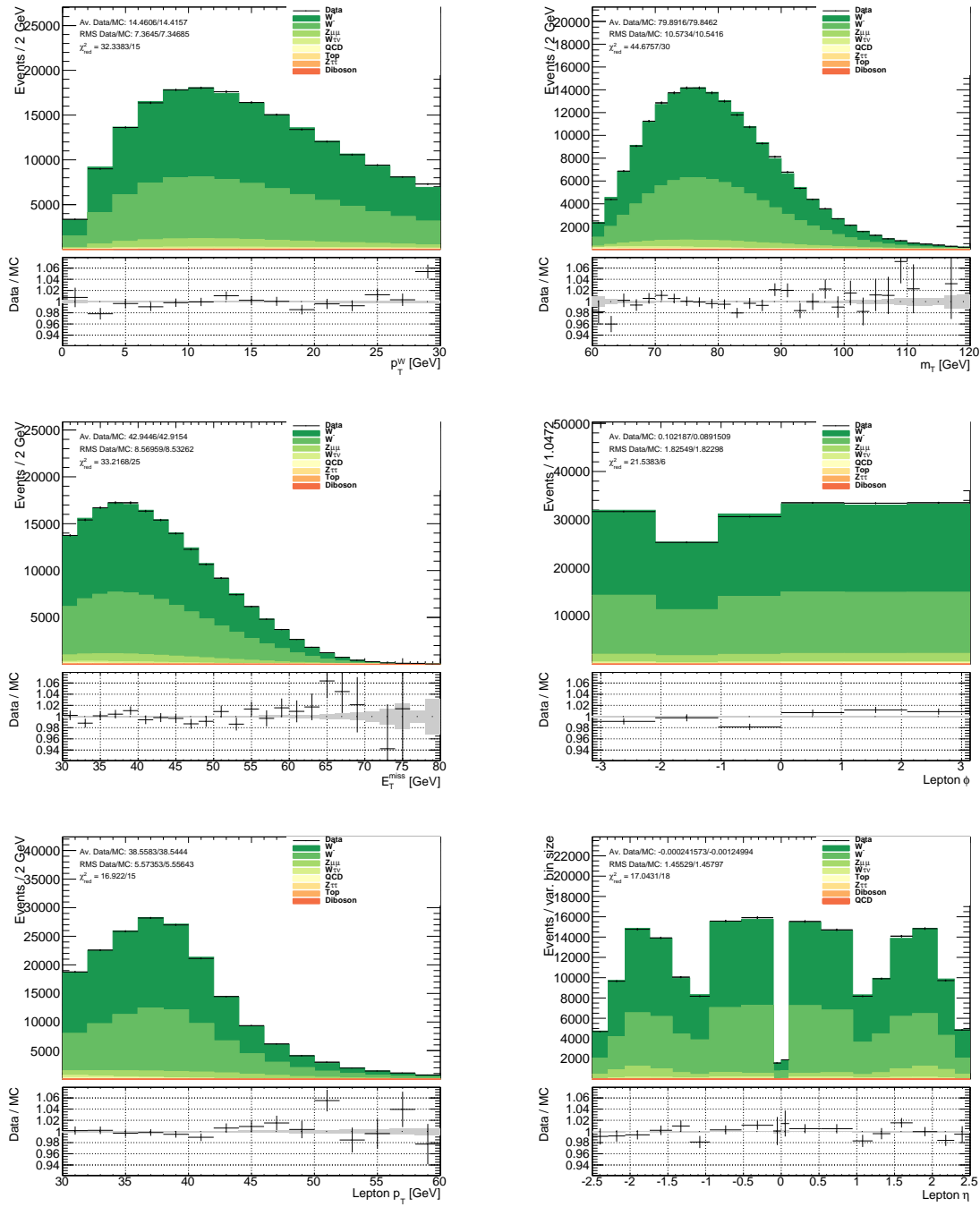


Figure 13.3.: Control Plots for $W \rightarrow \mu\nu$. From left to right, top to bottom: p_T^W , m_T , E_T^{miss} , ϕ , p_T^μ , η . In the ratio, the gray band denotes the statistical uncertainty from the combined Monte Carlo and background stack, while the error bars denote the uncertainty from data. Only the statistical uncertainty is shown and used for the χ^2 test shown in each control plot. This test shows the compatibility of the observation and prediction for each distribution.

13.4. Monte Carlo-based Cross-Checks

As was the case in the measurement of M_Z , the stability of the fitting approach, as well as the accuracy of the estimation of the three different sources of statistical uncertainty, was tested by performing a pure Monte Carlo study. To this end, the data was replaced by pseudo-data obtained from signal Monte Carlo. In this way, the internal consistency of the fitting package could be tested.

13.4.1. Numerical Stability

The additional uncertainty due to the interpolation discussed in Chapter 11.2 is estimated by replacing the data template with a Monte Carlo template. In this way, the fit is expected to yield exactly the injected value of 80.399 GeV. Any deviation from this value can be seen as inaccuracy. As can be seen in Figure 13.4(a), these deviations are below 1 MeV and therefore do not play a role in this analysis. Moreover, the observed deviations are larger in observables and regions in which less sensitivity to the mass of the W boson is expected, since these settings are connected with flatter χ^2 parabolas, leading to a larger uncertainty on the interpolated minimum.

As was the case in the Z -based cross-check (cf. Section 12.4), a small bias is discernible. In this case, this might also be attributed to the interpolation method, by which the minimum of the χ^2 parabola is estimated from the sampling points obtained with the different Monte Carlo templates. This interpolation is performed via a χ^2 fit, in which each point is weighted by the same value.

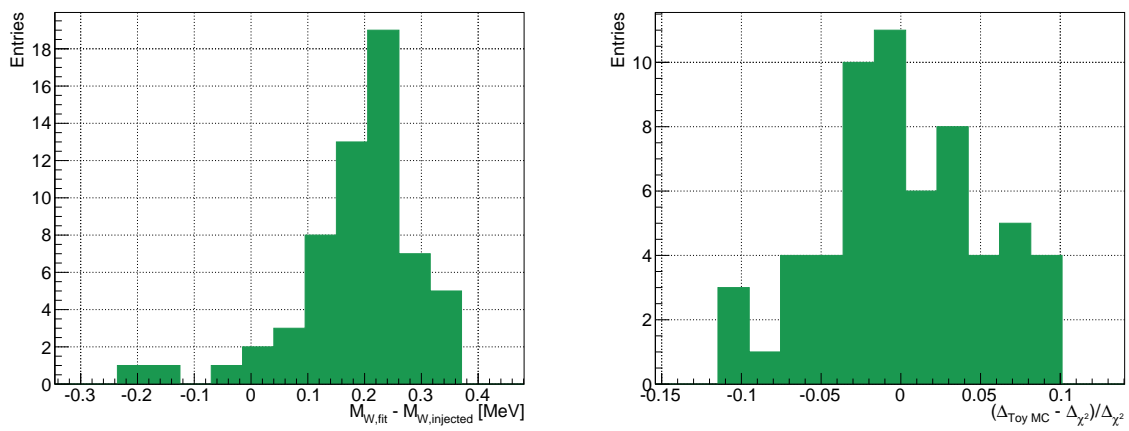
13.4.2. Estimation of Statistical Uncertainty

As discussed above, the statistical uncertainty can, in principle, be obtained from the width of the χ^2 parabola. Since this approach leads to a loss of all information concerning the contributions from data, Signal MC and background estimation, a Toy MC method was applied.

Four quantities are obtained:

- Δ_{χ^2} : uncertainty estimated from the width of the χ^2 parabola
- $\Delta_{\text{ToyMC}}^{\text{Data}}$: statistical uncertainty from data, estimated with the Toy MC method
- $\Delta_{\text{ToyMC}}^{\text{Bkg}}$: statistical uncertainty from background, estimated with the Toy MC method
- $\Delta_{\text{ToyMC}}^{\text{MC}}$: statistical uncertainty from Signal MC, estimated with the Toy MC method

In a cross-check, the three Toy MC uncertainties are added in quadrature and compared to the total uncertainty estimated from the width of the χ^2 parabola. This is shown in Figure 13.4(b). The regions cited in this plots are defined as in Table 13.1. It can be observed that the statistical uncertainties from both methods differ by less than 10% on average.



- (a) Comparison of the nominal values and the values obtained by the fit to pseudo-data in the measurement of M_W . (b) Distribution of total statistical uncertainty obtained with the Toy MC method and from the width of the χ^2 parabola. For the definition of the regions see Table 13.1.

Figure 13.4.: Results from the Monte Carlo-based cross-checks.

13.5. Data-based Cross-Checks

The final result of this thesis will be a best estimator for M_W . To justify the reduction of the full analysis into a single number, two prerequisites have to be met. On the one hand, the fit results obtained in the different observables have to agree with one other — any significant deviation has to be taken as a hint of a possible mis-modeling of either the physics processes or the detector simulation. On the other hand, and for the same reason, no dependence on the variables η^μ , p_T^W or pile-up, binned as defined in Table 13.1, must exist for each observable. These variables were chosen, because possible mis-modelings would be most clearly visible in these variables. For example, the muon reconstruction and trigger efficiencies show in part a strong dependence on η — any mis-modeling of this dependence might therefore be most clearly visible if the resulting values of M_W were obtained with respect to these variables.

Figure 13.5 shows an overview of the fit results obtained in the inclusive region. As can be seen, all results are compatible with each other, with a resulting χ^2 probability of 0.90. However, it has to be noted that the small value of χ^2 is in part also due to the correlations between these variables. For example, m_T is constructed from lepton p_T and E_T^{miss} .

Figure 13.6 gives an overview of the best and worst fitting templates, as well as the resulting χ^2 parabola. Since the width of the χ^2 parabola is a measure of the sensitivity of the observable to the mass of the W boson, lepton p_T emerges as most sensitive observable, followed by m_T and E_T^{miss} .

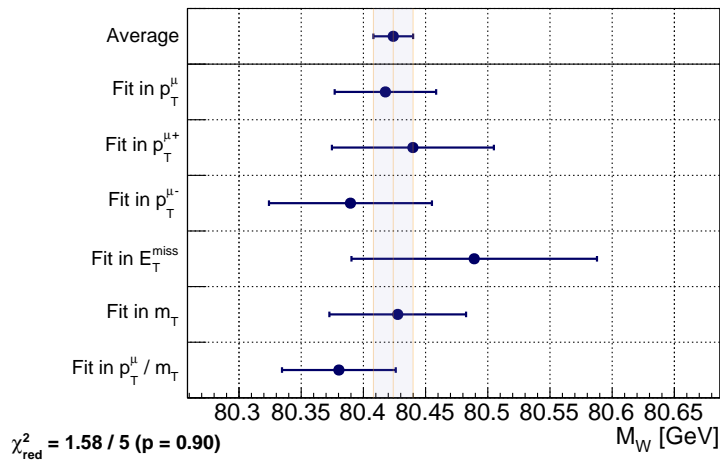


Figure 13.5.: Overview of the fit results for all observables in the *Inclusive* region. Also shown is the result of χ^2 test of all values against their mean, together with the resulting test probability.

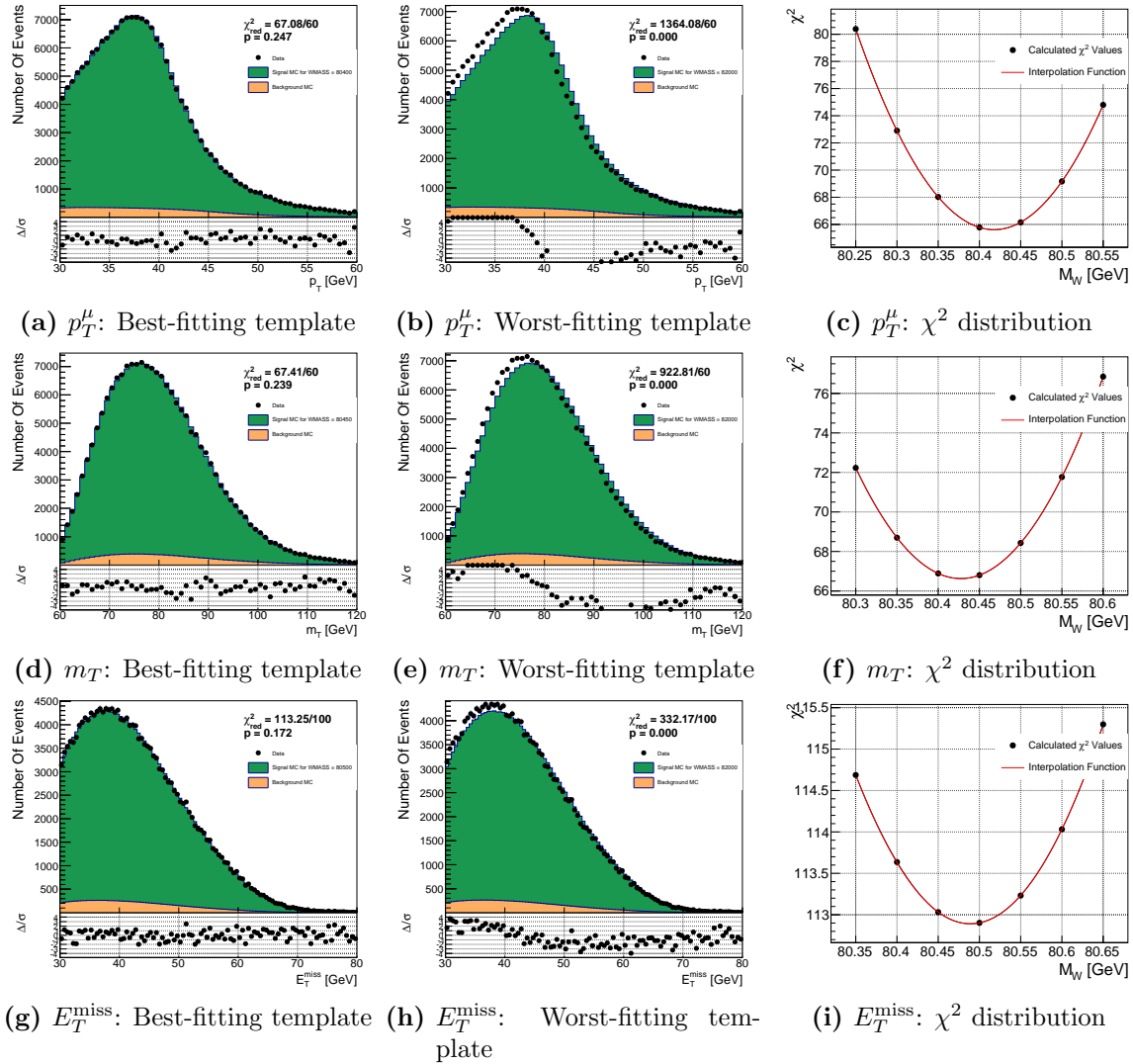


Figure 13.6.: Selected control plots from the consistency tests. Each row shows the template with the lowest value of χ^2 when compared to data, the template with the highest value of χ^2 when compared to data, and the resulting distribution of values of χ^2 for each template. From top to bottom the fit in lepton p_T , transverse mass m_T and missing transverse energy E_T^{miss} .

13. First Measurement of the Mass of the W Boson

Figure 13.7 show the results obtained in the observable p_T^μ . If separated with respect to p_T^W , both $p_T^{\mu^+}$ and $p_T^{\mu^-}$ lead to compatible results. Note that in both bins similar uncertainties on M_W are obtained. This is unlike the hierarchy observed in the measurement of M_Z , where the uncertainty in the low p_T^Z bin was significantly smaller. It is possible that this is due to the fact that p_T^W has to be estimated indirectly from the hadronic recoil, whereas p_T^Z could be estimated with high precision from the momenta of μ^+ and μ^- . This leads to a significant uncertainty on the measurement of p_T^W . If separated into the three pile-up bins, as well as into the four η^μ bins, no significant structures or deviations from the mean are visible.

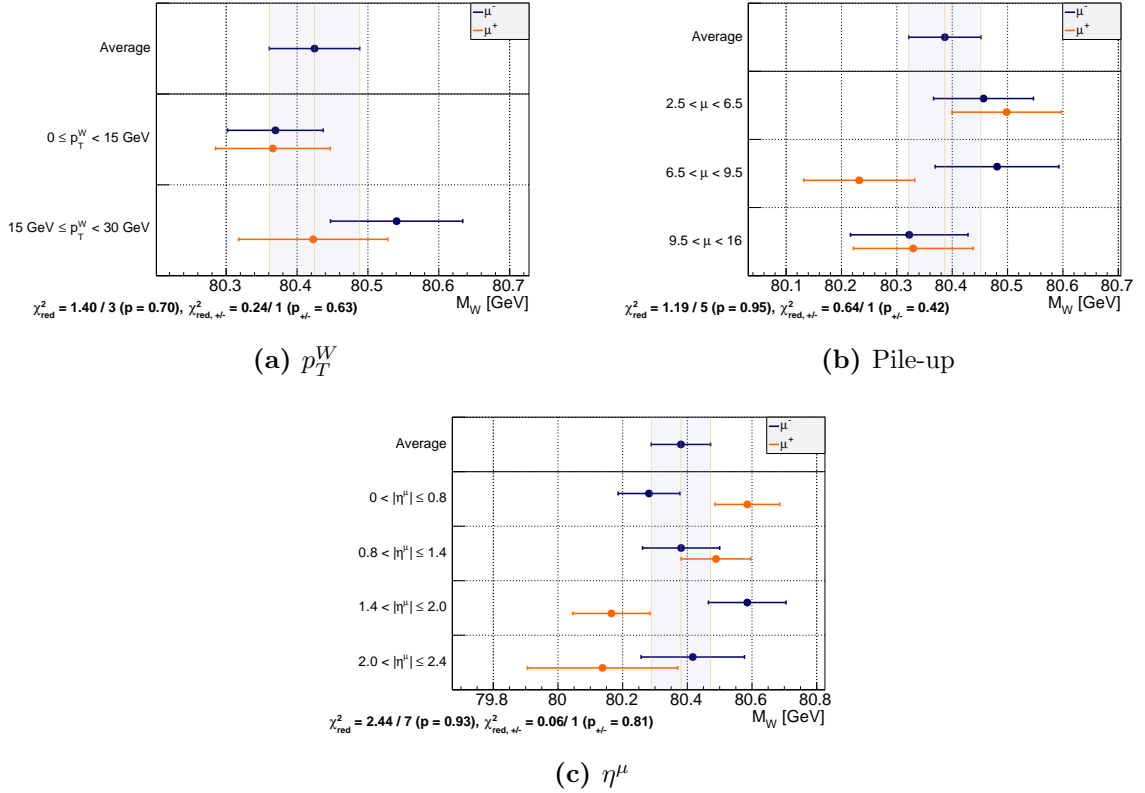


Figure 13.7.: Overview of the fit results obtained in the observable $p_T^{\mu^+}$ (orange) and $p_T^{\mu^-}$ (blue). In addition, the resulting value of χ^2_{red} and the probability of a χ^2 test comparing the obtained results and their mean are shown. Additionally, the result of a χ^2 test comparing the results for μ^+ and μ^- is also shown. For these tests, only the statistical uncertainties, without any possible correlations, were considered. From left to right, top to bottom, results separated for the two regions of p_T^W , three regions of pile-up and four regions of η^μ are shown.

Figure 13.8 shows the results in the observable m_T . As can be seen, no significant deviations or structures with respect to the mean are visible. This is also mirrored in the obtained values of χ_{red}^2 , which are mostly well-compatible with unity. Only in the case of the pile-up, a larger discrepancy can be seen. However, with a test probability of 22%, the result is not yet significant.

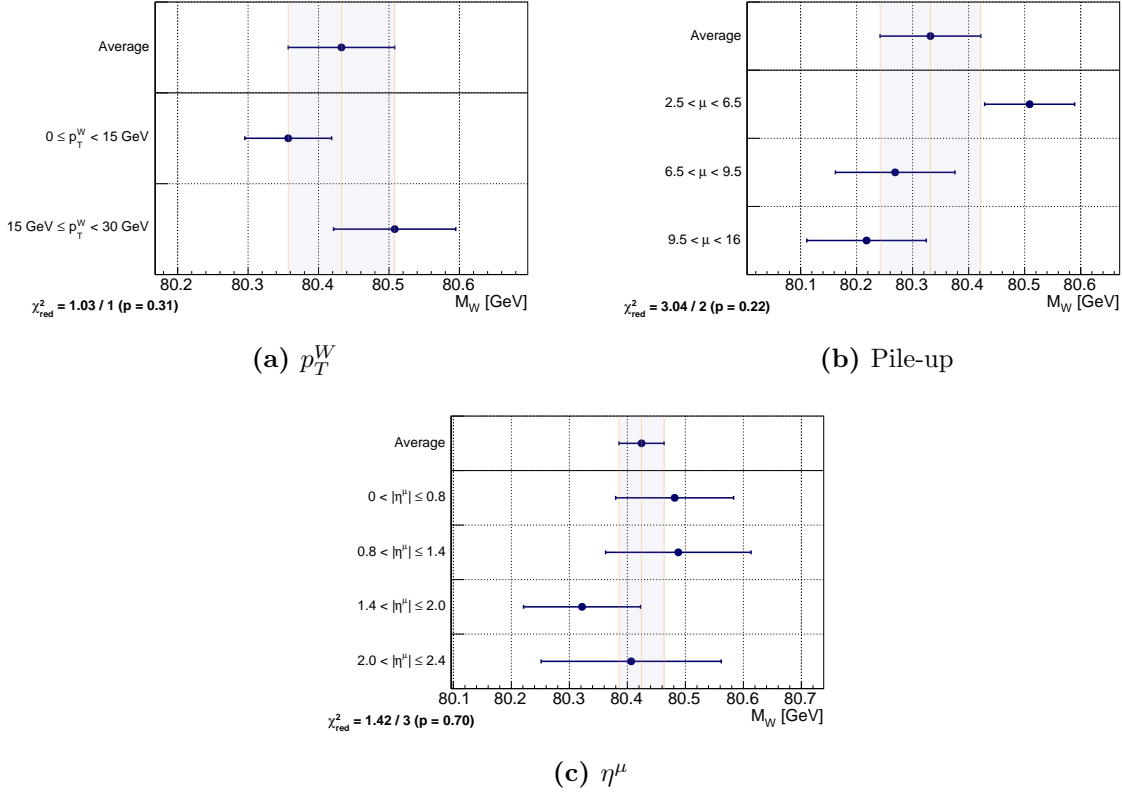


Figure 13.8.: Overview of the fit results obtained in the observable m_T . In addition, the resulting value of χ_{red}^2 and the probability of a χ^2 test comparing the obtained results and their mean are shown. For these tests, only the statistical uncertainties, without any possible correlations, were considered. From left to right, top to bottom, results separated for the two regions of p_T^W , three regions of pile-up and four regions of η^μ are shown.

13. First Measurement of the Mass of the W Boson

Figure 13.9 shows the results in the observable E_T^{miss} . As can be seen, the results obtained in the two bins in p_T^W , as well as in η^μ are well compatible with each other. If binned against the three pile-up bins, a hint at a mis-modeling can be detected, with a χ^2 test probability of 17%. This, however, is not statistically significant.

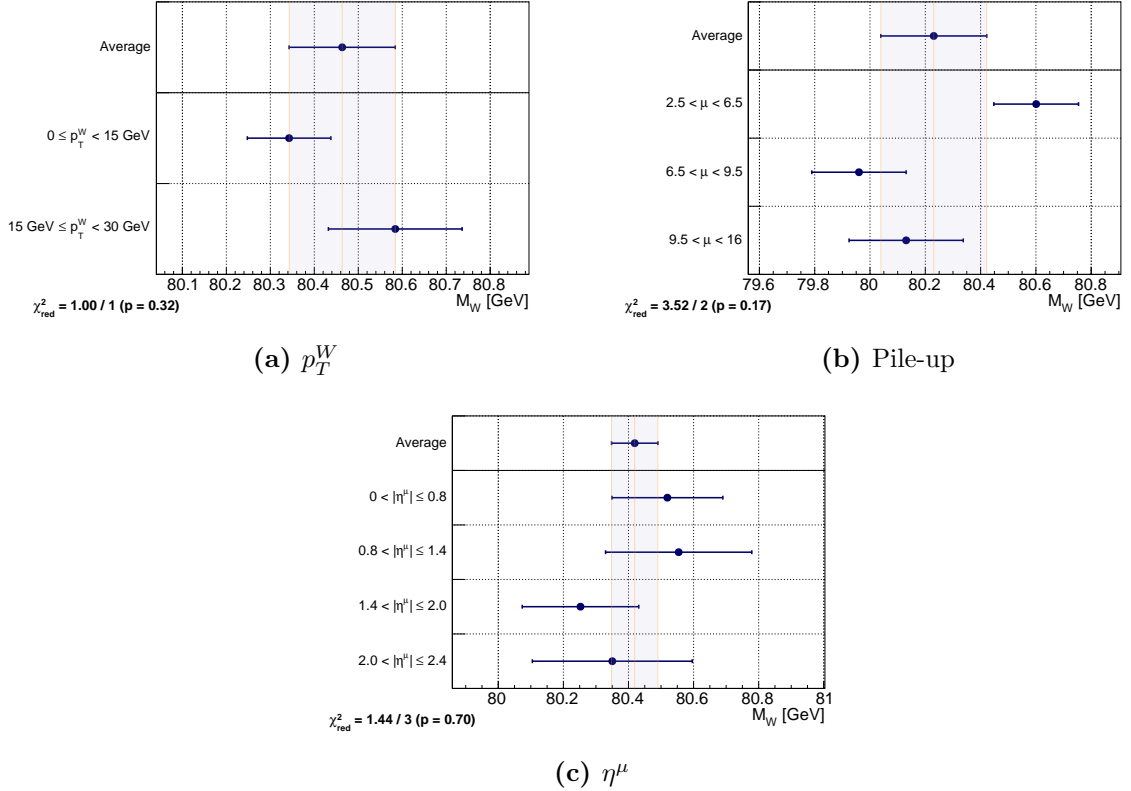


Figure 13.9.: Overview of the fit results obtained in the observable E_T^{miss} . In addition, the resulting value of χ_{red}^2 and the probability of a χ^2 test comparing the obtained results and their mean are shown. For these tests, only the statistical uncertainties, without any possible correlations, were considered. From left to right, top to bottom, results separated for the two regions of p_T^W , three regions of pile-up and four regions of η^μ are shown.

13.6. Result

Since the consistency tests in the last section showed no significant deviations that hint at a possible mis-modeling on part of the physics processes nor on the detector reconstruction, using only the results from the *Inclusive* region is justified. These results, as well as the estimated uncertainties, are presented in Table 13.5. These results have already been illustrated for the reason of testing their consistency in Figure 13.5. The result in the combined (p_T^μ, m_T) fit are very interesting: On one hand, the resulting value for M_W is smaller than for both the fit in p_T^μ and m_T , which can easily be understood through the strong positive correlation between both variables. On the other hand, and for the same reason, the uncertainty on the combined result is on the same order as that for p_T^μ and m_T . This can be tested using the BLUE software package for combining correlated measurements (cf. ref. [111, 112]) under the assumption of a strong correlation³. It may be expected, that in the final result the uncertainty in the combined p_T^μ and m_T will be somewhat smaller than in both variables alone, since not all uncertainties are correlated between both observables.

M_W [MeV], Fit in ...	p_T^μ	$p_T^{\mu+}$	$p_T^{\mu-}$	m_T	E_T^{miss}	(p_T^μ, m_T)
Nominal	80417.7	80439.8	80389.6	80427.6	80489.2	80380.3
Stat. Unc. Data	40.3	64.9	65.2	54.1	97.5	45.4
Interpolation	< 1	< 1	< 1	< 1	2.1	< 1
Stat. Unc. MC	4.2	5.2	6.2	5.1	10.3	3.8
Stat. Unc. Background	5.1	< 1	1.6	8.2	11.6	4.5
Cross Section	13.4	14.7	13.3	13.2	10.8	13.1
Hadronic Recoil Scale	< 1	< 1	< 1	< 1	2.6	< 1
Isolation Efficiency	1.4	2.1	1.7	1.1	< 1	1.2
Muon Scale	3.4	3.4	3.4	3.5	3.3	3.4
Muon Smearing	< 1	< 1	< 1	< 1	< 1	< 1
PDF	14.7	20.6	19.9	13.8	10.3	13.2
Reconstruction Efficiency	4.2	4.7	3.9	3.4	1.8	3.8
Trigger Efficiency	6.2	8.6	8.6	4.9	3.1	5.6
Tot. Sys. Unc.	22.6	27.9	26.8	22.5	22.3	20.9
Tot. Unc.	46.1	70.6	70.5	58.6	100.0	49.9

Table 13.5.: Final result for the measurement of M_W .

The systematic uncertainties presented in this table exhibit a strong hierarchy, with the leading uncertainties being the PDF uncertainty and the Cross Section uncertainty, followed by the muon efficiency scale factor uncertainty. These will be discussed in detail below. It has to be kept in mind, that the systematic uncertainties will be added in quadrature. This means, that almost the full systematic uncertainty is due to these leading contributions. Compared to these, the Monte Carlo and Background statistical uncertainty play only a smaller role, and the interpolation uncertainty can be neglected.

³For the test, the full uncertainty was used with an assumed correlation factor of 0.99, yielding a combined estimate of (80391 ± 27) MeV. This indicates that the combined estimate can very well be smaller than both single estimates, given appropriate correlations between both values.

The remaining uncertainties are due to the modeling of the hadronic recoil, which plays a minor role in p_T^μ since it enters only through modifications of the acceptance of the selection. For m_T , and more importantly E_T^{miss} , the effect is larger because here the hadronic recoil is a direct input to the construction of these variables. Muon scale and smearing also play a minor role. This is because the muon scale could be obtained with high precision from $Z \rightarrow \mu\mu$ events, and muon smearing has only higher order effects on the observed value of M_W . All these uncertainties were estimated through purely Monte Carlo-based studies, since the final corrections obtained as part of the W boson mass measurement effort were not yet public at the time of writing. These estimates can be expected to be close to the final results. In that case, these uncertainties can also be expected to play only a minor role in the final result.

As discussed in Section 11.3.2, the uncertainty due to the modeling of p_T^W could not be assessed here. An additional uncertainty on the order of 6 MeV is expected from this source in the fit to p_T^μ . Compared with the leading uncertainties, this will lead to a small additional contribution. The modeling is performed by using data on p_T^Z and performing a propagation to p_T^W relying on perturbative QCD. A precise measurement of p_T^Z was performed at ATLAS with data gathered in 2012 (cf. ref. [113]). For this analysis supporting tasks were performed as part of this thesis.

As also discussed in Section 11.3.2, the uncertainty due to the correction of the angular coefficients were also not finalized at the time of writing, such that an assessment was not possible. However, only a negligible additional contribution is expected from these corrections.

13.6.1. PDF uncertainty

The leading contribution originates from the uncertainty on the proton structure as encoded in the PDFs. The uncertainties observed in the measurement agree with the expected values in Section 11.3.2, and are mostly due to the effect of the proton composition on the angular distribution of the decay products as discussed therein. Since this uncertainty plays a major role, improving the knowledge of the proton structure is essential. To this end, ATLAS can contribute by precise studies of the process $pp \rightarrow Z + X \rightarrow \ell^+ \ell^- + X$, especially by constraining the low and high range of Bjorken x in very asymmetric configurations where one lepton is emitted close to the beam axis.

At ATLAS, such a precision measurement is only feasible using electrons in the final state, since in this case the inner wheel of the Electromagnetic Calorimeter, as well as the Forward Calorimeter can be incorporated in the measurement. In this way, the full acceptance can be increased from $|\eta^e| < 2.47$ to $|\eta^e| < 4.9$. Necessary prerequisites for such a measurement on 2012 data are an identification method as well as the associated scale factors. Both have been developed as part of this thesis and are presented in Appendix A.

A further possibility is the usage of *PDF profiling* as described in ref. [114]. This technique allows the inclusion of new measurements to constrain the PDF uncertainty without needing to perform a full, updated PDF fit. In this way, new measurements performed by ATLAS, even including information gained in the analysis presented in this thesis, can be used to reduce the PDF uncertainty. It has to be noted that the PDF uncertainty shown here acts only as a first estimate on the PDF uncertainty in the final result, since the gluon information was missing in the analyzed samples.

Concerning the uncertainty on the PDFs, it can also be noted, that with respect to the results obtained for the Z boson (cf. Table 12.4), the systematic uncertainty in the observables m_T and E_T^{miss} , is significantly less. This is because the largest contribution to the PDF uncertainty

originates from leptons emitted close to $|\eta| = 0$. This can be seen in Figure 13.10, where in addition to the statistical uncertainty from MC, the systematic uncertainty originating from the PDFs is also shown. In the case of Z bosons, m_T and E_T^{miss} had to be modeled by treating one muon as neutrino. In this way, the accessible range of η is restricted to $|\eta| < 2.4$. On the other hand, the kinematics of the neutrino in W events is estimated from the full set of calorimeters, reaching $|\eta| < 4.9$. In this way, neutrinos emitted at higher values of $|\eta|$ can also be taken into account. This allows accessing values of η with reduced PDF uncertainty. As a side remark, this also indicates the potential of using the high $|\eta|$ range for measurements sensitive to the PDF uncertainty. A similar effect was observed in the measurement of the Z boson forward-backward asymmetry (cf. ref. [110]).

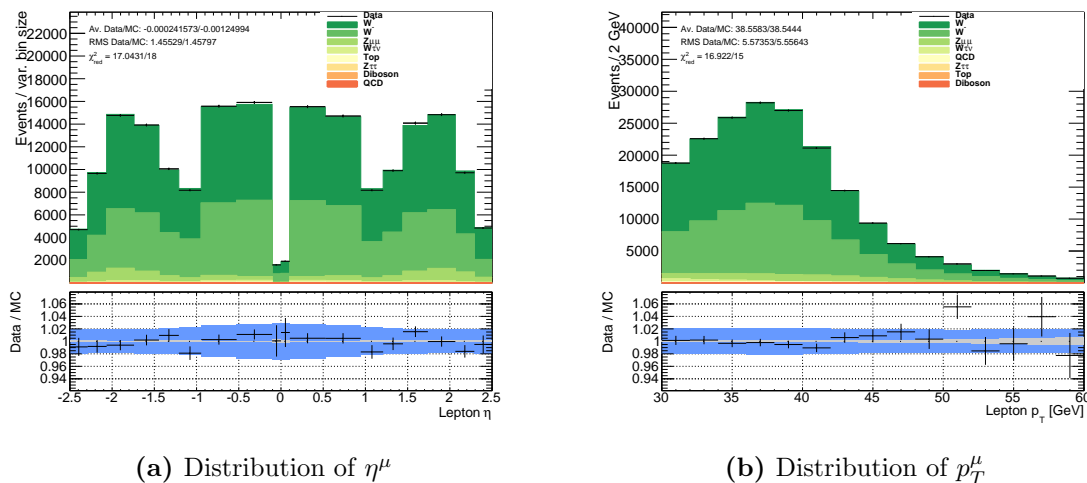


Figure 13.10.: Control distribution of η^μ and p_T^μ showing also the PDF uncertainty. Similar to Figure 13.3, the statistical uncertainty from the prediction, i.e. the combined Monte Carlo and background samples is shown as grey band in the ratio. The statistical uncertainty from data is shown as error bars in the ratio. In addition to the distribution shown in Figure 13.3, the additional uncertainty originating from the PDFs is shown as a blue band in the ratio.

13.6.2. Muon Efficiency Scale Factors

Of special importance are the uncertainties connected with the scale factors for the reconstruction, trigger and isolation factor obtained, as they were obtained as part of this thesis. If focusing on the results obtained in the observable p_T^μ , it can be seen that these uncertainties are 1.35 MeV for the isolation efficiencies, 4.20 MeV for the reconstruction efficiencies and 6.19 MeV for the trigger efficiencies. The hierarchy of these uncertainties can easily be attributed to the efficiencies for the three cuts involved.

This can be seen by the following consideration: The number of probe candidates passing the selection can be assumed to be distributed according to a binomial distribution, the uncertainty on the efficiency can be approximated as:

$$\Delta\varepsilon = \sqrt{\frac{\varepsilon(1-\varepsilon)}{N}} \quad (13.2)$$

Since the global isolation efficiency is on the order of 99.5%, the reconstruction efficiency on the order of 94.5% and the trigger efficiency on the order of 80%, the resulting statistical uncertainties should behave like 1:2:4. Due to the uncertainty of 16% on the estimated uncertainties itself (cf. Table 11.1), this is very well compatible with the observed values.

An overview of the sub-sources of the muon efficiency scale factors is shown in Table 13.6. It may be observed, that, as expected, the statistical uncertainty plays a dominant role. In the reconstruction scale factors, where a comparatively high level of background was observed, the uncertainty due to the QCD background subtraction is the next-to-leading uncertainty, but almost an order of magnitude smaller. In the case of the trigger scale factors, the next-to-leading uncertainty are the muon scales, which can be understood by keeping in mind that some trigger settings showed a significant dependence on the transverse momentum of the decay lepton. As has to be expected, the size of the uncertainty due to the muon efficiency corrections becomes smaller in the case of m_T and E_T^{miss} . In both cases, the kinematics of the decay neutrino are added as further source. However, even in the case of the fit being performed purely in the E_T^{miss} spectrum, the muon efficiencies still play an indirect role both in the calculation of E_T^{miss} (discussed in Section 7.2) as well as in the event selection.

13.6.3. Cross Section

A significant contribution to the total uncertainty comes from the uncertainty on the background normalization, in which the uncertainties on all background contributions, including the QCD contribution, are combined. This uncertainty is to a large extent due to two uncertainties: On one hand, the normalization of the QCD background, which was obtained in a dedicated fit, discussed in Section 13.2.1. Due to the limited size of the analyzed data set, as well as the additional sophistications available with a sufficiently large set, e.g. a separation into two background templates for positive and negative muons, it may be expected that the amount of this contribution will drop in the final measurement on the full sample.

On the other hand, the cross-section uncertainty originates from the uncertainty on the process $pp \rightarrow Z + X \rightarrow \mu\mu + X$. Table 13.3 indicates, that this background process has a significant contribution on the level of 5%. The relative uncertainty on the cross-section of this process is 5%, as shown in Table 5.2. Taken together, this indicates that a large contribution has to be expected from this sample.

Scale Factor	Uncertainty	p_T -Fit in $\Delta M_W [MeV]$	m_T -Fit in $\Delta M_W [MeV]$	E_T^{miss} -Fit in $\Delta M_W [MeV]$	(p_T, m_T) -Fit in $\Delta M_W [MeV]$
Trigger	Statistical	6.16	4.74	2.82	5.56
	Muon Scale	0.51	1.19	1.31	0.43
	HR Scale	0.00	0.00	0.00	0.00
	QCD Template	0.15	0.13	0.06	0.14
	Cross-Section	0.00	0.03	0.04	0.00
	Total	6.19	4.89	3.11	5.58
Reconstruction	Statistical	4.14	3.34	1.78	3.72
	Muon Scale	0.14	0.32	0.41	0.13
	HR Scale	0.00	0.00	0.00	0.00
	QCD Template	0.70	0.50	0.17	0.63
	Cross-Section	0.06	0.03	0.00	0.05
	Total	4.20	3.39	1.83	3.78
Isolation	Statistical	1.30	1.05	0.54	1.16
	Muon Scale	0.16	0.09	0.03	0.14
	HR Scale	0.00	0.00	0.00	0.00
	QCD Template	0.36	0.30	0.15	0.32
	Cross-Section	0.04	0.03	0.01	0.03
	Total	1.35	1.09	0.56	1.21

Table 13.6.: Overview of the uncertainties on M_W due to the different sub-sources of the muon efficiency scale factors.

13.7. Summary and Outlook

The results observed in the single observables, presented in the last section, showed no significant discrepancies. Therefore, it seems in order to combine these results into a single result. Since the observable E_T^{miss} is not expected to have a strong impact on the average due to its large uncertainty, it may be argued that the two-dimensional fit in the combined (p_T, m_T) -templates may be taken as final result of the analysis, yielding:

$$M_W = 80.380 \pm 0.045(\text{stat.}) \pm 0.021(\text{sys.}) \text{ GeV} \quad (13.3)$$

As a reminder, the current value of the world average is $(80.385 \pm 0.015) \text{ GeV}$ (cf. ref. [8]). Using this, the deviation δ from the world average can be calculated to be 5 MeV , with its corresponding significance:

$$s = \delta/\sigma = 0.096 \quad (13.4)$$

With a significance of 0.096, this value is almost identical to the current world average. Considering that s^2 follows a χ^2 distribution with one degree of freedom, if both world average and the result of this analysis is treated as following a Gaussian distribution around the true value, it is possible to calculate the probability to observe such a close fitting result or better to be 7.3%. This indicates that the result of this analysis is very well compatible with the current world average without showing a significant over-agreement. Recalling the overview in Table 3.1 of the measurements used in the calculation of the world average in ref. [8], it is able to compare this result with its projected uncertainty as shown in Table 13.7. As can be seen, the result presented here already is an improvement in precision with the results obtained at the LEP experiments.

Year	Experiment	$M_W[\text{GeV}]$	$\Delta M_W[\text{GeV}]$	Reference
2001	CDF (Tevatron)	80.433	0.079	[44]
2002	D0 (Tevatron)	80.483	0.084	[45]
2006	ALEPH (LEP)	80.440	$0.043(\text{stat.}) \pm 0.027(\text{sys.})$	[46]
2006	L3 (LEP)	80.270	$0.046(\text{stat.}) \pm 0.031(\text{sys.})$	[47]
2006	OPAL (LEP)	80.415	$0.042(\text{stat.}) \pm 0.031(\text{sys.})$	[48]
2008	DELPHI (LEP)	80.336	$0.055(\text{stat.}) \pm 0.039(\text{sys.})$	[49]
2012	CDF (Tevatron)	80.387	0.019	[50]
2014	D0 (Tevatron)	80.375	0.023	[51]
2015	World average	80.385	0.015	[8]
2016	This study	80.380	$0.045(\text{stat.}) \pm 0.021(\text{sys.})$	

Table 13.7.: Comparison of previous measurements of M_W with the results of this thesis. Only the values used by the Particle Data Group for the fit of the world average are shown. Values taken from ref. [8]. Added is the result of this study with its actual as well as its projected uncertainty if the full data sample was used.

Several changes with respect to the result shown here have to be expected in the final analysis on the 2011 data set. These do not only affect the statistical, but also the systematic uncertainty on the final result. It has to be noted, that the propagation of the uncertainty from each source into the uncertainty on M_W is purely Monte Carlo driven (cf. Section 11.3.1). This means, that the propagation itself is independent of the size of the data sample, and that only changes to the sources of uncertainty themselves have to be considered. In detail, the following modifications have to be expected for each source of uncertainty:

- **Muon Momentum Correction:** As discussed in Section 11.3.2, the uncertainties estimated for the muon momentum corrections — consisting of scale and smearing variations — were obtained from a Monte Carlo study performed before data taking. While the assumptions made in this study are generally valid, slight differences with respect to these estimations have to be expected.
- **Hadronic Recoil Correction:** The hadronic recoil correction was estimated from a Monte Carlo study as also discussed in Section 11.3.2. Unlike the case of the muon momentum corrections, the uncertainty due to the hadronic recoil correction is harder to estimate on Monte Carlo, since it depends on a number of variables. For example, the number of interactions per beam crossing has a significant impact on the resolution achievable in the final measurement. Therefore, the uncertainty due to hadronic recoil correction might show a larger difference compared to the estimation presented here.
- **Muon Efficiency Corrections:** The muon efficiency corrections, i.e. the combined set of reconstruction, isolation and trigger efficiencies, is finalized. Since the propagation of these uncertainties into M_W was performed purely Monte Carlo driven, the uncertainties presented here are close to those expected on the final result.
- **Cross-Section uncertainty:** The cross-section uncertainty is due to the uncertainty on the normalization factor for each background contribution. While the background is mostly Monte Carlo driven, with associated uncertainties driven by theoretical arguments and other experiments, this does not hold true for the multi-jet background. This background plays a large role, especially since the normalization factor could only be obtained with large uncertainty due to the limited data-set. It has to be expected, that the uncertainty on the final measurement, where the larger data sample allows for improved estimations of the multi-jet background, the uncertainty on the normalization factor will drop. Since the other major contribution comes from the cross-section uncertainty on the process $pp \rightarrow Z + X \rightarrow \mu\mu + X$, the actual uncertainty can be expected to be smaller than the uncertainty shown here, but larger than expected if fully data driven.
- **Parton Distribution Functions:** The total systematic uncertainty in the measurement of M_W is driven by the PDF uncertainty. As described above, several avenues to reduce this uncertainty are available. Depending on whether these measures are implemented in the final analysis, the final uncertainty might be reduced with respect to the values shown here. On the other hand, the inclusion of the missing gluon information (cf. Section 11.3.2) can increase the uncertainty, as well as the method by which differences between different PDF sets will be taken into account.

- **Statistical Uncertainties:** Naturally, the statistical uncertainty originating from the data sample will decrease. As was discussed at the beginning of Chapter 13, this decrease is estimated to be close to a factor of seven. The statistical uncertainty from Monte Carlo can be expected to be close to the final uncertainty, since no changes of the used samples are foreseen. The reduction due to the background samples is harder to estimate, since the background is to a significant extent data-driven. This means, that also this uncertainty is likely to be reduced.

With these caveats in mind, a first estimate for the uncertainty on the final result can be given. For this estimate, only the data and background statistical uncertainty will be modified. For this estimation, the assumption of the current data as well as background statistical uncertainty being data-driven will be made. The latter assumption can be made, because the statistical uncertainty on the background shows a large contribution from the data-driven QCD background. Due to its size, compared with the data statistical uncertainty, the background uncertainty only plays a minor role. The results for this are shown in Table 13.8.

Fit	Observed uncertainty [MeV]				Projected uncertainty [MeV]			
	Data	Signal	Background	Total	Data	Signal	Background	Total
p_T^μ	40.3	4.2	5.1	40.8	6.0	4.2	0.8	7.3
m_T	54.1	5.1	8.2	55.0	8.0	5.1	1.2	9.5
E_T^{miss}	97.5	10.3	11.6	98.7	21.1	10.3	1.7	23.6
$p_T^\mu - m_T$	45.4	3.8	4.5	45.7	6.7	3.8	0.7	7.7

Table 13.8.: Projections for the statistical uncertainty of M_W on the full data set.

As can be seen, if the full data set was used, the statistical uncertainty would no longer be dominating. Instead, it may be assumed that the final measurement will be limited by the systematic uncertainties, for which the current values appear to be reasonable estimates. Since the statistical uncertainty of the background contribution is considered as a source of systematic uncertainty on the final result, the extrapolated result on the final result in the muon channel would be:

$$\Delta M_W = (0.007 \text{ (stat)} \pm 0.020 \text{ (sys)}) \text{ GeV} \quad (13.5)$$

The impact on the world average is difficult to estimate, since it has to be expected that a significant correlation between the uncertainty of the world average, and the uncertainty of the measurement presented here, exists. This is because the world average is dominated by the measurements performed at Tevatron, which in turn have a large influence from PDF uncertainties. Since in both cases the same input data was used for the PDFs, a correlation has to be expected. The extent of such a correlation might be diminished by the different parton distributions and kinematic regions probed in proton-proton collisions and proton-antiproton collisions, as performed at the Tevatron. This is because anti-quarks in protons appear only as sea quarks, while in anti-protons they appear as sea as well as valence quarks. Both valence and sea quarks have different distributions with respect to Bjorken x . However, since the extent of these correlations might play a significant role, a detailed study would be needed, which is beyond the scope of this thesis. Moreover, the contributions from different sources on the final measurement are not yet known.

In the most optimistic case, correlations would play no role, and the new measurement is compatible with the world average. Following the PDG method to combine measurements (cf. ref. [8]), in this case both measurements can be combined with a simple weighted arithmetic mean, and, moreover, the uncertainties will not have to be artificially inflated. The equation used by the PDG to combine measurements x_i reads:

$$\bar{x} \pm \Delta x = \frac{\sum_i w_i x_i}{\sum_i w_i} \pm \left(\sum_i w_i \right)^{-1/2} \quad (13.6)$$

In this equation, w_i is the weight applied to each measurement, $w_i = 1/(\Delta x_i)^2$. Using this equation, the updated world average can be calculated by combining the current world average with the result presented in this thesis, or the estimated final result in the muon channel discussed in this section, respectively. In the first case, the result reads:

$$M_W = (80.385 \pm 0.014) \text{ GeV} \quad (13.7)$$

For the extrapolated result on the full data set, with all the caveats discussed concerning this extrapolation, the uncertainty of the world average would drop to 12 MeV. This underlines the ability of the ATLAS measurement to have a significant impact on the knowledge of M_W . Given the improvements mentioned, which are already underway, the final result of the analysis of the 2011 data in the muon channel might even surpass this estimation.

Part IV.
Conclusion

14. Conclusion

This thesis presented the first measurement of the mass of the W boson with muons in the final state at the ATLAS detector. The obtained value of $80.380 \pm 0.045(\text{stat.}) \pm 0.020(\text{sys.})$ GeV is in excellent agreement with the current world average of 80.385 ± 0.015 GeV (cf. ref. [8]) and a theoretical prediction, obtained from a fit to experimental input, excluding M_W , of 80.358 ± 0.008 GeV (cf. ref. [7]). The result was obtained on a limited sub-set of data gathered in 2011, corresponding to an integrated luminosity of 0.1 fb^{-1} at a center of mass energy of 7 TeV. If the full 2011 data-set was used, the uncertainty is estimated to drop significantly to $0.007(\text{stat.}) \pm 0.020(\text{sys.})$ GeV. In this case, the measurement will be limited by the systematic uncertainty.

It has to be noted, that both the result presented in this thesis, as well as the result in the muon channel, extrapolated to the full 2011 data-set, rests on several estimates of systematic uncertainties.

In the course of the analysis, the uncertainty originating from the parton distribution functions could be identified as the driving systematic uncertainty. As part of the efforts to improve the knowledge of the PDFs, a method to identify electrons in the forward calorimeters of the ATLAS detector was developed. With these electrons, it is feasible to probe the range of very high and low values of Bjorken x , which are otherwise almost inaccessible at the ATLAS detector, and which play a significant role in constraining the PDFs. A precise knowledge of the PDFs is not only important for the measurement of the W boson mass, but also for numerous other studies, such as the measurement of the weak mixing angle (cf. ref. [110]).

Further contributions to the systematic uncertainty originate from the uncertainty on the background normalization, which is mostly due to the multi-jet background, which could only be estimated using the limited data-set. With the full data-set, it should be feasible to reduce the uncertainty connected with this background — its normalization factor as well as the shape uncertainty — compared to the estimate shown here.

The uncertainties both for the muon momentum as well as for the hadronic recoil corrections had to be estimated from Monte Carlo studies. While the uncertainty connected with the muon momentum correction is expected to be close to the final result, the uncertainty connected with the hadronic recoil might show larger differences due to the inherent challenges in simulating this variable. This only affects the measurement in m_T and E_T^{miss} , with effects on p_T expected to be negligible. In summary, the uncertainties shown here can be seen as a reasonable estimate of the final uncertainty.

The fitting package developed to measure the mass of the W boson was cross-checked using Z bosons, yielding excellent results and indicating, that any additional uncertainties from the fitting method are well under control. Moreover, it could be shown that neither in the case of W nor Z bosons any significant dependencies on control variables, such as lepton η or the transverse momentum of the vector boson, exist. This indicates that an excellent understanding of the detector, as well as the underlying physics processes, could be gained.

A significant contribution to this understanding was obtained as part of this thesis: An evaluation of the full chain of muon efficiencies, consisting of the ID track reconstruction

14. Conclusion

efficiency, the combined reconstruction efficiency, the isolation and trigger efficiency. This evaluation resulted in a set of correction factors, so-called *scale factors*, which correct for differences in these efficiencies between data and Monte Carlo, depending on muon η , φ and p_T , as well as $u_{||}^l$, which is a kinematic variable constructed from muon and hadronic recoil kinematics. These scale factors could be obtained with high precision, leading only to minor contributions to the total systematic uncertainty.

If new experimental input is used to constrain the PDFs further with respect to the PDF set used in this analysis, a significant improvement of the obtainable precision can be expected. Therefore, a significant contribution to the current world average using the 2011 data-set does not seem out of reach. Moreover, the techniques developed as part of the analysis on the 2011 data-set can easily be used to include the data gathered in 2012, corresponding to 20 fb^{-1} , and data from Run II. Due to the larger number of interactions per bunch crossing, it is estimated that the resolution of the hadronic recoil, and the two observables m_T and E_T^{miss} constructed from it, will suffer with respect to the 2011 data-set. However, the estimation of the uncertainties of several sources shown here — for example the muon efficiencies as well as the muon momentum correction — is limited by the statistical uncertainty. This indicates, that, using the techniques developed as part of this thesis, an important contribution to the current knowledge of M_W , and therefore to the internal consistency of the Standard Model, can be obtained.

Part V.
Appendix

A. Forward Electron Performance

Note: The work presented in this chapter forms the basis of an internal ATLAS note as part of the forward electron calibration, cf. ref. [115]

A.1. Introduction

At ATLAS, the identification (ID) of electrons can be divided into two regions of the detector: the central area covering $|\eta| < 2.5$ and the forward area with $|\eta| > 2.5$. The forward area consists of the EMEC inner wheel (EMEC IW), with a coverage from $|\eta| = 2.5$ to 3.16 and the FCAL from $|\eta| = 3.35$ to 4.9. The forward area, unlike the central area, is not covered by the tracking system.

By increasing the acceptance for electrons from $|\eta| < 2.5$ to $|\eta| < 4.9$, forward electrons offer the possibility to access regions of phase space not accessible with central electrons. However, the identification of these electrons offers several challenges. Apart from the missing tracking information, the resolution of the forward calorimeters is worse than that of the central counterparts. Also, the Z boson line shape usually used for calibration studies is deformed by kinematic constraints (cf. Section A.2.3).

Work in the previous years has shown that these challenges can be overcome, and that the identification of forward electrons is possible with a good signal to background ratio. For the data taken in 2011, forward electrons were used in different analyses, such as the extraction of the weak mixing angle (cf. ref. [110]). In 2012, the instantaneous luminosity was increased with respect to 2011, leading to an increase of interactions per bunch crossing by a factor of approximately two (cf. ref. [116]). This, together with the change in the center of mass energy from 7 TeV to 8 TeV, leads to the question if the same ID can be used for data taken in 2011 and 2012.

The different running conditions in 2012 required a re-optimization of the 2011 IDs. This was assessed by applying the 2011 ID to 2012 data. In Figure A.1 it can be seen that the signal efficiencies are not close to the target efficiencies of 70% for the tight cut set, 80% for the medium cut set and 90% for the loose cut set. Figure A.2 and Figure A.3 show a clear pile-up dependence, visible at high numbers of primary vertices. This is not unexpected, since these pile-up conditions were not present in the 2011 data. The method for deriving these efficiencies as well as the selection criteria are explained in detail in Section A.2.2.

This chapter presents the results of the mentioned re-optimization of the electron ID for the 2012 data. The resulting electron ID is valid for isolated electrons, such as those stemming from Z boson decays, with transverse momenta $p_T \geq 20$. The features of this new ID were studied in great detail. Among the results presented in this chapter are signal efficiencies for data and Monte Carlo in Section A.3.1 and resulting scale factors, needed to tune Monte Carlo simulations. Of special interest are the bin-by-bin correlated systematic uncertainties, which can be used in Toy Monte Carlos. These were calculated for a large array of variations, and the results are discussed in Section A.3.3.

A. Forward Electron Performance

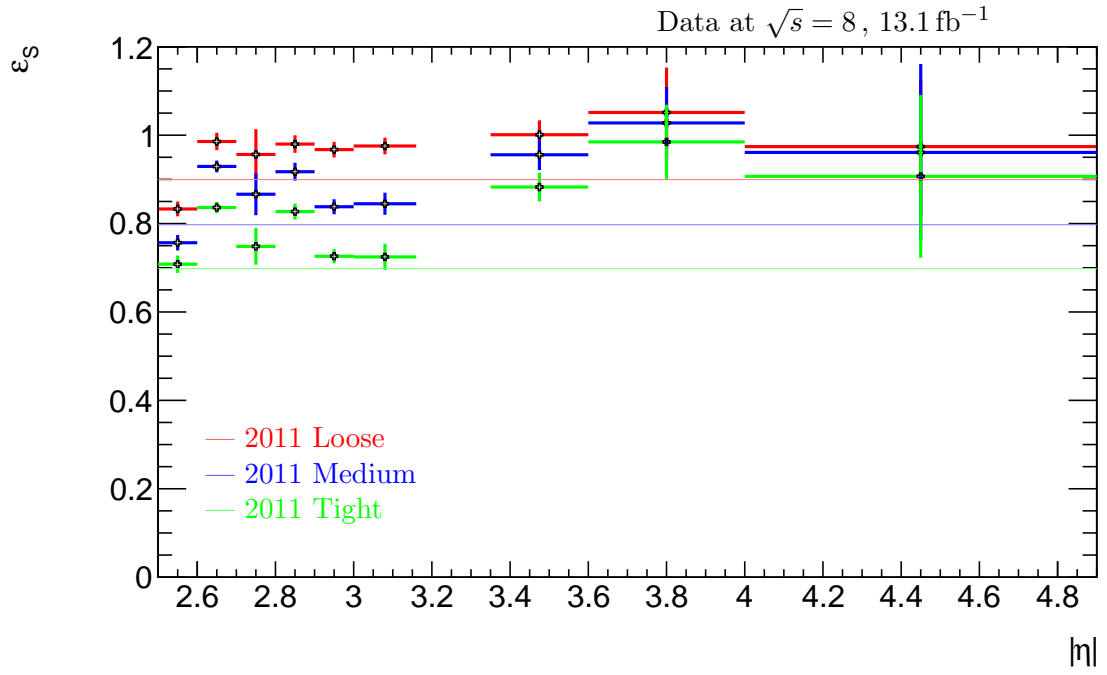


Figure A.1.: $|\eta|$ dependence of the signal efficiencies for the 2011 ID on 2012 data. Only statistical uncertainties shown.

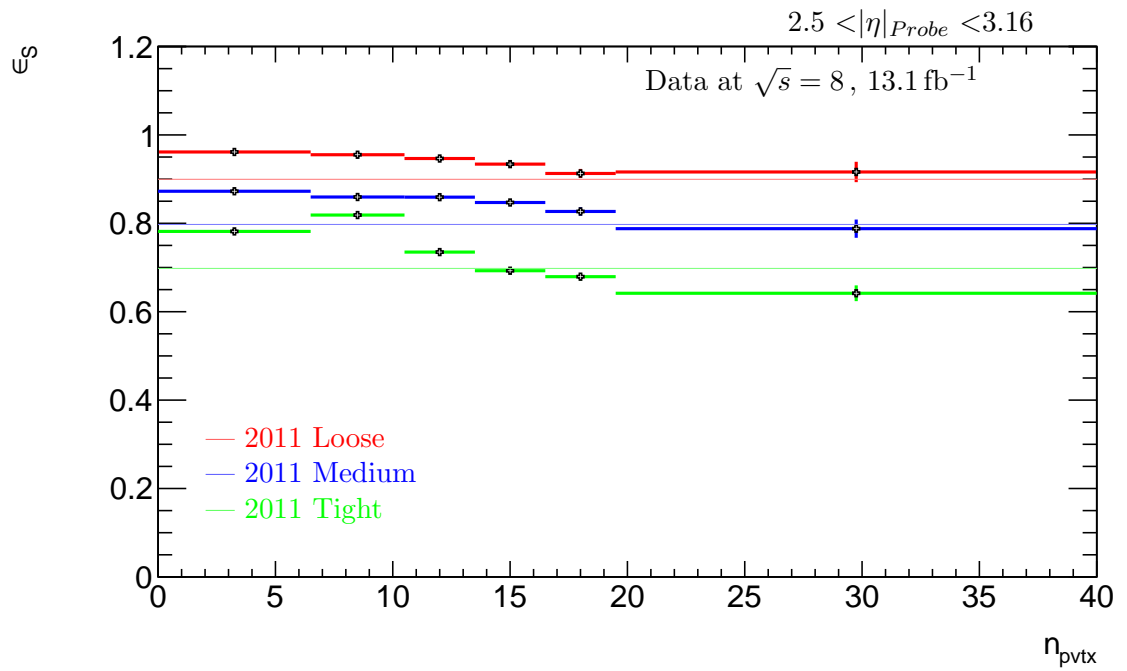


Figure A.2.: Pile-up dependence of the signal efficiencies in the EMEC inner wheel for the 2011 ID on 2012 data. Only statistical uncertainties shown.

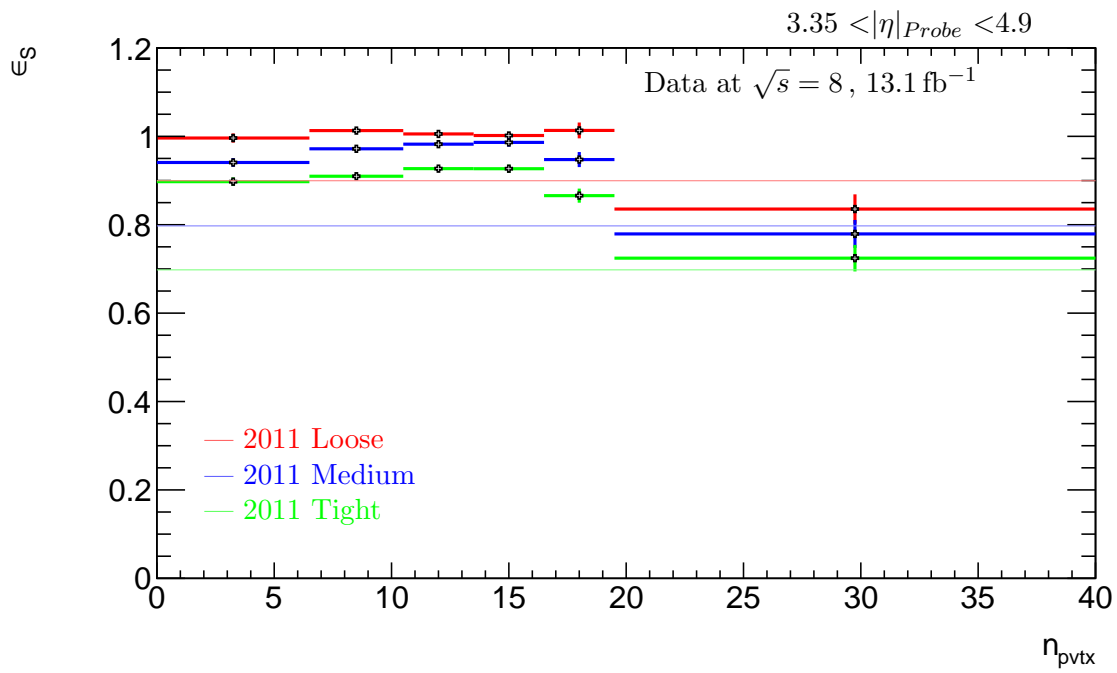


Figure A.3.: Pile-up dependence of the signal efficiencies in the FCAL for the 2011 ID on 2012 data. Only statistical uncertainties shown.

A.2. Methods

A.2.1. ID Method

The forward electron ID depends solely on the differences in the shower shapes of hadronic and electromagnetic energy deposition. Electromagnetic showers in general start earlier, are more compact and exhibit a larger energy density than hadronic showers. No distinction between electrons and photons can be performed without tracking information. From the signals in the calorimeter cells the Topocluster algorithm builds clusters (cf. ref. [117]), and these are then described by seven variables¹ (cf. Figure A.4):

- λ_{center} — distance center of the shower - front of calorimeter, measured along the longitudinal direction
- $\langle r^2 \rangle$ — mean square of lateral extension
- $\langle \lambda^2 \rangle$ — mean square of longitudinal extension
- $lat, long$ — Modified $\langle r^2 \rangle, \langle \lambda^2 \rangle$ with different cell weighting
- f_{max} — Fraction of energy deposited in highest energetic cell to rest
- ρ — Energy density

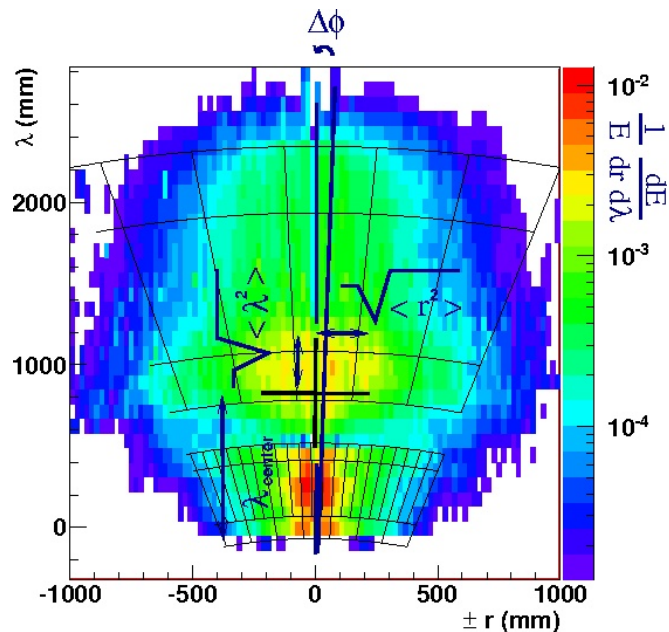


Figure A.4.: Example of a cluster in the central part of the detector with some of the cluster moments used for the forward electron ID. The particle comes from below. From ref. [118]

¹Here λ denotes distances along the shower axis and r distances perpendicular to it.

The size of the shower has only a very weak energy dependence. For the longitudinal extension this can be understood in a simple shower model. In this model it is assumed that the energy is split equally after each radiation length, until a critical energy is reached. At this point the shower ends. Taking into account that a shower with the typical energy of 500 has a depth of 16 radiation lengths in this model², it becomes clear that even a large increase in energy has almost no effect on the shower length. The lateral extension of the shower is governed by the Molière radius, and also exhibits only a small energy dependence. With the length and width of the shower staying almost constant, it is obvious that the energy density scales almost proportionally with the energy and cannot be used for an energy independent electron ID. Therefore, all variables with the exception of the energy density are used for electron identification³.

It was decided to move from the cut-based approach used for the 2011 ID to a Fisher discriminant (cf. ref. [119]). The Fisher discriminant is more powerful in taking correlations into account. It is also simple enough to understand its inner workings, which is important in precision physics. Moreover, it offers the possibility to derive an inclusive ID, i.e. that each electron candidate passing the tight ID level automatically passes the medium and loose ID level. The Fisher discriminant is defined as:

$$d = f_0 + \sum_{i=1}^{i=6} f_i x_i \quad (\text{A.1})$$

In this equation, $f_0..f_6$ are coefficients, and x_i represents the different variables describing the shower. The result d can be seen as a measure of the signal-likeness of the shower, and it is on this variable that the cuts are performed.

The ID is optimized independently in 9 bins in $|\eta|$ and 6 bins in n_{pvtx} , totaling 54 bins. An overview is shown in Table A.1.

		n_{pvtx}					
		0..6.5	6.5..10.5	10.5..13.5	13.5..16.5	16.5..19.5	19.5.. ∞
EMEC	$ \eta $						
	2.5..2.6	11	12	13	14	15	16
	2.6..2.7	21	22	23	24	25	26
	2.7..2.8	31	32	33	34	35	36
	2.8..2.9	41	42	43	44	45	46
	2.9..3.0	51	52	53	54	55	56
	3.0..3.16	61	62	63	64	65	66
Crack	3.16..3.35						
FCAL	3.35..3.6	71	72	73	74	75	76
	3.6..4.0	81	82	83	84	85	86
	4.0..4.9	91	92	93	94	95	96

Table A.1.: Map of the bin numbering scheme. As can be seen, 9 bins in $|\eta|$ and 6 bins in n_{pvtx} are used.

²Used was $E_c = 10, = 50, |\eta| = 3$ and $t = \log_2(E/E_c)$

³As a cross-check, the energy density normalized to the cluster energy was used as additional variable, but led to no significant improvement.

A.2.2. Estimation of Efficiencies

The efficiency had to be estimated on Monte Carlo simulations (MC) as well as on data. For this task a reasonably pure forward electron sample had to be extracted from data. In this analysis the Tag and Probe (T&P) method was used to select such a sample.

In this method the decay of Z bosons into electron pairs is used. Events are selected in which one electron candidate is in the central detector and fulfills tight identification requirements — this is the tag electron — and a second electron candidate in the forward detectors as the probe electron. The invariant mass of this pair is required to be close to the mass of the Z boson. In this way, the selected pair has a high probability of actually being an electron pair from a Z boson decay. The selection criteria were:

- Event cuts
 - GRL: DATA12_8.PERIODALLYEAR_HEAD_DQDEFECTS-00-01-00
_PHYS_STANDARDGRL_ALL_GOOD_EGAMMAFORWARD.XML (corresponding to an integrated luminosity of 20.3 fb^{-1} , production tags P1328, P1329)
 - Trigger: EF_E24VHLMEDIUM1 (lowest unrescaled since period B)
 - $E_T^{\text{miss}} < 25$
 - Truth matching on MC (ΔR cut at 0.1, post-FSR electrons)
- Quality cuts
 - TILEERROR != 2
 - COREERROR & 400 == 0
 - EL_OQ & 1446 = 0 on both electrons
 - LARERROR < 2
- Electron cuts
 - Forward electron author 8, central electron author 3
 - central electron: $p_T > 25$, forward electron: $p_T > 20$
 - $|\eta| < 2.5$ for central, $2.5 < |\eta| < 4.9$ for forward electron
 - Cracks excluded: $|\eta| = 1.375..1.52, 2.47..2.50, 3.16..3.35$
 - TIGHT++ on central electron
 - n_{ptx}, p_T corrected Calorimeter Isolation (ETCONE20) < 7 on central electron
 - PTCONE30 < 1 on central electron
- Corrections
 - Forward electron energy scales: new 2012 scales⁴ (cf. ref. [120])
 - Corrections on MC: k-Factor, pile-up and vertex position reweighting

⁴Included in EGAMMAANALYSISUTILS-00-04-46

The Monte Carlo sample used was a $pp \rightarrow Z + X \rightarrow e^+e^- + X$ sample produced with POWHEG+PYTHIA⁵. To improve the description below an invariant mass of 60 GeV of the electron pair, a low mass Drell-Yan MC was stitched⁶. Because the low-mass region is almost entirely dominated by the radiation tail from the Z boson resonance, this additional MC sample had negligible impact.

Since no ID could be applied to the forward electron without biasing the resulting signal efficiency, a significant contribution of fake pairs remained, leading to an impurity in the resulting sample. By fitting a signal and a background model to the mass spectrum of the selected sample the number of real and fake pairs was estimated. True pairs form the signal and are expected to be distributed according to a Breit-Wigner convolved with a Crystal Ball distribution. The latter distribution models bremsstrahlung and the energy resolution of the calorimeter. For the fake pairs, which form the background, a Landau distribution was used as a model. In summary:

- Signal model: Breit-Wigner * Crystal Ball (bremsstrahlung)
 - Free parameters: $\mu_{BW}, \sigma_{CB}, |\eta_{CB}, \alpha_{CB}$,
 - Fixed parameters: $\Gamma_{BW} = \Gamma_{Z,PDG}; \mu_{CB} = 0$
- Background model: Landau distribution
 - Free parameters: μ_L, σ_L

Fitting these functions to the mass spectra is challenging. With the ROOFIT package used (cf. ref. [121]), convergence of the fits was difficult to achieve. This became even more pronounced at high values of $|\eta|$, mostly due to acceptance effects (cf. Section A.2.3). For this analysis, methods were devised to stabilize the fitting procedure. This was achieved by running the fit several thousand times⁷ with different sets of starting values in each iteration and selecting the fit with the lowest χ^2 . An example of a fit obtained in such a way is shown in Figure A.5.

For some variations (cf. Section A.2.5), the signal model was replaced with a signal template. This template was obtained from signal Monte Carlo with the selection criteria given above.

In order to suppress the background contribution, not the entire fitting range was used to count the signal events. Instead, only a mass window between 80 and 100 was used. In Monte Carlo, the events were counted with their respective weight. From these numbers the signal efficiency can be calculated with:

$$\varepsilon_{S,i} = \frac{N_{\text{counting Range},i}}{N_{\text{conting Range, no ID}}} \quad \text{with } i \in \{\text{tight, medium, loose}\} \quad (\text{A.2})$$

Here, $N_{\text{conting Range, no ID}}$ stands for the number of all events passing the selection criteria given above. For the denominator $N_{\text{counting Range},i}$, only those events in which the probe electron fulfills the ID requirement are counted.

⁵MC12_8TeV.147806.POWHEGPYTH_CT10_ZEE.E1169_s1469_s1470_r3542_r3549_p1067

⁶MC12_8TeV.129501.POWHEGPYTH_CT10_DYEE.20M60.E1248_s1469_s1470_r3542_r3549_p1005

⁷6000 iterations for the fit on container level and 2000 iterations for the fits with applied ID were used in this analysis

A. Forward Electron Performance

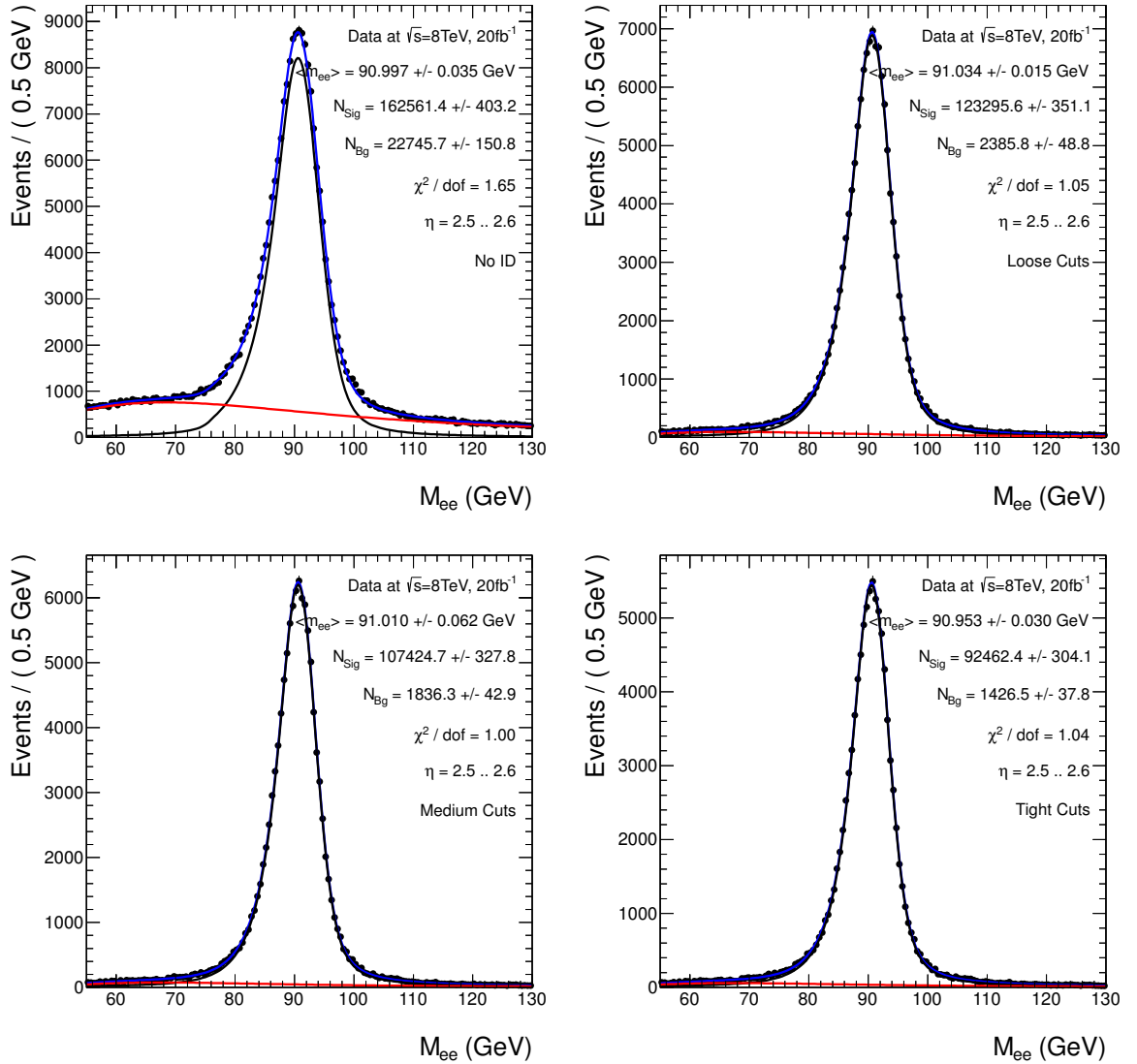


Figure A.5.: Example of fits performed to estimate the signal and background contribution. The sample shown is data with the forward electron $|\eta|$ between 2.5 and 2.6. From left to right and top to bottom, the plots show the spectrum without any ID on the forward electron, and with the loose, medium and tight ID.

A.2.3. Acceptance

The invariant mass of an electron pair can be calculated via:

$$m^2 = 2p_{T,1}p_{T,2}(\cosh \Delta\eta - \cos \Delta\varphi) \quad (\text{A.3})$$

Cuts are imposed on $p_{T,1}$ and $p_{T,2}$, and also on $\Delta\eta$ by requiring one electron in the central detector and one electron in the forward calorimeter. This leads to a turn-on in the mass spectrum, i.e. electron pairs with higher mass are more likely to pass the cuts than those with low mass. The effect becomes very pronounced when the probe electron is forced to be at high values of $|\eta|$ and can be observed in the upper row of Figure A.6. Here the acceptance α was calculated with PYTHIA8 (cf. ref. [29, 30]) by including only kinematic constraints and neglecting the remainder of the detector response. The value of α can be calculated as:

$$\alpha = \frac{N(p_T, |\eta|, m)}{N(\text{all}, |\eta|, m)} \quad (\text{A.4})$$

Here, $N(p_T, |\eta|, m)$ denotes the number of events in which both electrons pass the p_T cuts, whereas $N(\text{all}, |\eta|, m)$ denotes the total number of events. The acceptance is calculated as a function of $|\eta|$ of the probe electron and the mass m of the electron pair. It can be seen that the peak line shape becomes deformed at high values of the probe electron $|\eta|$, leading to significant problems in the fit to the spectrum of the invariant mass. The effect of the acceptance can be seen in the lower row of Figure A.6. Note, that in both cases the spectra on truth level are expected to be very similar. The differences between both are expected to be due to the different acceptance in both settings.

Counter-measures to the shown deformations were investigated, such as the introduction of an acceptance correction on the signal model, but no improvement was found. The corrections investigated were:

- **Linear acceptance correction:** It is obvious that when restricting the analysis to a small mass range, the acceptance function can be approximated with sufficient accuracy by a linear function. The acceptance can then be modeled by multiplying a linear function to the signal model — with the disadvantage of introducing two new parameters which have to be fitted. Another disadvantage is that inconsistencies occur since the background is also affected by the acceptance and should also be corrected.
- **Acceptance correction from simulation:** The acceptance can be calculated using truth quantities from signal MC. However, the mapping to reconstructed quantities is difficult and introduces new sources of uncertainties.

Since both strategies yielded no significant improvements, no acceptance correction was used in this analysis. With the deformation of the Z peak becoming very pronounced at high values of $|\eta|$, fitting became more difficult and an increase of the systematic uncertainties of the scale factors can be observed. Since the measurement of signal efficiencies via fits to the invariant mass spectrum using a pre-defined set of functions therefore is bound to fail with the increase of statistics and the introduction of higher cut values for electron p_T , a new method for the extraction of the signal efficiencies was devised, based on Monte Carlo templates instead of analytical functions. This approach is considered for the Run-II data.

A. Forward Electron Performance

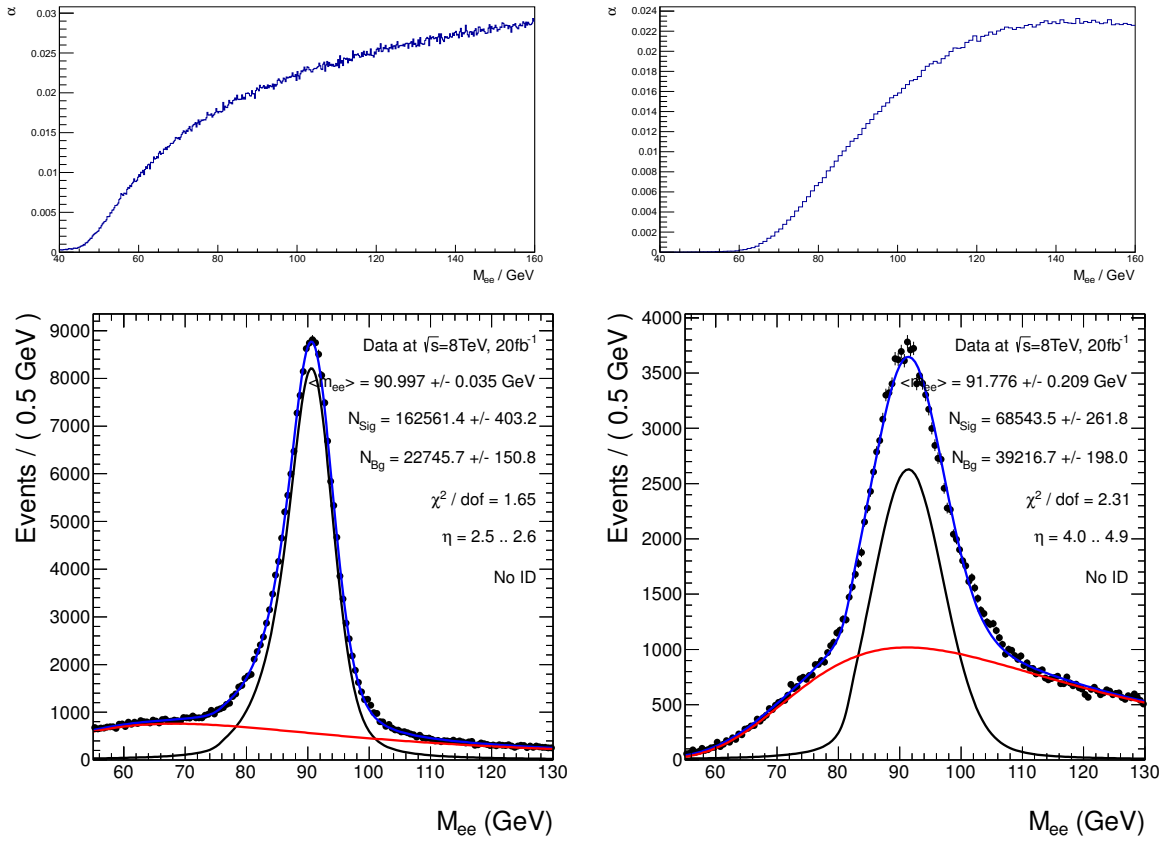


Figure A.6.: Acceptance and resulting spectra for the first bin in $|\eta|$ (2.5..2.6, left) and last bin in $|\eta|$ (4.0 to 4.9, right). Note the shift in the turn-on from low masses to higher masses with increasing $|\eta|$. The effect on the resulting spectra can be observed in the fits below. Note that the range of the x-axis in the upper and lower row is not identical.

A.2.4. Optimization

For the optimization, the TMVA analysis package was used (cf. ref. [122]) in the Fisher discriminant mode (cf. Equation (A.1)). TMVA automatically finds an optimal set of coefficients $f_0..f_6$ and produces histograms showing signal and background efficiencies as function of the cut value for d . However, it has to be provided with signal and background samples. Since the MC simulation of the shower shapes is known to be suboptimal, it was decided to extract these samples with the same method as was used for the efficiency estimation. The default Tag and Probe selection (cf. Section A.2.2) was modified for both samples:

- **Signal:**

Tag & Probe selection with additional safety cuts. These are very loose cuts⁸ on the variables used for electron ID and can be found in Table A.2. In addition, a simple forward electron isolation was used: This vetoes clusters with a second cluster of $E_T > 5$ within $\Delta R = 0.2$. Only pairs with masses between 76 and 106 are accepted.

- **Background:**

Tag & Probe selection with inverted ID on central electron: MEDIUM++, but not TIGHT++, no isolation required. Pairs with masses between 76 and 106 are excluded.

Variable	EMEC IW	FCAL
$\langle \lambda^2 \rangle$	$<6000 \text{ mm}^2$	$<15000 \text{ mm}^2$
lat	<0.8	<0.8
$long$	<0.8	<0.8
f_{max}	>0.1	>0.1
$\langle r^2 \rangle$	$<6000 \text{ mm}^2$	$<4000 \text{ mm}^2$
λ_{center}	$<350 \text{ mm}$	$<350 \text{ mm}$

Table A.2.: Values for the safety cuts used in the Tag and Probe signal selection.

For each bin defined in Table A.1, TMVA was applied, the results parsed into a macro and used as forward electron identification. To suppress the remaining small dependence on n_{pvtx} , the cut values on d were shifted in a second iteration⁹. In the first iteration, $\varepsilon_S = 70\%$, 80% and 90% were set as goal efficiencies in TMVA for the tight, medium and loose cut set respectively. In the second iteration, the efficiency obtained with the Tag and Probe method $\varepsilon_{S,TP}$ was used:

$$\begin{aligned}
 \varepsilon_{Goal} &= \varepsilon_S && \text{First iteration, } \varepsilon_S = 70, 80, 90\% \\
 \varepsilon_{Goal} &= \varepsilon_S \cdot \frac{\varepsilon_S}{\varepsilon_{S,TP}} && \text{Second iteration}
 \end{aligned}
 \tag{A.5}$$

With the suppression of the n_{pvtx} dependence, scale factors depending only on $|\eta|$ can be obtained. The results of these iterations are shown in Section A.3.1.

The stability of the TMVA optimization was tested by splitting the training samples into two sub-samples A and B of equal size. Then a TMVA optimization was performed on each

⁸These safety cuts were devised by dividing the sample into the EMEC inner wheel (EMEC IW, $|\eta| = 2.5..3.16$) and the FCAL ($|\eta| = 3.35..4.9$) and taking the weakest cut value from the 2011 ID for each respectively. To these values a 20% safety margin was added.

⁹Due to limited statistics, the shift was performed one-dimensionally in bins of n_{pvtx}

A. Forward Electron Performance

sub-sample and its result applied to the other sample. By counting the number of candidates surviving the selection, two efficiencies can be calculated — one for the ID optimized on sample B applied on sample A (ϵ_A), and vice versa (ϵ_B). From this the ratio $\epsilon_A/\epsilon_B - 1$ can be extracted. The results for the 56 bins in which the optimization was performed is shown in Figures A.7, A.8 and A.9. It can be discerned that within statistical uncertainties no large deviations are found. Moreover, the optimization for the ID presented here is founded on the combination A and B, and a reduction of the uncertainty of a factor $\sqrt{2}$ can be expected.

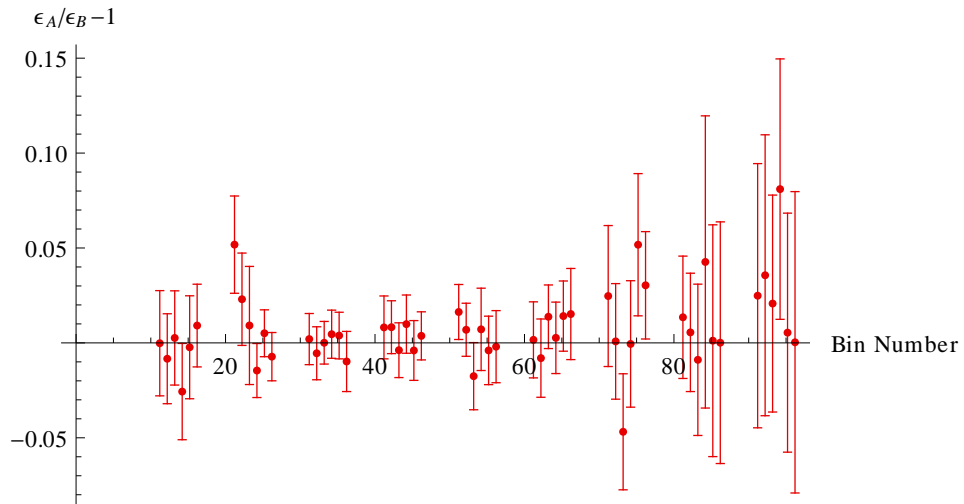


Figure A.7.: Comparison of signal efficiencies obtained with the ID optimized for sample A on sample B and conversely. The results shown are for the loose cut set. The errors shown are statistical uncertainties. Each group of five data points represents a bin in $|\eta|$, moving from small $|\eta|$ to large $|\eta|$. Within each group, each point represents a bin in n_{pvtx} , moving from low pile-up to high pile-up. The bin numbering follows Table A.1.

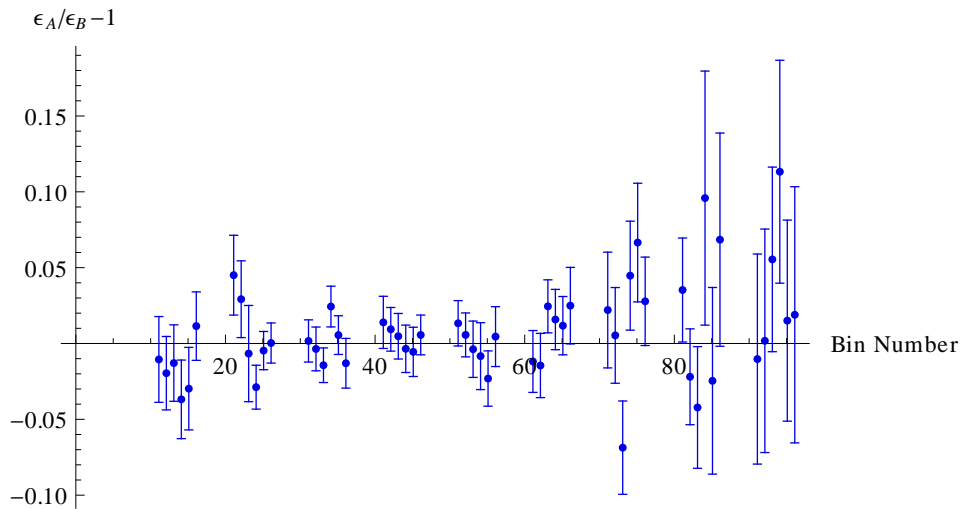


Figure A.8.: Comparison of signal efficiencies obtained with the ID optimized for sample A on sample B and conversely. The results shown are for the medium cut set. The errors shown are statistical uncertainties. Each group of five data points represents a bin in $|\eta|$, moving from small $|\eta|$ to large $|\eta|$. Within each group, each point represents a bin in n_{pvtx} , moving from low pile-up to high pile-up. The bin numbering follows Table A.1.

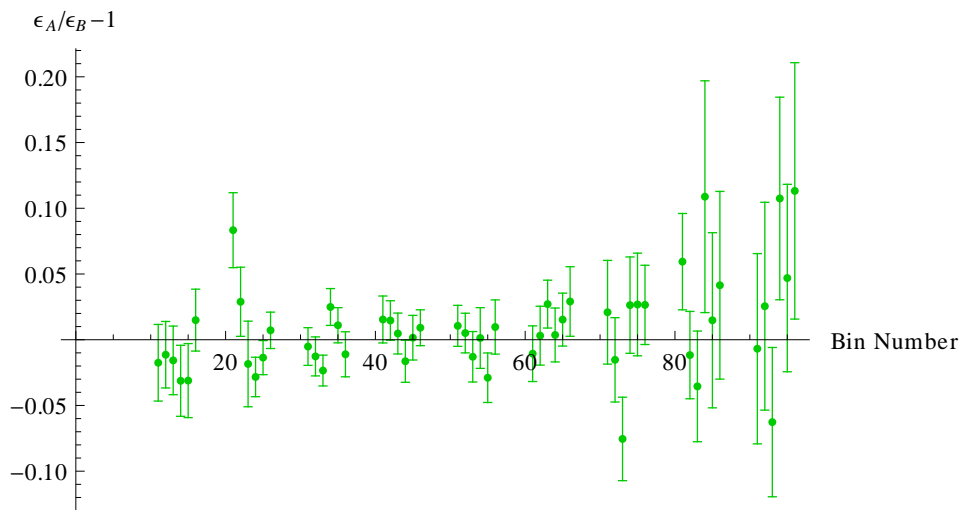


Figure A.9.: Comparison of signal efficiencies obtained with the ID optimized for sample A on sample B and conversely. The results shown are for the tight cut set. The errors shown are statistical uncertainties. Each group of five data points represents a bin in $|\eta|$, moving from small $|\eta|$ to large $|\eta|$. Within each group, each point represents a bin in n_{pvtx} , moving from low pile-up to high pile-up. The bin numbering follows Table A.1.

A.2.5. Systematic Variations

The default Tag and Probe selection was varied to estimate its influence on the estimated signal efficiencies. These variations were:

- **Fit range:** The mass range in which the signal and background model is fitted to the sample. Since no fitting is performed on the MC prediction, this variation has no effect in the MC Tag and Probe selection.
- **Count range:** As described in Section A.2.2, the number of true and fake electron pairs in data is calculated by integrating over a small fraction of the signal and background model around the Z peak. This is called the count range. In MC, no integration is performed since the sample is assumed to be pure after truth matching. Instead, a direct counting of pairs in the count range is performed.
- **Missing transverse energy (MET):** The cut on the maximum missing transverse energy of the event acts as a veto against pairs of electron candidates from W decays. Changing this cut influences the contribution from such events.
- **Template fits:** Instead of fitting a signal model consisting of a Breit-Wigner convolved with a Crystal Ball, the line shape of the signal can be extracted from signal MC. This is a so-called template fit. Since no MC prediction for the background exists, this can only be performed for the signal.
- **Chebyshev background:** The default model for the background is a Landau distribution. Since the model is not physics motivated, it is important to cross check the results with a different background model. A Chebyshev polynomial of 3rd order was chosen, which is able to model the peaking structure observed in the mass spectrum of the background. This variation is also not applicable to MC, since it only influences the models used in the fitting routine.
- **SBR variation:** Different cuts have an influence on the probability of the tag electron mis-identification rate and thereby on the signal to background ratio (SBR). Since the influence of these cuts is strongly correlated, it was chosen to combine the variation of these cuts into a single variation. An overview can be found in Table A.3.

An overview of the values in the variations is given in Table A.4. The resulting number of possible combinations is $3 \cdot 2 \cdot 3 \cdot 2 \cdot 2 \cdot 3 = 216$ variations on data and $2 \cdot 3 \cdot 3 = 18$ on MC. For each variation the signal efficiency was estimated with the method described above.

SBR variation	Calo isolation	Track isolation	ID requirement tag electron	SBR
Low	ETCONE20 <9	PTCONE30 <3	MEDIUM++	4.4
Medium	ETCONE20 <7	PTCONE30 <1	TIGHT++	7.5
High	ETCONE20 <5	PTCONE40 <1	TIGHT++	8.3

Table A.3.: Overview of the SBR variations. For reference, the signal to background ratio obtained in the counting range of the first bin in $|\eta|$ (2.5..2.6) is quoted.

Variation	Default value	Values	Applicable to MC
Fit range	55-130	60-120 , 50-140	No
Count range	80-100	70-110	Yes
MET	25	20 , 35	Yes
Template fits	Not used	Replacing signal model	No
Chebyshev background	Not used	Replacing Landau background model	No
SBR variation	Medium	Low,High	Yes

Table A.4.: Values used for the different variations

A.3. Results

A.3.1. Signal Efficiencies

As is described above, the cut values on d were shifted slightly with respect to the TMVA recommendations¹⁰. This was done in order to minimize the n_{pvtx} dependence of the resulting signal efficiencies. Results for the signal efficiencies as a function of n_{pvtx} before and after this shift are shown in Figure A.10. Here an integration over η for the EMEC IW and FCAL, respectively, was performed in order to have enough statistics in the bins with low and high pile-up. In Figure A.11, the resulting signal efficiencies as function of $|\eta|$ and integrated over n_{pvtx} are shown. All values shown here are for the default variation.

The p_T dependence of the signal efficiencies is difficult to investigate in data, since an upper cut on the forward electron p_T introduces a kinematic turn-off in addition to the kinematic turn-on described in Section A.2.3. The kinematic turn-on and turn-off strongly deform the spectrum, and fits are difficult to perform. On MC no such difficulties exist since no fitting is performed. Results for the p_T dependence are shown in Figure A.12. A small p_T dependence can be observed. This hints at the need for improving the fitting methods in further studies, possible approaches will be discussed in Section A.4. Without improved methods, a study of the dependence of the signal efficiencies on p_T will be very challenging.

¹⁰The shift was performed one-dimensionally in bins of n_{pvtx}

A. Forward Electron Performance

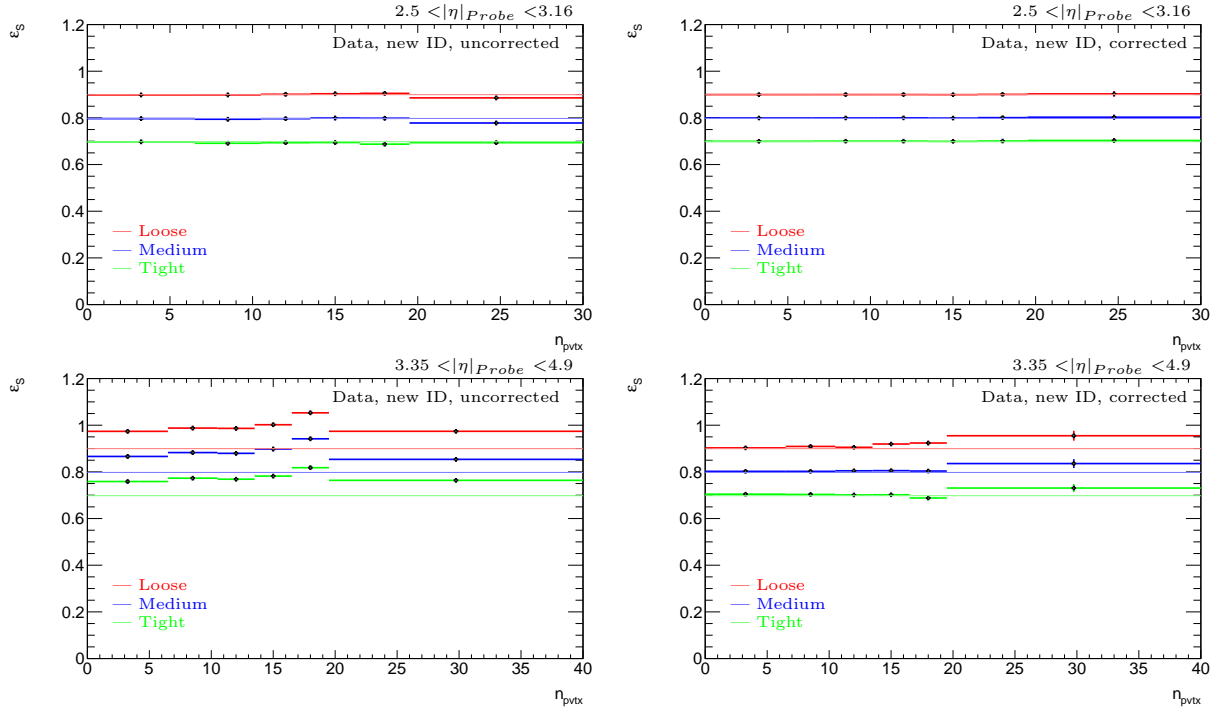


Figure A.10.: Signal efficiencies as function of n_{pvtx} , shown for the EMEC IW (upper row) and FCAL (lower row). The left column shows the result from the first iteration, in which the TMVA recommendations for the coefficients $f_0..f_6$ and the cut values for d was used. The right column shows the results after the cut values on d were shifted to minimize the n_{pvtx} dependence. Only statistical uncertainties are shown.

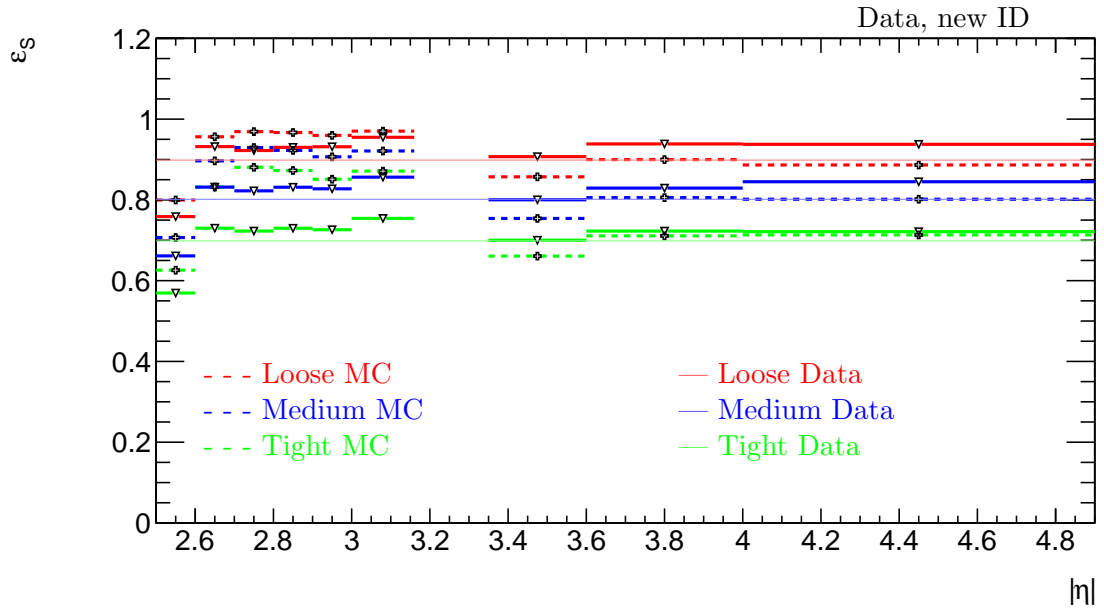


Figure A.11.: Resulting signal efficiencies as a function of $|\eta|$ after correcting the cut values on d . An integration over n_{pvtx} was performed in order to obtain these results.

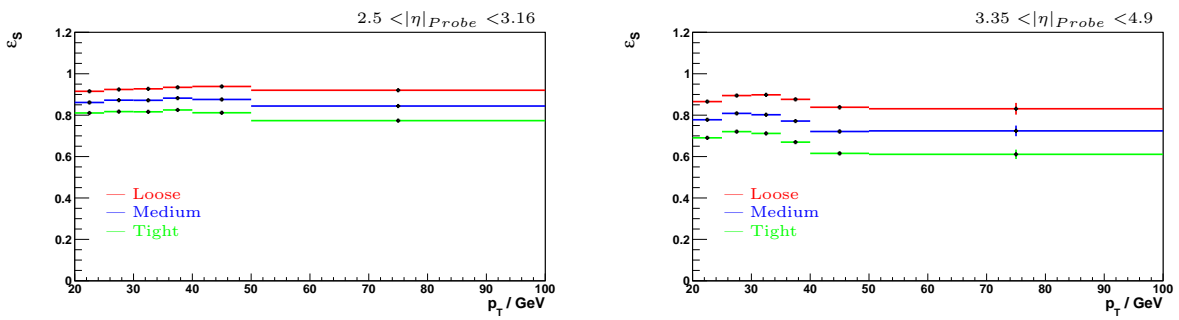


Figure A.12.: p_T dependence of the signal efficiencies in MC. As can be seen, for the EMEC IW the signal efficiencies exhibit almost no dependence on p_T , while for the FCAL a larger dependence is observed. The errors shown are statistical only.

A.3.2. Background Efficiencies

To estimate the background efficiency, the efficiency of the ID on the preselected background samples (cf. Section A.2.4) was used. Due to the small signal contamination expected in these background samples, an overestimation of the background efficiency is to be expected.

It is shown for the loose, medium and tight cuts in Figures A.13, A.14 and A.15. As can be seen, the first bin in $|\eta|$ has a rather large background contribution, as well as the highest $|\eta|$ bin in the EMEC IW. It can be assumed that these effects are due to border effects in the first $|\eta|$ bin. The increase in the last bin in the EMEC IW ($|\eta| = 3.0..3.16$) is probably due to its closeness to the crack and changes in geometry of the calorimeter. It can also be seen, to a much lesser extend, that the background efficiency becomes larger with higher pile-up.

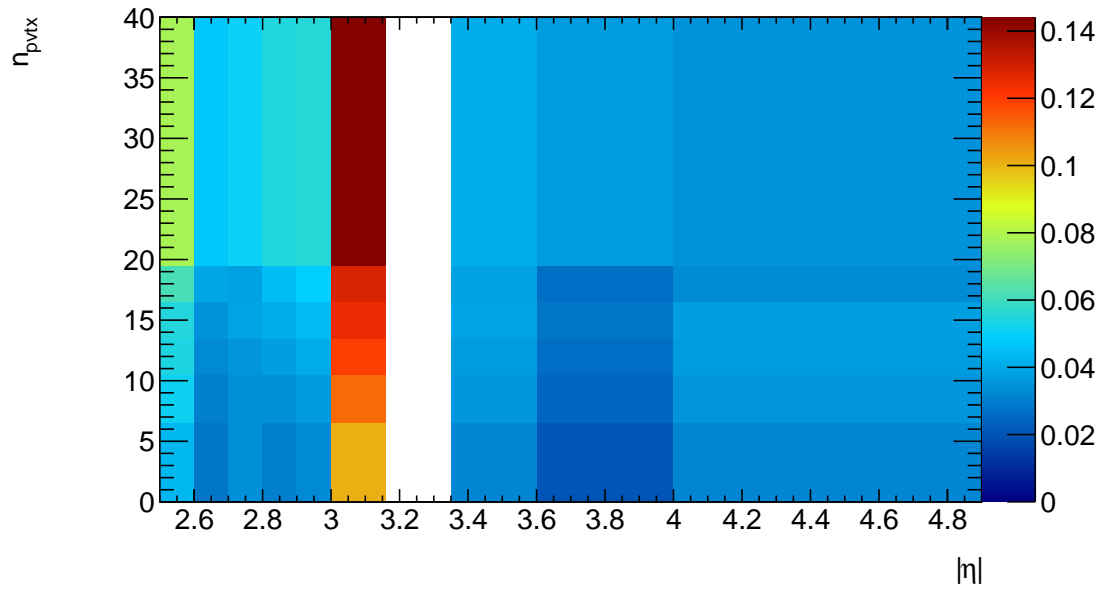


Figure A.13.: Background efficiencies for the loose cut set calculated on the background training samples.

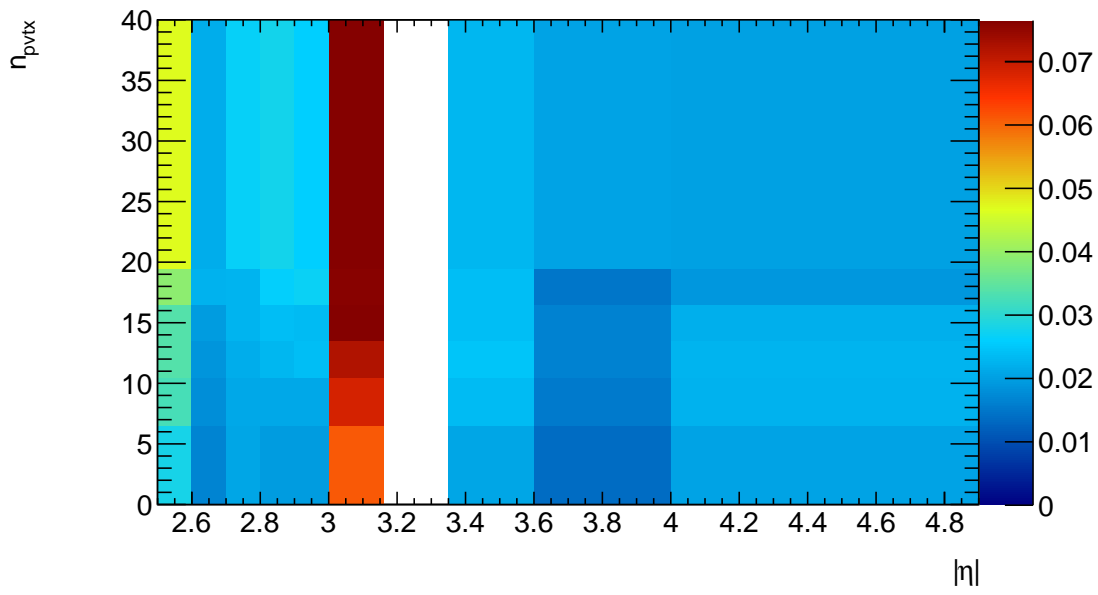


Figure A.14.: Background efficiencies for the medium cut set calculated on the background training samples.

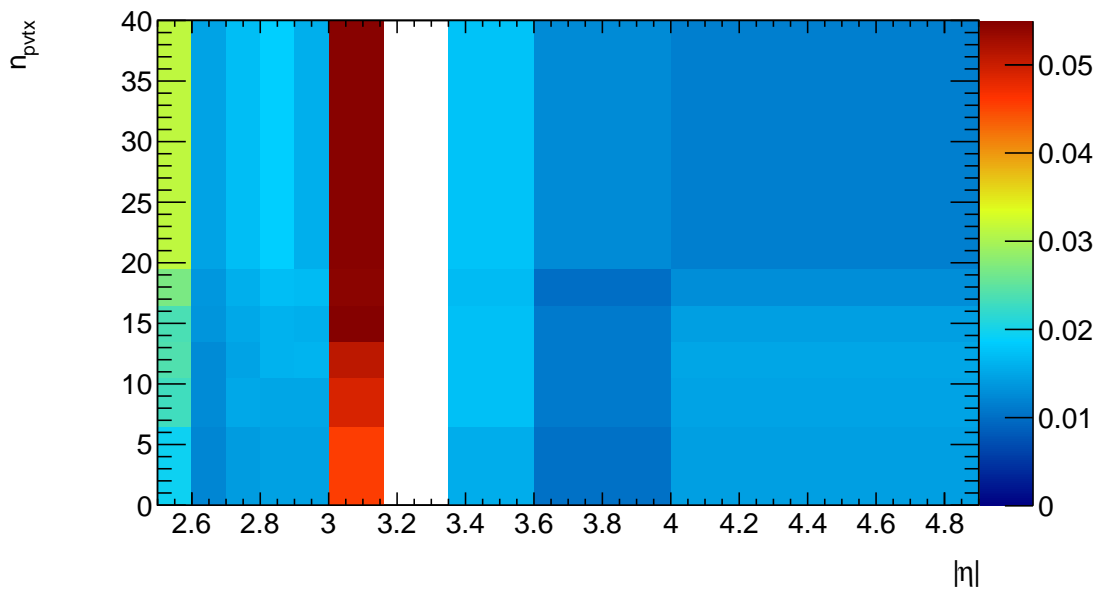


Figure A.15.: Background efficiencies for the tight cut set calculated on the background training samples.

A.3.3. Scale Factors

Ideally, data and MC should exhibit equal signal efficiencies. Since this is not the case, the MC prediction has to be corrected by applying a weight for each electron candidate, the so-called scale factor (SF). It is defined as:

$$SF = \frac{\varepsilon_{Data}}{\varepsilon_{MC}} \quad (\text{A.6})$$

The SFs and their uncertainties have to be determined with high precision and this was achieved with the methods described above. For each variation a scale factor was calculated from the data and MC signal efficiency. An overview is shown in Figure A.16 and A.17. The mean of all scale factors was taken as estimate of the true scale factor. The standard deviation of all scale factors was taken as estimate for the systematic uncertainty of the scale factor. Since each variation is performed on portions the same sample, the statistical uncertainties were assumed to be fully correlated, and the mean of all statistical uncertainties was taken as the total statistical uncertainty. The resulting scale factors are found in Table A.5. A graphical overview of all scale factors is shown in Figure A.18.

Mostly in higher bins of $|\eta|$, the distribution of the scale factors is non-Gaussian. It could be shown that even in these bins, the standard deviation covers close to 68% of the distribution, leading to the assumption that the standard deviation is still a good estimate of the systematic uncertainty.

It can be seen that the value of the scale factors differ significantly from unity for the EMEC inner wheel, an effect more pronounced with tighter cuts. It may be assumed that this is due to mismodelling of the shower shapes in the 2012 data. This can be best seen when comparing the measured and predicted distributions for $\langle \lambda^2 \rangle$, which describes the longitudinal extension of the shower. This plot is shown in Figure A.19.

$ \eta $	Tight			Medium			Loose		
	SF	Δ_{sys}	Δ_{stat}	SF	Δ_{sys}	Δ_{stat}	SF	Δ_{sys}	Δ_{stat}
2.5..2.6	0.9211	0.0198	0.0033	0.9480	0.0201	0.0028	0.9607	0.0180	0.0022
2.6..2.7	0.8855	0.0112	0.0022	0.9350	0.0113	0.0017	0.9840	0.0115	0.0011
2.7..2.8	0.8338	0.0184	0.0020	0.8978	0.0169	0.0016	0.9665	0.0154	0.0010
2.8..2.9	0.8493	0.0128	0.0021	0.9139	0.0127	0.0017	0.9754	0.0124	0.0011
2.9..3.0	0.8659	0.0109	0.0024	0.9277	0.0114	0.0019	0.9849	0.0108	0.0012
3.0..3.16	0.8587	0.0151	0.0018	0.9268	0.0145	0.0014	0.9879	0.0125	0.0009
3.35..3.6	1.0751	0.0178	0.0039	1.0762	0.0152	0.0030	1.0735	0.0147	0.0021
3.6..4.0	1.0054	0.0398	0.0032	1.0168	0.0383	0.0025	1.0321	0.0368	0.0016
4.0..4.9	0.8894	0.1155	0.0040	0.9053	0.1161	0.0032	0.9237	0.1158	0.0024

Table A.5.: Overview of the scale factors obtained with the methods described above. It can be seen that the systematic uncertainties are on the order of 1%, while the statistical uncertainties are on the order of 1‰. The rise of the uncertainties with higher values of $|\eta|$ is expected as described in Section A.2.3.

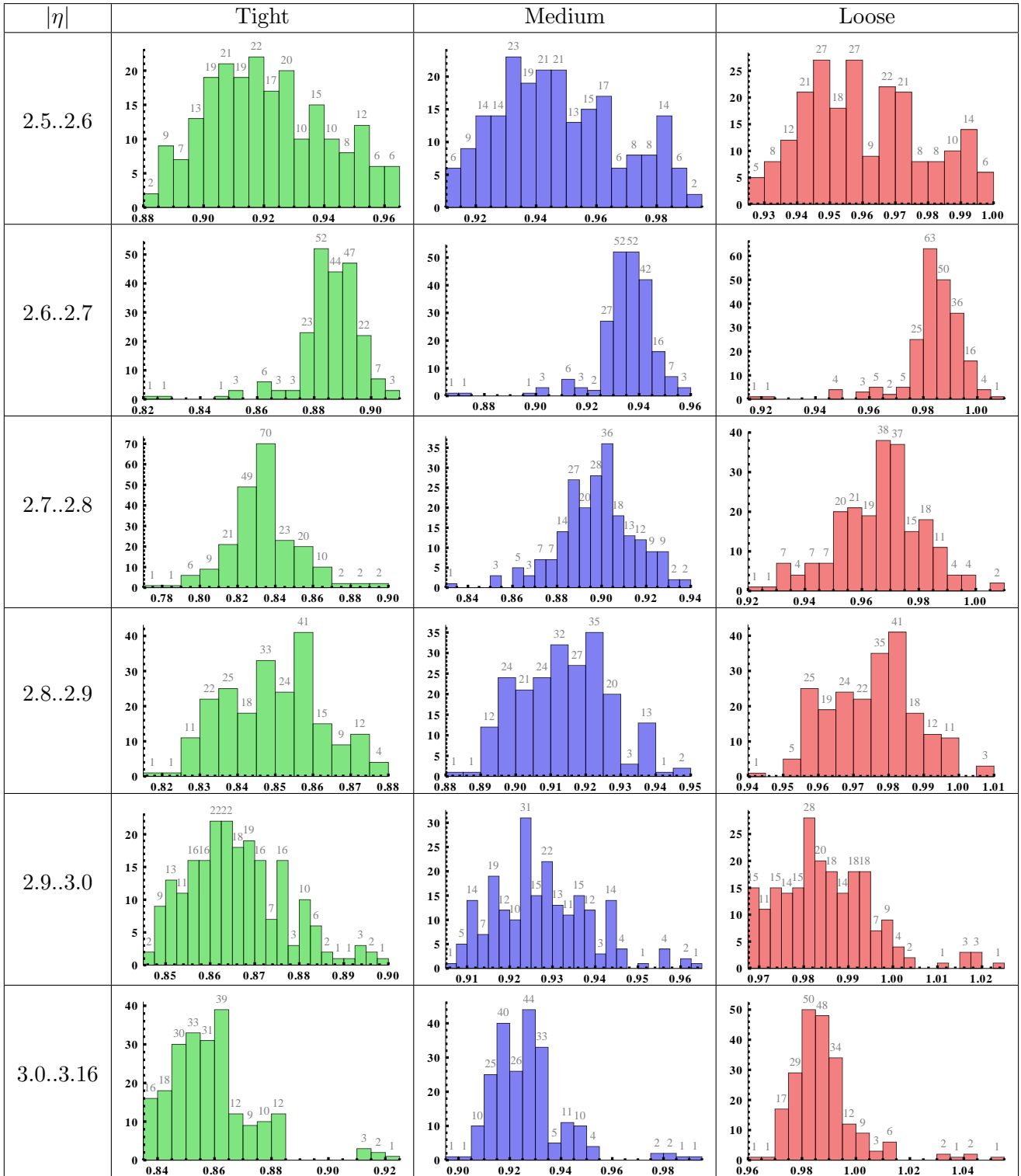


Figure A.16.: Overview of the scale factors for each variation in the EMEC IW.

A. Forward Electron Performance

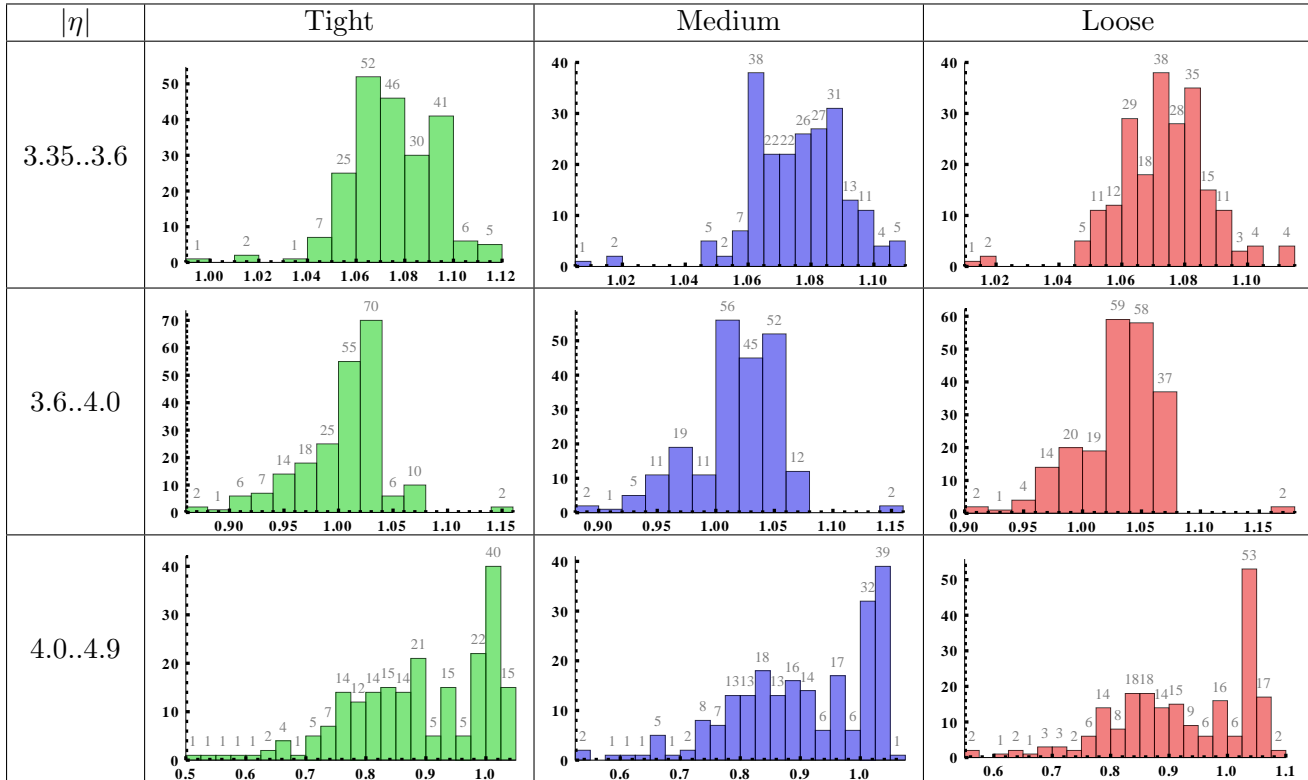


Figure A.17.: Overview of the scale factors for each variation in the FCAL.

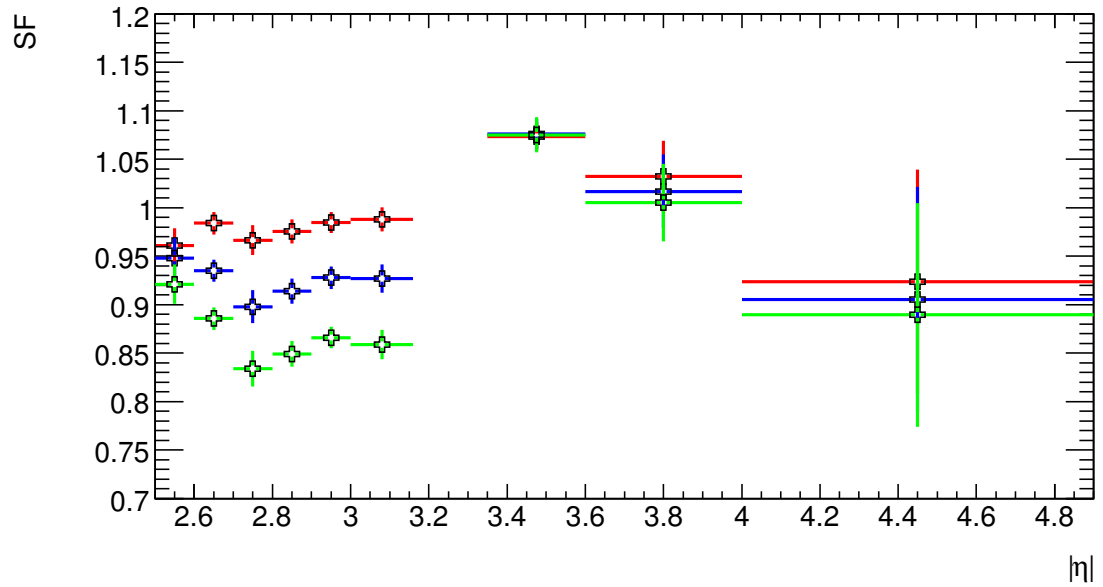


Figure A.18.: Graphical overview of all scale factors. The error bars show the total uncertainties. Tight is shown in green, Medium in blue and Loose in red.

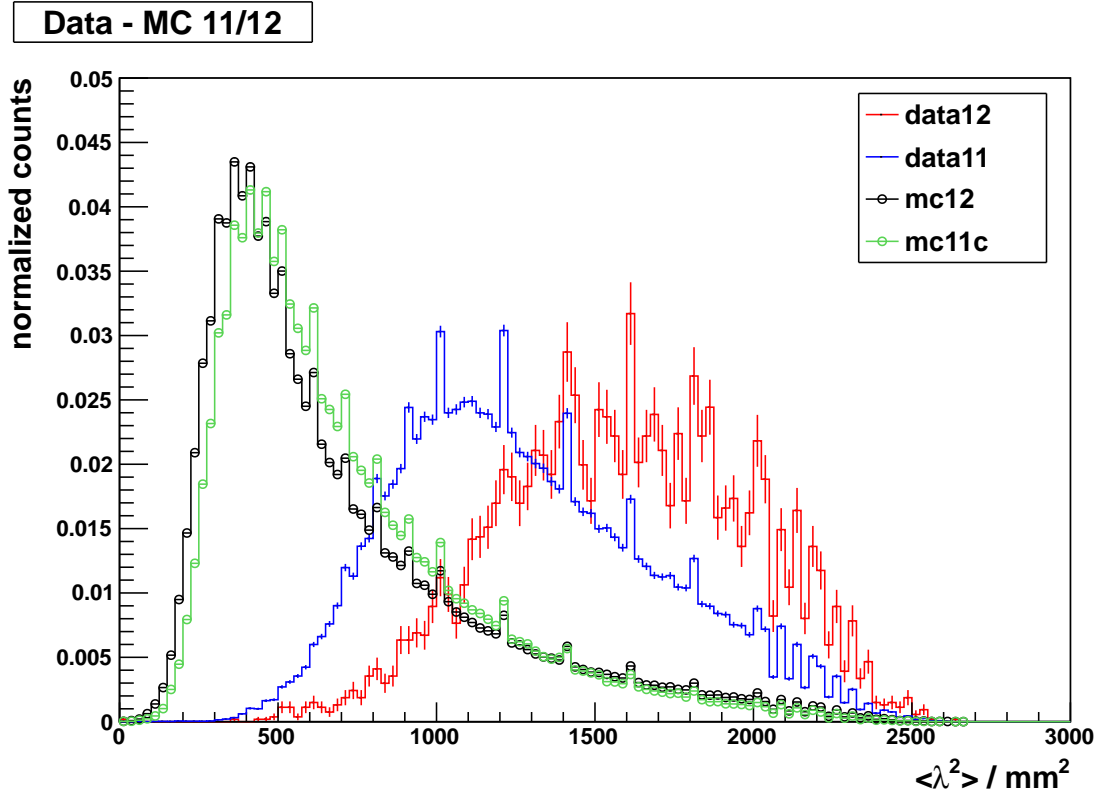


Figure A.19.: Comparison of the predicted and measured values for $\langle \lambda^2 \rangle$ as described in the text. For the production of these plots a Tag and Probe analysis with the 2011 TIGHT++ on the forward electron was performed. The background is not shown, but in general has higher values of $\langle \lambda^2 \rangle$ than the signal. A clear mismodelling of the longitudinal shower shape can be discerned. Courtesy of Christoph Weinsheimer.

A.4. Conclusion

In this chapter the optimization of the forward electron identification for the data gathered in 2012 was presented. Since only events with an high-energetic electron in the inner detector were triggered in 2012, these results cannot be directly used for the measurement of the W boson mass. Nevertheless, these results can have large indirect impact on M_W , especially by enhancing our knowledge of the PDFs. Moreover, as could be shown in ref. [110], this kinematic region significantly improves the measurement of the weak mixing angle via the so-called Z forward-backward asymmetry. This opens the door for a precision measurement of three of the free parameters of the electroweak sector — M_Z , M_W and — with the ATLAS detector.

The new electron ID described in this chapter uses a Fisher discriminant, and was obtained as a function of the number of primary vertices as well as the electron pseudorapidity. The new ID is inclusive, i.e. electron candidates passing a given ID level are guaranteed to pass all lower ID levels. This simplifies studies using fake factor methods for background estimations, such as the analysis of ZZ production.

Improvements in the method for efficiency estimation were introduced for careful studies of the resulting efficiencies and broad assessment of the resulting scale factors, describing the ratio of signal efficiencies on data and Monte Carlo. It could be shown that the challenges posed can be overcome and high precision in the resulting efficiencies can be obtained — for most of the bins, the total uncertainty is on the level of 2%, and only in the last $|\eta|$ bin it surpasses 10%.

Follow-up studies can profit from the experience gained. The following points deserve a special mention:

- **Acceptance:** It was observed that the acceptance has a significant mass dependence. This distorts the mass spectrum and leads to challenging fits. In principle, this can be overcome by either taking the acceptance into account when fitting with analytical functions, or circumvented by progressing to a template-based fit approach. The latter approach would take the acceptance into account by construction, but relies on precise forward electron energy scales¹¹ and a reliable modeling of the background.
- **Other multivariate approaches:** During the course of this analysis the central electron identification moved to a likelihood-based electron identification. This can also easily be performed for the forward electrons with the existing TMVA framework, thereby harmonizing the approaches. In detailed studies performed for the forward calorimeters it was observed that the performance of both methods is very similar.

¹¹Most importantly, with the current methods for the energy scales, the frequent overestimation of the forward electron energy smearing cannot be remedied, leading to an overestimation of the width of the Z peak

B. Further Results on the Study of Muon Trigger Efficiencies

In addition to the results shown for the EF_MU18_MEDIUM_STD trigger configuration discussed in Section 8, results were also obtained for the remaining three trigger settings described in Table 8.1.

The predicted MC trigger efficiency for MC Truth muons vs η and p_T for $W \rightarrow \mu\nu$ and $Z \rightarrow \mu\mu$ events is shown in Figure B.1. Note that, as for the results discussed in Section 8, a large zoom on the y axis was necessary to make the differences vs. p_T visible. The trigger efficiencies are very similar for both samples and differ by only around 5 %, which confirms the assumption that the determined trigger efficiencies in Z-boson data can also be applied for the W boson samples¹.

Table B.1, B.2 and B.3 show the measured number of data events for the three trigger settings not shown in Section 8.1 in addition to the predicted number of events from Monte Carlo simulations. Apart from the, naturally, different number of events, these tables do not show any significant differences to those presented in Chapter 8.

The same holds true for the control plots presented in Figures B.2, B.3 and B.4. The resulting efficiencies shown in Figures B.5, B.6 and B.7, however, show significant differences. As discussed in greater detail in Chapter 8, these can be traced back to an unforeseen trigger inefficiencies in period B-G5 and L3-L4. Of special importance is the dependence on p_T , which, as was also discussed in Chapter 8, could be to a large extent attributed to inefficiencies in η propagating into the one-dimensional projection onto p_T .

The uncertainties presented in Figures B.8, B.9 and B.10 are very similar. Compared to the efficiencies obtained for the reconstruction and isolation scale factors, it is notable that these uncertainties are significantly larger. This is because of the lower efficiency of the trigger matching cut, and the associated increase of uncertainty given a sample of probe muons of comparable size. The effect can be understood by modeling the trigger matching cut as a Bernoulli process with $p = \varepsilon$ and $n = N_{\text{probe}}$. The variance, divided by the number of probes N_{probe} might be used as an indicator for the uncertainty on the estimator of ε , and is given by:

$$V = p(1 - p) \tag{B.1}$$

This equation has a maximum for $p = 0$ and $p = 1$, and a minimum for $p = 1/2$. With the trigger efficiencies on the order of $\varepsilon=70\%$, the uncertainty is significantly increased with respect to the isolation and reconstruction efficiency, which were on the level of 95 to 99%.

¹Remaining differences can be explained by the difference in the underlying p_T or η distribution of the decay leptons from W and Z bosons.

B. Further Results on the Study of Muon Trigger Efficiencies

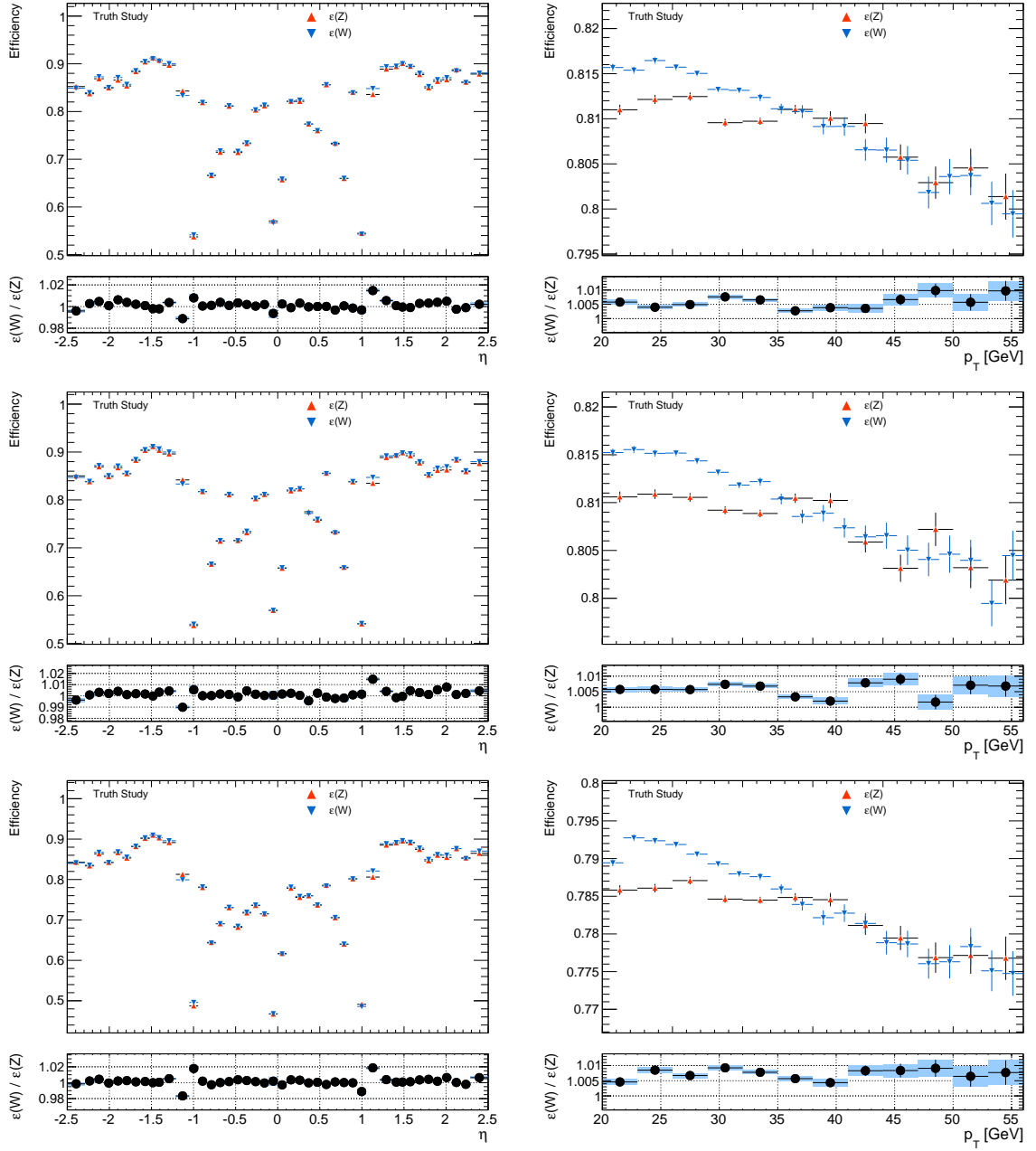


Figure B.1.: Trigger efficiency of muons in $W \rightarrow \mu\nu$ and $Z \rightarrow \mu\mu$ MC samples vs. η (left) and p_T (right). From top to bottom: EF_MU18_BG5, EF_MU18_G6I and EF_MU18_MEDIUM_L3L4. The uncertainties shown are purely statistical.

Sample	Numerator			Denominator		
	N	Δ_{stat}	Δ_{syst}	N	Δ_{stat}	Δ_{syst}
Data	329304	573	0	411951	641	0
POWHEG $Z\mu\mu$ (147407)	332601	217	16630	411163	242	20558
MC@NLO $t\bar{t}$ (105200)	159	2	9	203	2	12
HERWIG WW (105985)	38	1	2	46	1	3
HERWIG ZZ (105986)	159	1	11	198	2	13
HERWIG WZ (105987)	227	2	15	287	2	20
PYTHIA $Z\tau\tau$ (106052)	36	12	1	36	12	1
MC@NLO Single Top (108340)	0	0	0	0	0	0
MC@NLO Single Top (108341)	1	0	0	1	0	0
MC@NLO Single Top (108342)	0	0	0	0	0	0
MC@NLO Single Top (108343)	0	0	0	0	0	0
MC@NLO Single Top (108344)	0	0	0	0	0	0
MC@NLO Single Top (108345)	0	0	0	0	0	0
MC@NLO Single Top (108346)	12	1	0	15	1	1
MC@NLO QCD (data driven)	93	15	0	112	16	0

Table B.1.: Overview of selected events in the numerator and denominator for data and all background contributions for the determination of the EF_MU18_BG5 trigger scale factors.

Sample	Numerator			Denominator		
	N	Δ_{stat}	Δ_{syst}	N	Δ_{stat}	Δ_{syst}
Data	326880	571	0	394602	628	0
POWHEG $Z\mu\mu$ (147407)	318319	216	15915	393883	240	19694
MC@NLO $t\bar{t}$ (105200)	159	2	9	204	2	12
HERWIG WW (105985)	39	1	2	49	1	3
HERWIG ZZ (105986)	156	1	10	196	2	13
HERWIG WZ (105987)	216	2	15	270	2	18
PYTHIA $Z\tau\tau$ (106052)	22	9	1	31	11	1
MC@NLO Single Top (108340)	0	0	0	0	0	0
MC@NLO Single Top (108341)	0	0	0	0	0	0
MC@NLO Single Top (108342)	0	0	0	0	0	0
MC@NLO Single Top (108343)	0	0	0	0	0	0
MC@NLO Single Top (108344)	0	0	0	0	0	0
MC@NLO Single Top (108345)	0	0	0	0	0	0
MC@NLO Single Top (108346)	14	1	1	18	1	1
QCD (data driven)	42	11	0	60	13	0

Table B.2.: Overview of selected events in the numerator and denominator for data and all background contributions for the determination of the EF_MU18_G6I trigger scale factors.

B. Further Results on the Study of Muon Trigger Efficiencies

Sample	Numerator			Denominator		
	N	Δ_{stat}	Δ_{syst}	N	Δ_{stat}	Δ_{syst}
Data	182658	427	0	259397	509	0
POWHEG $Z\mu\mu$ (147407)	202316	161	10115	258908	183	12945
MC@NLO $t\bar{t}$ (105200)	101	1	6	134	2	8
HERWIG WW (105985)	23	0	1	30	0	2
HERWIG ZZ (105986)	102	1	7	130	1	9
HERWIG WZ (105987)	139	1	9	176	1	12
PYTHIA $Z\tau\tau$ (106052)	20	8	1	27	10	1
MC@NLO Single Top (108340)	0	0	0	0	0	0
MC@NLO Single Top (108341)	0	0	0	0	0	0
MC@NLO Single Top (108342)	0	0	0	0	0	0
MC@NLO Single Top (108343)	0	0	0	0	0	0
MC@NLO Single Top (108344)	0	0	0	0	0	0
MC@NLO Single Top (108345)	0	0	0	0	0	0
MC@NLO Single Top (108346)	8	0	0	12	0	0
QCD (data driven)	13	4	0	22	6	0

Table B.3.: Overview of selected events in the numerator and denominator for data and all background contributions for the determination of the EF_MU18_MEDIUM_L3L4 trigger scale factors.

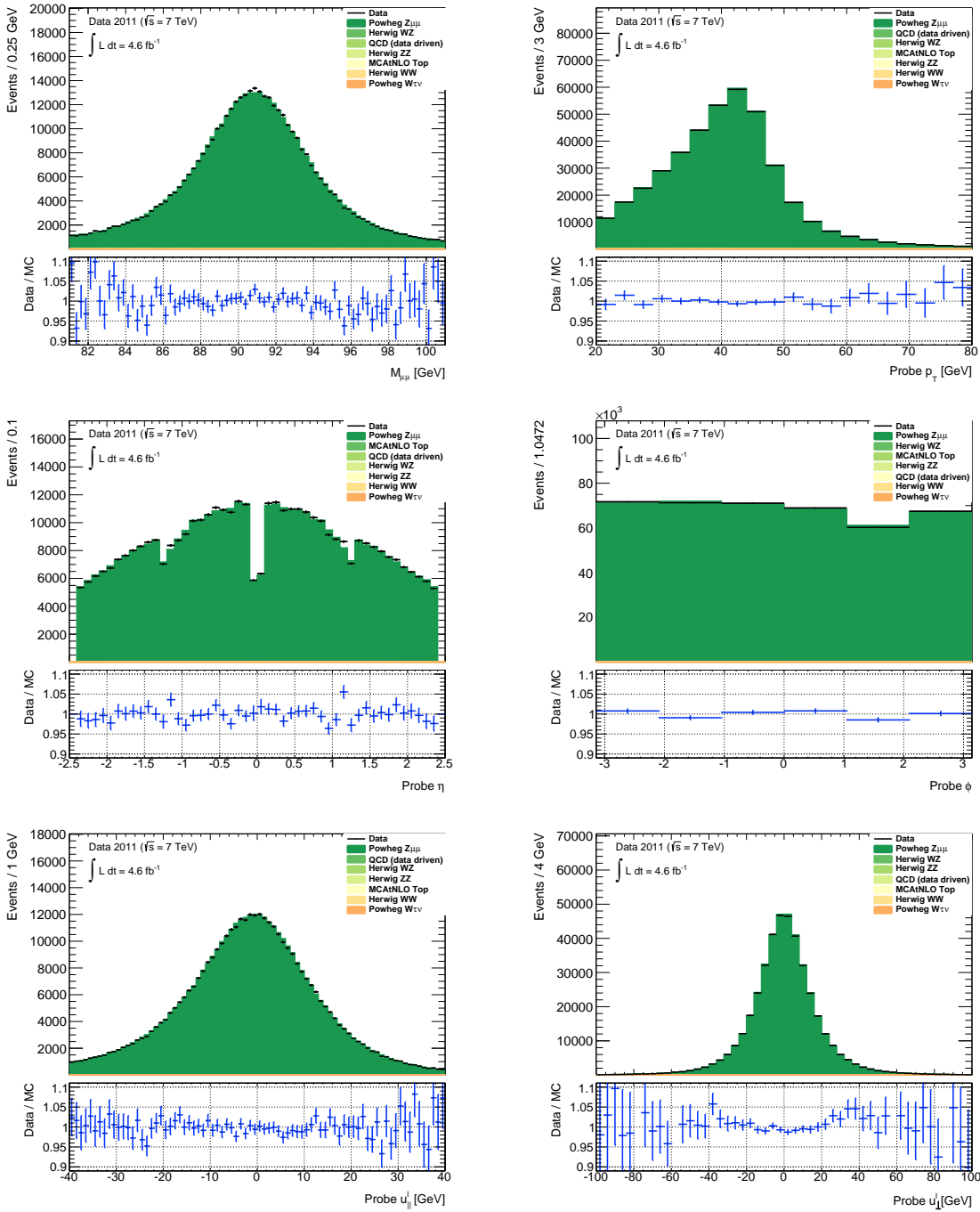


Figure B.2.: Kinematic distributions of probe-tracks comparing data to the combined signal and background prediction. From left to right, top to bottom: invariant mass of the selected $\mu\mu$ pair, probe p_T , η , φ , u_{\perp}^l and u_{\perp}^l . The control plots shown are for EF_MU18_BG5.

B. Further Results on the Study of Muon Trigger Efficiencies

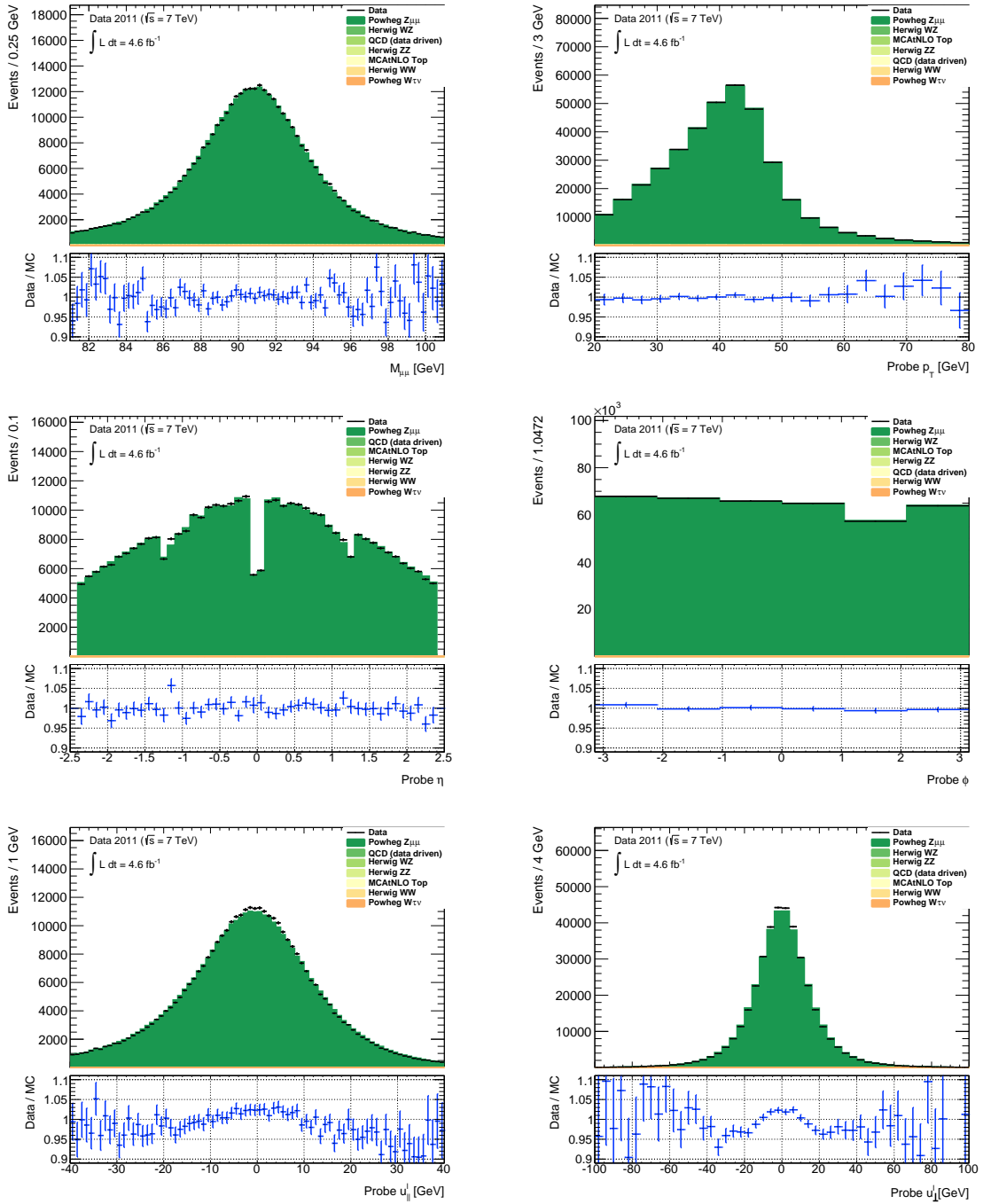


Figure B.3.: Kinematic distributions of probe-tracks comparing data to the combined signal and background prediction. From left to right, top to bottom: invariant mass of the selected $\mu\mu$ pair, probe p_T , η , φ , $u_{||}^l$ and u_{\perp}^l . The control plots shown are for EF_MU18-G6I.

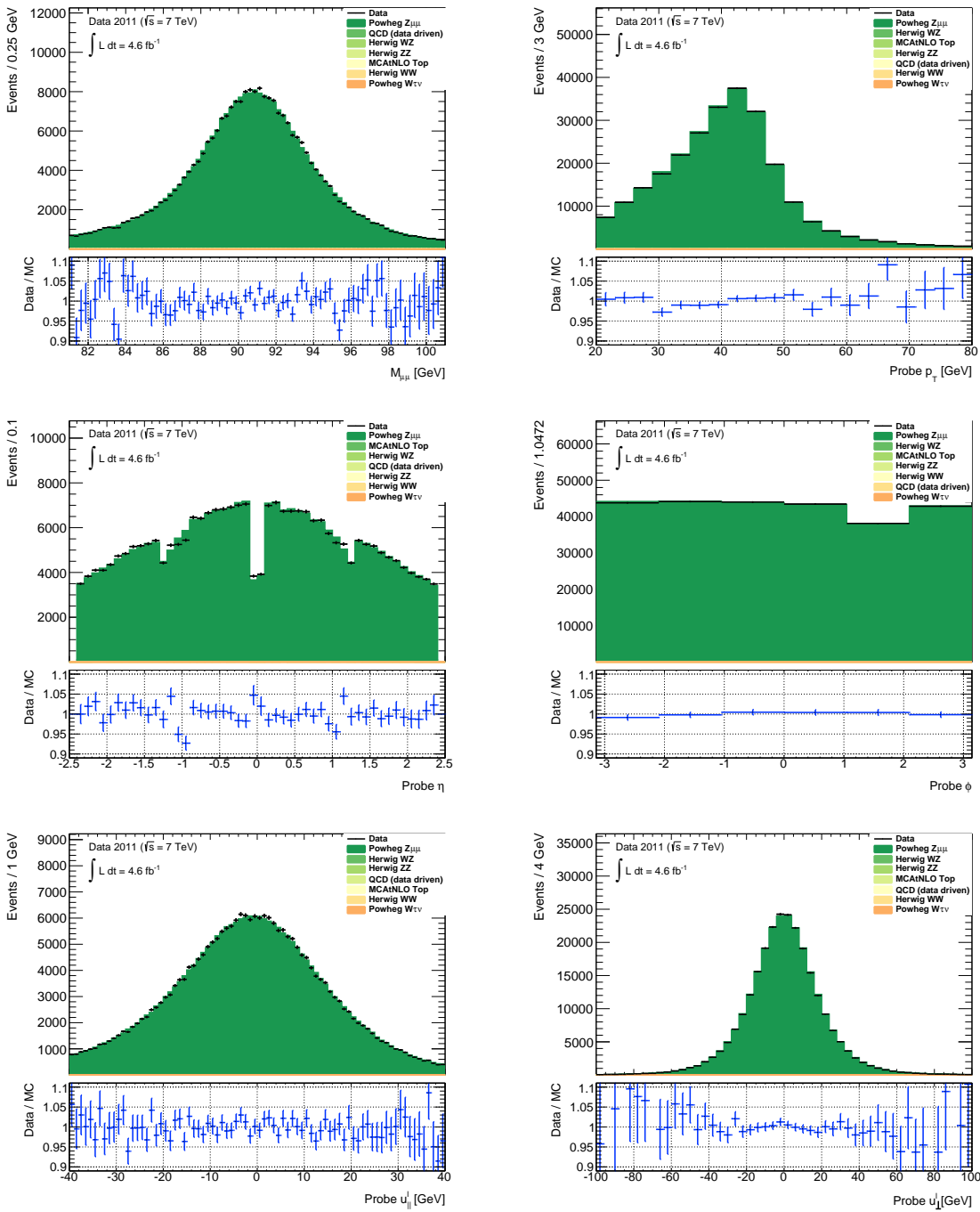


Figure B.4.: Kinematic distributions of probe-tracks comparing data to the combined signal and background prediction. From left to right, top to bottom: invariant mass of the selected $\mu\mu$ pair, probe p_T , η , φ , $u_{||}^l$ and u_{\perp}^l . The control plots shown are for EF_MU18_MEDIUM_L3L4.

B. Further Results on the Study of Muon Trigger Efficiencies

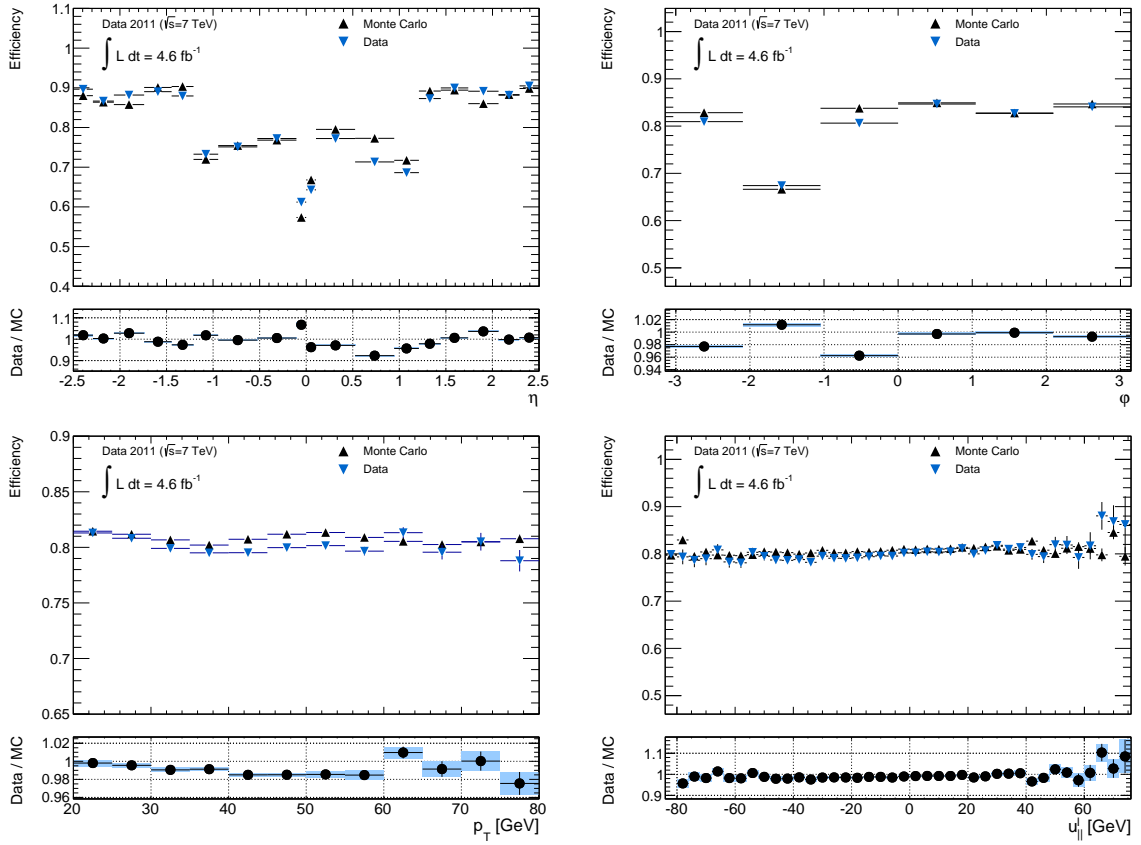


Figure B.5.: Determined trigger efficiency by the tag and probe method for data and MC. From top to bottom, left to right: η , ϕ , p_T , $u_{||}^1$. Results are only shown for EF_MU18_BG5. Only statistical uncertainties are shown.

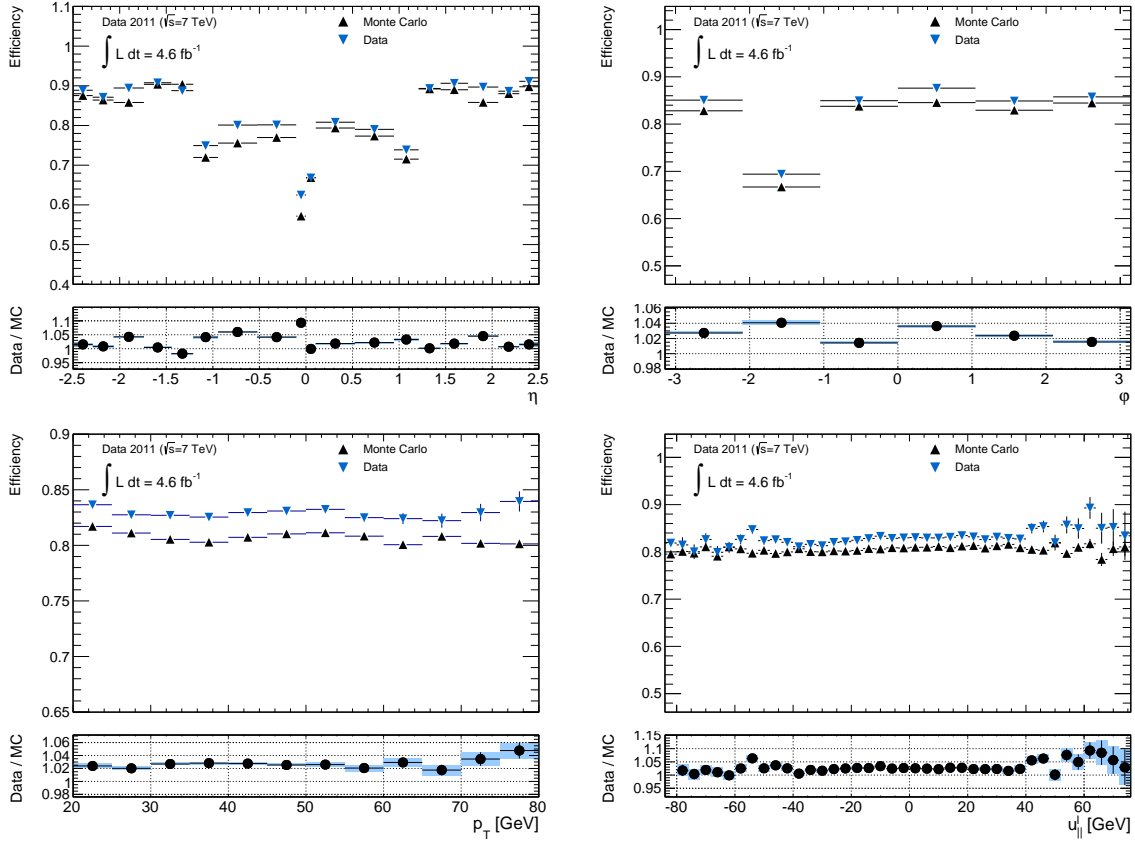


Figure B.6.: Determined trigger efficiency by the tag and probe method for data and MC. From top to bottom, left to right: η , ϕ , p_T , $u_{||}^l$. Results are only shown for EF_MU18_G6I. Only statistical uncertainties are shown.

B. Further Results on the Study of Muon Trigger Efficiencies

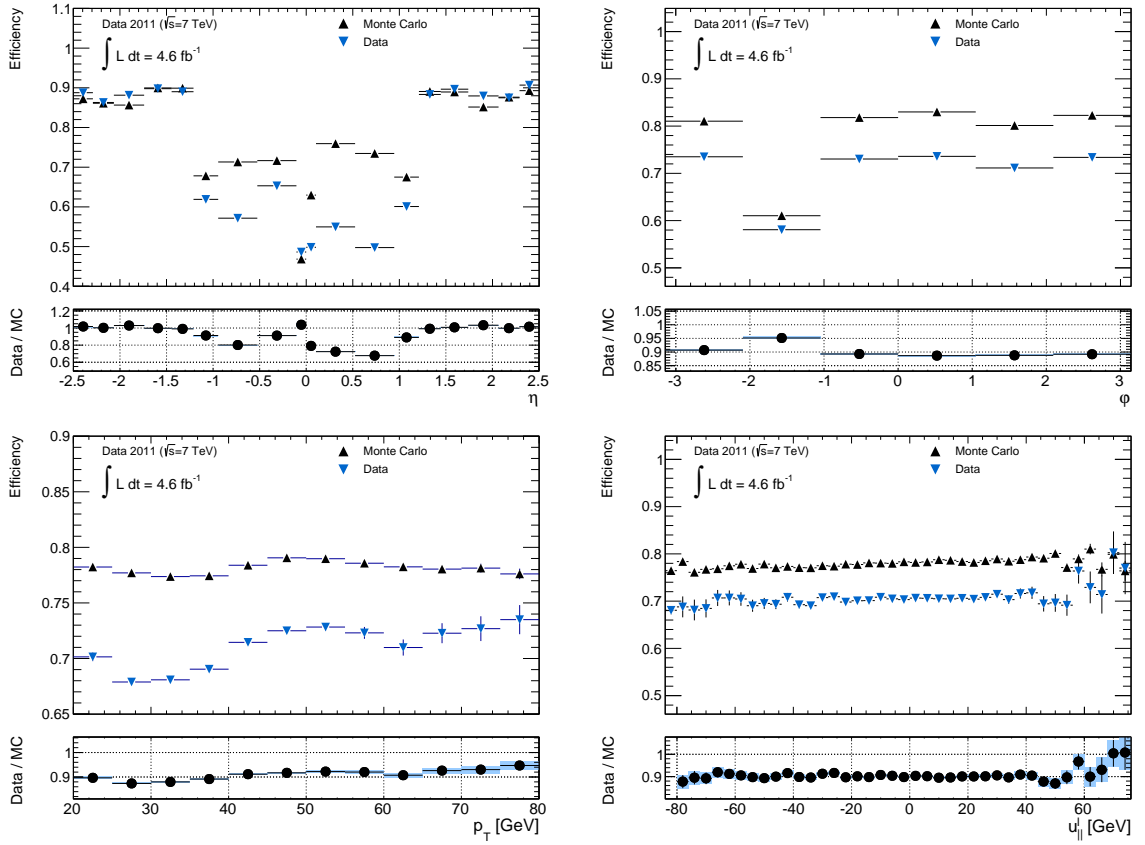


Figure B.7.: Determined trigger efficiency by the tag and probe method for data and MC. From top to bottom, left to right: η , φ , p_T , $u_{||}^l$. Results are only shown for EF_MU18_MEDIUM_L3L4. Only statistical uncertainties are shown.

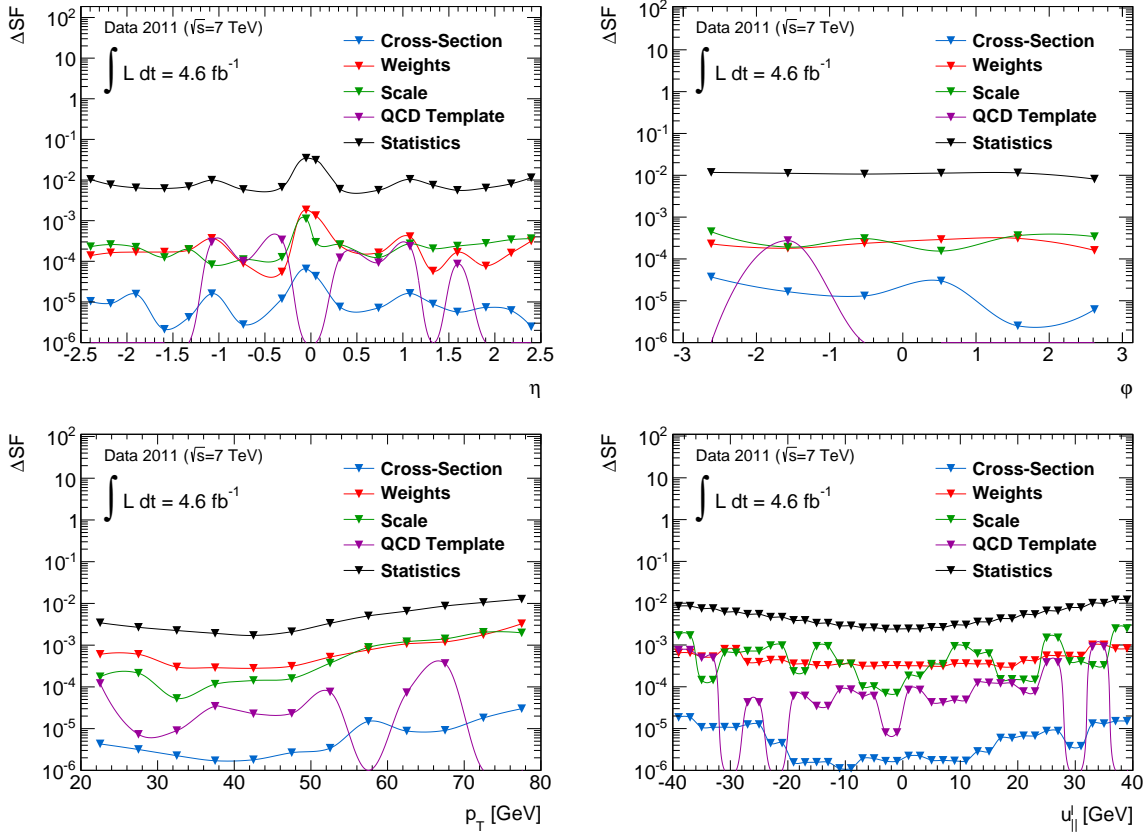


Figure B.8.: Uncertainties on the obtained trigger scale for the trigger EF_MU18_BG5. From left to right: η , p_T , u^l . Table 6.5 gives details on the categories shown in the plot.

B. Further Results on the Study of Muon Trigger Efficiencies

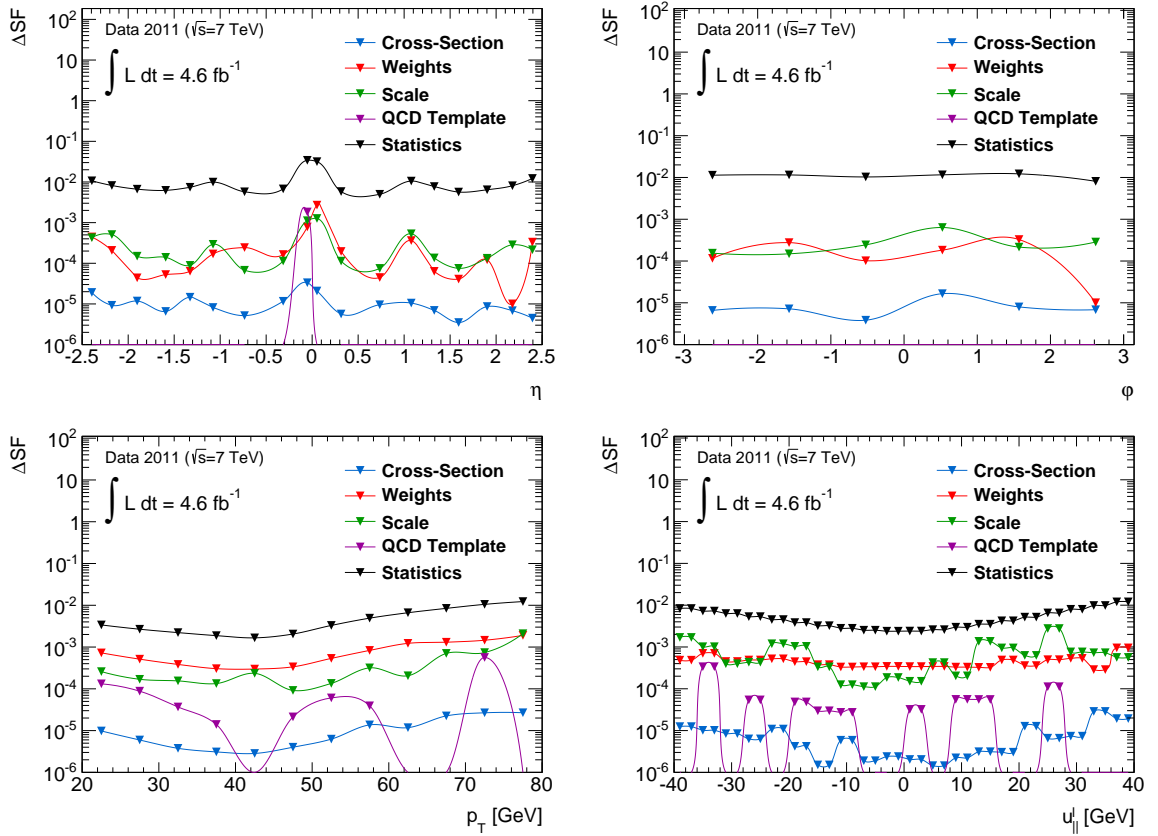


Figure B.9.: Uncertainties on the obtained trigger scale for the trigger EF_MU18_G6I. From left to right: η , p_T , u^l . Table 6.5 gives details on the categories shown in the plot.

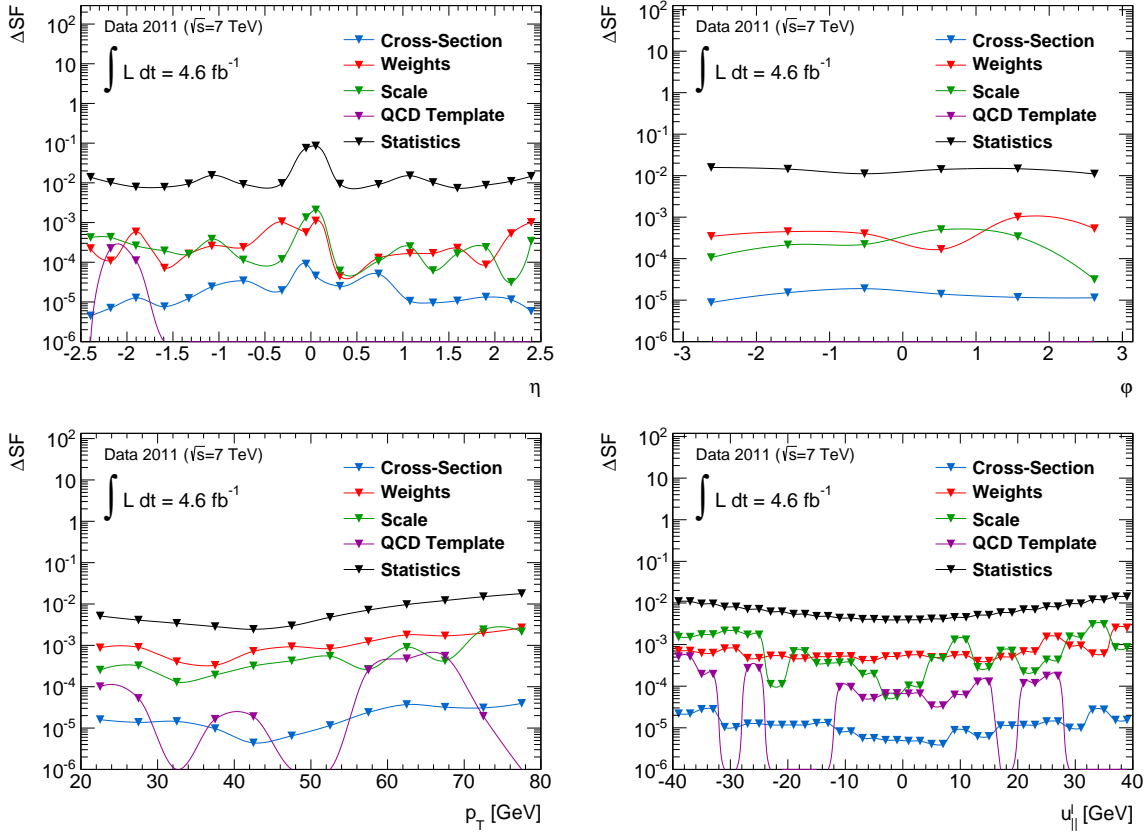


Figure B.10.: Uncertainties on the obtained trigger scale for the trigger EF_MU18_MEDIUM_L3L4. From left to right: η , p_T , u_{\parallel}^l . Table 6.5 gives details on the categories shown in the plot.

C. Muon ID Track Efficiency

In the determination of the muon reconstruction scale factors, it was assumed that ATLAS has almost full efficiency for muons to produce tracks in the inner detector. Furthermore, it was assumed that this efficiency is well modeled in Monte Carlo and therefore no additional scale factors are necessary. In this section, it is proven that these assumptions, which are well motivated from first principles, actually hold. To this end, a Tag and Probe analysis similar to the analyses described before is performed. The ID track efficiency is estimated as the probability for a muon reconstructed only in the muon system to be matched to a corresponding ID track.

C.1. Methodology, Event Selection and Corrections

The ‘tag’-object in this case is an isolated and triggered stand-alone muon, the ‘probe’-object is an isolated stand-alone muon which leads together with the tag-kinematics to an invariant mass close to the Z boson. Since the background contribution to this process is very low, the ID track efficiency of combined muons can be precisely determined. The selection criteria for the tag- and probe-object selection are summarized in the following:

Pairs of STACO muons were selected according to the following selection criteria:

- Event cuts:
 - Trigger: EF_MU18 up to period J, EF_MU18_MEDIUM from period J inclusive
 - Good Primary vertex Conditions: At least 3 tracks from primary vertex
- Muon Selection:
 - Quality cuts summarized in Table 6.3
 - $|\eta| \leq 2.4$
 - $p_T \geq 20$ GeV
 - Isolated with $p_T^{\text{cone20}}/p_T < 0.1$
 - $|z_{0,PV}| < 10$ mm
- Pair Selection:
 - $|z_{0,PV,1} - z_{0,PV,2}| < 3$ mm
 - $|M_{\mu\mu} - M_Z| \leq 10$ GeV
 - Opposite charge
 - Exactly one pair per vent
- Tag trigger matched

C. Muon ID Track Efficiency

The muon ID track efficiency is also determined in three dimensions, using the binning shown in Table 6.1 for the transverse momentum of the muon p_T , u_{\parallel}^l and also the detector region, which is a combined η - φ -binning. On average, several thousand probe muons per bin for the full 2011 data-set are found. Technically, the efficiencies are represented by two sets of histograms, one representing the kinematics of probe muons, the other representing the kinematics of those probe muons that could be matched to an ID track. A probe muon is defined as matched to an ID track if an ID track with a transverse momentum of more than 15 GeV is found within $\Delta R = 0.15$. The ID track efficiencies are obtained by dividing the two sets, after backgrounds are subtracted.

The background determination was already described in Section 6.2. An overview of the selected inclusive number of events in the numerator and denominator including the background estimations is given in Table C.1.

Sample	Numerator			Denominator		
	N	Δ_{stat}	Δ_{syst}	N	Δ_{stat}	Δ_{syst}
Data	3307894	1818	0	3344817	1828	0
POWHEG $Z\mu\mu$ (147407)	3310860	685	165543	3338763	688	166938
MC@NLO $t\bar{t}$ (105200)	1743	8	108	1760	8	109
HERWIG WW (105985)	377	3	26	380	3	26
HERWIG ZZ (105986)	1651	5	115	1666	5	116
HERWIG WZ (105987)	2310	7	161	2331	7	163
PYTHIA $Z\tau\tau$ (106052)	293	34	14	314	35	15
MC@NLO Single Top (108340)	0	0	0	0	0	0
MC@NLO Single Top (108341)	6	1	0	6	1	0
MC@NLO Single Top (108342)	0	0	0	0	0	0
MC@NLO Single Top (108343)	0	0	0	0	0	0
MC@NLO Single Top (108344)	0	0	0	0	0	0
MC@NLO Single Top (108345)	0	0	0	0	0	0
MC@NLO Single Top (108346)	141	3	9	143	3	10
QCD (data driven)	0	0	0	0	0	0

Table C.1.: Overview of selected events in the numerator and denominator for data and all background contributions for the determination of ID track reconstruction scale factors.

Several kinematic distributions of probe muon candidates are shown in Figure C.1, where all MC corrections have been applied. In general a good data/MC can be observed. It has to be noted that all corrections were obtained for ID kinematics, therefore the description of data is significantly worse with respect to the results shown in Figure 7.3

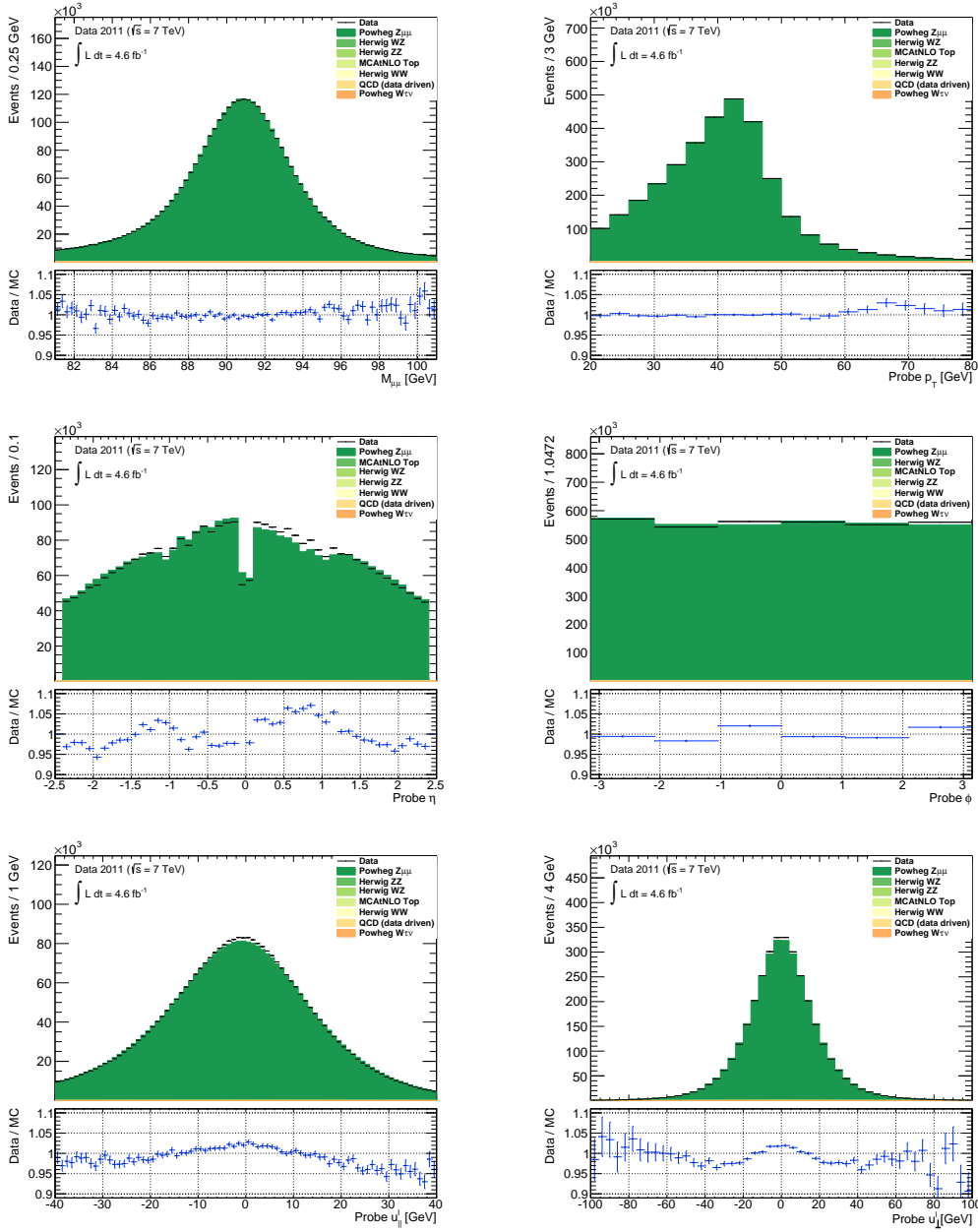


Figure C.1.: Kinematic distributions of probe muons comparing data to the combined signal and background prediction. From left to right, top to bottom: Invariant mass of the selected $\mu\mu$ pair, probe p_T , η , ϕ , u_{\parallel}^l and u_{\perp}^l .

C.2. Efficiency and Scale Factor Determination

The resulting efficiencies are shown in Figure C.2 in one-dimensional projections with a higher granularity, where the tag and probe method has been applied on both data and the POWHEG $Z \rightarrow \mu\mu$ sample. For clarity, instead of presenting the *region*, i.e. the combined η - φ binning, separate results for η and φ are shown in two separate histograms. As can be seen, the efficiency as function of η and φ is by no means featureless. Instead, a pronounced dip centered at $|\eta| = 0$ can be seen. In φ , two dips between -3 rad and -2 rad, as well as between 1 rad and 2 rad can be seen. At the time of writing, the origin of these structures is not clear. However, it has to be observed that overall the shape of these structures is described by Monte Carlo and has therefore to be a feature of the detector accounted for in the detector modeling. Note, that the scale factors are on the order of 0.996, with only small fluctuations on the order of several per mil. Therefore, the ID scale factors are expected to play a negligible role.

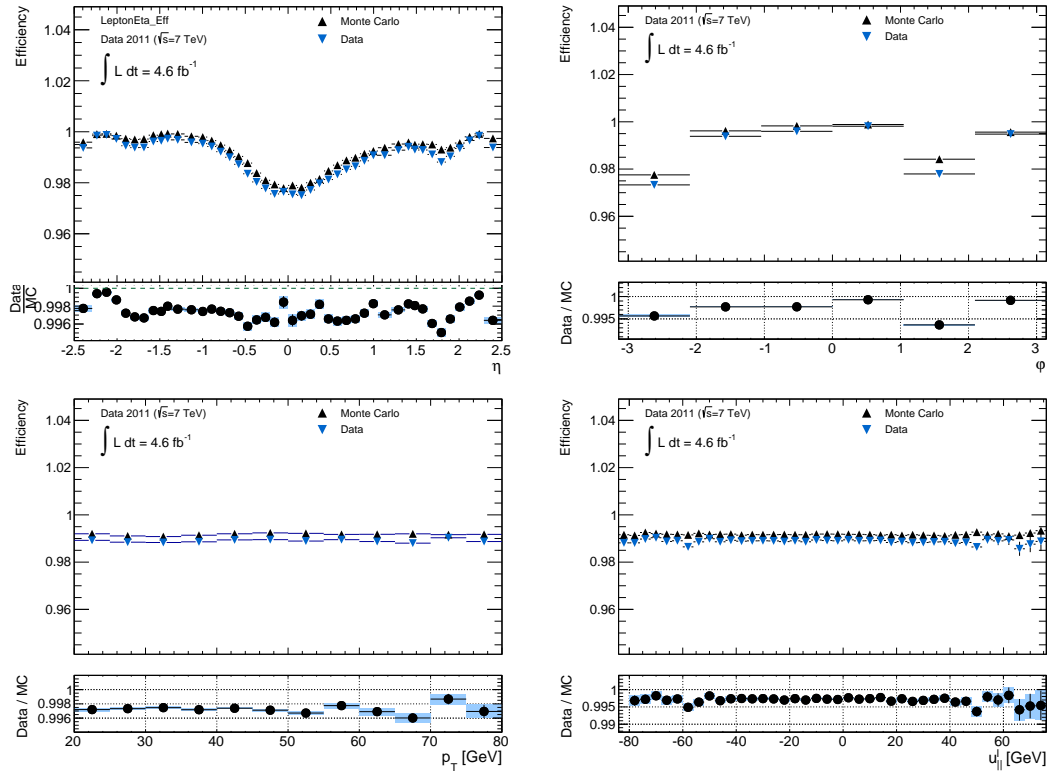


Figure C.2.: Determined ID track reconstruction efficiency using the tag- and probe-method for MC and data. From left to right, top to bottom: η , φ , p_T and u_{\parallel}^l . Only statistical uncertainties are shown.

As can be seen the efficiencies are close to 99% and well modeled by the Monte Carlo simulation. Moreover, no slope with respect to p_T can be detected — showing that the ID track efficiency is unlikely to influence the measurement of M_W . This is also supported by the negligible slopes detected in the scale factors, discussed below.

C.2. Efficiency and Scale Factor Determination

Scale factors are now defined as the ratio of the reconstruction efficiency in data and MC, $SF := \varepsilon_{Data}/\varepsilon_{MC}$. The resulting scale factors are shown in Figure 7.8. As it could already be assumed from the good description of the data efficiencies by Monte Carlo, the resulting scale factors are relatively flat and close to unity. The uncertainties shown are only statistical.

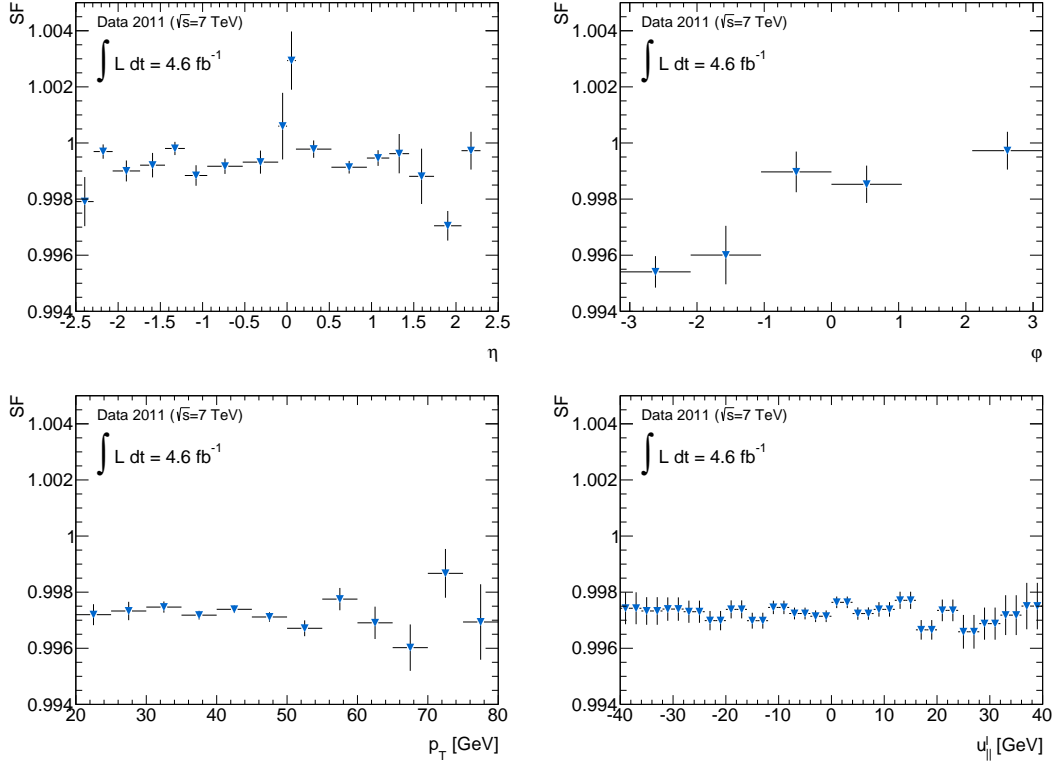


Figure C.3.: ID track reconstruction scale factors determined for the POWHEG MC simulation. From left to right, top to bottom: η , p_T , u_{\perp}^l . Uncertainties shown are the statistical uncertainties.

C. Muon ID Track Efficiency

The question arises, whether the fluctuations in p_T are indeed non-significant. To this end, the detectors is divided into four bins in η which have a relatively uniform reconstruction efficiency. These regions are $-2.065 \leq \eta \leq -1.445$, $-0.945 \leq \eta \leq -0.105$, $0.105 \leq \eta \leq 0.945$ and $1.445 \leq \eta \leq 2.065$, thereby excluding the crack regions between the endcaps and the barrel at $|\eta| \approx 1.05$ and the gap at $|\eta| = 0$. The resulting scale factors in p_T for these four regions can be seen in Figure C.4 and Table C.2. In this figure, the results from a fit for each of the distributions with a polynomial of the form $p_0 + p_1 \cdot p_T$ in the range of 25 to 60 GeV is also shown. In addition, the significance $p_1/\Delta p_1$ is shown. As can be seen, the distribution of the scale factors appears to be compatible with a flat distribution in all four regions. A full overview is shown in Figure C.5.

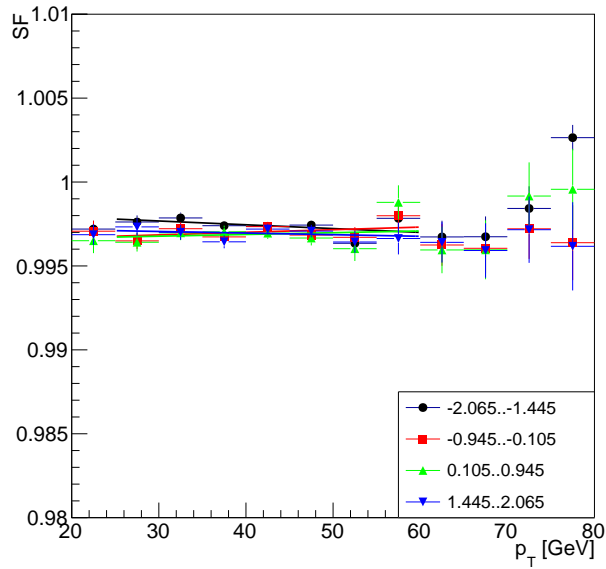


Figure C.4.: ID track reconstruction scale factors in four regions of the detector with uniform efficiency. The corresponding fit values are shown in Table C.2.

η	χ^2/dof	p_1 [GeV $^{-1}$]	Δp_1 [GeV $^{-1}$]	$p_1/\Delta p_1$
-2.065..-1.445	5.2/5	$-2.27 \cdot 10^{-5}$	$1.62 \cdot 10^{-5}$	-1.40
-0.945..-0.105	4.8/5	$1.55 \cdot 10^{-5}$	$2.02 \cdot 10^{-5}$	0.77
0.105..0.945	5.9/5	$1.04 \cdot 10^{-5}$	$2.37 \cdot 10^{-5}$	0.44
1.445..2.065	3.6/5	$-9.56 \cdot 10^{-6}$	$2.20 \cdot 10^{-5}$	-0.43

Table C.2.: Resulting fit values for the fits shown in Figure C.4.

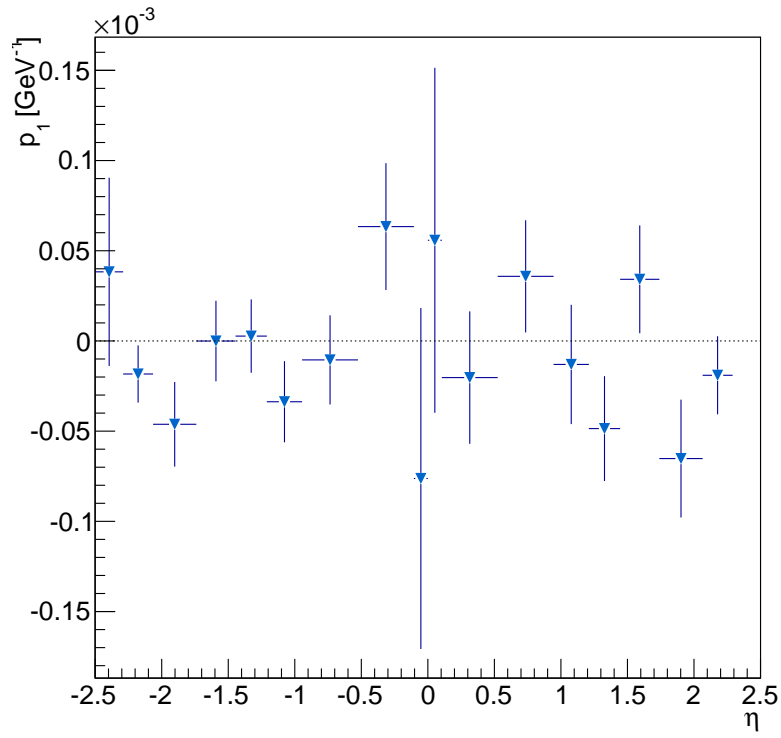


Figure C.5.: Value of p_1 for each of the 44 η bins.

C. Muon ID Track Efficiency

The general approach for the treatment and estimation of uncertainties is described in Section 6.3. In Figure C.6, only the statistical uncertainties are shown, which are the leading uncertainties. As expected, the statistical uncertainty grows in areas where less data could be taken.

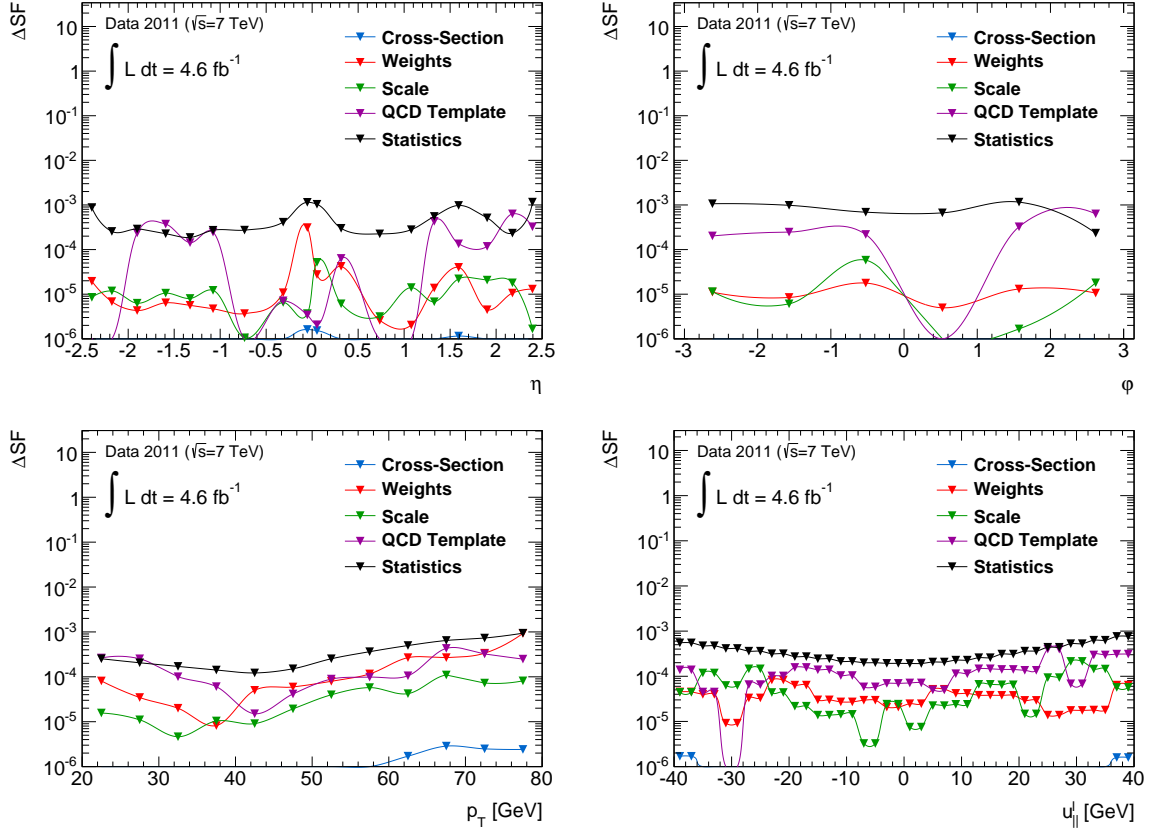


Figure C.6.: Uncertainties on the ID track reconstruction scale factors for the POWHEG MC prediction. From left to right: η , p_T , $u_{||}^l$. Table 6.5 gives details on the categories shown in the plot.

D. Acknowledgments

This thesis marks the endpoint of a journey spanning almost four years. It would not have been feasible without the assistance I have received, and I would like to thank for this.

[REDACTED]

[REDACTED]

[REDACTED]

[REDACTED]

[REDACTED]

[REDACTED]

[REDACTED]

[REDACTED]

I would also like to thank for the financial support necessary, which came from several sources: First of all, this thesis has been supported by a fellowship through GRK Symmetry Breaking (DFG/GRK 1581). I am very thankful for the opportunities opened to me by this graduate school, both in terms of personal as well as professional development through

D. Acknowledgments

meetings, lectures and summer schools. The measurement of the W boson mass received additional funding by the Volkswagen Foundation. And, of course, I would like for the opportunities opened to me by my advisors, and the funding for my research visits, and the summer schools in St. Andrews and at the Fermilab. I think, few PhD students had the opportunity to get a lecture on the Higgs boson by ██████████, as I had at the Scottish Universities Summer School in St. Andrews — thank you!

Bibliography

- [1] A. Salam and C. Lai.
Ideals and Realities: Selected Essays of Abdus Salam.
World Scientific, 1987.
ISBN 9789971503154.
- [2] P. A. R. Ade et al. (Planck).
Planck 2015 results. XIII. Cosmological parameters, 2015.
arXiv:1502.01589.
- [3] M. Thomson.
Modern particle physics.
Cambridge University Press, New York, 2013.
ISBN 9781107034266.
- [4] W. H. Jefferys and J. O. Berger.
Ockham's Razor and Bayesian Analysis.
In *American Scientist*, vol. **80**(1) pp. 64–72, 1992.
- [5] G. Aad et al. (ATLAS).
Observation of a new particle in the search for the Standard Model Higgs boson with the ATLAS detector at the LHC.
In *Physics Letters*, vol. **B716** pp. 1–29, 2012.
doi:10.1016/j.physletb.2012.08.020.
arXiv:1207.7214.
- [6] S. Chatrchyan et al. (CMS).
Observation of a new boson at a mass of 125 GeV with the CMS experiment at the LHC.
In *Physics Letters*, vol. **B716** pp. 30–61, 2012.
doi:10.1016/j.physletb.2012.08.021.
arXiv:1207.7235.
- [7] M. Baak, J. Cúth, J. Haller et al. (Gfitter Group).
The global electroweak fit at NNLO and prospects for the LHC and ILC.
In *European Physical Journal*, vol. **C74** p. 3046, 2014.
doi:10.1140/epjc/s10052-014-3046-5.
arXiv:1407.3792.
- [8] K. Olive et al. (Particle Data Group).
Review of Particle Physics.
In *Chin.Phys.*, vol. **C38** p. 090 001, 2014.
doi:10.1088/1674-1137/38/9/090001.
- [9] T. Morii, C. Lim and S. Mukherjee.
The Physics of the Standard Model and Beyond.
World Scientific, 2004.
ISBN 9789812795601.

BIBLIOGRAPHY

- [10] M. E. Peskin and D. V. Schroeder.
An Introduction To Quantum Field Theory (Frontiers in Physics).
Westview Press, 1995.
ISBN 0201503972.
- [11] T. W. B. Kibble.
History of electroweak symmetry breaking.
In Journal of Physics Conference Series, **vol. 626**(1) 012001, 2015.
doi:10.1088/1742-6596/626/1/012001.
arXiv:1502.06276.
- [12] A. Jaffe and E. Witten.
Quantum Yang-Mills Theory.
URL <http://www.claymath.org/sites/default/files/yangmills.pdf>.
- [13] K. Schmieden.
Measurement of the Weak Mixing Angle and the Spin of the Gluon from Angular Distributions in the Reaction $pp \rightarrow Z/\gamma^ + X \rightarrow \mu^+ \mu^- + X$ with ATLAS*.
Ph.D. thesis, Rheinische Friedrich-Willhelms-Universität Bonn, 2012.
Presented 22 Apr 2013, URL <https://cds.cern.ch/record/1566623>.
- [14] G. Arnison, A. Astbury, B. Aubert et al. (UA1).
Experimental observation of isolated large transverse energy electrons with associated missing energy at $\sqrt{s}=540$ GeV.
In Physics Letters, **vol. B122**(1) pp. 103 – 116, 1983.
doi:[http://dx.doi.org/10.1016/0370-2693\(83\)91177-2](http://dx.doi.org/10.1016/0370-2693(83)91177-2).
- [15] G. Arnison, A. Astbury, B. Aubert et al. (UA1).
Experimental observation of lepton pairs of invariant mass around 95 GeV/c² at the CERN SPS collider.
In Physics Letters, **vol. B126**(5) pp. 398 – 410, 1983.
doi:[http://dx.doi.org/10.1016/0370-2693\(83\)90188-0](http://dx.doi.org/10.1016/0370-2693(83)90188-0).
- [16] M. Banner, R. Battiston, P. Bloch et al. (UA2).
Observation of single isolated electrons of high transverse momentum in events with missing transverse energy at the CERN anti- p p collider.
In Physics Letters, **vol. B122**(5–6) pp. 476 – 485, 1983.
doi:[http://dx.doi.org/10.1016/0370-2693\(83\)91605-2](http://dx.doi.org/10.1016/0370-2693(83)91605-2).
- [17] P. Bagnaia, M. Banner, R. Battiston et al. (UA2).
Evidence for $Z^0 \rightarrow e^+ e^-$ at the CERN $\bar{p}p$ collider.
In Physics Letters, **vol. B129**(1) pp. 130 – 140, 1983.
doi:[http://dx.doi.org/10.1016/0370-2693\(83\)90744-X](http://dx.doi.org/10.1016/0370-2693(83)90744-X).
- [18] J. Ellis, M. K. Gaillard and D. V. Nanopoulos.
An Updated Historical Profile of the Higgs Boson, 2015.
arXiv:1504.07217.
- [19] R. P. Feynman.
Space-Time Approach to Non-Relativistic Quantum Mechanics.
In Rev. Mod. Phys., **vol. 20** pp. 367–387, 1948.
doi:10.1103/RevModPhys.20.367.

- [20] R. P. Feynman.
Space-Time Approach to Quantum Electrodynamics.
In *Physical Review*, **vol. 76** pp. 769–789, 1949.
doi:10.1103/PhysRev.76.769.
- [21] J. Smit.
Introduction to Quantum Fields on a Lattice.
Cambridge Lecture Notes in Physics. Cambridge University Press, 2002.
ISBN 9780521890519.
- [22] G. 't Hooft and M. J. G. Veltman.
Regularization and Renormalization of Gauge Fields.
In *Nuclear Physics*, **vol. B44** pp. 189–213, 1972.
doi:10.1016/0550-3213(72)90279-9.
- [23] S. Roth.
Precision Electroweak Physics at Electron-Positron Colliders.
Springer Tracts in Modern Physics. Springer Berlin Heidelberg, 2007.
ISBN 9783540351658.
- [24] B. Povh, K. Rith, C. Scholz et al.
Particles and Nuclei: An Introduction to the Physical Concepts.
Graduate Texts in Physics. Springer Berlin Heidelberg, 2015.
ISBN 9783662463215.
- [25] M. Awramik, M. Czakon, A. Freitas et al.
Precise prediction for the W boson mass in the standard model.
In *Physical Review*, **vol. D69** p. 053006, 2004.
doi:10.1103/PhysRevD.69.053006.
arXiv:hep-ph/0311148.
- [26] S. D. Drell and T.-M. Yan.
Massive Lepton-Pair Production in Hadron-Hadron Collisions at High Energies.
In *Physical Review Letters*, **vol. 25** pp. 316–320, 1970.
doi:10.1103/PhysRevLett.25.316.
- [27] S. D. Drell and T.-M. Yan.
Massive Lepton-Pair Production in Hadron-Hadron Collisions at High Energies.
In *Physical Review Letters*, **vol. 25** pp. 902–902, 1970.
doi:10.1103/PhysRevLett.25.902.2.
- [28] M. Schott and M. Dunford.
Review of single vector boson production in pp collisions at $\sqrt{s} = 7$ TeV.
In *European Physical Journal*, **vol. C74** p. 2916, 2014.
doi:10.1140/epjc/s10052-014-2916-1.
arXiv:1405.1160.
- [29] T. Sjöstrand, S. Mrenna and P. Skands.
PYTHIA 6.4 Physics and Manual, 2006.
doi:10.1088/1126-6708/2006/05/026.
arXiv:hep-ph/0603175.
- [30] T. Sjöstrand, S. Mrenna and P. Skands.
A Brief Introduction to PYTHIA 8.1.

BIBLIOGRAPHY

- In Computer Physics Communications, **vol. 178**(11) pp. 852–867, 2007.
doi:10.1016/j.cpc.2008.01.036.
arXiv:0710.3820.
- [31] J. C. Collins, D. E. Soper and G. F. Sterman.
Factorization of Hard Processes in QCD.
In Advanced Series on Directions in High Energy Physics, **vol. 5** pp. 1–91, 1989.
doi:10.1142/9789814503266-0001.
arXiv:hep-ph/0409313.
- [32] J. M. Campbell, J. W. Huston and W. J. Stirling.
Hard Interactions of Quarks and Gluons: A Primer for LHC Physics.
In Reports on Progress in Physics, **vol. 70** p. 89, 2007.
doi:10.1088/0034-4885/70/1/R02.
arXiv:hep-ph/0611148.
- [33] P. M. Nadolsky, H.-L. Lai, Q.-H. Cao et al.
Implications of CTEQ global analysis for collider observables.
In Physical Review, **vol. D78** p. 013004, 2008.
doi:10.1103/PhysRevD.78.013004.
arXiv:0802.0007.
- [34] A. D. Martin, W. J. Stirling, R. S. Thorne et al.
Parton distributions for the LHC.
In European Physical Journal, **vol. C63** pp. 189–285, 2009.
doi:10.1140/epjc/s10052-009-1072-5.
arXiv:0901.0002.
- [35] S. Alekhin, J. Blumlein, S. Klein et al.
The 3, 4, and 5-flavor NNLO Parton from Deep-Inelastic-Scattering Data and at Hadron Colliders.
In Physical Review, **vol. D81** p. 014032, 2010.
doi:10.1103/PhysRevD.81.014032.
arXiv:0908.2766.
- [36] M. Gluck, P. Jimenez-Delgado and E. Reya.
Dynamical parton distributions of the nucleon and very small- x physics.
In European Physical Journal, **vol. C53** pp. 355–366, 2008.
doi:10.1140/epjc/s10052-007-0462-9.
arXiv:0709.0614.
- [37] R. D. Ball, V. Bertone, L. Del Debbio et al.
Precision NNLO determination of $\alpha_s(M_Z)$ using an unbiased global parton set.
In Physics Letters, **vol. B707** pp. 66–71, 2012.
doi:10.1016/j.physletb.2011.11.053.
arXiv:1110.2483.
- [38] H.-L. Lai, M. Guzzi, J. Huston et al.
New parton distributions for collider physics.
In Physical Review, **vol. D82** p. 074024, 2010.
doi:10.1103/PhysRevD.82.074024.
arXiv:1007.2241.

- [39] G. Aad et al. (ATLAS).
Studies of theoretical uncertainties on the measurement of the mass of the W boson at the LHC.
 Tech. Rep. ATL-PHYS-PUB-2014-015, CERN, Geneva, 2014.
 URL <https://cds.cern.ch/record/1956455>.
- [40] G. Aad et al. (ATLAS).
Measurement of the Z/γ^ boson transverse momentum distribution in pp collisions at $\sqrt{s} = 7$ TeV with the ATLAS detector.*
 In Journal of High Energy Physics, **vol. 09** p. 145, 2014.
 doi:10.1007/JHEP09(2014)145.
 arXiv:1406.3660.
- [41] F. Siegert.
Monte-Carlo event generation for the LHC.
 Ph.D. thesis, University of Durham, 2010.
- [42] D. Fournier.
Performance of the LHC, ATLAS and CMS in 2011.
 In European Physical Journal Web of Conferences, **vol. 28** p. 01 003, 2012.
 doi:10.1051/epjconf/20122801003.
 arXiv:1201.4681.
- [43] M. Karnevskiy, T.-H. Lin, M. Schott et al.
Measurement of the transverse momentum and azimuthal decorrelation of leptons in DrellYan events at $\sqrt{s} = 8$ TeV with ATLAS.
 Tech. Rep. ATL-COM-PHYS-2014-281, CERN, Geneva, 2014.
 URL <https://cds.cern.ch/record/1694674>.
- [44] T. Affolder et al. (CDF).
Measurement of the W boson mass with the Collider Detector at Fermilab.
 In Physical Review, **vol. D64** p. 052 001, 2001.
 doi:10.1103/PhysRevD.64.052001.
 arXiv:hep-ex/0007044.
- [45] V. M. Abazov et al. (D0).
Improved W boson mass measurement with the DØ detector.
 In Physical Review, **vol. D66** p. 012 001, 2002.
 doi:10.1103/PhysRevD.66.012001.
 arXiv:hep-ex/0204014.
- [46] S. Schael et al. (ALEPH).
Measurement of the W boson mass and width in e^+e^- collisions at LEP.
 In European Physical Journal, **vol. C47** pp. 309–335, 2006.
 doi:10.1140/epjc/s2006-02576-8.
 arXiv:hep-ex/0605011.
- [47] P. Achard et al. (L3).
Measurement of the mass and the width of the W boson at LEP.
 In European Physical Journal, **vol. C45** pp. 569–587, 2006.
 doi:10.1140/epjc/s2005-02459-6.
 arXiv:hep-ex/0511049.

BIBLIOGRAPHY

- [48] G. Abbiendi et al. (OPAL).
Measurement of the mass and width of the W boson.
In European Physical Journal, **vol. C45** pp. 307–335, 2006.
doi:10.1140/epjc/s2005-02440-5.
arXiv:hep-ex/0508060.
- [49] J. Abdallah et al. (DELPHI).
*Measurement of the Mass and Width of the W Boson in e^+e^- Collisions at $\sqrt{s} = 161$ -
 $GeV - 209-GeV$.*
In European Physical Journal, **vol. C55** pp. 1–38, 2008.
doi:10.1140/epjc/s10052-008-0585-7.
arXiv:0803.2534.
- [50] T. Aaltonen et al. (CDF).
Precise measurement of the W-boson mass with the CDF II detector.
In Physical Review Letters, **vol. 108** p. 151 803, 2012.
doi:10.1103/PhysRevLett.108.151803.
arXiv:1203.0275.
- [51] V. M. Abazov et al. (D0).
Measurement of the W boson mass with the D0 detector.
In Physical Review, **vol. D89**(1) p. 012 005, 2014.
doi:10.1103/PhysRevD.89.012005.
arXiv:1310.8628.
- [52] F. Marcastel.
CERN's Accelerator Complex. La chaîne des accélérateurs du CERN, 2013.
General Photo, URL <https://cds.cern.ch/record/1621583>.
- [53] G. Aad et al. (ATLAS).
The ATLAS Experiment at the CERN Large Hadron Collider.
In Journal of Instrumentation, **vol. 3** p. S08 003, 2008.
doi:10.1088/1748-0221/3/08/S08003.
- [54] S. Chatrchyan et al. (CMS).
The CMS experiment at the CERN LHC.
In Journal of Instrumentation, **vol. 3** p. S08 004, 2008.
doi:10.1088/1748-0221/3/08/S08004.
- [55] J. Schukraft (ALICE).
The ALICE heavy-ion experiment at the CERN LHC.
In Nuclear Physics, **vol. A566** pp. 311 – 319, 1994.
doi:http://dx.doi.org/10.1016/0375-9474(94)90637-8.
- [56] M. Harrison, T. Ludlam and S. Ozaki.
RHIC project overview.
In Nuclear Instruments and Methods in Physics Research, **vol. A499**(2–3) pp. 235 –
244, 2003.
doi:http://dx.doi.org/10.1016/S0168-9002(02)01937-X.
- [57] A. A. Alves, Jr. et al. (LHCb).
The LHCb Detector at the LHC.
In Journal of Instrumentation, **vol. 3** p. S08 005, 2008.

doi:10.1088/1748-0221/3/08/S08005.

- [58] A. D. Sakharov.
Violation of CP invariance, C asymmetry, and baryon asymmetry of the universe.
 In Soviet Physics Uspekhi, **vol. 34**(5) p. 392, 1991.
 URL <http://stacks.iop.org/0038-5670/34/i=5/a=A08>.
- [59] G. Anelli et al. (TOTEM).
The TOTEM Experiment at the CERN Large Hadron Collider.
 In Journal of Instrumentation, **vol. 3**(08) p. S08 007, 2008.
 URL <http://stacks.iop.org/1748-0221/3/i=08/a=S08007>.
- [60] O. Adriani et al. (LHCf).
The LHCf detector at the CERN Large Hadron Collider.
 In Journal of Instrumentation, **vol. 3** p. S08 006, 2008.
 doi:10.1088/1748-0221/3/08/S08006.
- [61] L. Fabbri.
Forward Detectors in ATLAS: ALFA, ZDC and LUCID.
 Tech. Rep. ATL-LUM-SLIDE-2009-071, 2009.
 URL <https://cds.cern.ch/record/1172844>.
- [62] G. Aad et al. (ATLAS).
Studies of the performance of the ATLAS detector using cosmic-ray muons.
 In European Physical Journal, **vol. C71** p. 1593, 2011.
 doi:10.1140/epjc/s10052-011-1593-6.
 arXiv:1011.6665.
- [63] J. Pequenao and P. Schaffner.
An computer generated image representing how ATLAS detects particles.
 Tech. Rep. CERN-EX-1301009, 2013.
 URL <https://cds.cern.ch/record/1505342>.
- [64] *Luminosity Public Results.*
<https://twiki.cern.ch/twiki/bin/view/AtlasPublic/LuminosityPublicResults>.
 Accessed: 2015-10-31.
- [65] H. Wilkens and the ATLAS LArg Collaboration.
The ATLAS Liquid Argon calorimeter: An overview.
 In Journal of Physics: Conference Series, **vol. 160**(1) p. 012 043, 2009.
 URL <http://stacks.iop.org/1742-6596/160/i=1/a=012043>.
- [66] G. Aad et al. (ATLAS).
Measurement of the Inelastic Proton-Proton Cross-Section at $\sqrt{s} = 7$ TeV with the ATLAS Detector.
 In Nature Communications, **vol. 2** p. 463, 2011.
 doi:10.1038/ncomms1472.
 arXiv:1104.0326.
- [67] W. Liebig and D. Orestano.
Muon Reconstruction Performance.
 Tech. Rep. ATLAS-COM-CONF-2010-065, CERN, Geneva, 2010.
 (Was originally 'ATL-COM-PHYS-2010-430'), URL <https://cds.cern.ch/record/1273758>.

BIBLIOGRAPHY

- [68] G. Aad et al. (ATLAS).
Expected Performance of the ATLAS Experiment - Detector, Trigger and Physics, 2009.
arXiv:0901.0512.
- [69] G. Aad et al. (ATLAS).
Electron reconstruction and identification efficiency measurements with the ATLAS detector using the 2011 LHC proton-proton collision data.
In European Physical Journal, **vol. C74(7)** p. 2941, 2014.
doi:10.1140/epjc/s10052-014-2941-0.
arXiv:1404.2240.
- [70] G. Aad et al. (ATLAS).
Jet energy measurement with the ATLAS detector in proton-proton collisions at $\sqrt{s} = 7$ TeV.
In European Physical Journal, **vol. C73(3)** p. 2304, 2013.
doi:10.1140/epjc/s10052-013-2304-2.
arXiv:1112.6426.
- [71] M. Cacciari, G. P. Salam and G. Soyez.
The Anti- $k(t)$ jet clustering algorithm.
In Journal of High Energy Physics, **vol. 04** p. 063, 2008.
doi:10.1088/1126-6708/2008/04/063.
arXiv:0802.1189.
- [72] T. Sakuma (CMS).
Missing E_T Reconstruction with the CMS Detector.
In Journal of Physics Conference Series, **vol. 404** p. 012 010, 2012.
doi:10.1088/1742-6596/404/1/012010.
arXiv:1210.4221.
- [73] G. Aad et al.
The ATLAS Simulation Infrastructure.
In The European Physical Journal, **vol. C70(3)** pp. 823–874, 2010.
doi:10.1140/epjc/s10052-010-1429-9.
- [74] G. Corcella, I. G. Knowles, G. Marchesini et al.
HERWIG 6: An Event generator for hadron emission reactions with interfering gluons (including supersymmetric processes).
In Journal of High Energy Physics, **vol. 01** p. 010, 2001.
doi:10.1088/1126-6708/2001/01/010.
arXiv:hep-ph/0011363.
- [75] M. Bahr et al.
Herwig++ Physics and Manual.
In European Physical Journal, **vol. C58** pp. 639–707, 2008.
doi:10.1140/epjc/s10052-008-0798-9.
arXiv:0803.0883.
- [76] T. Gleisberg, S. Hoeche, F. Krauss et al.
Event generation with SHERPA 1.1.
In Journal of High Energy Physics, **vol. 02** p. 007, 2009.
doi:10.1088/1126-6708/2009/02/007.

arXiv:0811.4622.

- [77] S. Catani, F. Krauss, R. Kuhn et al.
QCD matrix elements + parton showers.
 In Journal of High Energy Physics, **vol. 11** p. 063, 2001.
 doi:10.1088/1126-6708/2001/11/063.
 arXiv:hep-ph/0109231.
- [78] F. Krauss.
Matrix elements and parton showers in hadronic interactions.
 In Journal of High Energy Physics, **vol. 08** p. 015, 2002.
 doi:10.1088/1126-6708/2002/08/015.
 hep-ph/0205283.
- [79] M. L. Mangano, M. Moretti and R. Pittau.
Multijet matrix elements and shower evolution in hadronic collisions: $Wb\bar{b} + n$ jets as a case study.
 In Nuclear Physics, **vol. B632** pp. 343–362, 2002.
 doi:10.1016/S0550-3213(02)00249-3.
 arXiv:hep-ph/0108069.
- [80] S. Frixione and B. R. Webber.
Matching NLO QCD computations and parton shower simulations.
 In Journal of High Energy Physics, **vol. 06** p. 029, 2002.
 doi:10.1088/1126-6708/2002/06/029.
 arXiv:hep-ph/0204244.
- [81] S. Frixione, P. Nason and C. Oleari.
Matching NLO QCD computations with Parton Shower simulations: the POWHEG method.
 In Journal of High Energy Physics, **vol. 11** p. 070, 2007.
 doi:10.1088/1126-6708/2007/11/070.
 0709.2092.
- [82] C. Balazs and C. P. Yuan.
Soft gluon effects on lepton pairs at hadron colliders.
 In Physical Review, **vol. D56** pp. 5558–5583, 1997.
 doi:10.1103/PhysRevD.56.5558.
 arXiv:hep-ph/9704258.
- [83] E. Barberio, B. van Eijk and Z. Was.
PHOTOS: A Universal Monte Carlo for QED radiative corrections in decays.
 In Computer Physics Communications, **vol. 66** pp. 115–128, 1991.
 doi:10.1016/0010-4655(91)90012-A.
- [84] S. Catani and M. Grazzini.
An NNLO subtraction formalism in hadron collisions and its application to Higgs boson production at the LHC.
 In Physical Review Letters, **vol. 98** p. 222002, 2007.
 doi:10.1103/PhysRevLett.98.222002.
 arXiv:hep-ph/0703012.
- [85] S. Catani, L. Cieri, G. Ferrera et al.

BIBLIOGRAPHY

- Vector boson production at hadron colliders: a fully exclusive QCD calculation at NNLO.*
In Physical Review Letters, **vol. 103** p. 082001, 2009.
doi:10.1103/PhysRevLett.103.082001.
arXiv:0903.2120.
- [86] G. Aad et al. (ATLAS).
ATLAS Run 1 Pythia8 tunes.
Tech. Rep. ATL-PHYS-PUB-2014-021, CERN, Geneva, 2014.
URL <http://cds.cern.ch/record/1966419>.
- [87] S. Agostinelli et al. (GEANT4).
GEANT4: A Simulation toolkit.
In Nuclear Instruments and Methods in Physics Research, **vol. A506** pp. 250–303, 2003.
doi:10.1016/S0168-9002(03)01368-8.
- [88] G. Grindhammer and S. Peters.
The Parameterized simulation of electromagnetic showers in homogeneous and sampling calorimeters.
In *International Conference on Monte Carlo Simulation in High-Energy and Nuclear Physics - MC 93 Tallahassee, Florida, February 22-26, 1993*. 1993.
arXiv:hep-ex/0001020.
- [89] G. Duckeck, D. Barberis, R. Hawkings et al. (ATLAS).
ATLAS computing: Technical design report.
Tech. Rep. CERN-LHCC-2005-022, ATLAS-TRD-017, 2005.
- [90] N. Andari, M. Boonekamp, R. Hanna et al.
Measurement of m_W at 7 TeV: Physics modeling.
Tech. Rep. ATL-COM-PHYS-2014-1436, CERN, Geneva, 2014.
URL <https://cds.cern.ch/record/1966965>.
- [91] K. Bachas et al.
Measurement and QCD Analysis of Differential Inclusive $W^\pm \rightarrow l\nu$ and $Z \rightarrow ll$ Production and Leptonic Decay Cross Sections with ATLAS.
Tech. Rep. ATL-COM-PHYS-2013-217, CERN, Geneva.
URL <https://cds.cern.ch/record/1517987>.
- [92] G. Altarelli, R. Kleiss and C. Verzegnassi (eds.).
Z Physics at LEP 1, CERN-89-08-V-1, CERN-YELLOW-89-08-V-1. 1989.
- [93] W. T. Giele and S. Keller.
Determination of W-boson properties at hadron colliders.
In Physical Review D, **vol. 57** pp. 4433–4440, 1998.
doi:10.1103/PhysRevD.57.4433.
- [94] N. Vranjes, T. Petersen and M. Karnevskiy.
Measurement of m_W at 7 TeV: Muon momentum corrections and uncertainties.
Tech. Rep. ATL-COM-PHYS-2014-1433, CERN, Geneva, 2014.
URL <https://cds.cern.ch/record/1966962>.
- [95] A. Dimitrievska, N. Vranjes, M. Schott et al.
Measurement of M_W at 7 TeV: Hadronic recoil corrections.
Tech. Rep. ATL-COM-PHYS-2015-344, CERN, Geneva, 2015.
URL <https://cds.cern.ch/record/2013274>.

- [96] L. Devroye.
Non-uniform random variate generation.
 Springer-Verlag, 1986.
 ISBN 9783540963059.
- [97] J. Beringer, B. T. Amadio, C. Gwilliam et al.
Offline beam spot reconstruction in ATLAS during Run 1.
 Tech. Rep. ATL-COM-DAPR-2014-013, CERN, Geneva, 2014.
 URL <https://cds.cern.ch/record/1978679>.
- [98] C. Zimmermann, M. Schott and M. Karnevskiy.
Measurement of M_W at 7 TeV: Muon efficiency corrections and uncertainties.
 Tech. Rep. ATL-COM-PHYS-2015-073, CERN, Geneva, 2015.
 URL <https://cds.cern.ch/record/1987497>.
- [99] F. Kohn.
Measurement of the charge asymmetry in top quark pair production in pp collision data at $\sqrt{s} = 7$ TeV using the ATLAS detector.
 Ph.D. thesis, Georg-August-Universität Göttingen, 2012.
 Presented 07 Mar 2012, URL <http://cds.cern.ch/record/1434377>.
- [100] M. Baak, C. Guyot, M. Hauschild et al.
Data Quality Status Flags and Good Run Lists for Physics Analysis in ATLAS.
 Tech. Rep. ATL-COM-GEN-2009-015, CERN, Geneva, 2009.
 URL <https://cds.cern.ch/record/1168026>.
- [101] O. Arnaez et al.
Electron efficiency measurements using ATLAS 2010 data at $\sqrt{s} = 7$ TeV: Supporting note for the 2010 egamma paper.
 Tech. Rep. ATL-COM-PHYS-2011-322, CERN, Geneva, 2011.
 URL <https://cds.cern.ch/record/1340242>.
- [102] M. Bellomo et al.
Muon reconstruction efficiency in reprocessed 2010 LHC proton-proton collision data recorded with the ATLAS detector.
 Tech. Rep. ATLAS-CONF-2011-063, CERN, Geneva, 2011.
 URL <https://cds.cern.ch/record/1345743>.
- [103] J. Almond et al.
Performance of the ATLAS muon trigger in 2011.
 Tech. Rep. ATLAS-COM-CONF-2012-087, CERN, Geneva, 2012.
 URL <https://cds.cern.ch/record/1452620>.
- [104] B. Abbott et al. (D0).
A measurement of the W boson mass.
 In Physical Review, **vol. D58** p. 092003, 1998.
 doi:10.1103/PhysRevD.58.092003.
 arXiv:hep-ex/9712029.
- [105] G. Watt and R. Thorne.
Study of Monte Carlo approach to experimental uncertainty propagation with MSTW 2008 PDFs.
 In Journal of High Energy Physics, **vol. 1208** p. 052, 2012.

BIBLIOGRAPHY

- doi:10.1007/JHEP08(2012)052.
arXiv:1205.4024.
- [106] K. Knight.
Mathematical Statistics.
Chapman & Hall/CRC Texts in Statistical Science. CRC Press, 1999.
ISBN 9781584888567.
- [107] N. Besson, M. Boonekamp, E. Klinkby et al. (ATLAS).
Re-evaluation of the LHC potential for the measurement of M_W .
In European Physical Journal, **vol. C57** pp. 627–651, 2008.
doi:10.1140/epjc/s10052-008-0774-4.
arXiv:0805.2093.
- [108] M. L. Mangano and J. Rojo.
Cross Section Ratios between different CM energies at the LHC: opportunities for precision measurements and BSM sensitivity.
In Journal of High Energy Physics, **vol. 08** p. 010, 2012.
doi:10.1007/JHEP08(2012)010.
1206.3557.
- [109] N. Andari, M. Boonekamp, J.-B. Blanchard et al.
Measurement of M_W at 7 TeV: Z-based cross check measurements.
Tech. Rep. ATL-COM-PHYS-2014-1437, CERN, Geneva, 2014.
URL <https://cds.cern.ch/record/1966966>.
- [110] G. Aad et al. (ATLAS).
Measurement of the forward-backward asymmetry of Z/γ^ bosons decaying into electron and muon pairs with the ATLAS detector at $\sqrt{s} = 7$ TeV*.
Tech. Rep. ATLAS-CONF-2013-043, CERN, Geneva.
URL <https://cds.cern.ch/record/1544035>.
- [111] R. Nisius.
On the combination of correlated estimates of a physics observable.
In European Physical Journal, **vol. C74(8)** p. 3004, 2014.
doi:10.1140/epjc/s10052-014-3004-2.
arXiv:1402.4016.
- [112] R. Nisius.
BLUE: a software package to combine correlated uncertainties of physics observables within ROOT using the Best Linear Unbiased Estimate method - Program manual, Version 2.1.0.
URL <http://blue.hepforge.org>.
- [113] G. Aad et al. (ATLAS).
Measurement of the transverse momentum and φ_η^ distributions of Drell-Yan lepton pairs in proton-proton collisions at $\sqrt{s} = 8$ TeV with the ATLAS detector*.
Tech. Rep. CERN-PH-EP-2015-275, 2015.
arXiv:1512.02192.
- [114] H. Paukkunen and P. Zurita.
PDF reweighting in the Hessian matrix approach.
In Journal of High Energy Physics, **vol. 12** p. 100, 2014.

- doi:10.1007/JHEP12(2014)100.
arXiv:1402.6623.
- [115] C. Zimmermann.
Optimized electron identification with the forward calorimeters of the ATLAS detector for the 2012 data.
Tech. Rep. ATL-COM-PHYS-2013-1589, CERN, Geneva, 2013.
URL <https://cds.cern.ch/record/1633158>.
- [116] G. Aad et al. (ATLAS).
Luminosity Determination in pp Collisions at $\sqrt{s} = 7$ TeV using the ATLAS Detector at the LHC.
In European Physical Journal, **vol. C71** p. 1630, 2011.
arXiv:1101.2185.
- [117] G. Aad et al. (ATLAS).
Electron performance measurements with the ATLAS detector using the 2010 LHC proton-proton collision data, 2012.
arXiv:1110.3174.
- [118] S. Menke.
ClusterMoments.
Web Site, 2013.
Available online at <https://twiki.cern.ch/twiki/bin/viewauth/AtlasComputing/ClusterMoments>; visited on 2013-12-02.
- [119] R. A. Fisher.
The Use of Multiple Measurements in Taxonomic Problems.
In Annals of Eugenics, **vol. 7(2)** pp. 179–188, 1936.
doi:10.1111/j.1469-1809.1936.tb02137.x.
- [120] C. Weinsheimer.
Forward energy scales.
Web Site, 2013.
Available online at <https://indico.cern.ch/contributionDisplay.py?contribId=64&sessionId=15&confId=219420>; visited on 2014-01-08.
- [121] W. Verkerke and D. Kirkby.
The RooFit toolkit for data modeling, 2003.
arXiv:physics/0306116.
- [122] A. Hoecker, P. Speckmayer, J. Stelzer et al.
TMVA: Toolkit for Multivariate Data Analysis.
In Proceedings of Science, **vol. ACAT** p. 040, 2007.
arXiv:physics/0703039.
- [123] M. Boonekamp, R. Caputo, G. Cattani et al.
Measurement of the forward-backward asymmetry of Z/γ^ bosons decaying into electron and muon pairs with the ATLAS detector at $\sqrt{s} = 7$ TeV.*
Tech. Rep. ATLAS-COM-CONF-2013-046, CERN, Geneva, 2013.
URL <https://cds.cern.ch/record/1537994>.
- [124] R. Hanna et al.
Measurement of M_W with 7 TeV data: W boson mass measurement.

BIBLIOGRAPHY

Tech. Rep. ATL-COM-PHYS-2014-1569, CERN, Geneva, 2014.
URL <https://cds.cern.ch/record/1976186>.

List of Tables

2.1.	Exchange bosons in the Standard Model	8
2.2.	Particle content of the Standard Model	9
3.1.	Overview of previous measurements of M_W and Γ_W	33
4.1.	Overview of the PIX detector.	41
4.2.	Summary of the different calorimeter sub-systems.	43
4.3.	Granularity of the electromagnetic calorimeters.	45
4.4.	Overview of the different components of the ATLAS muon system.	46
4.5.	Different regions of the muon system.	48
5.1.	Overview of the different Monte Carlo generators used at ATLAS.	57
5.2.	Overview of the MC samples used for the analyses performed on 2011 data.	58
6.1.	Bin definitions for the 1-D, 2-D and 3-D scale factors.	68
6.2.	Overview of the MC samples used for the Tag and Probe analyses performed on 2011 data.	72
6.3.	Quality cuts enforced on the track segment in the inner detector.	73
6.4.	Overview of the isolation definitions used to obtain the muon efficiency scale factors.	75
6.5.	Groups of uncertainties as used in the control plots in the following sections.	76
7.1.	Overview of selected events in the numerator and denominator for data and all background contributions.	79
7.2.	Resulting fit values for the fits shown in Figure 7.10(a).	88
8.1.	Definition of the trigger periods	91
8.2.	Overview of selected events in the numerator and denominator for data and all background contributions for the determination of the EF_MU18_MEDIUM_STD trigger scale factors.	94
8.3.	Values obtained in the fit to the trigger scale factors shown in Figure 8.11.	103
9.1.	Overview of selected events in the numerator and denominator for data and all background contributions.	112
9.2.	Overview of the fitted values.	120
10.1.	χ_{red}^2 for a sample of control distributions.	124
10.2.	Overview of the values of χ_{red}^2 for the W -like selection.	130
11.1.	Overview of the relative uncertainty on the uncertainty obtained via Toy MCs.	142
11.2.	Uncertainties investigated in the measurement of M_W and M_Z	143

LIST OF TABLES

11.3. Estimations for the relative uncertainty $\Delta a/a$ on the muon scale and resolution, as well as for the hadronic recoil scale and resolution.	144
12.1. Bin definitions for the measurement of M_Z	147
12.2. Number of pre-selected muons per cut for each sample used in the measurement of M_Z	149
12.3. Number of selected events per cut for each sample used in the measurement of M_Z	149
12.4. Fit results for M_Z in the inclusive fit region.	161
12.5. Overview of the deviations between the fit results and the world average of M_Z	162
13.1. Bin definitions for the measurement of M_W	163
13.2. Number of pre-selected muons per cut for each sample used in the measurement of M_W	166
13.3. Number of selected events per cut for each sample used in the measurement of M_W	167
13.4. Overview of the estimated fraction of QCD background events in each fit region.	169
13.5. Final result for the measurement of M_W	179
13.6. Overview of the uncertainties on M_W due to the different sub-sources of the muon efficiency scale factors.	183
13.7. Comparison of previous measurements of M_W with the results of this thesis.	184
13.8. Projections for the statistical uncertainty of M_W on the full data set.	186
A.1. Map of the bin numbering scheme.	199
A.2. Safety cuts for the signal selection	205
A.3. Overview of the SBR variations	208
A.4. Values used for the different variations	209
A.5. Overview of the scale factors obtained with the methods described above.	214
B.1. Overview of selected events in the numerator and denominator for data and all background contributions for the determination of the EF_MU18_BG5 trigger scale factors.	221
B.2. Overview of selected events in the numerator and denominator for data and all background contributions for the determination of the EF_MU18_G6I trigger scale factors.	221
B.3. Overview of selected events in the numerator and denominator for data and all background contributions for the determination of the EF_MU18_MEDIUM_L3L4 trigger scale factors.	222
C.1. Overview of selected events in the numerator and denominator for data and all background contributions for the determination of ID track reconstruction scale factors.	234
C.2. Resulting fit values for the fits shown in Figure C.4.	238

List of Figures

1.1.	Current state of the consistency test of the Standard Model via M_W , M_H and M_t	5
2.1.	Illustration of the potential $V = -\mu^2\phi^\dagger\phi + \lambda(\phi^\dagger\phi)^2$ as a function of φ^+ and φ^0	13
2.2.	Feynman diagram for one of the processes for electron scattering.	16
2.3.	Leading order diagram for the e^-e^- scattering process.	17
2.4.	Next-to-Leading order diagram for the e^-e^- scattering process.	17
2.5.	Next-to-leading order corrections to the propagator of the W boson.	19
3.1.	Feynman diagram of the Drell-Yan process.	21
3.2.	Typical spectra of lepton p_T and transverse mass m_T	24
3.3.	Broadening of the distribution of lepton p_T due to non-zero transverse momentum of the intermediary vector boson.	24
3.4.	Probability density to find a parton of given flavor as function of Bjorken x	27
3.5.	Kinematic plane spanned by Bjorken x and Q^2 with a selection of experiments and their coverage.	27
3.6.	Examples for higher-order QCD contributions to the Drell-Yan process.	28
3.7.	Higher-order electroweak contributions to the Drell-Yan process	28
3.8.	Illustration of a proton-proton collision	29
3.9.	Pile-up distribution for data taken in 2011.	30
3.10.	Examples for electroweak background processes.	31
3.11.	Example for a process producing $t\bar{t}$ pairs.	32
4.1.	Overview of the CERN accelerator complex.	36
4.2.	Illustration of the ATLAS detector	38
4.3.	Working principle of the ATLAS detector	39
4.4.	Illustration of the Inner Detector	41
4.5.	Illustration of the calorimeter	43
4.6.	Illustration of the muon system	46
4.7.	Illustration of the different regions of the muon system	48
4.8.	Illustration of the hadronic recoil in the production of a Z boson.	52
6.1.	Definition of the <i>region</i> variable	68
6.2.	Illustration of the Tag and Probe method	70
6.3.	Illustration of the selections for the ABCD method	74
7.1.	Reconstruction efficiency of muons in $W \rightarrow \mu\nu$ and $Z \rightarrow \mu\mu$ MC samples vs. η and p_T	77
7.2.	Control plots from the QCD background estimation.	79

LIST OF FIGURES

7.3.	Kinematic distributions of probe-tracks comparing data to the combined signal and background prediction.	81
7.4.	Kinematic distributions of probe-tracks comparing data to the combined signal and background prediction.	82
7.5.	Determined reconstruction efficiency by the tag and probe method for data and MC.	83
7.6.	Comparison of reconstruction efficiencies as a function of u_{\parallel}^l , calculated from the hadronic recoil and from p_T^Z	84
7.7.	Determined reconstruction efficiency, using the tag and probe method for Data and MC as a function of p_T	85
7.8.	Reconstruction scale factors determined for the POWHEG MC Simulation.	86
7.9.	Uncertainties on the reconstruction scale factors for the POWHEG MC prediction	87
7.10.	Test of the flatness of the reconstruction scale factors.	88
7.11.	Comparison of Reconstruction scale factors obtained for negative and positive probes.	89
7.12.	Comparison of the reconstruction scale factors obtained with the official ATLAS package and from this analysis in dependence of η	90
8.1.	Trigger efficiency of muons in $W \rightarrow \mu\nu$ and $Z \rightarrow \mu\mu$ MC samples vs. η and p_T	92
8.2.	Control plots from the QCD background estimation.	93
8.3.	Kinematic distributions of probe-tracks comparing data to the combined Signal and Background prediction.	95
8.4.	Determined trigger efficiency by the tag and probe method for Data and MC.	96
8.5.	Determined trigger efficiency by the tag and probe method for Data and MC.	97
8.6.	Resulting trigger scale factors for EF_MU18_BG5.	98
8.7.	Resulting trigger scale factors for EF_MU18_G6I.	99
8.8.	Resulting trigger scale factors for EF_MU18_MEDIUM_L3L4.	100
8.9.	Resulting trigger scale factors for EF_MU18_MEDIUM_STD.	101
8.10.	Uncertainties on the obtained trigger scale for EF_MU18_MEDIUM_STD.	102
8.11.	Trigger scale factors in four regions of the detector.	104
8.12.	Value of p_1 for each of the 18 η bins.	105
8.13.	Comparison of trigger scale factors obtained for negative and positive probes for the trigger EF_MU18_BG5.	106
8.14.	Comparison of trigger scale factors obtained for negative and positive probes for the trigger EF_MU18_G6I.	107
8.15.	Comparison of trigger scale factors obtained for negative and positive probes for the trigger EF_MU18_MEDIUM_L3L4.	108
8.16.	Comparison of trigger scale factors obtained for negative and positive probes for the trigger EF_MU18_MEDIUM_STD.	109
8.17.	Comparison of the trigger scale factors obtained with the official ATLAS package and from this analysis in dependence of η and p_T . The official scale factors were not supplied as function of lepton p_T or u^l	110
9.1.	Isolation efficiency of muons in $W \rightarrow \mu\nu$ and $Z \rightarrow \mu\mu$ MC samples.	112
9.2.	Control plots from the QCD background estimation.	114
9.3.	Kinematic distributions of probe-tracks comparing data to the combined Signal and Background prediction.	115

9.4.	Isolation efficiencies for $p_T^{\text{cone20}}/p_T < 0.1$	116
9.5.	Determined isolation efficiency using the tag and probe method for Data and MC as a function of p_T	117
9.6.	Isolation scale factors determined as a function η , p_T , u_{\parallel}^l	118
9.7.	Uncertainties on the isolation scale factors.	119
9.8.	Test of the flatness of the isolation scale factors.	120
9.9.	Comparison of isolation scale factors obtained for negative and positive probes.	121
10.1.	Distributions of lepton p_T for different settings of the scale factors.	125
10.2.	Distributions of lepton η for different settings of the scale factors.	126
10.3.	Distributions of lepton η for different settings of the scale factors.	127
10.4.	Distributions of the invariant mass for different settings of the scale factors.	128
10.5.	Distributions of u_{\parallel}^l for different settings of the scale factors.	129
10.6.	Distributions for η^+ , φ^+ and p_T^+ in the case of the W -like selection.	131
10.7.	Distributions for η^- , φ^- and p_T^- in the case of the W -like selection.	132
11.1.	Example of the interpolation used to obtain the global minimum of the χ^2 parabola.	139
11.2.	Illustration of the two methods available to obtain MC systematic uncertainties.	140
12.1.	Control Plots for $Z \rightarrow \mu\mu$	151
12.2.	Results from the Monte Carlo-based cross-checks.	153
12.3.	Overview of the fit results for all observables in the <i>Inclusive</i> region.	154
12.4.	Selected control plots from the consistency tests.	155
12.5.	Overview of the fit results obtained in the observable $M_{\mu\mu}$	156
12.6.	Overview of the fit results obtained in the observable p_T^+ and p_T^-	157
12.7.	Overview of the fit results obtained in the observable m_T	158
12.8.	Overview of the fit results obtained in the observable E_T^{miss}	159
13.1.	Example of the E_T^{miss} spectrum, used to estimate the amount of QCD background events.	168
13.2.	Control plot for lepton φ , including the full systematic uncertainty.	170
13.3.	Control Plots for $W \rightarrow \mu\nu$	171
13.4.	Results from the Monte Carlo-based cross-checks.	173
13.5.	Overview of the fit results for all observables in the <i>Inclusive</i> region.	174
13.6.	Selected control plots from the consistency tests.	175
13.7.	Overview of the fit results obtained in the observable p_T^μ	176
13.8.	Overview of the fit results obtained in the observable m_T	177
13.9.	Overview of the fit results obtained in the observable E_T^{miss}	178
13.10.	Control distribution of η^μ and p_T^μ showing also the PDF uncertainty.	181
A.1.	$ \eta $ dependence of the signal efficiencies for the 2011 ID on 2012 data	196
A.2.	Pile-up dependence of the signal efficiencies in the EMEC inner wheel for the 2011 ID on 2012 data.	196
A.3.	Pile-up dependence of the signal efficiencies in the FCAL for the 2011 ID on 2012 data.	197
A.4.	Example of a cluster in the central part of the detector with some of the cluster moments used for the forward electron ID.	198

LIST OF FIGURES

A.5. Example of fits performed to estimate the signal and background contribution.	202
A.6. Acceptance and resulting spectra for the first and last bin in $ \eta $	204
A.7. Comparison of signal efficiencies obtained with the ID optimized for sample A on sample B and conversely.	206
A.8. Comparison of signal efficiencies obtained with the ID optimized for sample A on sample B and conversely.	207
A.9. Comparison of signal efficiencies obtained with the ID optimized for sample A on sample B and conversely.	207
A.10. Signal efficiencies as function of n_{pvtx}	210
A.11. Resulting signal efficiencies as a function of $ \eta $ after correcting the cut values on d	210
A.12. p_T dependence of the signal efficiencies in MC.	211
A.13. Background efficiencies for the loose cut set calculated on the background training samples.	212
A.14. Background efficiencies for the medium cut set calculated on the background training samples.	213
A.15. Background efficiencies for the tight cut set calculated on the background training samples.	213
A.16. Overview of the scale factors for each variation in the EMEC IW.	215
A.17. Overview of the scale factors for each variation in the FCAL.	216
A.18. Graphical overview of all scale factors.	216
A.19. Comparison of the predicted and measured values for $\langle \lambda^2 \rangle$ as described in the text.	217
B.1. Trigger efficiency of muons in $W \rightarrow \mu\nu$ and $Z \rightarrow \mu\mu$ MC samples	220
B.2. Kinematic distributions of probe-tracks comparing data to the combined signal and background prediction.	223
B.3. Kinematic distributions of probe-tracks comparing data to the combined signal and background prediction.	224
B.4. Kinematic distributions of probe-tracks comparing data to the combined signal and background prediction.	225
B.5. Determined trigger efficiency by the tag and probe method for Data and MC.	226
B.6. Determined trigger efficiency by the tag and probe method for Data and MC.	227
B.7. Determined trigger efficiency by the tag and probe method for Data and MC.	228
B.8. Uncertainties on the obtained trigger scale for EF_MU18_BG5.	229
B.9. Uncertainties on the obtained trigger scale for EF_MU18_G6I.	230
B.10. Uncertainties on the obtained trigger scale for EF_MU18_MEDIUM_L3L4.	231
C.1. Kinematic distributions of probe muons comparing data to the combined signal and background prediction.	235
C.2. Determined ID track reconstruction efficiency using the tag- and probe-method for MC and data.	236
C.3. ID track reconstruction scale factors determined for the POWHEG MC simulation.	237
C.4. ID track reconstruction scale factors in four regions of the detector with uniform efficiency.	238
C.5. Value of p_1 for each of the 44 η bins.	239

C.6. Uncertainties on the ID track reconstruction scale factors for the POWHEG MC prediction. 240

E. Curriculum Vitae

Christoph Zimmermann

Address	Pfaffengrunder Terrasse 5 D-69115 Heidelberg Germany
Date and Place of Birth	1986-09-07, Essen, Germany
Family Status	married, no children

ACADEMIC CAREER

November 2015 – present	Data Scientist at <i>Blue Yonder</i> , Karlsruhe, Germany
January 2012 – October 2015	PhD Studies at the Institute of Physics, Johannes-Gutenberg- University Mainz, Germany Advisors: ██████████, ██████████
November 2011	Diploma (equivalent to Master) in Physics, Thesis: <i>Feasibility Studies and First Measurement of Initial State Radiation at BES-III</i> , Advisor: ██████████, Grade: 1.0 with distinction
August 2009 – December 2009	Study of Physics, Royal Institute of Technology, Stockholm, Sweden
April 2006 – November 2011	Study of Physics, Johannes-Gutenberg-University Mainz, Germany
August 1997 – March 2006	Gymnasium an der Heizenwies, Idar-Oberstein, Degree: Abitur (equivalent to high school diploma)

SCHOLARSHIPS

Fellow of the Graduate School 'Symmetry Breaking' (DFG/GRK 1581)

KEY PUBLICATIONS

Optimized electron identification with the forward calorimeters of the ATLAS detector for the 2012 data, ref. [115]

Measurement of the forward-backward asymmetry of Z/γ^ bosons decaying into electron and muon pairs with the ATLAS detector at $\sqrt{s}=7$ TeV, ref. [123], forming the basis of ref. [110]*

Measurement of the transverse momentum and azimuthal decorrelation of leptons in Drell-Yan events at $\sqrt{s} = 8$ TeV with ATLAS, ref. [43]

Measurement of M_W at 7 TeV: Muon efficiency corrections and uncertainties, ref. [98]

Measurement of M_W with 7 TeV data: W boson mass measurement, ref. [124]
